High-pressure synthesis, structure and properties of cubic zirconium(IV)- and hafnium(IV) nitrides

Vom Fachbereich Material- und Geowissenschaften
der Technischen Universität Darmstadt
zur Erlangung des akademischen Grades eines
Doctor rerum naturalium
(Dr. rer. nat.)
genehmigte Dissertation

von

M. Sc. Dmytro A. Dzivenko
aus Kramatorsk, Ukraine

Referent:	Prof. Dr. rer. nat. Dr. h. c. Ralf Riedel
Korreferent:	Prof. Dr.-Ing. Dr. h. c. Hartmut Fueß
Tag der Einreichung:	10.11.2008
Tag der mündlichen Prüfung:	17.12.2008

Darmstadt 2009
D 17

dedicated to my parents

Abstract

This thesis is concerned with recently discovered high-pressure (HP) zirconium- and hafnium nitrides having cubic Th_3P_4-type structure, c-M_3N_4 (M = Zr or Hf). These compounds belong to a rapidly growing group of new hard HP nitrides exhibiting advanced properties. The research was focused on (i) synthesis of macroscopic amounts of c-M_3N_4, (ii) investigation of their solid state structure, composition and morphology and (iii) measurement of properties related to potential industrial applications of these compounds as hard wear-resistant materials.

Nitrogen-rich starting materials for high-pressure high-temperature (HP/HT) synthesis of c-M_3N_4, namely nanocrystalline powders of M_3N_{4+x} with distorted NaCl-type structure, had to be prepared in this work because they were not commercially available. They were obtained via HT ammonolysis of the corresponding metal dialkylamides, $M[N(C_2H_5)_2]_4$, at moderate temperatures up to 873 K. Both, c-Zr_3N_4 and c-Hf_3N_4, were synthesized from the nanocrystalline M_3N_{4+x} powders applying a pressure of 12 GPa and a temperature of 1873 K using a multi-anvil HP-apparatus. The products were characterized using various techniques including powder XRD (Rietveld refinement), TEM, EPMA, SEM/EDX and Raman spectroscopy.

In the case of zirconium nitride, formation of a single phase crystalline material was verified by both XRD and TEM. The presence of a small amount of oxygen in the sample, revealed by EPMA, suggested the formation of oxygen-bearing zirconium(IV) nitride (or oxynitride) having Th_3P_4-type structure, c-$Zr_{2.86}(N_{0.88}O_{0.12})_4$. The measured composition was found to correspond to the general formula $Zr_{3-u}(N_{1-u}O_u)_4$ which fulfils the electrical neutrality condition. A high quality of the Rietveld structure refinement of the powder XRD data for c-$Zr_{2.86}(N_{0.88}O_{0.12})_4$ supported the above findings. Further, the assignment of the structure of the obtained oxygen-bearing zirconium nitride to the Th_3P_4-type was confirmed by Raman spectroscopic measurements. In contrast to zirconium nitride, a minor oxidation of the hafnium nitride sample led to formation of a mixture of oxygen-poor c-Hf_3N_4 and an oxidic material. The latter was evident from the XRD, EPMA, and SEM/EDX measurements. A detailed analysis of the powder XRD patterns and Rietveld refinement suggested that the oxidic material is comprised of a mixture of the known γ-Hf_2N_2O and oI-HfO_2.

The last part of the thesis concerned the investigation of the properties of the synthesized materials. The bulk moduli of c-$Zr_{2.86}(N_{0.88}O_{0.12})_4$ and c-Hf_3N_4 were determined via their quasi-hydrostatic compression in a diamond anvil cell up to 45 GPa. The obtained values are $B_0 = 219$ GPa ($B_0' = 4.4$) and $B_0 = 227$ GPa ($B_0' = 5.3$) for c-$Zr_{2.86}(N_{0.88}O_{0.12})_4$ and c-Hf_3N_4, respectively. The reduced elastic modulus, $E_r = 224$ GPa, of porous c-$Zr_{2.86}(N_{0.88}O_{0.12})_4$ (volume fraction porosity of 0.3) was measured using nanoindentation techniques. Combining B_0 and E_r values, the lower limits of the shear modulus $G_0 = 96$ GPa, and of the Young's modulus $E_0 = 252$ GPa were determined for the oxygen-bearing c-Zr_3N_4. The nanoindentation hardness and Vickers microhardness, $H_V(1)$, of the porous zirconium nitride sample were measured to be 18 GPa and 12 GPa, respectively. Using a relation between hardness and volume fraction porosity, suggested in the literature, the $H_V(1)$ of the fully dense c-Zr_3N_4 was estimated to exceed 25 GPa. The indentation fracture toughness of 3.2 MPa $m^{1/2}$ for porous c-$Zr_{2.86}(N_{0.88}O_{0.12})_4$ was evaluated from the Vickers indentation cracks. The linear thermal expansion coefficient of the oxygen-bearing c-Zr_3N_4 was found to increase from 6.6×10^{-6} K^{-1} at room temperature to about 14×10^{-6} K^{-1} at 873 K. Onset of the material oxidation in air was observed at 773 K. Finally, the obtained results were compared with existing experimental and theoretical data for c-M_3N_4 and for other related technological materials and discussed with respect to potential industrial applications of c-M_3N_4.

Zusammenfassung

In dieser Arbeit wurden die kürzlich entdeckten kubischen Hochdrucknitride von Zirconium und Hafnium mit der Struktur vom Typ Th_3P_4, c-M_3N_4 (M = Zr or Hf), untersucht. Diese Materialien gehören zu der schnell wachsenden Gruppe harter Hochdrucknitride mit herausragenden Eigenschaften. Folgende Experimente wurden in der Arbeit durchgeführt: (i) Synthese makroskopischer Mengen von c-M_3N_4 bei hohen Drücken, (ii) Untersuchung der Kristallstruktur, der Zusammensetzung und der Morphologie der erhaltenen Produkte und (iii) Bestimmung ihrer Eigenschaften für mögliche Anwendungen als verschleißfeste Werkstoffe.

In dieser Arbeit wurden stickstoffreiche, für die Hochdruck-Hochtemperatursynthese von c-M_3N_4 geeignete Ausgangsmaterialien hergestellt, da sie kommerziell nicht erhältlich sind. Hierbei handelte es sich konkret um Pulver von nanokristallinem M_3N_{4+x} mit verzerrter NaCl-Struktur. Sie wurden mittels Ammonolyse entsprechender Metalldialkylamiden, $M[N(C_2H_5)_2]_4$, bei moderaten Temperaturen bis 873 K hergestellt. Sowohl c-Zr_3N_4 als auch c-Hf_3N_4 wurden aus den nanokristallinen M_3N_{4+x} bei hohen Drücken von 12 GPa und Temperaturen von 1873 K in einer Hochdruck-Vielstempelapparatur synthetisiert. Die Produkte wurden mittels solcher experimentellen Techniken wie Röntgen-Pulverdiffraktometrie (XRD) mit Rietveld-Strukturverfeinerung, Transmissionselektronenmikroskopie (TEM), Elektronenstrahl-Mikroanalyse (ESMA), Rasterelektronenmikroskopie (REM) mit Energiedispersiver Röntgenanalyse (EDX) und Raman-Spektroskopie untersucht.

In Experimenten an Zirconiumnitrid wurde die Bildung eines einphasigen kristallinen Materials sowohl mittels XRD als auch TEM nachgewiesen. Bei ESMA-Untersuchungen wurden in dem Probenmaterial geringe Mengen an Sauerstoff festgestellt, was auf die Bildung von sauerstoffhaltigem Zirconiumnitrid (oder Zirconium-Oxinitrid) mit Struktur vom Typ Th_3P_4 und der Zusammensetzung c-$Zr_{2.86}(N_{0.88}O_{0.12})_4$ hindeutet. Die gemessene Zusammensetzung entspricht zudem der allgemeinen Formel $Zr_{3-u}(N_{1-u}O_u)_4$, welche die Elektroneutralitätsbedingung erfüllt. Ergebnisse der Rietveld-Strukturverfeinerung, die an einem Röntgen-Pulverdiffraktogramm von c-$Zr_{2.86}(N_{0.88}O_{0.12})_4$ durchgeführt wurde, bekräftigten den vorherigen Befund. Raman-spektroskopische Untersuchungen des hergestellten sauerstoffhaltigen Zirconiumnitrids bestätigten ebenfalls diesen Strukturtyp. Im Gegensatz zu Zirconiumnitrid führte eine geringe Verunreinigung des Probenmaterials mit

Sauerstoff bei Hafniumnitrid zur Bildung eines Gemisches aus sauerstoffarmem c-Hf_3N_4 und oxidiertem Material. Dieses Ergebnis folgt aus den XRD-, ESMA-, REM- und EDX-Messungen. Eine detaillierte Analyse des Pulver-Diffraktogramms und die Rietveld-Strukturverfeinerung ergaben, dass das oxidierte Material eine Mischung aus den bereits bekannten Phasen γ-Hf_2N_2O und oI-HfO_2 ist.

Der abschließende Teil der Doktorarbeit befasst sich mit Eigenschaftsuntersuchungen der hergestellten Materialien. Die Kompressionsmodule von c-$Zr_{2.86}(N_{0.88}O_{0.12})_4$ und c-Hf_3N_4 wurden unter quasihydrostatischer Komprimierung in einer Diamantstempelzelle bis 45 GPa gemessen. Die Kompressionsmodule von c-$Zr_{2.86}(N_{0.88}O_{0.12})_4$ und c-Hf_3N_4 wurden zu $B_0 = 219$ GPa ($B_0' = 4.4$) und $B_0 = 227$ GPa ($B_0' = 5.3$) bestimmt. Der so genannte reduzierte elastische Modul E_r von porösem c-$Zr_{2.86}(N_{0.88}O_{0.12})_4$ (Porositätsanteil 30 Vol %) wurde mittels der Nanoindentation-Methode mit 224 GPa gemessen. Durch Verwendung der B_0- und E_r-Werte konnte der untere Grenzwert für das Schubmodul von sauerstoffhaltigem c-Zr_3N_4 auf $G_0 = 96$ GPa und der des Elastizitätsmodul auf $E_0 = 252$ GPa bestimmt werden. Die Nanoindentationshärte von porösem Zirconiumnitrid beträgt 18 GPa, die Vickers-Mikrohärte beträgt $H_V(1) = 12$ GPa. Mit dem literaturbeschriebenen Zusammenhang zwischen Härte und Porosität wird erwartet, dass die Vickers-Mikrohärte von komplett verdichtetem c-Zr_3N_4 25 GPa übersteigt. Aus den bei den Vickers-Härtemessungen entstandenen Risslängen wurde die Bruchzähigkeit des porösen c-$Zr_{2.86}(N_{0.88}O_{0.12})_4$ auf 3.2 MPa $m^{1/2}$ abgeschätzt. Der lineare Wärmeausdehnungskoeffizient des sauerstoffhaltigen c-Zr_3N_4 erwies sich als temperaturabhängig und nahm von 6.6×10^{-6} K^{-1} bei Zimmertemperatur bis auf 14×10^{-6} K^{-1} bei 873 K zu. Eine Oxidation des Materials an der Luft wurde erst bei 773 K beobachtet. Abschließend werden die in dieser Arbeit bestimmten Werte mit früheren experimentellen und theoretischen Ergebnissen für c-M_3N_4 als auch mit Werten von anderen technologisch wichtigen Materialien verglichen. Mögliche Anwendungen von c-M_3N_4 in der Industrie werden diskutiert.

Contents

Abstract ..... **i**

Zusammenfassung ..... **iii**

Contents ..... **v**

List of Figures ..... **viii**

List of Tables ..... **x**

Nomenclature ..... **xi**

1 Introduction and motivation **1**

1.1 High pressure in materials chemistry 4
1.1.1 Phase transitions 4
1.1.2 Chemical reactions 9
1.1.3 Summary 10

1.2 Stiffness and hardness 11
1.2.1 Elastic moduli 11
1.2.1.1 Equation of state 14
1.2.1.2 Correlation of elastic moduli with intrinsic material properties 15
1.2.1.3 Correlation of elastic moduli with material microstructure 17
1.2.2 Hardness 18
1.2.2.1 Definition and measurement of hardness 18
1.2.2.2 Correlation of hardness with elastic moduli 21

1.3 Recent advances in high-pressure nitrides 23
1.3.1 Group 14 nitrides 24
1.3.1.1 Carbon nitride 24
1.3.1.2 Spinel nitrides: γ-Si_3N_4, γ-Ge_3N_4 and γ-Sn_3N_4 25
1.3.2 Group 4 transition metal nitrides: δ-MN and c-M_3N_4 28

1.4 Subject of the work 33

2 Experimental techniques **35**

2.1 Preparation of starting material 35
2.1.1 Ammonolysis of metal dialkylamides 35
2.1.2 Hot-gas-extraction elemental analysis 36

2.2 High-pressure techniques for synthesis and in situ examination 38
2.2.1 Introduction to high-pressure techniques 38
2.2.2 Multi-anvil (MA) apparatus 43
2.2.2.1 Walker-type module 43
2.2.2.2 The octahedral pressure assembly 46
2.2.2.3 Pressure and temperature measurement 48
2.2.2.4 HP-HT experimental procedure 48
2.2.2.5. Sample recovery 49

2.3 Analytical methods 49
2.3.1 Powder X-ray diffraction 49
2.3.1.1 In-house X-ray diffractometers 50
2.3.1.2 Synchrotron radiation 51
2.3.1.3 Data processing 52
2.3.2 Electron probe microanalysis (EPMA) 52
2.3.3 Transmission electron microscopy (TEM) 53
2.3.4 Scanning electron microscopy (SEM) 54
2.3.5 Raman spectroscopy 54

2.4 Elasto-mechanical properties 55
2.4.1 Compressibility measurements 55
2.4.2 Vickers indentation 57
2.4.2.1 Indentation size effect (ISE) 57
2.4.2.2 Indentation fracture toughness 58
2.4.2.3 Measurement procedure 61
2.4.3 Instrumented nanoindentation 61
2.4.3.1 Oliver-Pharr method (O&P) 62
2.4.3.2 Continuous stiffness measurement (CSM) technique 64
2.4.3.3 Hertzian contact analysis 65
2.4.3.4 Measurement procedure 67
2.4.4 Elastic moduli evaluation 68

2.5 Thermal expansion and high-temperature oxidation 68

3 Results and discussion 70

3.1 Synthesis of nanocrystalline Zr_3N_{4+x} and Hf_3N_{4+x} powders 71

3.2 High-pressure multi-anvil synthesis of c-Zr_3N_4 and c-Hf_3N_4 73

3.3 Samples characterisation 79
3.3.1 Chemical composition of the high-pressure products 79
3.3.2 Rietveld structure refinement 82
3.3.2.1 Oxygen-bearing c-Zr_3N_4 82
3.3.2.2 c-Hf_3N_4 86
3.3.3 Raman spectroscopy of oxygen-bearing c-Zr_3N_4 90
3.3.4 Thermodynamics of c-$Zr_{2.86}(N_{0.88}O_{0.12})_4$ 92
3.3.5 Microstructure 95

3.4 Elasto-mechanical properties 99
3.4.1 Compressibility measurement 99
3.4.1.1 Oxygen-bearing c-Zr_3N_4 100
3.4.1.2 c-Hf_3N_4 104
3.4.2 Vickers indentation of c-$Zr_{2.86}(N_{0.88}O_{0.12})_4$ 107
3.4.2.1 Vickers microhardness 107
3.4.2.2 Indentation fracture toughness 111
3.4.3 Nanoindentation measurements on c-$Zr_{2.86}(N_{0.88}O_{0.12})_4$ 113
3.4.4 Elastic moduli of c-$Zr_{2.86}(N_{0.88}O_{0.12})_4$ 117

3.5 Thermal properties of c-$Zr_{2.86}(N_{0.88}O_{0.12})_4$ 118
3.5.1 Thermal expansion coefficient 118
3.5.2 High-temperature oxidation stability 120

4 Summary **123**

References **128**

Acknowledgements **141**

Eidesstattliche Erklärung **143**

Curriculum Vitae **144**

List of Figures

1.1 Gibbs free energy - pressure dependence for a first-order phase transition at constant temperature and schematic pressure-temperature phase diagram 5

1.2 Discontinuous changes of volume and entropy accompanying first-order phase transitions 6

1.3 Schematic energy diagrams 8

1.4 Hardness with respect to shear and bulk moduli for a common set of stiff materials 22

1.5 Crystal structures of β- and γ-Si_3N_4 26

1.6 Crystal structure of group 4 transition metal mononitrides, δ-MN 29

1.7 Crystal structure of orthorhombic Zr_3N_4 30

1.8 Crystal structure of c-M_3N_4 (cubic Th_3P_4-type, M = Zr or Hf) 32

2.1 Schematic drawing of the ammonolysis setup 36

2.2 Heating schedules for ammonolysis of $Zr(NEt_2)_4$ and $Hf(NEt_2)_4$ 37

2.3 Schematic drawing of a piston-cylinder and Bridgman's opposite anvils 39

2.4 Schematic drawing of belt and toroid-type high-pressure apparatuses 40

2.5 Principle of a diamond anvil cell and a multi-anvil apparatus 42

2.6 Working principle of the Walker-type module 44

2.7 Second compression stage of a 6/8-type multi-anvil apparatus 45

2.8 Schematic drawing of the octahedral pressure cell 46

2.9 Schematic drawing of a DAC used for compressibility measurements 56

2.10 Crack systems for Vickers indentations: half-penny and Palmqvist cracks 59

2.11 Schematic load-displacement curve and representation of indentation procedure 63

2.12 Schematic CSM load-displacement curve and dynamic model of CSM module 65

2.13 Elastic contact between nonrigid spherical indenter and nonrigid flat surface 66

3.1 SEM pictures of preliminary polished surfaces of zirconium nitride- and hafnium nitride high-pressure products 75

3.2 Preliminary powder XRD pattern of zirconium nitride sample (Z2-01) synthesized at 12 GPa and 1873 K 76

3.3 Preliminary powder XRD pattern of hafnium nitride sample (H1-01) synthesized at 12 GPa and 1873 K 77

3.4 Back scattered electron (BSE) image and element mappings of a portion of the polished surface of the c-Zr_3N_4 sample (Z2-01) measured using EPMA 80

3.5 Back scattered electron (BSE) image and element mappings of the polished surface of the hafnium nitride sample (H1-01) measured using EPMA 81

3.6 Powder XRD pattern of oxygen-bearing c-Zr_3N_4 (Z2-01) 83
3.7 Powder XRD pattern of c-Hf_3N_4 sample (H1-01) 87
3.8 Sections of the powder XRD pattern of the hafnium nitride sample (H1-01) for different 2θ regions 88
3.9 Ambient pressure Raman spectra of c-$Zr_{2.86}(N_{0.88}O_{0.12})_4$ synthesized using a multi-anvil apparatus and of c-Zr_3N_4 synthesized in a LH-DAC 91
3.10 The enthalpy of formation of c-$ZrN_{3w/4}O_{2-2w}$ as a function of oxygen content 94
3.11 SEM pictures of c-$Zr_{2.86}(N_{0.88}O_{0.12})_4$ (sample Z2-01) 96
3.12 SEM pictures of hafnium nitride sample (H1-01) 97
3.13 SEM picture and N- and O- element mappings of hafnium nitride sample (H1-01) 97
3.14 ED-XRD patterns of c-$Zr_{2.86}(N_{0.88}O_{0.12})_4$ at ambient and high pressures. 100
3.15 V/V_0-pressure dependence of c-$Zr_{2.86}(N_{0.88}O_{0.12})_4$ 101
3.16 $F(f)$-compression data of c-$Zr_{2.86}(N_{0.88}O_{0.12})_4$ 102
3.17 ED-XRD patterns of c-Hf_3N_4 at ambient and high pressures 104
3.18 V/V_0-pressure dependence of c-Hf_3N_4 105
3.19 $F(f)$-compression data of c-Hf_3N_4 106
3.20 SEM pictures of Vickers indentations made in c-$Zr_{2.86}(N_{0.88}O_{0.12})_4$ 108
3.21 Vickers microhardness of c-$Zr_{2.86}(N_{0.88}O_{0.12})_4$ as a function of applied load 109
3.22 Applied load as a function of corresponding mean diagonal of Vickers impression for c-$Zr_{2.86}(N_{0.88}O_{0.12})_4$ 110
3.23 Radial cracks at the corners of the Vickers impression made in c-$Zr_{2.86}(N_{0.88}O_{0.12})_4$ ... 111
3.24 Indentation fracture toughness of porous c-$Zr_{2.86}(N_{0.88}O_{0.12})_4$ in comparison with the K_{Ic} values of δ-MN (M = Ti, Zr, Hf), SiC, Si_3N_4, c-BN and diamond 112
3.25 Typical nanoindentation load-displacement curves for c-$Zr_{2.86}(N_{0.88}O_{0.12})_4$ 114
3.26 Nanoindentation hardness and reduced elastic modulus of c-$Zr_{2.86}(N_{0.88}O_{0.12})_4$, as functions of indentation depth, measured by CSM technique 115
3.27 *In situ* high-temperature X-ray powder diffractograms of c-$Zr_{2.86}(N_{0.88}O_{0.12})_4$ 118
3.28 Lattice parameter of c-$Zr_{2.86}(N_{0.88}O_{0.12})_4$ as a function of temperature. 119
3.29 Linear thermal expansion coefficients of c-$Zr_{2.86}(N_{0.88}O_{0.12})_4$, δ-ZrN and o-$Zr_3N_4$ 120
3.30 X-ray powder diffractograms of c-$Zr_{2.86}(N_{0.88}O_{0.12})_4$ heated in air to 773 K and 873 K, and of the final oxidation product measured at room temperature 121

List of Tables

2.1 Standard multi-anvil OEL/TEL assemblies, corresponding pressure ranges, gasket dimensions and approximate sample volume 45

3.1 Elemental composition of the nanocrystalline M_3N_{4+x} (M = Zr or Hf) powders 72

3.2 Parameters of the HP-HT multi-anvil synthesis experiments along with a brief information on phase content of the products 74

3.3 Elemental composition of the high-pressure zirconium nitride product (Z2-01) determined by EPMA 79

3.4 Results of the Rietveld structure refinement for c-$Zr_{2.86}(N_{0.88}O_{0.12})_4$ 85

3.5 Results of the Rietveld structure refinement for c-Hf_3N_4 89

3.6 Raman shifts of c-$Zr_{2.86}(N_{0.88}O_{0.12})_4$ in comparison with experimental and theoretical values for c-Zr_3N_4 92

3.7 The enthalpies of formation, densities, molar masses, and molar volumes of o-Zr_3N_4, c-Zr_3N_4, m-ZrO_2 and c-$Zr_{2.86}(N_{0.88}O_{0.12})_4$ 95

3.8 Experimental and theoretical values of bulk modulus and its first pressure derivative for c-$Zr_{2.86}(N_{0.88}O_{0.12})_4$, c-$Zr_3N_4$, δ-ZrN, c-$Hf_3N_4$, δ-HfN, c-$Si_3N_4$, c-BN and diamond 103

3.9 Elastic moduli and nanoindentation hardness of c-$Zr_{2.86}(N_{0.88}O_{0.12})_4$ in comparison with earlier experimental and theoretical results for c-Zr_3N_4 and c-$Zr_3(N,O)_4$ 116

Nomenclature

Latin symbols

Symbol	Definition
$\mathbf{A}$	Helmholtz free energy
A	surface area of indenter impression
A_p	projected area of indenter impression
a, a_0	cubic lattice parameter
a_1, a_2, a_3	parameters in proportional specimen resistance model
B, B_0	bulk modulus
B_0'	bulk modulus pressure derivative
B_iso	isotropic temperature factor
b	exponential parameter for porosity dependence
c	crack length or half-penny crack radius
c_{ijkl}	stiffness tensor
d	spacing between atomic planes in crystal lattice
d_v	diagonal length of Vickers impression
$\mathbf{E}$	energy
E, E_0	Young's modulus
$\mathbf{E}_\mathrm{a}$	molar activation energy
E_r	reduced elastic modulus
F	normalized pressure
f	Eulerian strain
$\mathbf{G}$	Gibbs free energy
G, G_0	shear modulus
$\mathbf{H}$	enthalpy
H	hardness
$\Delta\mathbf{H}_\mathrm{f}^{298}$	standard enthalpy of formation
H_V	Vickers hardness
H_V^{true}	load-independent "true" hardness
h	indenter displacement (indentation depth)
h_c	effective contact depth
h_f	residual impression depth
h_max	maximum displacement
h_s	amount of surface depression (sink in)
K_I	stress intensity factor

Symbol	Definition
K_{Ic}	fracture toughness (critical stress intensity factor)
$K_{Ic\text{-}if}$	indentation fracture toughness
L	applied load (force)
L_{max}	maximum applied load
l	Palmqvist crack length
M	elastic modulus (generic notation)
M_m	molar mass
N_c	coordination number
P	pressure
p	volume fraction porosity
P_{tr}	pressure of phase transition
q	exponential parameter in load-displacement relation
R_B, R_p, R_{wp}	Bragg-, profile- and weighted profile agreement factors in Rietveld analysis
R_i	indenter tip radius
$\boldsymbol{r}$	radius vector
r_c	contact area radius
S	entropy
S_c	contact stiffness
sf	scattering factor
T	temperature
T_{tr}	temperature of phase transition
t	time
$\mathbf{U}$	internal energy
$\boldsymbol{u}$	displacement vector
u_z	surface displacement function
V	volume
V_0	volume at ambient pressure
x, y, z	Cartesian coordinates

Greek symbols

Symbol	Definition
α	linear thermal expansion coefficient
β	indenter geometry factor (indentation fracture toughness)
δ_{ij}	Kronecker delta
ε	indenter geometry factor (nanoindentation)
ε_{ij}	strain tensor
η	correction constant for axially nonsymmetrical indenters

Symbol	Definition
2θ	diffraction angle
κ	pre-exponential parameter in load-displacement relation
λ	wavelength
ν, ν_0	Poisson's ratio
ξ	ratio between anion and cation X-ray scattering factors
ρ	density
ρ_e	valence electron density
σ_{ij}	stress tensor
χ^2	chi-squared (goodness-of-fit indicator)
ψ	pyramid half-apex angle

Abbreviations

Abbreviation	Definition
AD-XRD	angle dispersive X-ray diffraction
BM-EOS	Birch-Murnaghan equation of state
BSE	backscattered electrons
CCD	charge-coupled device
CSM	continuous stiffness measurement
DAC	diamond anvil cell
EDX	energy dispersive X-ray (spectroscopy)
ED-XRD	energy dispersive X-ray diffraction
EOS	equation of state
EPMA	electron probe microanalysis
FWHM	full width at half maximum
HP	high pressure
HT	high temperature
HT-XRD	*in situ* high-temperature X-ray diffraction
ICSD	Inorganic Crystal Structure Database
IR	infrared
ISE	indentation size effect
LED	light-emitting diode
LH-DAC	laser-heated diamond anvil cell
M-PSR	modified proportional specimen resistance model
O&P	Oliver-Pharr method
OEL	octahedral edge length
PSR	proportional specimen resistance
PVD	physical vapour deposition

Abbreviation	Definition
RT	room temperature
SEM	scanning electron microscopy
TEL	truncation edge length
TEM	transmission electron microscopy
VFP	volume fraction porosity
VIF	Vickers indentation fracture
XRD	X-ray diffraction

1 Introduction and motivation

Technological progress requires continuous development of new tools and devices. This includes application of novel materials having advanced properties. The main families of solids, which are explored and extensively used today in industry, are those of metals and oxides. For oxides this is not surprising since oxygen accounts for nearly half of the mass of the Earth's crust (49.2 wt.%) as a constituent element of the most abundant minerals (Lide 2005). Accordingly, the majority of studies in materials chemistry and physics is focused, along with metals, on oxygen-based compounds having a great variation of physical and chemical properties. Despite of this fact, amounts of natural oxidic materials satisfying technical requirements do not always cover the actual needs. Alternatively, properties of those which could be mined from the environment or synthesised using standard methods in sufficient amounts do not always fulfil the increasing technical demands. As a consequence, efforts are undertaken to find new oxygen-free compounds satisfying the needs of modern industry and to develop economical methods of their production and application.

One of the alternative families to oxides which could have similar number of members is that of nitrides. However, in contrast to oxides, pure nitrides are very rare in nature. Such mineral as siderazot (Fe_5N_2) occurs in some volcano complexes, a few other (such as osbornite TiN, nierite Si_3N_4, roaldite $(Fe,Ni)_4N$ and carlsbergite CrN) were found in meteorites. [*] Nevertheless, some nitrides have found extended application in the industry because they exhibit unique combination of physical, chemical, electrical, optical or mechanical properties and can be synthesised in large amounts for reasonable costs (Samsonov 1969; Toth 1971; Holleck 1984). Nitrides are used for different applications as refractory ceramics (hexagonal BN, α- and β-Si_3N_4, AlN, TiN), hard grinding materials (cubic BN, α- and β-Si_3N_4), in light emitting semiconductor diodes (GaN, InN), as catalysts (Mo_2N, W_2N), sintering additives, and a solid-state electrolyte in lithium batteries (Li_3N) (e.g. Ettmayer & Lengauer 1991; Markel & Leaphart 1998). However, the number of known nitrogen-based compounds is dramatically lower than that of oxygen-based ones (Gregory 1999; Kroke & Schwarz 2004; Zerr et al. 2006a). For example, analysis of the ICSD crystallographic database revealed that

[*] http://www.mindat.org, http://webmineral.com/

there are 569 binary (1672 ternary) nitrides with determined structure but 2374 binary (14454 ternary) oxides.

Recent progress in nitride chemistry is related, without any doubt, to the development of new synthetic routes which allow not only routine preparation of known compounds with well-determined properties in large amounts but also the discovery of novel compounds (DiSalvo 1990; Schnick 1993; Kniep 1997; Niewa & DiSalvo 1998; Gregory 1999; Marchand et al. 1999). Most of new synthetic approaches in nitrides chemistry are based on manipulation of such "input" parameters as temperature and reaction time, as well as on variation of precursors and/or catalysts. Pressure, a thermodynamic parameter considered to be "as fundamental as temperature" (Badding 1998) is, in contrast, only rarely used for nitrides synthesis. For the largest group of known oxides, namely minerals, it is known from petrological experiments that almost all of them undergo phase transitions at high pressures and temperatures. For example, silicon dioxide (SiO_2) has at least ten high-pressure structural modifications (Tsuchida & Yagi 1989; Griffen 1992; Murakami et al. 2003; Luo et al. 2004). On compression of any substance, distances between constituting atoms decrease and its electronic structure deforms. This leads to increase of the internal energy of the substance, and formation of denser structures could become energetically favourable on further compression. Such structures are characterized by shorter interatomic distances and/or higher coordination numbers of the constituent atoms, when compared with the lower pressure phases. If chemical reactions occur at high-pressure conditions, formation of compounds with constituting elements in unusual oxidation states can take place (e.g. Neuhaus 1964; Jayaraman et al. 1976; Chandran et al. 1992; Demazeau 2002). Referring to these facts Zerr et al. (2006a) have pointed out in their recent review that in nitrides chemistry "*the application of pressure, in addition to temperature and composition variations*, *increases the chances of obtaining new materials not attainable at ambient atmosphere*". The authors have further emphasized that the tendency of transition elements to higher oxidation states on compression favours formation of their higher nitrides. Moreover, since the thermal stability of nitrides at ambient pressure is limited (e.g. DiSalvo 1990; Schnick 1993; DiSalvo & Clarke 1996) the application of high nitrogen pressure can allow to process them at significantly higher temperatures.

One of the reasons for the above mentioned limited use of high-pressure routes is the fact that the synthesis techniques are demanding and that production costs are relatively high. For static techniques the production is also limited by material yields in one synthesis run. Accordingly, only diamond and cubic boron nitride (c-BN), the stiffest and hardest known

solids, are commercially produced today at high pressures and temperatures. These materials are broadly used for various cutting and grinding applications (e.g. Sigalas & Caveney 2000). Nevertheless, both compounds have limitations in their applications since diamond strongly reacts with ferrous alloys during grinding and high production costs make c-BN less competitive. This is why there are forthcoming efforts in the solid state chemistry to develop new high-pressure materials which have not only high hardness but other useful properties superior to those of diamond and c-BN. Materials having interesting properties other than hardness were also a subject of recent high-pressure research (Badding et al. 1995; Takano & Onodera 1997; Badding 1998; McMillan 1999; Haines et al. 2001; Demazeau 2002; Kroke 2002; McMillan 2002, 2003; Huppertz 2004; Horvath-Bordon et al. 2006; Zerr et al. 2006a; Brazhkin 2007). With respect to nitrides the research led to discovery of a few novel potentially important technological materials such as spinel-type γ-Si_3N_4 and γ-Ge_3N_4 (Zerr et al. 1999; Leinenweber et al. 1999; Serghiou et al. 1999), orthorhombic γ-P_3N_5 (Landskron et al. 2001), diamondlike c-BC_2N (Solozhenko et al. 2001), and cubic c-Zr_3N_4 and c-Hf_3N_4 (Zerr et al. 2003).

The present work extends research on the recently discovered high-pressure nitrides of the group 4 elements, namely nitrides of zirconium(IV) and hafnium(IV) having cubic Th_3P_4-type structure, c-M_3N_4 (where M = Zr, Hf) (Zerr et al. 2003). These compounds were expected to outperform the ambient-pressure mononitrides of titanium, zirconium and hafnium having cubic NaCl-type structure (δ-TiN, δ-ZrN and δ-HfN), in hardness, thermal stability, wear- and oxidation resistance. It should be emphasised that the mentioned mononitrides themselves are well known as hard refractory materials (Toth 1971; Pierson 1996; Lengauer 2000). Additionally, c-Zr_3N_4 and c-Hf_3N_4 were expected to have some interesting optoelectronic and/or superconducting properties (Kroll 2003; Mattesini et al. 2003; Zerr et al. 2003; Chhowalla & Unalan 2005; Xu et al. 2006). Within the frame of the present work the formation at high pressures and high temperatures of novel oxygen-bearing zirconium(IV)- and hafnium(IV) nitrides having Th_3P_4-type structure, namely c-$M_3(N,O)_4$, was discovered. The compounds were synthesized in macroscopic amounts (about 1 mm^3) using a large-volume high-pressure apparatus. This allowed refinement of their structure and determination of the composition using standard techniques. Properties of the obtained compounds were investigated with respect to their potential application as stiff and hard refractory materials.

An essential part of this thesis deals with high-pressure synthesis. Therefore the following paragraph of the introduction gives a brief discussion of the role of pressure, the second main thermodynamic parameter, in synthesis of new materials. Since the obtained materials were

expected to be stiff, a brief introduction to relevant elastic properties is made in Chapter 1.2. Further, basic concepts of hardness and its correlation with elastic moduli and dependence on morphology are considered. After the overview of recent advances in synthesis of novel high-pressure nitrides, a detailed description of the subject of the present work will conclude this introduction chapter.

1.1 High pressure in materials chemistry

High-pressure routes to new solid materials can be described by two general approaches. New materials can be obtained either via phase transitions or chemical reactions. In the first case, when chemical composition of a treated compound remains unchanged, increase of pressure and temperature can cause a phase transition to a new structure, in which the compound can have novel interesting properties. One of the most prominent examples is the transformation of graphite to diamond. In the case of a multi-component system, high pressure can shift equilibrium of chemical reaction as well as increase chemical activity of atoms. Thus, combination- or displacement reactions, not possible at ambient pressure, can take place. Alternatively, compounds can decompose at high pressures and temperatures into more simple constituents. The considered approaches can result in formation of novel high-pressure substances, some of which can be recovered to ambient conditions.

1.1.1 Phase transitions

Thermodynamic description of phase transitions can be found in a number of textbooks (e.g. Kubo 1968; Atkins 1998; Stolen & Grande 2004). Here, some general concepts of phase stability and phase transition at high pressures and temperatures, which are relevant to the present work, are briefly discussed. According to the second law of thermodynamics, a system is in equilibrium when its Gibbs free energy, **G**, is at minimum. At particular *P*-*T*-conditions that phase is stable which Gibbs free energy is lower. If the Gibbs free energy of a starting phase α, $\mathbf{G}_\alpha$, becomes higher upon change of *P* or *T* than $\mathbf{G}_\beta$ of another phase β, a phase transition to the phase β occurs (Figure 1.1a). Two phases (α and β) coexist in thermodynamic equilibrium at the *P*-*T*-conditions where their Gibbs free energies are equal, i.e.

$$\Delta\mathbf{G}_{\alpha\beta} = \mathbf{G}_\beta - \mathbf{G}_\alpha = \mathbf{H}_\beta - \mathbf{H}_\alpha - T(S_\beta - S_\alpha) = \Delta\mathbf{H}_{\alpha\beta} - T\Delta S_{\alpha\beta} = 0 \text{, with } \mathbf{H} = \mathbf{U} + PV \text{,}$$

where **H**, *S*, **U**, *V* are specific enthalpy, entropy, internal energy and volume of the phases α or β, respectively. These pressure-temperature conditions can be represented on the *P*-*T* phase diagram as a line defined as a phase boundary (Figure 1.1b).

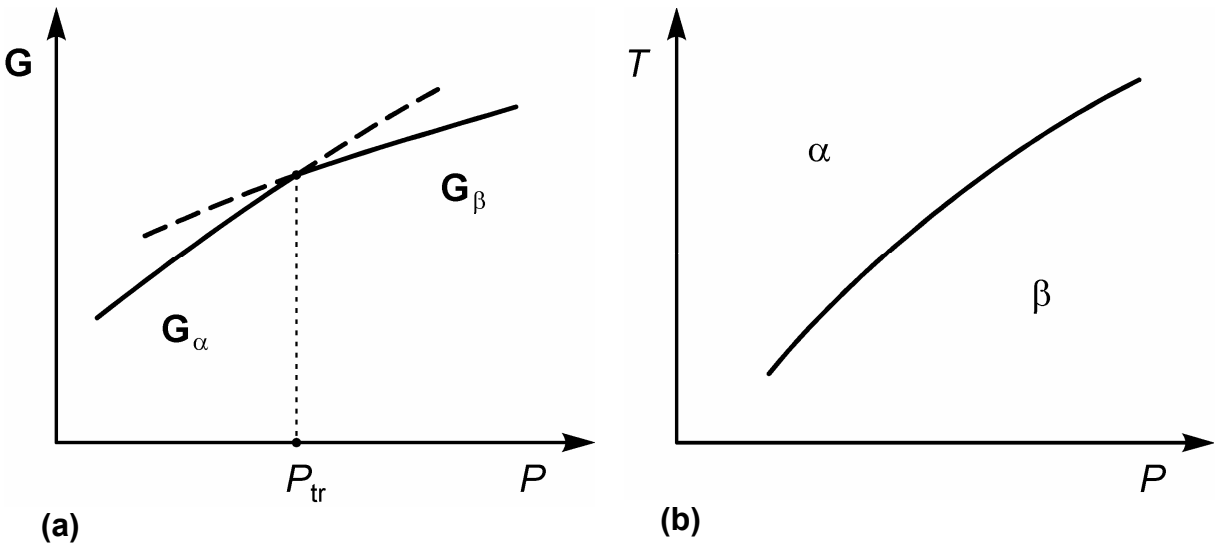

Figure 1.1. (a) Schematic Gibbs free energy-pressure dependence for a first-order phase transition at pressure P_{tr} and constant temperature. Solid lines represent the minimum of **G**, i.e. stable state. Dashed lines correspond to metastable state (s. text). (b) Schematic pressure-temperature phase diagram for a one component system. The phase boundary (solid line) represents the *P*-*T* conditions where phases α and β coexist in thermodynamic equilibrium.

Transition from one phase to another can be accompanied by discontinuities in first partial derivatives of Gibbs free energy with respect to pressure and temperature, i.e. in specific volume $\Delta(\partial \mathbf{G}/\partial P)_T = \Delta V_{\alpha\beta} \neq 0$ and entropy $\Delta(\partial \mathbf{G}/\partial T)_P = -\Delta S_{\alpha\beta} \neq 0$. Such phase transitions are defined as those of the *first-order*.* According to the Le Chatelier's principle (Le Chatelier 1884), for a first-order phase transition ΔV should be negative on compression and positive on decompression. Upon increase of temperature ΔS should be positive. In the most general form Le Chatelier's principle can be expressed as: "*A system at equilibrium, when subjected to a disturbance, responds in a way that tends to minimize the effect of the disturbance*" (Atkins 1998). Thus, the increase of temperature *T* (at *P* = *const*) will favour the formation of a phase with higher entropy *S*, while the increase of pressure *P* (at *T* = *const*) – the formation of a phase with lower specific volume *V* (Figure 1.2). Therefore, high-pressure phases have denser structures with shorter interatomic distances and/or higher coordination numbers of atoms when compared with lower-pressure phases.

* Second order phase transitions (e.g. order-disorder or metallic-superconducting state transitions) are characterized by discontinuities in the second partial derivatives of free Gibbs energy (i.e. compressibility, thermal expansion and heat capacity). However, such phase transitions are not considered in the present work.

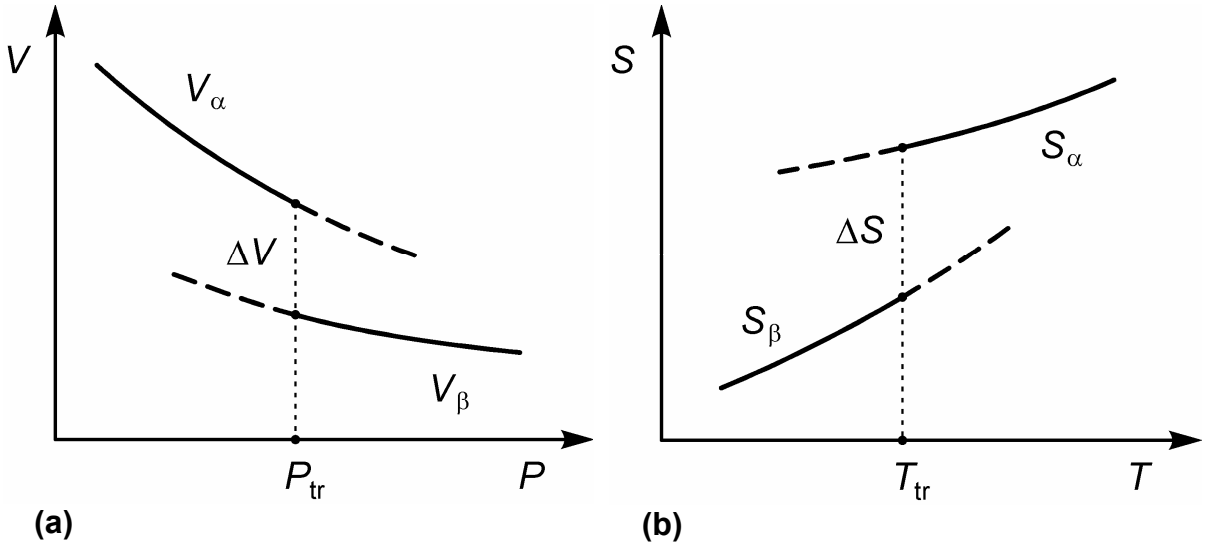

Figure 1.2. An example of discontinuous changes of thermodynamic parameters accompanying first-order phase transitions: (a) volume as a function of pressure, $V(P)$; (b) entropy as a function of temperature, $S(T)$.

The slope of a phase boundary can be derived from a simple consideration as follows: let pressure and temperature change along the phase boundary infinitesimally, so their changes are dP and dT, respectively. Since both phases are at equilibrium, their Gibbs energies are equal in both initial and final states, i.e. $d\mathbf{G}_\alpha = d\mathbf{G}_\beta$. Alternatively, this can be written as $V_\alpha dP - S_\alpha dT = V_\beta dP - S_\beta dT$. Hence, the slope of the phase boundary, dP/dT, at a transition point is determined by the ratio of enthalpy change, $\Delta S_{\alpha\beta}$, to volume change, $\Delta V_{\alpha\beta}$. Introducing the latent heat of transition as $Q_{\alpha\beta} = T\Delta S_{\alpha\beta}$, one can write for the slope of the phase boundary: $dP/dT = \Delta S_{\alpha\beta}/\Delta V_{\alpha\beta} = Q_{\alpha\beta}/T\Delta V_{\alpha\beta}$. This expression is known as the Clausius-Clapeyron equation. Position and slope of a phase boundary is of importance with respect to industrial synthesis of high pressure phases: if, for a particular transition, the slope is positive then the synthesis pressure decreases with temperature and the costs of synthesis can be strongly suppressed. However, synthesis conditions are defined not only by thermodynamic stability of the phase of interest but also by other parameters as, for example, kinetics of the transition (s. below) or by the applied method of controlling load and heating. Critical parameters influencing kinetics of a transition is the excess in temperature or pressure with respect to the conditions at the phase boundary. For ceramic materials these excess values can be significant. For a phase boundary with a positive slope reasonable transformation rates can be approached at relatively low P or T conditions by using catalysts. In absence of catalysts slow kinetics of a transition at low temperatures can result in its

infinitely long persistence outside the field of the thermodynamic stability. Such state of the phase is defined as a metastable one (s. below).

Kinetics of solid-state transformations is, in general, very complex (Bradley 1963a; Spain & Bolsaitis 1977; West 1989). Despite catalyst there are other factors which can influence the rates of solid-solid phase transitions. Their quantification is usually very difficult, if not impossible. Therefore, only a brief summary of the qualitative effects of those factors on the phase transitions kinetics is given below.

When considering the rate of a phase transition, one can distinguish two main factors. Firstly, the transition rate v_{tr} increases with temperature T according to the Arrhenius equation: $v_{tr} \sim k \exp(-\mathbf{E}_a / RT)$, where k is the pre-exponential coefficient, $\mathbf{E}_a$ molar activation energy of the transition and R the universal gas constant. Second factor is the difference of molar Gibbs free energy between two phases, $\Delta\mathbf{G}_{\alpha\beta}$, at given conditions. It represents a measure of the transition driving force and is usually expressed by a multiplier $\{1 - \exp(\Delta\mathbf{G}_{\alpha\beta} / RT)\}$ (e.g. Bradley 1956). Thus, the higher $\Delta\mathbf{G}_{\alpha\beta}$, the higher probability for phase transition to occur. The influence of both activation energy and driving force on the transition rate v is illustrated in Figure 1.3a. With respect to $\mathbf{E}_a$ and $\Delta\mathbf{G}_{\alpha\beta}$ the following additional points should be mentioned:

1) Mechanism of the phase transition is the major factor defining $\mathbf{E}_a$. Reconstructive phase transitions have high activation energies since both breaking of atomic bonds and formation of nuclei of stable phase take place. Therefore such transitions are slow. In contrast, displacement, dilatational and martensitic transitions occur without full structural reconstruction. Having very low (or zero) activation energies, such transitions occur rapidly (e.g. Spain & Bolsaitis 1977; West 1989).

2) Nature of starting material plays an important role in the nucleation of the product phase. Large sample surface and high impurity and defect concentrations make positive contribution to the Gibbs free energy of the initial phase. Thus, activation energy for product phase nucleation decreases and transition driving force increases. This leads to a higher rate of phase transition (Christian 1975; Spain & Bolsaitis 1977). For example, use of nanocrystalline (or amorphous) precursors can significantly increase rates and lower P-T conditions for initiation of transitions, however, not below the phase boundary. This approach was used by Schwarz et al. (2000) in order to synthesize large amounts of the recently discovered cubic γ-Si_3N_4 .

3) Formation of product-phase nuclei during solid-state transformation is usually accompanied by developing of elastic strains in material due to volume and/or shape changes. The elastic strain energy makes a positive contribution to the Gibbs free energy of a product phase, thus decreasing the transition driving force and, hence, the transition rate. If phase transition occurs with large volume change, significant strain energy effects can completely hinder the transformation. It is therefore necessary to supercool/heat or, alternatively, supercompress/decompress starting phase with respect to the phase transition boundary in order to initiate its transformation (Christian 1975; Spain & Bolsaitis 1977).

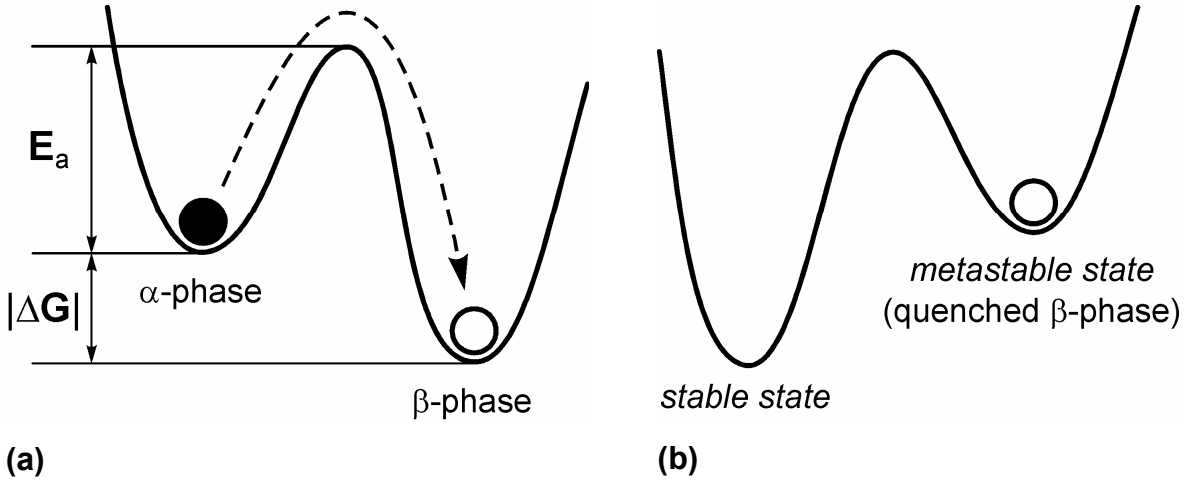

Figure 1.3. Schematic energy diagrams: (a) energy barrier encountered during first-order phase transition, where $\mathbf{E}_a$ and $\Delta\mathbf{G}$ is activation energy and driving force of the transition, respectively; (b) metastable existence of thermodynamically unstable phase due to high activation energy of reverse transition.

As was mentioned above, slow rates of solid-solid phase transitions explain the metastable existence of high-pressure (high-temperature) polymorphs at ambient conditions for infinitely long times. Having high driving forces of reverse transition at ambient conditions, these phases are kinetically hindered to transform to stable low-pressure phases (Figure 1.3b). Metastable high-pressure phases can be often obtained by a rapid quenching to low temperatures after synthesis at high pressures and subsequent decompression to atmospheric pressure. This procedure allows obtaining of metastable materials with unique structural and functional properties useful for industrial applications (Badding et al. 1995; Takano & Onodera 1997; Badding 1998; McMillan 1999; Demazeau 2002; McMillan 2002, 2003; Brazhkin 2007). Diamond (high-pressure phase of carbon) and martensite (the Fe-C phase allowing hardening of steel) are classical examples of technologically important metastable materials.

1.1.2 Chemical reactions

Description of effects of pressure on chemical reactions is well known and can be found elsewhere in the literature (e.g. Bradley 1963b; Spain & Paauwe 1977; van Eldik & Hubbard 1997). Basically, pressure can shift the equilibrium and influence the rate of chemical reactions. According to the Le Chatelier's principle, application of external pressure shifts the chemical equilibrium toward reduced volume products. Similarly, the reaction rate increases with pressure, if the volume of a transition state* is lower than that of reactants. The quantitative treatment of these effects deals predominantly with gaseous and liquid state reactions at pressures considerably below 1 GPa. Therefore, it is not further discussed here. As regards solid-state reactions, their thermodynamics and kinetics are much more complex. The Le Chatelier's principle, however, holds here as well: high pressures favour the formation of compounds with lower specific volume. For example, c-Zr_3N_4 at 16 GPa has specific volume of 72.3 $Å^3$ per Zr_3N_4 unit (Zerr et al. 2003), while the specific volume of the mixture $3ZrN + ½N_2$ at the same pressure, as calculated from the compressibilities of mononitride (Chen et al. 2005) and nitrogen (Olijnyk 1990), is 78.9 $Å^3$. Thus, at 16 GPa the formation of c-Zr_3N_4 from ZrN and N_2 is favoured.

The factors which influence kinetics of reactions in solid state, in principle, are analogous to those described in the previous chapter regarding solid-state phase transitions (e.g. Arrhenius equation). Similar to reconstructive phase transitions, composition change of the constituents during chemical reaction involves mass transfer by diffusion. In solids and, especially, at high pressures diffusion processes are extremely slow. Therefore, sample heating (even up to melting points of reactants) is often the only way to approach acceptable rate of a chemical reaction at high pressures.

In addition to the above described effects, pressure can increase the reactivity of atoms and molecules (Badding et al. 1995; 1998; Hemley 2000; Demazeau 2002; McMillan 2002; Schettino & Bini 2003). If pressure is high enough it can significantly change the electronic structure of the constituent atoms. In some cases the gap between ground and excited electronic states of atoms can decrease and the atoms can be easer excited, for example, thermally or by laser radiation. The excited atoms, thus, can readily react with each other

*According to the transition state (activated complex) theory (e.g. Hamann 1963), a reaction proceeds through some kind of "transition state", i.e. an intermediate state of maximum energy, which is in equilibrium with both reactants and products.

forming compounds with composition/stoichiometry not attainable at ambient pressure. For example, platinum (Pt) is known to be inert to nitrogen at ambient pressures. When sufficiently compressed, however, it reacts with N_2 resulting in formation of PtN_2 (Gregoryanz et al. 2004; Crowhurst et al. 2006). Moreover, elements in new high-pressure compounds can exhibit unusual oxidation numbers. For example, high pressures force elements (mostly transition metals, lanthanides and actinides) to their higher oxidation states (Neuhaus 1964; Jayaraman et al. 1976; Chandran et al. 1992). This occurs, in particular, by formation of c-Zr_3N_4 and c-Hf_3N_4 from elements (Zerr et al. 2003). With respect to molecular systems having unsaturated (double and/or triple) bonds, changes in electronic structure at high pressures can favour polymerization of those molecules into single-bonded frameworks (Badding et al. 1995; Hemley 2000; Schettino & Bini 2003). Even molecular nitrogen, having the most stable covalent triple bond, transforms at high pressures and high temperatures into a single-bonded polymeric form having cubic-gauche structure (Eremets et al. 2004). Similar to high-pressure phases, some products of high-pressure reactions can be recovered to ambient conditions, where they can metastably exist due to a slow kinetics of the reverse reaction.

1.1.3 Summary

As follows from the above consideration, application of high pressures in addition to high temperatures can induce phase transitions in substances, increase chemical activity of atoms and molecules, significantly shift chemical equilibria and affect reaction rates. Solid compounds which can be synthesized at high pressures and high temperatures, have dense structures, often with increased coordination numbers of the constituent atoms. New high-pressure compounds can have unusual composition/stoichiometry and oxidation numbers of the constituent elements which cannot be realized at ambient conditions. Furthermore, these high-pressure phases can be quenched to ambient conditions with their properties intact, where they can be thermodynamically unstable while persist metastably due to slow kinetics of the reverse transformations. Such metastable products can have a number of unique physical and chemical properties, from high hardness and corrosion stability to interesting optoelectronic, magnetic or superconducting properties. Therefore, they can be of potential interest for various industrial applications.

High stiffness (i.e. high elastic moduli) and high hardness are the distinctive features of a large number of dense high-pressure materials, especially of ceramics (Haines et al. 2001; McMillan 2002; Brazhkin 2007). One of the particular families of such ceramics is nitrides of the group 4 elements, synthesis and properties of which were investigated in the present work.

Therefore definitions and concepts of stiffness and hardness are discussed in the following paragraph.

1.2 Stiffness and hardness

1.2.1 Elastic moduli

One of the important characteristics of structural materials is their response on action of an external force. Knowledge of such a response allows choosing appropriate material for construction of structural components, so they will not excessively deform or fail during exploitation. A solid body under external load exhibits deformation, i.e. change of its volume and/or shape. The interatomic forces which tend to return a deformed body to initial state are called internal stresses. In general stress is defined as a force per unit area and has the same SI unit as pressure, namely pascals (1 Pa = 1 N/m^2). Accordingly, stress at any point of a body can be described as a force per unit area across every plane drawn through this point. The magnitude and orientation of the state of stresses at a point within a deformed body can be completely defined by nine stress components, σ_{ij}. These nine components represent a second-rank tensor also referred to as the *stress tensor* (Landau & Lifshitz 1975):

$$\sigma_{ij} = \begin{bmatrix} \sigma_{xx} & \sigma_{xy} & \sigma_{xz} \\ \sigma_{yx} & \sigma_{yy} & \sigma_{yz} \\ \sigma_{zx} & \sigma_{zy} & \sigma_{zz} \end{bmatrix},$$

where σ_{ii} and $\sigma_{ij}\,(i \neq j)$ are the components of normal (perpendicular to a given plane) and shear (parallel to a given plane) stresses, respectively. Any stress tensor is symmetric, i.e. $\sigma_{ij} = \sigma_{ji}\,(i \neq j)$, and the stress state of a body is completely defined by six independent stress components. The sum of diagonal components of a stress tensor (trace of tensor) is an invariant: $\sum \sigma_{ii} = const$. The stress tensor's trace is nothing else than hydrostatic pressure, $P = -\frac{1}{3}\sum \sigma_{ii}$. Consequently, any stress tensor can be resolved into the sum of hydrostatic and deviatoric stress components:

$$\sigma_{ij} = -P\delta_{ij} + (\sigma_{ij} + P\delta_{ij}) = -P \begin{bmatrix} 1 & 0 & 0 \\ 0 & 1 & 0 \\ 0 & 0 & 1 \end{bmatrix} + \begin{bmatrix} \sigma_{xx}+P & \sigma_{xy} & \sigma_{xz} \\ \sigma_{yx} & \sigma_{yy}+P & \sigma_{yz} \\ \sigma_{zx} & \sigma_{zy} & \sigma_{zz}+P \end{bmatrix} \qquad (1.1)$$

Thus hydrostatic stress tensor, $-P\delta_{ij}$, is responsible for pure isostatic compression, i.e. for change of volume without shape change. Deviatoric stress tensor, $(\sigma_{ij} + P\delta_{ij})$, is responsible for pure shear stress, i.e. for the change of shape with constant volume.

Deformation of a body under stress (i.e. change of its volume and shape) can be geometrically described in terms of the *strain tensor* (Landau & Lifshitz 1975). If radius vectors $\boldsymbol{r}(x, y, z)$ and $\boldsymbol{r'}(x', y', z')$ define initial and final position of a point within a body before and after deformation, respectively, vector $\boldsymbol{u} = \boldsymbol{r'} - \boldsymbol{r}$ is the displacement of this point under deformation. The strain at this point is completely described by the strain tensor:

$$\varepsilon_{ij} = \begin{bmatrix} \varepsilon_{xx} & \varepsilon_{xy} & \varepsilon_{xz} \\ \varepsilon_{yx} & \varepsilon_{yy} & \varepsilon_{yz} \\ \varepsilon_{zx} & \varepsilon_{zy} & \varepsilon_{zz} \end{bmatrix},$$

where for small deformations $\varepsilon_{xx} = \partial u_x / \partial x$, $\varepsilon_{yy} = \partial u_y / \partial y$ and $\varepsilon_{zz} = \partial u_z / \partial z$ are normal (or linear) strains along axes x, y and z, respectively, and $\varepsilon_{xy} = \frac{1}{2}(\partial u_x / \partial y + \partial u_y / \partial x)$, $\varepsilon_{yz} = \frac{1}{2}(\partial u_y / \partial z + \partial u_z / \partial y)$ and $\varepsilon_{xz} = \frac{1}{2}(\partial u_x / \partial z + \partial u_z / \partial x)$ are shear strains. Thus, strain is a dimensionless quantity. Analogous to the stress tensor, strain tensor is symmetric and has an invariant trace which is also known as volumetric strain $\sum \varepsilon_{ii} = \Delta V / V = const$. Strain tensor can be also resolved into hydrostatic and shear strain components, $\varepsilon_{ij} = \Delta V \delta_{ij} / 3V + (\varepsilon_{ij} - \Delta V \delta_{ij} / 3V)$, where the first and the second term on the right side represent hydrostatic compression and pure shear deformation, respectively.

The response of a body on action of external forces can be described via relationship between stress state within a body and corresponding strains. For small deformations this stress-strain relation is expressed by the generalised Hook's law:

$$\sigma_{ij} = \sum_{kl} c_{ijkl} \varepsilon_{kl}, \tag{1.2}$$

where σ_{ij} and ε_{kl} is stress and strain tensor, respectively, and c_{ijkl} is the forth-rank stiffness tensor containing 81 components, also known as *elastic constants*. The elastic constants have the same units as stress and are usually measured in gigapascals, GPa (1 GPa = 10^9 Pa). Due to the symmetry of the stress- and strain tensors, the number of independent elastic constants

is in general 21 (e.g. for a triclinic single crystal) (Landau & Lifshitz 1975). In the case of homogeneous isotropic body* the Hook's law (Equation 1.2) transforms into a simple form:

$$\sigma_{ij} = 3B\left(\frac{1}{3}\frac{\Delta V}{V}\delta_{ij}\right) + 2G(\varepsilon_{ij} - \frac{1}{3}\frac{\Delta V}{V}\delta_{ij}), \tag{1.3}$$

where B and G is bulk and shear modulus of isotropic material, respectively. From Equations 1.1 and 1.3 follows that the bulk modulus B is the proportionality constant between pressure and volumetric strain ($P = -B\Delta V / V$), thus it describes the material resistance to volume change under hydrostatic load. The volume-pressure relationship is nothing else as an isothermal *equation of state* (EOS). The above expression is a particular case of small deformations where bulk modulus is considered to be a pressure independent parameter. For this case one can rewrite this equation in a differential form $1/B = -1/V(\partial V / \partial P)_T$, where $(\partial V / \partial P)_T$ is the partial derivative of volume V with respect to pressure P at constant temperature (Landau & Lifshitz 1975). The differential form is also correct for large deformations if a pressure dependence of B is included and the $V(P)$ relation is not linear anymore (s. below).

The shear modulus G, in turn, determines the material resistance to a pure shear (deformation of shape at constant volume) and is the proportionality constant between shear stress and shear strain ($\sigma_{ij} = 2G\varepsilon_{ij}$ where $i \neq j$). Shear modulus is also dependent on pressure; however, in contrast to bulk modulus, there is no established relationship between G and P.

Alternatively, elastic properties of isotropic body can be described by another two elastic moduli: Young's modulus, E, and Poisson's ratio, ν. The Young's modulus, defined as tensile stress divided by tensile strain, describes material resistance to uniaxial deformation ($E = \sigma_i / \varepsilon_i$ for simple tension along i axis) and is usually measured in GPa. The Poisson's ratio describes tendency of material under tension in one direction to contract in lateral directions. It is equal to the lateral strain divided by tensile strain (for simple tension along i axis $\nu = -\varepsilon_j / \varepsilon_i$ where $i \neq j$) and is a dimensionless quantity. Thus, the Hook's law for isotropic body (Equation 1.3) can be expressed in terms of E and ν:

$$\sigma_{ij} = \frac{E}{1+\nu}\left(\varepsilon_{ij} + \frac{\nu}{1-2\nu}\varepsilon_{kk}\delta_{ij}\right).$$

* Elastic properties of an isotropic body are the same in all directions. Hereafter only isotropic materials are considered.

If a pair of elastic moduli is known for a given isotropic material, the other pair can be calculated according to well known relations, e.g. $E = 9BG/(3B+G)$ and $\nu = (3B-2G)/(6B+2G)$ (Landau & Lifshitz 1975). These expressions were used in the present work for determination of shear modulus and Poisson's ratio of the investigated material using experimentally determined bulk and reduced elastic modulus (Chapter 3.4.4).

1.2.1.1 Equation of state

As already mentioned above, bulk modulus generally depends on pressure (strictly speaking, it also depends on temperature, however, this dependence will not be considered here). Thus, under strong compression, the Hook's law as a description of the $V(P)$ relationship is no longer valid. In order to describe the behaviour of solids under strong compression, several (semi)empirical isothermal equations of state were suggested. They differ in the chosen approximation of the dependence of elastic free energy on strain and in the strain definition in terms of specific volume (e.g. Murnaghan 1944; Birch 1947, 1978; Vinet et al. 1989; Holzapfel 1998; Poirier & Tarantola 1998; Stacey 2000). The parameters in these equations are the starting volume (V_0) the isothermal bulk modulus (B_0) and its pressure derivative (B_0' and sometimes B_0'') at zero pressure.* Thus, if the $V(P)$ dependence for a particular solid is measured, the bulk modulus and its pressure derivatives can be determined by fitting of the chosen EOS to the compression data.

One of the most frequently used in high-pressure physics and geophysics is the third-order† Birch-Murnaghan equation of state (BM-EOS): $P = 3B_0 f(1+2f)^{5/2} \times [1 + 3/2(B_0' - 4)f]$, where $f = ((V/V_0)^{-2/3} - 1)/2$ represents the Eulerian finite-strain (Birch 1947, 1978), so

$$P = \frac{3}{2} B_0 \left(\left(\frac{V}{V_0} \right)^{-7/3} - \left(\frac{V}{V_0} \right)^{-5/3} \right) \times \left\{ 1 - \frac{3}{4}(4 - B_0') \left[\left(\frac{V}{V_0} \right)^{-2/3} - 1 \right] \right\}. \qquad (1.4)$$

The analysis of a large amount of experimental geophysical data has shown that the third-order BM-EOS reliably describes behaviour of most solids within pressure range accessible

---

* Difference between zero- and ambient pressure values for *V, B* and *B′* for solids is usually negligibly small; therefore, the subscript 0 for elastic moduli throughout the thesis will denote the ambient pressure values.

† Here the order of the EOS is determined by the order of the last considered term of the Helmholtz free energy, **A**, given as a function of Eulerian strain, i.e. $\mathbf{A} = c_2 f^2 + c_3 f^3 + \ldots$ (Jeanloz 1988). The pressure-volume relation can be derived by differentiation of **A** with respect to V: $P = -(\partial \mathbf{A}/\partial V)_T$.

by modern high-pressure techniques (e.g. Jeanloz 1988). Therefore, this equation was used in the present work to determine the bulk moduli and their first pressure derivatives of the investigated nitrides from the experimentally measured $V(P)$-dependences (s. Chapter 3.4.1).

The third-order BM-EOS can be reduced to that of second-order by assuming $B_0' = 4$, so

$$P = 3B_0 f(1+2f)^{5/2} = \frac{3}{2} B_0 \left(\left(\frac{V}{V_0} \right)^{-7/3} - \left(\frac{V}{V_0} \right)^{-5/3} \right). \quad (1.5)$$

This form of the BM-EOS can be used for determination of B_0 for materials with $B_0' \approx 4$ (for example, metals having NaCl-type structure (Chen et al. 2005)) or for rough estimation of bulk moduli when both statistics and uncertainties of $V(P)$-data do not allow determination of B_0' with a reliable accuracy.

It is sometimes convenient to express BM-EOS in terms of the Eulerian strain, f, and normalized pressure, $F = P/(3f(1+2f)^{5/2})$, so F is a linear function of f:

$$F = B_0 + 3B_0(B_0' - 4)f/2 . \quad (1.6)$$

Thus, if compression data are presented on the $F(f)$-plot, the intercept with F-axis and the slope of the line yields B_0 and B_0', respectively. The $F(f)$ form of representation of the $V(P)$-dependence is also very sensitive to scattering of data and to experimental uncertainties (Chapter 3.4.1).

There is a critique of the BM-EOS in the literature, with respect to its applicability for extremely high pressures (>> 100 GPa) and for particular cases of strongly compressible materials having $B_0' >> 4$ (Hofmeister 1993; Hama & Suito 1996; Holzapfel 1996; Poirier & Tarantola 1998; Stacey & Davis 2004). However, significant deviation of the BM-EOS from other suggested equations is observed only after a considerable volume reduction by 30-50 % (Jeanloz 1988; Hama & Suito 1996; Holzapfel 1996; Singh 2005). In the present work the maximum sample volume decrease during compressibility measurements did not exceed 20 %. Therefore, the BM-EOS can be used for evaluation of the obtained $V(P)$-data without any limitations.

1.2.1.2 Correlation of elastic moduli with intrinsic material properties

Elastic moduli of a compound are generally determined by its crystal structure and interaction of the constituting atoms. In particular, the bulk modulus, B, can be related to the effective

valence electron density ρ_e as $B \propto \rho_e^n$, where $1 \le n \le 5/3$ (Haines et al. 2001; Brazhkin et al. 2002). Thus, high bulk moduli are expected for materials composed of elements having high valence electron densities. Another factor enhancing bulk modulus is the presence of short high energy bonds. With respect to shear modulus, it has similar relation to ρ_e ($G \propto \rho_e^n$) (Haines et al. 2001; Brazhkin 2007). However, in contrast to bulk modulus, the major determinative factor for *G* is distribution of the valence electron density rather than mean ρ_e value. More precisely, high shear modulus is expected for materials with highly directional (covalent) bonds. Such bonds are much stiffer to lattice shear than ionic and, particularly, metallic ones, where the electron density is distributed more uniformly. This is also supported by the following experimental observation. Since for isotropic materials $G = \frac{3}{2}B(1-2\nu)/(1+\nu)$, the shear modulus is high with respect to *B* when the Poisson's ratio is small. Experimental studies show that the typical value of ν for covalent compounds is about 0.1, for ionic about 0.25 and for metals about 0.33 (Haines et al. 2001). Thus, covalent compounds have the highest values for *G* relative to *B*. For example, covalent diamond has the Poisson's ratio of 0.07, *B* of 443 GPa and *G* of 535 GPa. Another important factor influencing elastic moduli is geometrical rigidity of the structure. Evidently, three-dimensional structure of diamond (formed by sp^3-hybridized carbon) is rigid in all directions in contrast to layered structure of graphite (composed of sp^2-hybridized carbon) (Haines et al. 2001). Furthermore, geometrical rigidity of three-dimensional structure increases with increasing number of nearest neighbours of atoms (coordination number, N_c) (Haines et al. 2001; Brazhkin et al. 2002). For example, quartz (α-SiO_2) with 4-fold coordinated Si atoms ($N_c = 4$) has bulk and shear moduli of about 36 GPa and 31 GPa, respectively, while stishovite (high-pressure SiO_2-polymorph) with $N_c(Si) = 6$ is stiffer than quartz by almost one order of magnitude ($B = 305$ GPa, $G = 220$ GPa). However, there is opinion in the literature that too high N_c (well above 4) can result in delocalisation and more uniform distribution of valence electron density, thus can decrease the shear stiffness of crystal lattice (Brazhkin et al. 2002).

Summarizing, high bulk and shear moduli are expected for materials with high valence electron density and rigid crystal structure. This could be dense covalent compounds of light elements (2 and 3 period of the periodic table) or partially covalent borides, carbides, nitrides and oxides of transition metals (group 4-7) with cations in coordination states providing topological stiffness of crystal lattices (Haines et al. 2001; Brazhkin et al. 2002). Apparently, high-pressure transition metal nitrides of zirconium(IV) and hafnium(IV) studied in the present work belong to the latter group of potentially stiff materials.

1.2.1.3 Correlation of elastic moduli with material microstructure

The above consideration concerns an ideal case of pure homogeneous materials. Real materials usually contain inhomogeneities, such as weak phases, porosity, etc. The presence of such inhomogeneities can significantly affect the elastic properties of material. The effective elastic moduli of a two-phase compound can be estimated using the following approach. The upper limit for the effective elastic modulus M can be estimated using the Voigt model (Voigt 1928). According to this model the strain is assumed to be uniform throughout a body, so $M = M_1V_1 + M_2V_2$, where M_i and V_i is elastic modulus and volume fraction of each component, respectively. If one considers the stress to be uniform throughout a body (Reuss 1929), such approach gives the lower limit for the effective elastic modulus: $1/M = V_1/M_1 + V_2/M_2$. An average of these upper and lower limits is usually considered as a good approximation for effective elastic modulus of a two-phase compound (Rice 1996; Sherman & Brandon 2000). For description of porosity influence on elastic moduli the above mentioned approach appears to be very rough. Therefore different (semi)empirical equations are usually used. For example, decrease of elastic modulus with porosity increase can be expressed by exponential law: $M = M_0 \exp(-bp)$, where b is a constant, p is volume fraction porosity (VFP), M and M_0 are elastic moduli of porous and dense material, respectively (Duckworth 1953; Ryshkewitch 1953; Spriggs 1961; Rice 1996; Reynaud & Thevenot 2000). Thus, standard methods used for examination of bulk elastic properties such as tension and torsion tests, sound velocity and resonant vibration methods or instrumented indentation (s. Chapter 2.4.3) provide the values for effective elastic moduli of material rather than intrinsic ones (those determined by atomic interaction and crystal structure exclusively). As was mentioned above, the bulk modulus can be alternatively derived by fitting EOS to experimental compression data, $V(P)$. The $V(P)$ relation, in turn, can be measured by (quasi)hydrostatic compression of crystal lattice using *in situ* high-pressure X-ray diffraction (s. Chapter 2.4.1). The bulk modulus value obtained in such a way is not affected by microstructural defects (e.g. porosity) and represents the intrinsic property of the investigated material.

1.2.2 Hardness

1.2.2.1 Definition and measurement of hardness

Extensive efforts were undertaken to find a way for the synthesis of diamond, the hardest known material having hardness of about 100 GPa. It is a well-known fact that the first industrial route to synthetic diamonds involved application of high-pressure methods (e.g. Hazen 1999). By analogy, cubic boron nitride having hardness around 50 GPa was first synthesised at high pressures and temperatures. In contrast to diamond, c-BN does not exist in nature. These two compounds constitute the class of the so called *superhard* [*] materials which are of great importance for grinding and cutting tool industry (e.g. Sigalas & Caveney 2000). The search for new superhard materials is of fundamental and technological interest (Riedel 1994; Leger & Haines 1997; Teter 1998; Veprek 1999; Zerr & Riedel 2000; Kaner et al. 2005) and remains one of the most dominated areas of the high-pressure research (Takano & Onodera 1997; Badding 1998; Haines et al. 2001; Brazhkin et al. 2002; McMillan 2002, 2003; Brazhkin 2007). Intensive research in this field continues up today and, as a result, a few novel high-pressure compounds with hardness exceeding 30 GPa were discovered. Among them, for example, stishovite SiO_2 (33 GPa) (Stishov & Popova 1961; Leger et al. 1996), cubic Si_3N_4 (30-43 GPa) (Zerr et al. 1999; Zerr et al. 2002a), cotunnite-type TiO_2 (38 GPa) (Dubrovinsky et al. 2001), partially polymerized fullerites C_{60} (25-90 GPa) (e.g. Brazhkin et al. 1998) and cubic BC_2N (76 GPa) (Solozhenko et al. 2001). High hardness is also expected for other novel high-pressure compounds, namely c-Zr_3N_4 and c-Hf_3N_4 (Mattesini et al. 2003; Zerr et al. 2003; Chhowalla & Unalan 2005), which synthesis and properties examination is the subject of the present work. Therefore, definition of hardness and its dependence on measurement procedure, morphology (e.g. defects and impurities) and elastic properties of investigated material will be discussed below.

Although hardness is very important and widely used parameter for characterisation of technological materials, it is quite difficult both unambiguously define and measure it. One of the today accepted general definitions is given by Szymanski & Szymanski (1989), in which the authors define hardness as "*the resistance offered by a given material to external mechanical action endeavouring to scratch, abrade, indent or in any other way permanently affect its surface*." Accordingly, hardness can be measured using scratching (Mohs,

[*] The term „superhard" can be used for materials with microhardness exceeding 40 GPa, see e.g. (Teter 1998)

Bierbaum), abrasion (Rosiwal), impact (Shore, Herbert) and static indentation (e.g. Brinell, Rockwell, Vickers, Knoop) * methods (Szymanski & Szymanski 1989; McColm 1990). However, the values which can be obtained using those methods have different units and scales, and generally can not be compared with each other (e.g. McColm 1990). Today the most frequently used are the indentation methods, where material is indented by a hardened steel ball (Brinell, Rockwell), diamond cone (Rockwell) or diamond pyramid (Vickers, Knoop). The indentation hardness value is determined from the ratio of the loading force to the area or depth of the remaining indentation after indenter, forced into the surface of a material, is removed. For example, Vickers hardness is defined as applied load L divided by the surface area of the residual imprint A made by the square-based diamond pyramid, i.e. $H_V = L/A$ and hence has units of pressure, e.g. GPa (Chapter 2.4.2). Thus, indentation hardness value depends generally on the material resistance to a local plastic deformation. However, it is known that a partial elastic recovery usually takes place after indenter is removed (e.g. Bull et al. 1989; Li & Bradt 1993). At low loads, the relative part of the compression energy consumed by the elastic deformation increases significantly, thus the measured hardness, L/A, increases with the load decrease. This phenomenon is observed for both metals and ceramics and referred to as an indentation size effect (ISE) (e.g. Tabor 1951; McColm 1990). In fact ISE is not only due to elastic recovery alone but to a complex combination of different material- and measurement technique related factors, e.g. new surfaces formation, friction, fracture and hardening of material during indentation, residual stresses, sharpness and geometry of the indenter, loading rate, etc. (e.g. Quinn & Quinn 1997; Bull 2003). Therefore it is usually suggested to perform hardness measurement through a wide range of loads, in order to find the load conditions where the major part of the deformation energy is spent on plastic deformation of material. Under such conditions the measured L/A value is almost load-independent and is usually referred to as the *true hardness* (Fröhlich et al. 1977; Hirao & Tomozawa 1987; Li & Bradt 1993; Quinn & Quinn 1997). For hard ceramic material, the critical load of onset of the load-independent hardness can vary from about 1 N up to several hundreds newtons (McColm 1990; Quinn & Quinn 1997; Brazhkin et al. 2004).

The information on both elastic and plastic behaviour of the indented material can be obtained using the so called *instrumented indentation* (also known as *load-depth sensing indentation*)

* For the precise definition of the Brinell, Rockwell, Vickers and Knoop hardness tests see, e.g., ISO 6506, 6508 6507 and 4545 (or ASTM E0010, E0018, E0092 and C1326), respectively.

technique (ISO 14577). This method allows measurement of the indenter displacement (and, consequently, the imprint area A) during loading and unloading as a function of the applied load L. Stimulated by the requirement of testing mechanical properties of materials in very small volumes, the instrumented indentation was scaled down to nanometer dimensions. Modern *nanoindentation* techniques allow precise control of the applied load down to a few micronewtons with the indenter displacements in the nanometer range. Thus it is suitable for investigation of single grains, thin films, nanocomposites, etc. (Oliver & Pharr 1992; Li & Bhushan 2002). This technique, in particular, was used in the present work for examination of hardness and elastic properties of the synthesized materials (Chapter 3.4.3).

In addition to the chosen measurement technique and load range, the real hardness of the investigated material depends on its morphology. The hardness of single crystals usually depends on the tested crystallographic plane and orientation of the indenter. For polycrystalline materials hardness is strongly influenced by defects, porosity, grain size, presence of a contaminating layer on the grain surface, impurities, grains orientation, residual stresses and the like (Szymanski & Szymanski 1989; McColm 1990; Riedel 2000). For example, hardness of material decreases rapidly with porosity increase (Ryshkewitch 1953; Spriggs 1961; Rice 1996). Similar to elastic moduli (Chapter 1.2.1.3) such behaviour can be expressed by an exponential law, i.e. $H = H_0 \exp(-bp)$, where b is a constant, p is the volume fraction porosity (VFP), H and H_0 is the hardness of the corresponding porous and dense specimen, respectively (Duckworth 1953; McColm 1990; Luo & Stevens 1999; Milman et al. 1999). This relationship was used in the present work to estimate the hardness of fully dense c-Zr_3N_4 (Chapter 3.4.2).

Influence of the grain size on material hardness is related to the Hall-Petch effect: the grain size decrease is accompanied by increase of yield strength (and, consequently, of hardness) of a polycrystalline material, because generation and propagation of dislocations under indenter is hindered by grain boundaries (Hall 1951; Petch 1953; McColm 1990; Hertzberg 1996). Such concept of introduction of energetic barriers for creation and movement of dislocations is widely employed today for strengthening of metals (Hertzberg 1996) and production of two- and three-dimensional superhard nanostructural materials (e.g. Veprek 1999). With respect to potential application of the materials examined in the present work, they can be suggested for potential use as hard components of such superhard nanolayers or nanocomposites.

It can be concluded that the measured hardness value depends on chosen method and particular measurement conditions. Therefore, in order to compare hardness of different materials, the measurement procedure should preferably be the same. If it is not possible, then the details of a particular experiment should be comprehensively described. Furthermore, hardness of a given material depends on a number of factors, which include composition, morphology, texture and history of the sample fabrication and preparation. However, the "intrinsic" hardness is controlled by the atomic interaction, and a few methods to correlate it with better defined physical properties, such as elastic moduli, were suggested (Gilman 1968; Gerk 1977; Sung & Sung 1996; Leger & Haines 1997; Teter 1998; Zerr & Riedel 2000; Haines et al. 2001; Brazhkin et al. 2002). In particular, correlations of hardness with bulk or shear modulus were considered. These approaches are briefly discussed below.

1.2.2.2 Correlation of hardness with elastic moduli

In contrast to reversible elastic deformation, plastic deformation caused, for example, by indentation is permanent and involves irreversible displacement of atoms with respect to each other via generation and motion of dislocations. Despite this fact, indentation hardness of materials was often suggested to correlate with their elastic properties. Such correlation attracted the attention, because modern first-principles computational methods allow a routine calculation of elastic moduli for a given material if its crystal structure is known. Hence, potentially hard or superhard materials could be predicted theoretically. Plastic deformation induced during hardness tests is, however, closely related to the deformation of shear character, which is initially elastic and under further load is followed by irreversible shape change. Shear strength of material is, in turn, proportional to shear modulus, G (Kelly & Macmillan 1986; Hertzberg 1996). Indeed, an acceptable correlation was found between hardness and shear modulus (Gilman 1968; Gerk 1977; Teter 1998; Zerr & Riedel 2000; Brazhkin 2007). As shown on Figure 1.4a, hardness almost monotonically increases with G. A reasonable correlation between hardness and bulk modulus was reported for the particular class of covalent or partially covalent materials, such as diamond-like semiconductors (group 14, 13-15, 12-16 compounds) or selected hard ceramics (e.g. Al_2O_3, AlN, ZrO_2) (Leger et al. 1994; Sung & Sung 1996; Leger & Haines 1997). However, in general case there is no monotonic relation (Figure 1.4b). For example, osmium has the bulk modulus comparable to that of diamond (Cynn et al. 2002), while its hardness is only about 4 GPa. As can be seen from Figure 1.4b, condition of high bulk modulus is required but not sufficient for material to be hard. Thus, search for hard materials should be concentrated on those having both high bulk and high shear moduli. They are predominantly covalent or partially covalent

compounds of light elements (B, C, N, O, Al, Si) or borides, carbides, nitrides and oxides of the group 4-7 transition metals (s. Chapter 1.2.1.2). High-pressure modifications of such compounds usually have denser structures with higher coordination numbers of constituent atoms as compared to ambient-pressure phases. Thus the former can be considered as potentially stiff and hard materials.

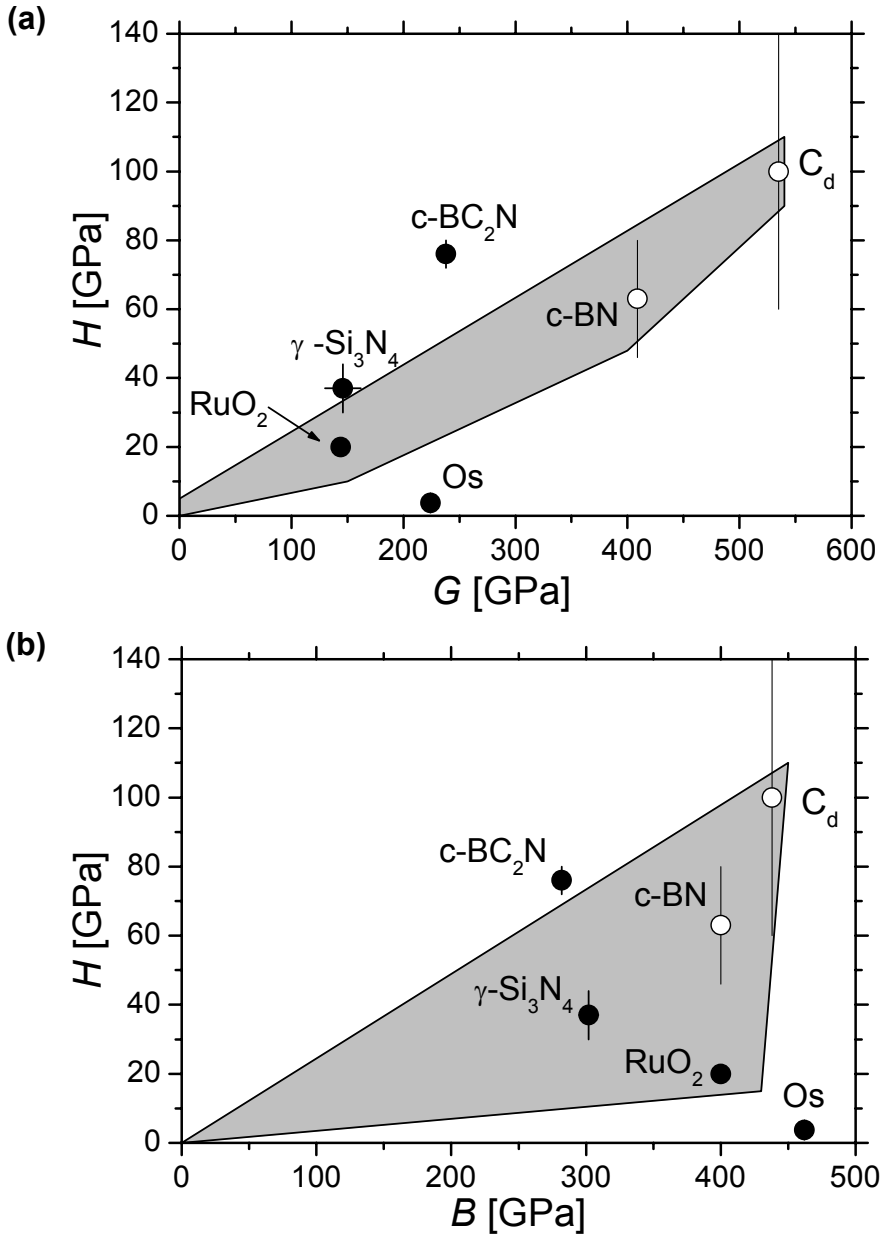

Figure 1.4. Hardness with respect to (a) shear and (b) bulk moduli for a common set of stiff materials. Gray areas represent the summarized data after Teter (1998). Open circles correspond to the data for superhard diamond (C_d) and cubic boron nitride (c-BN). Solid circles correspond to the data for low compressible osmium (Cynn et al. 2002) and a few recently discovered hard high-pressure materials, i.e. γ-Si_3N_4 (Zerr et al. 1999), c-BC_2N (Solozhenko et al. 2001), RuO_2 (Leger et al. 2001).

1.3 Recent advances in high-pressure nitrides

Until the end of the last century the high-pressure research on nitrides was mainly concentrated on those of the group 13 elements, namely BN, AlN, GaN, InN (e.g. Bradley et al. 1966; Davis 1991; Vel et al. 1991; Ruoff & Li 1995; Auckland 2001; Mujica et al. 2003). High-pressure cubic phase of boron nitride, c-BN, is known as the second hardest material after diamond. Interest in AlN, GaN and InN has grown due to their interesting semiconducting properties. In particular wurtzite-type GaN has a direct band gap of 3.5 eV which suggests its application for production of blue light-emitting diodes (LEDs) (Maruska & Tietjen 1969; Monemar 1974). Systematic high-pressure investigation of nitrides of other elements with a few exceptions (e.g. carbon nitrides, s. Chapter 1.3.1.1) was not performed (Zerr et al. 2006a).

During the last decade the interest in high-pressure nitrides has strongly increased (Kroke 2002; Horvath-Bordon et al. 2006; Zerr et al. 2006a). This is partially related to the discovery of a new family of high-pressure cubic spinel nitrides of the group 14 elements, namely γ-A_3N_4 (A = Si, Ge or Sn) (Zerr et al. 1999; Leinenweber et al. 1999; Scotti et al. 1999; Serghiou et al. 1999). Their most prominent representative, γ-Si_3N_4, was found to have a unique combination of high hardness, thermal and oxidation stability as well as to be wide band gap semiconductor suitable for fabrication of blue LEDs (s. below). Accompanied by theoretical predictions of existence and calculations of properties of new high-pressure phases, a number of experimental efforts to synthesize novel nitrides were made. The high-pressure high-temperature experiments with other tetravalent elements (group 4 transition metals) resulted in the discovery of another previously unknown family of high-pressure nitrides, c-Zr_3N_4 and c-Hf_3N_4, having cubic Th_3P_4-type structure (Zerr et al. 2003) (s. Chapter 1.3.2). The research was further extended to high-pressure nitrides of other transition metals such as molybdenum (Soignard et al. 2003), cobalt (Hasegawa & Yagi 2005), platinum, iridium and osmium (Gregoryanz et al. 2004; Crowhurst et al. 2006; Young et al. 2006). One should also mention high-pressure synthesis of superhard c-BC_2N (H_V = 76 GPa) having diamond-like structure (Solozhenko et al. 2001) and phosphorus nitride γ-P_3N_5 with five-fold coordinated P-cations (Landskron et al. 2001). Despite the latter compound is composed of light elements, its hardness was found to be less than 10 GPa (Landskron et al. 2002), most probably due to its layered crystal structure.

The first part of this chapter briefly reviews the research on novel high-pressure nitrides of group 14 elements (C, Si, Ge, Sn). In the second part synthesis methods, structure as well as up-to-date experimental and theoretical studies of recently discovered high-pressure zirconium(IV)- and hafnium(IV) nitrides are discussed in detail.

1.3.1 Group 14 nitrides

1.3.1.1 Carbon nitride

In the middle of 1980s it was predicted that hypothetical dense carbon(IV) nitride polymorph β-C_3N_4 (isostructural to β-Si_3N_4) could have the bulk modulus comparable to or even higher than that of diamond (Cohen 1985; Sung & Sung 1996). Based on the controversial opinion that hardness of material is primarily determined by its bulk modulus (s. Chapter 1.2.2.2) the authors suggested that this hypothetical carbon nitride can surpass diamond in hardness. In addition to β-C_3N_4, a few other hypothetical carbon nitride polymorphs, such as α- (isostructural to α-Si_3N_4), cubic- and pseudocubic C_3N_4, were also suggested to be competitive with diamond in stiffness and hardness (e.g. Liu & Wentzcovitch 1994; Teter & Hemley 1996). Since diamond is the hardest material known, such prediction excited the scientific community. As a result, an enormous amount of further theoretical investigations and experimental efforts to synthesize postulated carbon nitrides was made during the last two decades. The results of these studies are summarized and critically analyzed in several review articles (Fang 1995; Badding 1997; Matsumoto et al. 1999; Muhl & Mendez 1999; Malkow 2000; Kroke & Schwarz 2004; Horvath-Bordon et al. 2006; Goglio et al. 2008). Despite a number of reports of "successful synthesis" using different deposition or high-pressure techniques, most of the synthesized C-N materials were amorphous or nanocrystalline with nitrogen to carbon ratio (N/C) significantly lower than 4/3 as well as with structure and/or composition being not unambiguously determined. Moreover, the reported hardness and elastic moduli values of synthesized C-N compounds were much lower than those of diamond. Thus, up to this date there is no clear evidence for existence of a pure crystalline C_3N_4 phase, as well as no experimental confirmation of the predicted superior properties.

After more than ten years of "harder-than-diamond" fever several review articles reminded the scientific community that the shear modulus is "*a significantly better qualitative predictor of hardness*" than the bulk modulus (Teter 1998; Zerr & Riedel 2000; Haines et al. 2001; Brazhkin et al. 2002) (s. Chapter 1.2.2.2). Since the calculated shear moduli of hypothetical dense carbon nitrides are only 60 % that of diamond, the hardness of dense C_3N_4 is unlikely to

surpass even that of c-BN (Teter 1998). Diamond appears to remain the hardest and the most stiff material known, therefore it was suggested to focus the search on materials "*more useful than diamond, rather than harder than diamond*" (Teter 1998).

1.3.1.2 Spinel nitrides: γ-Si_3N_4, γ-Ge_3N_4 and γ-Sn_3N_4

While none of the postulated dense C_3N_4 phases was undoubtedly confirmed, predictions of their existence have initiated, for a long period of time, extensive high pressure studies on different C-N compounds and motivated high-pressure experiments with other group 14 element nitrides. These experiments led to the discovery of novel cubic spinel nitrides of silicon(IV) and germanium(IV), denoted γ-Si_3N_4 and γ-Ge_3N_4, respectively (Zerr et al. 1999; Leinenweber et al. 1999; Serghiou et al. 1999). Moreover, almost simultaneously and independently the first tin nitride, γ-Sn_3N_4, was prepared at ambient pressure (Scotti et al. 1999). The discovery of principally novel class of nitrogen based materials has attracted much attention and motivated further experimental and theoretical studies on high-pressure nitrides.

The novel γ-Si_3N_4 having cubic spinel-type structure was first synthesized via chemical reaction of elemental silicon with nitrogen as well as from amorphous and crystalline (α and β) Si_3N_4 at high pressures (15-30 GPa) and high temperatures (2200-2800 K) using laser heated diamond anvil cell technique (LH-DAC) (Zerr et al. 1999). In the spinel-type structure two-thirds of Si-atoms are octahedrally coordinated by N-atoms and one-third is tetrahedrally coordinated (Figure 1.5b). In contrast, ambient-pressure α- and β-Si_3N_4 have all Si-cations in tetrahedral coordination (Figure 1.5a). The increase of atomic coordinations in high-pressure γ-Si_3N_4 results in significant increase of its density (by almost 26 %) when compared with the ambient-pressure phases (Zerr et al. 1999). Computational studies indicated high bulk and shear moduli for γ-Si_3N_4 of 300 GPa and 340 GPa, respectively (for reference β-Si_3N_4 was reported to have $B_0 \approx 260$ GPa and $G_0 \approx 130$ GPa). Based on the earlier suggested empirical relations between hardness and bulk or shear moduli (Chapter 1.2.2.2) the authors have predicted the hardness of γ-Si_3N_4 to be close to that of stishovite (33 GPa) (Zerr et al. 1999). Soon after discovery, synthesis of γ-Si_3N_4 in a LH-DAC was reproduced by another research group (Soignard et al. 2001a). Successful preparation of bulk amounts of cubic silicon nitride at high pressures and high temperatures using multi-anvil apparatus was independently reported by Schwarz et al. (2000) and Jiang et al. (2000a). At the same time γ-Si_3N_4 was synthesized using shock-wave techniques (He et al. 2000; Sekine et al. 2000). The materials obtained using these different techniques were further investigated with various methods in

order to derive their structure, composition, elasto-mechanical, thermal and opto-electronical properties.

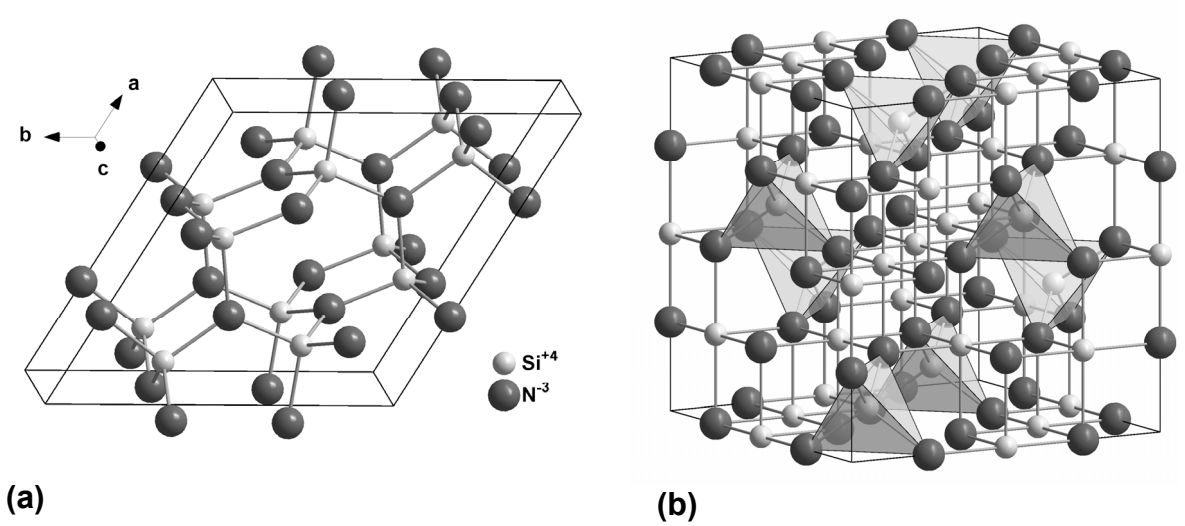

Figure 1.5. Schematic crystal structures of Si_3N_4: (a) ambient-pressure hexagonal β-Si_3N_4 (space group $P6_3/m$, No. 176) with all Si-atoms in tetrahedral (4-fold) coordinations; (b) high-pressure cubic spinel γ-Si_3N_4 (space group $Fd\bar{3}m$, No. 227) with Si-atoms in both octahedral (light-grey spheres) and tetrahedral (grey tetrahedrons) coordinations.

The bulk modulus of γ-Si_3N_4 was determined using both static- and dynamic compression techniques and the values between 290-317 GPa were obtained (He et al. 2000; Soignard et al. 2001a; Jiang et al. 2002; Zerr et al. 2002a). Applying nanoindentation technique Zerr et al. (2002a) have determined the Young's modulus, shear modulus and Poisson's ratio of γ-Si_3N_4. It should be mentioned that the resulted shear modulus of 148 GPa is almost two times lower than the theoretically predicted values. Moreover, the authors estimated the Vickers hardness $H_V(0.5)$ [*] for oxygen free polycrystalline material to be between 30-43 GPa. Further investigation of hardness of γ-Si_3N_4 also revealed high values of about $H_V(?) = 35$ GPa (Jiang et al. 2001) and of $H_V(0.001) = 43$ GPa for material with low oxygen content (< 0.5 wt.%) (Tanaka et al. 2002). These results indicated that cubic silicon nitride is the third hardest material after diamond and c-BN. Another property which is very important for different applications is the thermal stability. The studies of high-temperature behaviour of γ-Si_3N_4 in argon atmosphere showed that the reverse γ-to-β transformation of nanocrystalline shock-wave powders starts at about 1673 K (Sekine & Mitsuhashi 2001). Bulk multi-anvil samples were found to be stable in air at least up to 1673 K and have transformed to a mixture of α-

[*] The value in parenthesis indicates the applied load in kilograms, i.e. $H_V(0.5)$ means the Vickers hardness measured at a load of 0.5 kg ($L = 4.9$ N).

and β-Si_3N_4 phases at 1873 K (Jiang et al. 2001). Thus, γ-Si_3N_4 drastically outperforms other superhard materials, such as diamond, c-BN, c-BC_2N, stishovite-SiO_2, B_4C and B_6O in thermal (meta)stability in air. Additionally, γ-Si_3N_4 was found to be a semiconductor with an energy band gap between 3.3 and 4.3 eV. The lower value was determined from optical transmission spectra and cathodoluminescence (Zerr et al. 2002b), the upper was obtained by a combination of X-ray absorption and emission spectroscopy (Leitch et al. 2004). These findings suggested cubic silicon nitride to be suitable for fabrication of blue LEDs.

Combination of such useful properties of novel γ-Si_3N_4 as high hardness, exceptional thermal and oxidation stability, wide energy band gap, as well as ability to produce γ-Si_3N_4 powder in commercial amounts and for reasonable costs using shock-wave methods (Zerr et al. 2006a) opens a broad area for its potential industrial applications.

By analogy with γ-Si_3N_4 cubic spinel γ-Ge_3N_4 was synthesized at high pressures and high temperatures independently by two research groups. Serghiou et al. (1999) have prepared γ-Ge_3N_4 from elemental germanium and nitrogen above 14 GPa and 2000 K employing LH-DAC. Leinenweber et al. (1999) have transformed the mixture of α- and β-Ge_3N_4 into the cubic spinel phase using both LH-DAC and the multi-anvil technique at 24 GPa / 700 K and 12 GPa / 1300 K, respectively. Later, a successful preparation of γ-Ge_3N_4 nanopowder using shock-wave methods was reported (He et al. 2001). Being almost 20 % denser than the ambient-pressure phases, high-pressure γ-Ge_3N_4 was also found to have high bulk modulus of 295 GPa (Somayazulu et al. 2000) (in a reasonable agreement with predicted values) and high hardness of $H_V(0.1)$ = 28 GPa (Shemkunas et al. 2004). The bulk modulus of γ-Ge_3N_4 is significantly higher than B_0 of α- and β-Ge_3N_4 (Soignard et al. 2004a).

Simultaneously with the discovery of γ-Si_3N_4 and γ-Ge_3N_4, cubic spinel Sn_3N_4 was synthesized via a chemical reaction of $SnBr_2$ (or SnI_4) with KNH_2 at 573 K and ambient pressure (Scotti et al. 1999). Later Shemkunas et al. (2002) obtained spinel tin nitride by solid state metathesis reaction of SnI_4 with Li_3N at 623 K and elevated pressure of NH_4Cl (2.5 GPa) using piston-cylinder apparatus. The Vickers hardness of 11 GPa for γ-Sn_3N_4 measured at 0.1 kg load (Shemkunas et al. 2004) is, however, significantly lower than those reported for γ-Ge_3N_4 and γ-Si_3N_4.

The discovery and further experimental studies of spinel nitrides were accompanied by a number of theoretical calculations. Electronic structure, optical, elastic, thermal, thermodynamic and vibrational spectroscopic properties of binary γ-A_3N_4 (A = Si, Ge, Sn) were investigated using different computational methods (e.g. Mo et al. 1999; Dong et al.

2000; Bagayoko & Zhao 2001; Ching et al. 2001; Fang et al. 2003; Ching & Rulis 2006). Existence and interesting properties of these compounds motivated further theoretical studies of other hypothetical nitrides having spinel-type structure. Cubic spinel γ-C_3N_4, γ-Ti_3N_4, γ-Zr_3N_4 and γ-Hf_3N_4 were initially postulated to exist. Based on this supposition the stability and properties of ternary spinel nitrides were investigated for all possible combinations of tetravalent cations of the group 14 (C, Si, Ge, Sn) and the group 4 (Ti, Zr, Hf) elements (Ching et al. 2000; Ching et al. 2001; Ching et al. 2002a; Dong et al. 2003). Of all hypothetical ternary nitrides only nine were suggested to be stable with respect to their decomposition into binary constituents. Three of them, γ-CSi_2N_4, γ-CGe_2N_4 and γ-$SiGe_2N_4$ were calculated to be semiconductors, the others γ-CTi_2N_4, γ-$SiTi_2N_4$, γ-$GeTi_2N_4$, γ-$ZrTi_2N_4$, γ-$SnTi_2N_4$, γ-$ZrHf_2N_4$ were predicted to be metals (Ching et al. 2001; Ching et al. 2002a). First principle studies of the postulated spinel nitrides of the group 4 transition metals, γ-M_3N_4 (M = Ti, Zr, Hf), revealed that γ-Ti_3N_4 and γ-Zr_3N_4 could be narrow band gap semiconductors whereas γ-Hf_3N_4 a metal (Ching et al. 2000; Ching et al. 2002a). A detailed theoretical examination of Zr_3N_4 has shown that an ordered defect rock-salt structure, $Zr_3\square N_4$, has the lowest energy at ambient pressure when compared with spinel γ-Zr_3N_4 and orthorhombic o-Zr_3N_4 (Ching et al. 2002b). This does not agree with later calculations of Kroll (2003), where o-Zr_3N_4 was found to be stable at ambient conditions. It should be mentioned, however, that none of the above discussed hypothetical binary and ternary spinel nitrides were synthesized so far.

The theoretical predictions were accompanied by experimental work on new binary and ternary spinel nitrides. Investigation of Si_3N_4-Ge_3N_4 system at high pressures and high temperatures revealed the existence of a continuous spinel-type solid solution above 23 GPa and 2000 K (Soignard et al. 2004b). At lower pressures two immiscible phases of γ-Ge_3N_4 and γ-Si_2GeN_4 (in contrast to the suggested γ-$SiGe_2N_4$) have been observed (Soignard et al. 2001b). In turn, high-pressure high-temperature experiments with group 4 transition metal nitrides resulted in the discovery of novel c-Zr_3N_4 and c-Hf_3N_4 having cubic Th_3P_4-type structure (Zerr et al. 2003). Synthesis and results of earlier experimental and theoretical studies of c-M_3N_4 (M = Zr, Hf) are highlighted in the following paragraph.

1.3.2 Group 4 transition metal nitrides: δ-MN and c-M_3N_4

At ambient pressure, the group 4 transition metal nitrides commonly appear in the 1:1 stoichiometry and possess a cubic NaCl-type structure (Figure 1.6). They are also referred to as mononitrides and denoted δ-MN (where M is Ti, Zr or Hf). The δ-MN are well known

refractory materials with unique combinations of mechanical, thermal, chemical and electromagnetic properties (s. below). They have found a broad industrial application as hard wear resistant coatings of cutting tools, corrosion and abrasion protection layers on mechanical and optical components, diffusion barriers and superconductors in microelectronics (Toth 1971; Ettmayer & Lengauer 1991; Oyama 1996; Pierson 1996; Lengauer 2000).

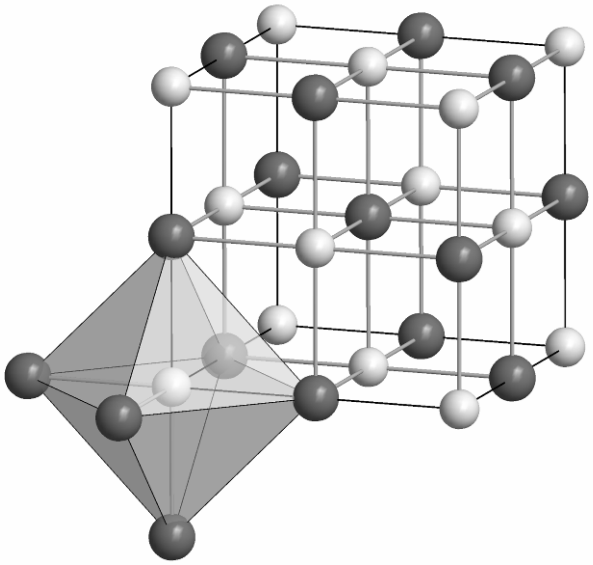

Figure 1.6. Crystal structure of group 4 transition metal mononitrides, δ-MN (NaCl-type, space group $Fm\bar{3}m$, No. 225). Both metal atoms (light-grey spheres) and nitrogen atoms (dark-grey spheres) are in octahedral (6-fold) coordinations.

The group 4 transition metal mononitrides exhibit metallic behaviour. However, in contrast to the related transition metals, they are brittle and hard. The Vickers hardness values for δ-MN are reported to vary between 14 and 20 GPa depending on composition and microstructure (Samsonov 1969; Ettmayer & Lengauer 1991; Lengauer 2000). These compounds also possess high elastic moduli (e.g. B_0 and G_0 of about 250-400 GPa and 140-200 GPa, respectively) and high strength (Kral et al. 1998; Teter 1998; Brazhkin et al. 2002). The δ-MN belong to a class of refractory materials due to their high melting points (3300-3700 K in nitrogen atmosphere) and a comparatively high thermal oxidation resistance (start to oxidize in air between 800 and 1000 K) (e.g. Samsonov 1969; Toth 1971; Wiame et al. 1998). Moreover, they are superconductors with relatively high critical temperatures of 5.8, 10.5 and 6.9 K for TiN, ZrN and HfN, respectively (Lengauer 2000). Another important property of these nitrides is their defect structure. Maintaining NaCl-type structure, the mononitrides may exhibit significant variation in stoichiometry toward both metal and nitrogen rich compounds by formation of vacancies on the corresponding lattice sites. For example, for δ-HfN_x x can

vary from 0.74 to 1.7, while for δ-ZrN_x from 0.54 to 1.35 (Toth 1971; Fix et al. 1991; Kral et al. 1998). The presence of vacancies in δ-MN_x significantly affects all their properties – mechanical, thermal, electrical, magnetic and superconducting. In particular, δ-HfN_x and δ-ZrN_x with $x > 1$ transform from metallic to insulating phases with increase of nitrogen content, whereas δ-TiN_x is metal for all known compositions (Andrievski 1997). The structure of the transition metal nitrides with high nitrogen content was suggested to be related to that of NaCl-type with rhombohedral distortion; however, it is not completely clear yet.

With respect to stoichiometric M_3N_4 compounds of the group 4 transition metals, only orthorhombic zirconium(IV) nitride, o-Zr_3N_4 (Figure 1.7), was known for a long time (Juza et al. 1964; Yajima et al. 1983; Lerch et al. 1996). The o-Zr_3N_4 was found to be non-conductive and diamagnetic. On heating in nitrogen it decomposes above 1100 K into δ-ZrN and N_2. In air it starts to oxidise at 800 K (Lerch 1997). Other properties of this material were not investigated so far. It should be also mentioned that the density of o-Zr_3N_4 (6.32 g/cm^3) is considerably higher than that of predicted γ-Zr_3N_4 (5.77 g/cm^3). Therefore it is very unlikely for spinel zirconium nitride to be stable at high pressures.

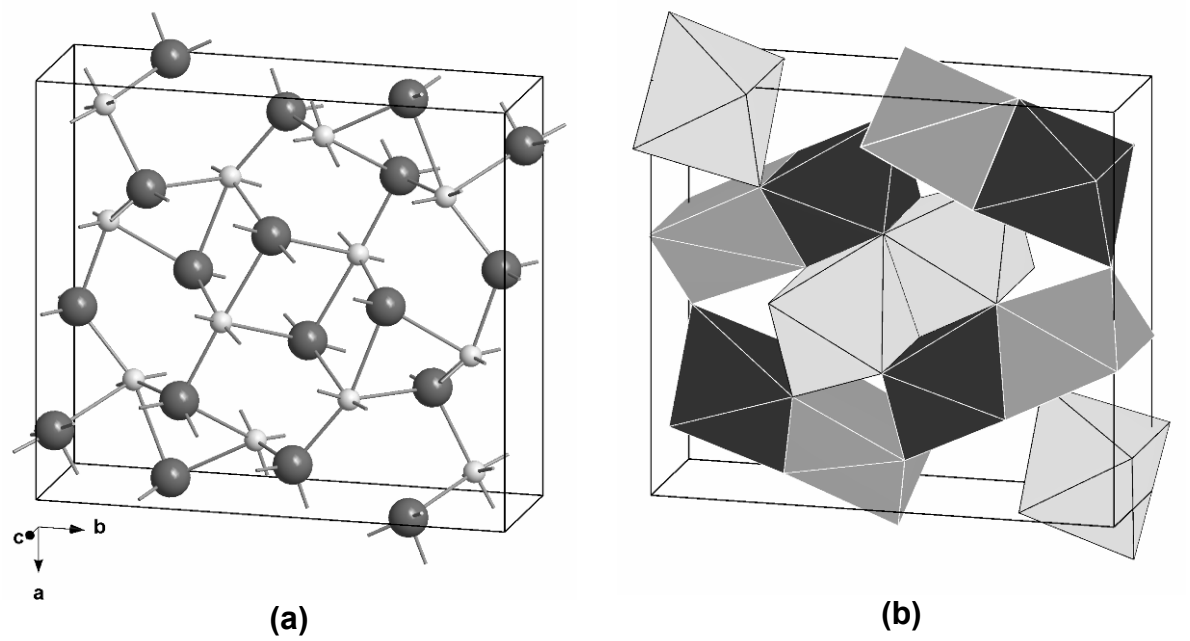

Figure 1.7. Crystal structure of orthorhombic zirconium(IV) nitride, o-Zr_3N_4 (space group *Pnam*, No. 62): (a) unit cell with Zr- and N-atoms represented by grey and black spheres, respectively; (b) the polyhedral structure plot showing the interconnection of ZrN_6-polyhedra.

The high-pressure high-temperature investigation of group 4 transition metal nitrides was a logical extension of the studies on spinel nitrides. The discovery of novel γ-A_3N_4 (A = Si, Ge,

Sn) has entailed speculations on possible stability of spinel nitrides of other tetravalent elements (i.e. group 4 transition metals). To verify this supposition the chemical reaction of Ti, Zr and Hf metals or their mononitrides (δ-MN) with molecular nitrogen, was performed at high pressures and temperatures using a LH-DAC (Zerr et al. 2003). In the experiments with Ti-N system no formation of any other phase besides δ-TiN was observed at pressures of 17.5-25 GPa and temperatures of 1500-3000 K. In contrast to titanium, the experiments with Zr-N system at 15.6-18 GPa and 2500-3000 K and Hf-N system at 18 GPa and 2800 K resulted in synthesis of novel compounds. The examination of structure and stoichiometry using XRD and EDX has shown that the reaction products are stoichiometric nitrides Zr_3N_4 and Hf_3N_4 with cubic Th_3P_4-type structure (space group $I\bar{4}3d$, No. 220) (Figure 1.8a) (Zerr et al. 2003). Compounds having such structure are denoted throughout the thesis as c-M_3N_4, where M = Zr or Hf. The structure solution was confirmed by observation of Raman-active vibrational modes, allowed by the symmetry group ($I\bar{4}3d$ or T_d^6). In the Th_3P_4 structure type cations are eight-fold coordinated by nitrogen atoms (Figure 1.8b), which themselves are six-fold coordinated by metal atoms (Figure 1.8c). The cation coordination number of eight is higher than those in the NaCl-type mononitrides and in o-Zr_3N_4 (six-fold coordination) as well as in the predicted spinel nitrides (four- and six-fold coordinations). As a result, the density of c-Zr_3N_4 is almost 13 % higher than that of o-Zr_3N_4. In fact, c-Zr_3N_4 and c-Hf_3N_4 are the first binary nitrides with such a high cation coordination number (Zerr et al. 2003). Preliminary compressibility measurements have indicated high bulk moduli of ≈ 250 GPa and ≈ 260 GPa (assuming $B_0' = 4$) for zirconium(IV) and hafnium(IV) nitride, respectively, which could indicate high hardness. By analogy with γ-Si_3N_4, the authors have also presumed a high thermal (meta)stability for c-M_3N_4 (Zerr et al. 2003).

Subsequent theoretical studies of the electronic properties of these transition metal nitrides supported the structure assignment and low compressibility of c-M_3N_4 (B_0 of 195-265 GPa and 215-283 GPa for c-Zr_3N_4 and c-Hf_3N_4, respectively) (Kroll 2003; Mattesini et al. 2003; Lowther 2005) as well as their semiconducting behaviour, suggested in the original synthesis work. The indirect band gap, depending on the calculation method, was predicted to be between 0.56 and 1.1 eV for c-Zr_3N_4 and between 0.84 and 1.8 eV for c-Hf_3N_4 (Kroll 2003; Mattesini et al. 2003; Xu et al. 2006). The band structure analysis of c-M_3N_4 has also indicated “fingerprints” of superconductivity, which is expected in these materials after appropriate electron doping (Kroll 2003). It was also shown that c-Zr_3N_4 and c-Hf_3N_4 have relatively large static dielectric constants (Xu et al. 2006). Such combination of opto-electronic and superconducting properties could suggest these materials for potential

applications in microelectronics. Kroll (2003) has also computed and assigned the Raman-active vibrational modes for c-M_3N_4, which, however, are difficult to compare with experimental spectra measured at high pressures (Zerr et al. 2003). Additionally, the elastic constants of c-M_3N_4 were calculated using *ab initio* methods. Using these results and a correlation between hardness and shear modulus reported by Teter (1998), Mattesini et al. (2003) suggested a Vickers hardness value of about 20 GPa for both transition metal nitrides.

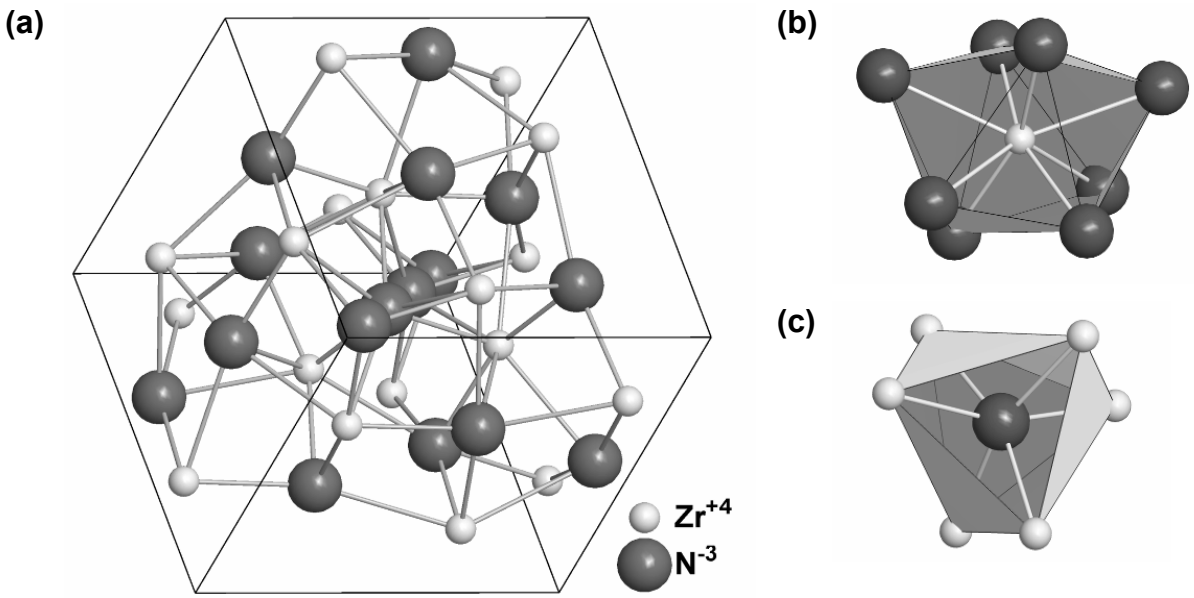

Figure 1.8. (a) Crystal structure of c-M_3N_4 (cubic Th_3P_4-type, space group $I4\bar{3}d$, No. 220), where the grey spheres represent the metal atoms (M = Zr or Hf) and the black spheres represent the N-atoms. In this structure cations and anions are eight- (b) and six-fold coordinated (c), respectively.

Later, theoretical investigation of nitrogen rich part of Ti-N, Zr-N and Hf-N *P-T* phase diagrams has provided data on phase equlibria conditions between δ-MN + N_2 and c-M_3N_4 (Kroll 2004). Calculated minimum *P-T* conditions for stabilization of c-M_3N_4, however, significantly overestimate experimental ones. Kroll (2004) has also suggested that phase transition from low-pressure orthorhombic structure (o-M_3N_4) to high-pressure Th_3P_4-type phase will occur at 6 GPa and 9 GPa for Zr_3N_4 and Hf_3N_4, respectively.

Further interest in these materials was excited by the recent finding that thin films composed of c-Zr_3N_4 are significantly harder than those of δ-ZrN and, moreover, dramatically outperform δ-TiN in wear resistance during machining of a low-carbon steel (Chhowalla & Unalan 2005). Titanium mononitride, in turn, is a well known hard wear-resistant material. It is traditionally used in mono- and multilayer coating of cutting and milling tools, because it considerably increases their service life (e.g. Ettmayer & Lengauer 1991; Su & Kao 1998).

The films of c-Zr_3N_4 were prepared via the technique of physical vapour deposition (PVD) (Chhowalla & Unalan 2005). For deposition, a modified filtered cathodic arc (FCA) method was applied. In this method the metal vapour, generated by an arc discharge on pure zirconium cathode, was reacted with fully ionized atomic nitrogen. The authors were able to control the stoichiometry and the structure of the nitrides and to deposit stoichiometric δ-ZrN or Zr_3N_4 with either orthorhombic or cubic structure. The formation of c-Zr_3N_4 was confirmed by XRD and Raman spectroscopy examination: the measured X-ray diffractogram and Raman spectrum agree with those of the material synthesized in a LH-DAC. It was suggested that, during deposition, the high-pressure c-Zr_3N_4 was stabilized by large compressive stress (> 9 GPa) in the film and high temperature in the deposition zone. In nanoindentation tests with maximum applied load of 5 mN, the c-Zr_3N_4 films were found to be significantly harder (≈ 36 GPa) than δ-ZrN films (≈ 27 GPa) obtained using the same deposition technique. Moreover, milling tests with low carbon steel showed that a carbide tool coated with c-Zr_3N_4 is almost one order of magnitude more wear resistant than an uncoated one or a tool coated with traditional δ-TiN (Chhowalla & Unalan 2005). These results demonstrated a great potential of c-M_3N_4 for industrial application as hard wear-resistant coatings.

In summary, the recently discovered cubic zirconium(IV)- and hafnium(IV) nitrides are of potential interest for use in microelectronics and for wear-resistant applications. However, up to this work there was no information on bulk synthesis of these materials, as well as only limited preliminary experimental data on their properties were available. The present work extends the knowledge on the high-pressure bulk synthesis and on the properties of c-Zr_3N_4 and c-Hf_3N_4.

1.4 Subject of the work

The aim of the present work is the exploration of the recently discovered cubic zirconium(IV)- and hafnium(IV) nitrides having Th_3P_4-type structure. In the frame of this study the high-pressure high-temperature synthesis of macroscopic amounts of oxygen-bearing c-Zr_3N_4 and c-Hf_3N_4 was performed. Furthermore, structure and composition of the synthesized high-pressure nitrides were determined, as well as their elasto-mechanical and thermal properties relevant for potential industrial applications were investigated.

The initial part of the experimental work is concerned with preparation of starting material for high-pressure synthesis. Since solid zirconium- and hafnium nitrides with nitrogen to metal ratio $\geq 4/3$ are not commercially available, a simple ambient-pressure method for the

preparation of large amounts of nanocrystalline M_3N_{4+x} powders (M = Zr or Hf, $x > 0$) was developed (Li et al. 2005). The method and its further improvement with respect to higher nitrogen and lower oxygen content in the resulting materials are introduced in Chapters 2.1 and 3.1.

The high-pressure high-temperature synthesis of c-M_3N_4 from nanocrystalline nitride powders was performed employing a multi-anvil apparatus. The choice of the appropriate high-pressure technique and experimental details of the synthesis are described in Chapters 2.2 and 3.2. The samples were recovered under ambient conditions and characterized using various methods. In particular the phase content and the structure of the high-pressure nitrides were investigated using powder X-ray diffraction (XRD) and transmission electron microscopy (TEM) (Chapters 3.2, 3.3.2). Electron probe microanalysis (EPMA) was used for determination of the sample composition (Chapter 3.3.1). Morphology of the high-pressure materials was examined employing scanning electron microscopy (SEM) combined with energy dispersive X-ray analysis (EDX) (Chapter 3.3.5). Analysis of the results from XRD, TEM and EPMA suggested the formation of cubic oxygen-bearing zirconium(IV) nitride (or oxynitride) having Th_3P_4-type structure, c-$Zr_3(N,O)_4$. In the case of hafnium nitride, contamination of the sample with minor amount of an oxidic phase didn't allow to conclude unambiguously about extent of oxygen incorporation into c-Hf_3N_4 structure. The Rietveld refinement of the XRD data was performed in order to derive the structure parameters for c-$Zr_3(N,O)_4$ and c-Hf_3N_4 (Chapter 3.3.2).

The investigation of elasto-mechanical properties included determination of elastic moduli (B_0, G_0, E_0, ν) and hardness of the synthesized materials. The bulk moduli of c-$Zr_3(N,O)_4$ and c-Hf_3N_4 were derived from their equations of state, $V(P)$, measured on quasi-hydrostatic compression to 50 GPa in a diamond anvil cell using *in situ* XRD (Chapter 3.4.1). For c-$Zr_3(N,O)_4$ the Vickers hardness and the nanoindentation hardness were measured (Chapters 3.4.2 and 3.4.3). Moreover, the isotropic shear modulus, Young's modulus and Poisson's ratio of c-$Zr_3(N,O)_4$ were determined by combination of compression and nanoindentation measurement results (Chapter 3.4.4). Since SEM revealed high porosity of both high-pressure materials, its influence on the measured hardness and elastic moduli values is additionally discussed. The high-temperature behaviour of c-$Zr_3(N,O)_4$ was also investigated in air between room temperature and 900 K using *in situ* XRD. The thermal expansion coefficient was derived from the high-temperature XRD data (Chapter 3.5). Finally, the results of this work are summarized and the structural features as well as the property profiles of c-M_3N_4 are compared with those of other hard high-pressure materials.

2 Experimental techniques

The present chapter introduces experimental methods and devices employed in this work. Firstly, equipment for preparation of nitrogen-rich zirconium and hafnium nitrides via ammonolysis is described. They were used as starting materials in high-pressure synthesis experiments. The following chapter briefly overviews modern high-pressure techniques; a multi-anvil apparatus used for high-pressure high-temperature synthesis of c-Zr_3N_4 and c-Hf_3N_4 is described in detail. Analytical methods applied for characterisation of recovered materials, namely powder X-ray diffraction, transmission and scanning electron microscopy, electron probe microanalysis, Raman spectroscopy, are presented in Chapter 2.3. The last part of this chapter deals with techniques for investigation of elasto-mechanical properties (compressibility measurement, indentation methods) and high-temperature behaviour (high-temperature X-ray diffraction) of the synthesized high-pressure nitrides.

2.1 Preparation of starting material

In order to synthesize c-Zr_3N_4 and c-Hf_3N_4 in macroscopic amounts at high pressures, appropriate starting materials were required. Since solid nitrides with N/M-ratio $\geq$ 4/3 (M = Zr, Hf) are not commercially available, a simple ambient-pressure method for preparation of large amounts of nanocrystalline M_3N_4 powders having distorted NaCl-type structure was developed in our research group (Li et al. 2005). Some improvement of this method, as described below, allowed obtaining such powders with N/M ratio even higher than 4/3 and with minimised amount of oxygen.

2.1.1 Ammonolysis of metal dialkylamides

Powders of nanocrystalline Zr_3N_{4+x} and Hf_3N_{4+x} having distorted NaCl-type structure were synthesized by ammonolysis of metal dialkylamides, namely tetrakis(diethylamido)zirconium and -hafnium ($Zr(NEt_2)_4$ and $Hf(NEt_2)_4$, where Et $\equiv C_2H_5$), at high temperatures up to 873 K (Li et al. 2005). Since the metal dialkylamides are highly air- and moisture sensitive fluids, they were kept and handled only in a glove-box under controlled oxygen-free dry argon atmosphere. The synthesis procedure was as follows: prior to ammonolysis of $M(NEt_2)_4$ (M = Zr or Hf) a quartz Schlenk-type tube with a quartz boat inside was dried by heating in

the tube furnace at 873 K for 3 h in order to remove residual moisture. Heating of the tube was conducted under continuous dry argon flow. This preliminary treatment of quartz glassware improved the composition of the nanocrystalline Zr_3N_{4+x} so that it exhibited higher nitrogen and lower oxygen content than in the products obtained in the earlier work (Li et al. 2005). The quartz boat was filled with up to about 4 ml of $Zr(NEt_2)_4$ or $Hf(NEt_2)_4$ and placed into the Schlenk-type tube (Figure 2.1). The tube with the boat inside was then mounted in a tube furnace. Following the work of Li et al. (2005), the ammonolysis of the metal dialkylamides was performed using high-purity ammonia (99.999 %) supplied with the rate of about 1-1.5 l/h. The ammonia was fed from a gas bottle to the quartz tube through the inner part of a coaxial hose: in order to diminish hydrolysis of ammonia during ammonolysis, continuous dry argon flow was sustained in the outer hose (Figure 2.1). The heating schedules for ammonolysis of $Zr(NEt_2)_4$ and $Hf(NEt_2)_4$ are given on Figure 2.2. After step-wise heating, the furnace was switched off and the samples allowed to cool slowly down to room temperature. The ammonolysis of about 4 ml (i.e. 10.8 mmol) of $M(NEt_2)_4$ yielded typically about 1.2 g and 1.7 g of powder for M = Zr and Hf, respectively. In order to prevent contamination with moisture, the obtained nanocrystalline powders were handled in the glove-box under inert dry argon atmosphere.

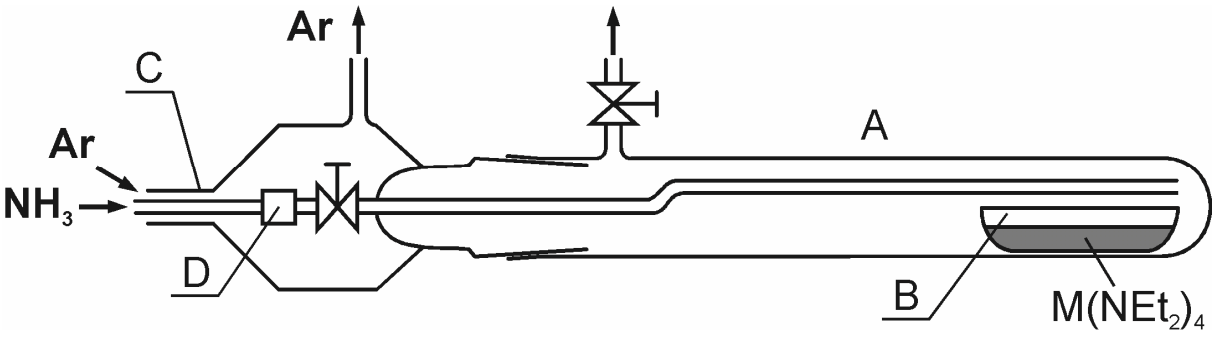

Figure 2.1. Schematic drawing of the ammonolysis setup: (A) quartz Schlenk-type tube, (B) quartz boat, (C) coaxial hose, (D) teflon fitting.

2.1.2 Hot-gas-extraction elemental analysis

The nitrogen and oxygen content in the nanocrystalline Zr_3N_{4+x} and Hf_3N_{4+x} powders was determined using a hot-gas-extraction analyser LECO TC-436 (LECO Corporation). The powdered samples were burned in a graphite crucible at about 3000 K under helium atmosphere. Oxygen in the samples reacted with carbon forming carbon monoxide which was oxidized to CO_2 using CuO catalyst. The CO_2 was then quantitatively analysed by infrared

absorption spectroscopy. Thermally released molecular nitrogen was measured by thermal conductivity method. * Titanium nitride (TiN), O-containing titanium metal and N/O-containing steels (LECO Corporation) were used as standards for the analyser calibration. The nitrogen and oxygen contents in the samples were determined with accuracies of 5 ppm and 1 % of the measured amount, respectively. In order to obtain good statistics at least five measurements were made for each sample.

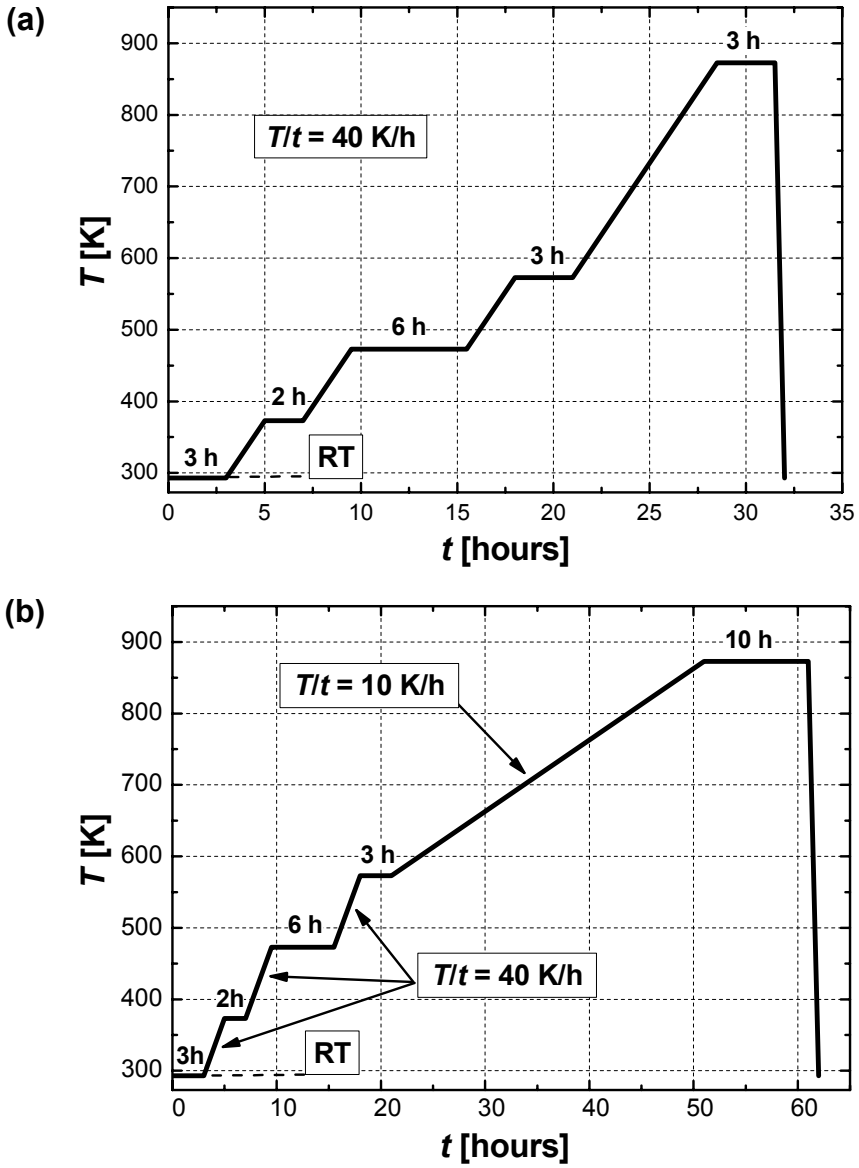

Figure 2.2. Heating schedules for ammonolysis of $Zr(NEt_2)_4$ (a) and $Hf(NEt_2)_4$ (b). These schedules allowed to obtain nanocrystalline powders of M_3N_{4+x} (M = Zr or Hf) with N/M ratio > 4/3 and low oxygen content.

*ASTM E1019; LECO TC-436 instrument manual

2.2 High-pressure techniques for synthesis and *in situ* examination

High-pressure techniques were used in the present work for two purposes. Firstly, macroscopic amounts of cubic Zr_3N_4 and Hf_3N_4 were synthesized at pressures of 12 GPa and high temperatures. Secondly, compressibility of the nitrides was measured on compression up to about 50 GPa.

This chapter gives an introduction to the most important static high-pressure techniques able to generate pressures in excess of 1 GPa. The main attention is paid to a multi-anvil apparatus and a diamond anvil cell (DAC) which were employed in the present work. A multi-anvil apparatus used for high-pressure high-temperature (HP-HT) synthesis of c-Zr_3N_4 and c-Hf_3N_4 is described in detail in Chapter 2.2.2. An extended description of the DAC technique is given in Chapter 2.4.1. The moderate-pressure equipment (up to 1.5 GPa), such as cold-seal vessels and auto-claves (e.g. Spain & Paauwe 1977; Holloway & Wood 1988), is not considered here because it operates below the pressures related to this work. Description of dynamic methods of pressure generation is also omitted. These methods allow achievement of ultra-high pressures ≈ 100 GPa and higher and simultaneous ultra-high temperatures via generation in a sample of shock waves by hypervelocity impact or explosion (Davison et al. 2002; Fortov et al. 2004). Despite large amounts of shock-wave products (in order of 10 cm^3), very short compression times (microseconds or less) usually result in formation of ultradispersed powders with reduced crystallinity.

2.2.1 Introduction to high-pressure techniques

For generation of static pressures exceeding 1 GPa a few high-pressure apparatuses can be used: piston-cylinder systems, belt-type apparatuses, toroid-type cells, multi-anvil apparatuses and diamond anvil cells (DAC). In addition to the principal difference in design and production/operation costs, these techniques also differ in the maximal achievable pressure, temperature and sample volume. One should mention that design of the devices listed above is based on two main principles of static pressure generation: piston-cylinder and opposite anvils (s. below).

In a piston-cylinder system (Boyd & England 1960; Eremets 1996) pressure is generated by forcing a piston into a sample chamber within a cylinder (Figure 2.3a). The volume of a high-pressure chamber can vary from 1 to 100 cm^3. The maximum pressure (about 5 GPa) achievable with this apparatus is limited by the tensile yield strength of the cylinder and

decreases with the sample volume increase. Samples can be heated by a resistance furnace assembly located within the pressure chamber up to 2000 K.

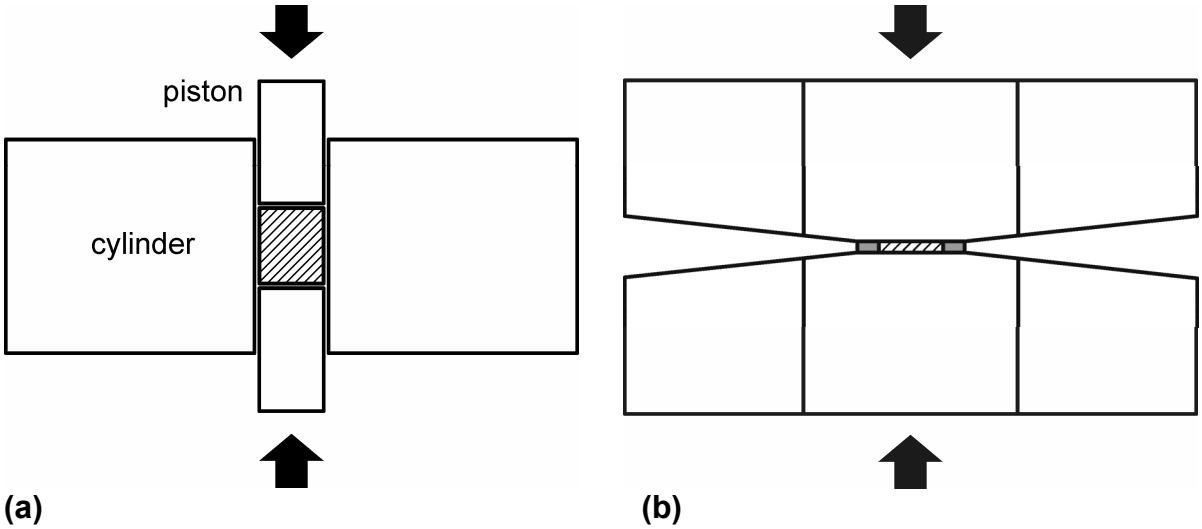

Figure 2.3. Schematic drawing of a piston-cylinder (a) and Bridgman's opposite anvils (b). Hutched and grey areas represent pressure volume and gasket, respectively. Arrows indicate the direction of applied load.

Another principle of pressure generation implies opposite anvils, originally designed by P. W. Bridgman (Bridgman 1952). In this method thin disc of sample material is compressed between two opposite anvils made of hard and strong material (Figure 2.3b). The sample disc is contained by a gasket ring which seals the pressure chamber by friction. The maximum pressure achievable by this method is determined by the ratio between the force applied to anvils and the anvil-face (culet) area and is limited by the compressive yield strength of the anvil material. For example, use of the laterally supported tungsten carbide anvils allows reaching pressures around 10 GPa (Eremets 1996). While the original Bridgman's anvils are rarely used today, the principle of gasketed opposite anvils is implemented, to a variable extent, in design of the most modern high-pressure devices.

The efforts to generate pressures exceeding 5 GPa in the comparably large volumes (> 0.1 cm^3) resulted in development of new high-pressure techniques, such as belt, toroid and multi-anvil apparatuses. Belt-type apparatus (Hall 1960; Kanke et al. 2002) consists of two conical tungsten carbide semi-pistons which compress the sample in a tungsten carbide cylinder with specially shaped walls. Both cylinder and pistons are laterally supported by stressed binding rings (Figure 2.4a). Belt-type apparatus allows routine experiments up to 8 GPa and temperatures of 2300 K in the volume of about 100 mm^3. Different versions of this high-pressure device are used today for industrial production of diamond and cubic boron nitride.

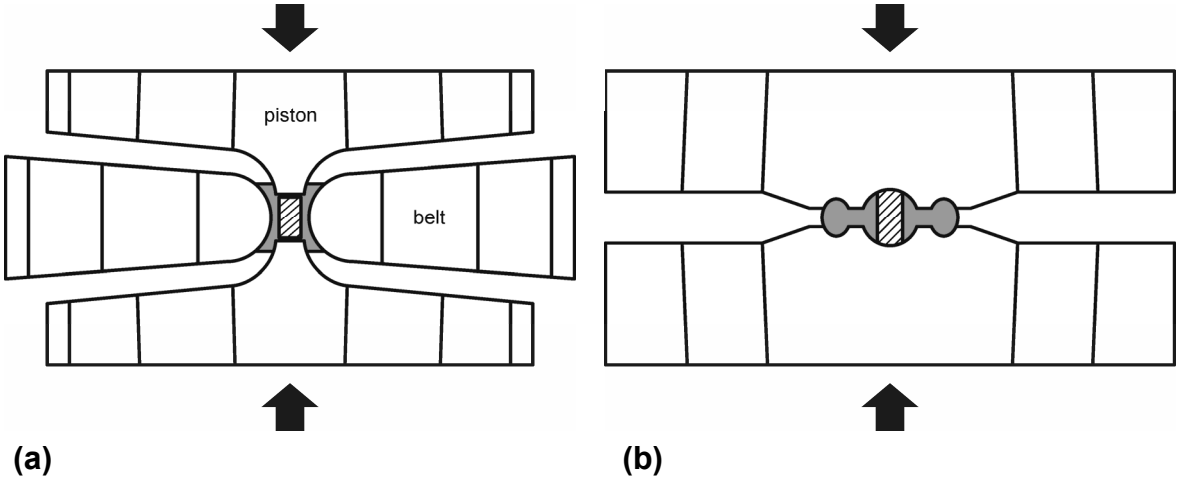

Figure 2.4. Schematic drawing of belt (a) and toroid-type (b) high-pressure apparatuses, where pressure volume and gasket are represented by hatched and grey areas, respectively. The direction of applied load is shown by arrows.

Toroid-type cells (Khvostantsev et al. 1977; Khvostantsev et al. 2004) represent the modification of Bridgman's opposite anvils where each anvil has a lens-shaped pressure chamber encircled by a toroidal recess (Figure 2.4b). Such geometry allows generation of pressures up to 11 GPa within the volume of 300 mm^3. However, the toroid cell has disadvantages as compared with the belt apparatus: significant pressure gradients are present within the pressure chamber; considerably higher press loads are required for achievement of similar pressure and sample volume.

The above described high-pressure apparatuses can produce large amounts of material (up to several hundreds cm^3 per one load). Therefore, they are widely used today for materials syntheses on industrial scales. However, the maximum pressure achieved in these apparatuses commonly does not exceed 10 GPa. Considerably higher pressures can be created by another two devices: diamond anvil cells and multi-anvil apparatuses.

A diamond anvil cell (DAC), combined with laser-heating technique, is, apparently, the most powerful high-pressure device with respect to generation of high pressures and high temperatures and to employment for *in situ* studies (Ming & Bassett 1974; Boehler & Chopelas 1991; Holzapfel & Isaacs 1997; Boehler 2000; Zerr et al. 2000). The principle of pressure generation in a DAC is similar to that in the Bridgman's anvils: a diamond anvil cell consists of two opposed diamond anvils with flat-polished tips (culets) between which a sample is compressed (Figure 2.5a). Owing to exceptional strength of diamond (more than 20 times as much as that of tungsten carbide (Eremets et al. 2005)), a DAC can generate much higher pressures than can be achieved, for example, with WC-Co anvils. The diamonds are usually mounted on tungsten carbide seats. The typical diamond culet diameter is between 0.1

and 0.5 mm, while the diameter of the diamond table (surface opposite to the culet) is usually around 3 mm. The conical shape of diamond anvils allows pressure multiplication: the maximum pressure achievable in a DAC increases with the ratio of table area to culet area of diamonds. Accordingly, a DAC with sufficiently small culets can reach pressures in excess of 500 GPa (Ruoff et al. 1992).

A sample in a DAC can be either simply squeezed between the diamond culets or placed inside a hole drilled in the centre of preindented thin metal gasket which is then compressed between the anvils (Figure 2.5a). In particular, gasket is required for compression of liquids and gases. It seals the pressure chamber by friction and provides lateral support to diamond anvils at high pressures. Liquids or gases can also be used as a nearly hydrostatic pressure transmitting medium even if they transform to solid state on compression. This is of particular importance for compressibility measurements, when non-hydrostatic stresses in a sample chamber can bias the measured values and thus are unacceptable (s. Chapter 2.4.1).

A great benefit of a DAC technique is related to the diamond transparency to X-ray radiation, IR and visible light. This allows application of a variety of spectroscopic and diffractional methods for examination of samples *in situ* at high pressures in a DAC. In particular, the compressibility of the synthesized materials was measured in the present work in a DAC using *in situ* X-ray powder diffraction. The detailed description of this method is given in the corresponding section below (Chapters 2.3.1.2 and 2.4.1). For heating of samples in a DAC several techniques can be used. The external heating with a resistance heater located around the diamonds is limited to about 1800 K. Above this temperature diamond transforms to graphite even in inert atmosphere (Eremets 1996). Heating of conductive samples can be performed internally by passing of electric current through them. Alternatively, samples in a DAC can be heated internally via optical absorption of infrared laser radiation. In this method intense Nd-YAG or CO_2 lasers are focused on a sample through the IR-transparent diamond anvil (Boehler & Chopelas 1991; Boehler 2000; Zerr et al. 2000). High temperatures up to 7300 K can be achieved using this technique (Zerr et al. 2006b). The only significant disadvantage of a laser-heated DAC is the extremely small sample size. The typical culet diameter of 0.1-0.5 mm implies that only very small samples ($< 10^{-4}$ mm^3) can be loaded in a DAC. Such sample amounts can be characterized only using microscale techniques and are well below industrial scale.

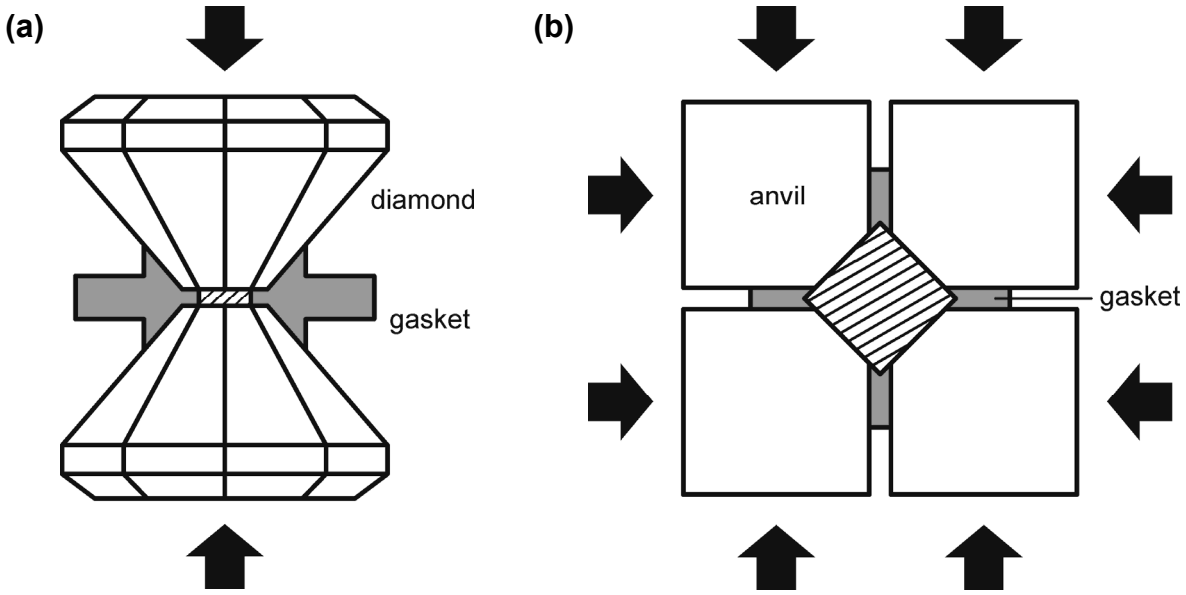

Figure 2.5. Principle of a diamond anvil cell (a) and a multi-anvil device (b). The hutched area represents the pressure volume. An opposite anvil system (a) is loaded uniaxially. In multi-anvil system (b) pressure chamber in the shape of a regular tetrahedron, cube, or regular octahedron is compressed from several directions by four, six or eight identically shaped anvils, respectively. Load directions are shown by arrows.

In experiments with piston-cylinder and opposite-anvils devices samples are compressed by applying uniaxial load. Thus, (quasi)hydrostatic conditions within the pressure chamber can be achieved only by using a soft pressure medium. More homogeneous load distribution can be attained by sample compression from several directions simultaneously. This idea led to development of multi-anvil apparatuses, where a sample volume in the shape of a regular polyhedron is compressed by several identically shaped anvils (Figure 2.5b). The compression is achieved by forcing the anvils along their axis toward the centre of a polyhedron. Thus four-, six- and eight-anvil apparatuses for compression of tetrahedral, cubic and octahedral volumes, respectively, were designed and successfully employed (Hall 1958; Von Platen 1962; Osugi et al. 1964; Kawai 1966; Kawai & Endo 1970). Today the most used devices are the various versions of two-stage octahedral (also known as 6/8-type) multi-anvil apparatus (Kawai & Endo 1970; Onodera 1987; Walker et al. 1990). The name "6/8" is due to the number of anvils in each stage: eight cubic tungsten carbide inner-anvils (second stage) are enclosed by six hardened steel outer-anvils (first stage). The eight cubic anvils have corner truncations so that, when assembled together, they form an octahedral pressure chamber. As the first stage, different cubic-compression system are used, such as split-sphere system (Kawai & Endo 1970), split-cylinder cluster (Walker et al. 1990) (s. below) or a DIA-type cubic multi-anvil apparatus (Osugi et al. 1964; Kondo et al. 1993). The geometrical

construction of a 6/8-type system allows redistribution of the uniaxial load of a hydraulic press into a nearly uniform (quasi-hydrostatic) compression of the octahedral pressure chamber. The 6/8-type multi-anvil apparatus has met particular success, because it allows generation of pressures up to 25 GPa and temperatures up to 3000 K in comparably large sample volume (≈ 1 mm^3). Moreover, it allows holding stable HP-HT conditions for significant periods of time (up to several weeks). Even higher pressures (up to 40 GPa) are achievable with inner-anvils made of sintered diamond, however for a smaller sample volume of about 0.1 mm^3 (Ohtani et al. 1989).

In the present work the 6/8-type multi-anvil apparatus was chosen for HP-HT synthesis of c-Zr_3N_4 and c-Hf_3N_4 because, in contrast to other considered high-pressure devices, it operates within a wide range of pressures (up to 25 GPa) and temperatures (up to 3000 K), and the amount of synthesized material (> 1 mm^3) is sufficient for characterization using standard techniques. The detailed description of the multi-anvil high-pressure assembly and of the sample environment is given in the following chapter.

2.2.2 Multi-anvil (MA) apparatus

For HP-HT synthesis of c-Zr_3N_4 and c-Hf_3N_4 presented in this thesis, a 6/8-type multi-anvil apparatus with a Walker-type module (Walker et al. 1990) was employed. The experiments were performed at the Institut für Geowissenschaften, J. W. Goethe-Universität, Frankfurt am Main, Germany. Description of this device, its working principle and sample environment is given below.

2.2.2.1 Walker-type module

As was mentioned above, in the 6/8-type multi-anvil system the uniaxial load of a hydraulic press is uniformly distributed through six outer anvils (first stage) between eight inner cubic anvils (second stage), thus providing quasi-hydrostatic compression of the octahedral pressure chamber. A Walker-type module (Walker et al. 1990) represents a simple method of such load redistribution and combines satisfactory compression efficiency with reasonable costs of parts. It consists of a set of six tool-steel anvils (or wedges), cut as segments from a cylinder and shaped so as to compress the cubic second stage (Figure 2.6a). This cylindrical assembly (with cubic second stage inside) fits into a massively supported containment ring and is loaded with an uniaxial hydraulic press via pressure distribution plates (Figure 2.6b-d).

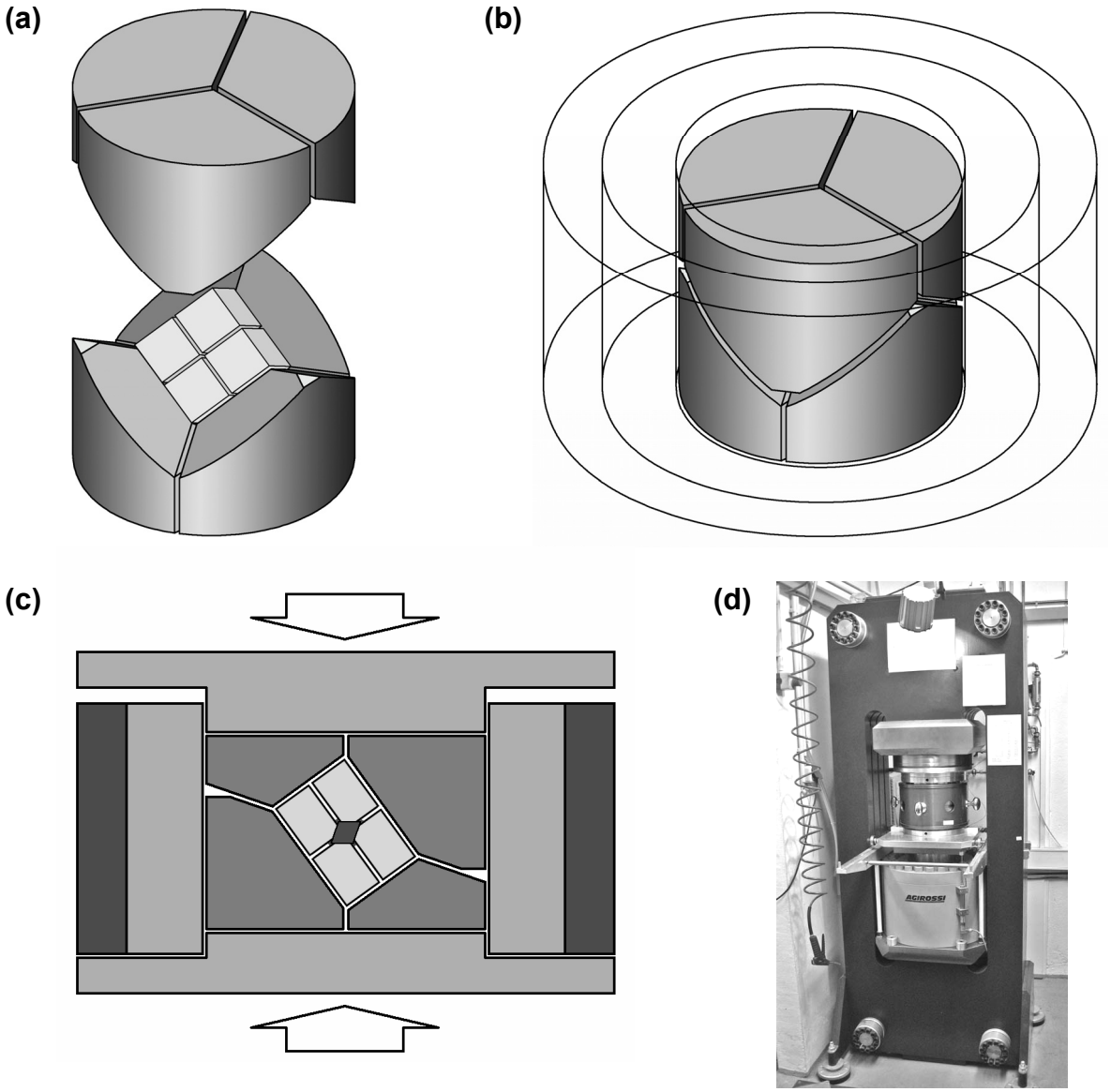

Figure 2.6. Working principle of the Walker-type module: the cubic second compression stage is nested within split-cylinder six-wedge cluster (a) which fits into the containment ring (b); the module is loaded uniaxially via pressure distribution plates (c) using the 800-tonnes hydraulic press (d).

The second compression stage consists of eight cubes made of tungsten carbide cermet (WC5-6%Co composite). Each cube has a triangular corner truncation so that when all eight anvils assembled in a cubic set, the corner truncations form an octahedral pressure chamber (Figure 2.7a). In this chamber a ceramic pressure-transmitting medium containing encapsulated sample, furnace and thermocouple is placed (s. below). In order to allow volume reduction, to support the anvils on loading, and to seal the high-pressure chamber, pyrophyllite gaskets are placed between the WC-Co cubes as shown on Figure 2.7b.

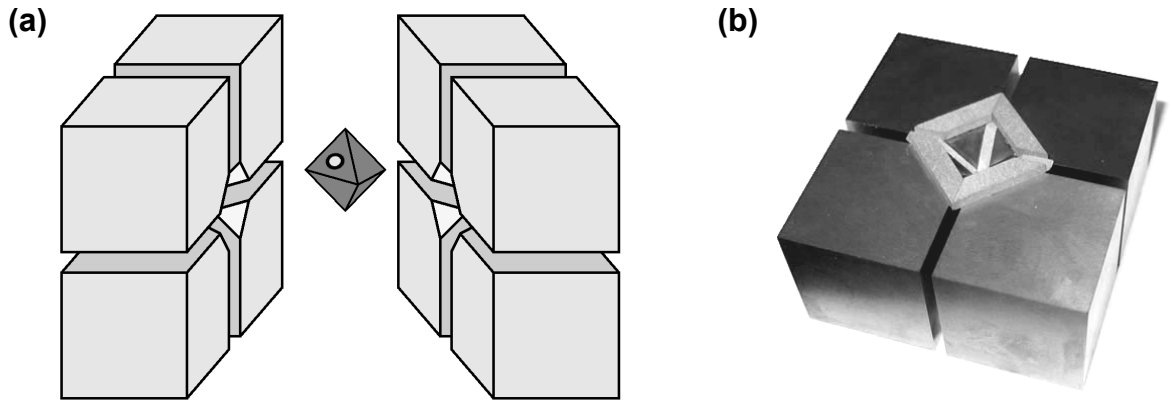

Figure 2.7. Second compression stage of a 6/8-type multi-anvil apparatus: (a) schematic view of eight tungsten carbide cubes with corner truncations arranged around octahedral pressure medium; (b) trapezoidal pyrophyllite gaskets are attached to the WC-Co cubes faces close to truncations so as to properly fit around octahedron.

The maximal pressure which can be achieved with the Walker-type module is determined by the maximal applied uniaxial load and effective area of "anvils-to-pressure medium" contact. The maximal applied load is usually limited by the capability of a hydraulic press or by the strength of the containment ring. On the other hand, attainable pressure can be increased (up to the compressive strength of the anvils) by decreasing of truncation area of the anvils (i.e. truncation edge length, TEL) and, correspondingly, of volume of the octahedral pressure medium (characterized by octahedral edge length, OEL). There exist several particular sizes of assemblies, described by the OEL/TEL notations (e.g. Walter et al. 1995; Huppertz 2004; Keppler & Frost 2005). The commonly used OEL/TEL combinations and corresponding pressure ranges attainable with employed in the present work 800-tonnes uniaxial hydraulic press are listed in Table 2.1. For present high-pressure experiments the 14/8 assembly was chosen. It employs 32 mm edge length WC-Co cubes with TEL of 8 mm and ceramic octahedral pressure medium with OEL of 14 mm.

Table 2.1. Standard OEL/TEL assemblies employed at the Institut für Geowissenschaften, J. W. Goethe-Universität, Frankfurt am Main, and corresponding pressure ranges, gasket dimensions and approximate sample volume (Steinberg 2005).

Assembly OEL/TEL [mm]	Pressure range [GPa]	Gasket thickness × width × inner length [mm]	Approx. sample volume [mm^3]
18/11	3-8	3.0 × 5.0 × 16.5	8
14/8	6-14	2.75 × 5.0 × 12.0	3
10/4	10-24	2.75 × 5.0 × 7.5	1

In order to heat the sample at high pressures, a resistance furnace was used (s. below). An external power supply (maximal AC power of 3 kW) allows to apply a voltage to the opposite tungsten carbide cubes which are in contact with the furnace. The resulting electric current sent through the furnace leads to heat emission. In order to prevent short circuit between the anvils, WC-Co cubes faces were additionally insulated from each other by an adhesive teflon tape and from the Walker module by fibre-glass plastic plates. The heater design and materials used for the furnace and thermal insulation are described below.

2.2.2.2 The octahedral pressure assembly

As described in the previous chapter, a 6/8-type multi-anvil system compresses an octahedral pressure medium (ceramic octahedron), which contains not only the sample, but also a resistance furnace, a thermal insulation and a thermocouple for temperature control. The details of the octahedron assemblage are given below.

MgO-octahedron. The octahedron with OEL of 14 mm used in the multi-anvil experiments was made of porous MgO ceramic doped with 5 wt.% of Cr_2O_3 (Ceramic Substrates & Components Ltd). The MgO-based ceramics are usually used as a pressure transmitting medium in multi-anvil apparatuses because magnesium oxide has high melting point and is soft at high-temperatures, thus providing nearly hydrostatic pressure conditions (e.g. Keppler & Frost 2005).

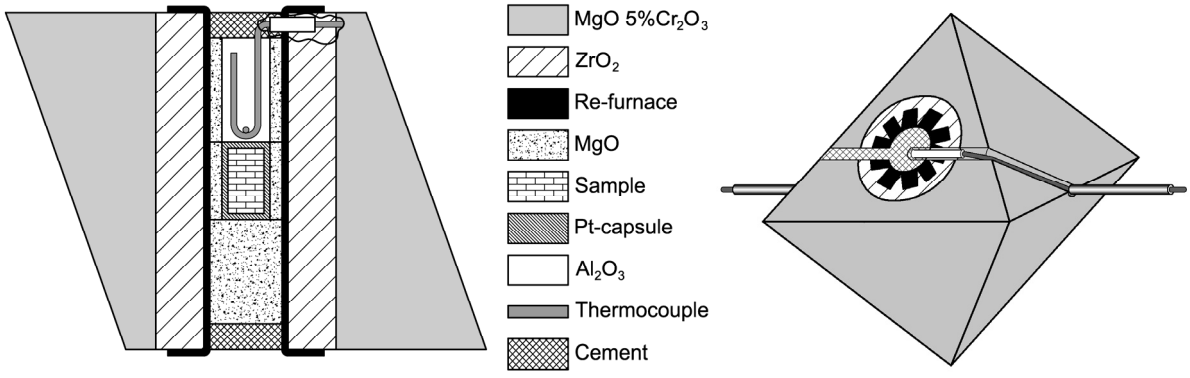

Figure 2.8. Schematic drawing of the octahedral pressure cell: (a) cross section (b) assembled octahedron; thermocouple wires are guided through the grooves to opposite edges of the octahedron and leave pressure medium via soft steel tubes.

Thermal insulation. In order to reduce the heat loss and to smooth temperature gradients in the sample at high-temperatures, the thermal insulation layer is usually placed around the heating element. In the present work a ZrO_2-sleeve with outer and inner diameters of 6.0 and 2.6 mm, respectively, served as thermal insulator. It was mounted in the hole drilled in the MgO-octahedron as shown on Figure 2.8a.

Furnace. The cylindrical resistance furnace was made by wrapping a rhenium foil of 0.125 mm in thickness. The rhenium cylinder was 3 mm longer than ZrO_2-sleeve. Both ends of the furnace, inserted in the ZrO_2-sleeve, were then incised and bent as shown on Figure 2.8b in order to provide electrical contact between the furnace and WC-Co cubes.

Sample encapsulation. In order to prevent reaction of sample material with the surrounding pressure medium, the sample is usually loaded in a noble metal capsule. When having high thermal conductivity, the encapsulating material can also smooth temperature gradients within the sample.[*] In the present work the capsules were made of platinum tubing with outer diameter of 1.6 mm and wall thickness of 0.1 mm. The piece of the Pt-tubing of about 4 mm in length was first closed from one side with a Pt-cap, arc-welded and formed with a pressing mould. The sample powder was filled in the capsule and tightly compacted using a punch and a hammer. The filled capsule was closed then with the Pt-disc (0.1 mm thick and 1.4 mm in diameter) and Pt-cap and sealed afterwards mechanically in a pressing mould. The sample loading and capsule sealing were performed in a glove-box under controlled argon atmosphere in order to diminish contamination with oxygen and moisture. The final safe sealing of the capsule was performed under ambient atmosphere in the pressing mould using a small hydraulic press. Finally, the sample capsule of about 2-2.5 mm in height was placed in the centre of the octahedron and was insulated from the Re-furnace by MgO-sleeve. MgO-tube (for thermocouple insertion) and MgO-rod filled the space at the top and the bottom of the sample capsule, respectively (Figure 2.8a).

In order to reduce contamination of sample with oxygen, which can diffuse from oxide pressure medium through the Pt-capsule during heating (Schwarz et al. 2000) a “double encapsulation” was performed in some experiments. The sealed Pt-capsule was inserted in the molybdenum capsule made of two wrapped layers of 0.025 mm thick Mo-foil. The outer capsule was closed and sealed mechanically in the way described above.

[*] http://multianvil.asu.edu

Thermocouple. The temperature at high pressures was monitored using a W5%Re-W26%Re thermocouple (0.127 mm wires diameter, Omega Engineering Inc.) which is suitable for temperature measurements up to about 2600 K. An additional advantage of the W-Re based thermocouples is a lower pressure effect on the electromotive force, when compared with other thermocouple types (Walter et al. 1995; Li et al. 2003). The thermocouple wires were inserted in alumina sleeve and crossed, thus forming a junction. The thermocouple assembly was then inserted in the MgO-tube above the capsule so that the junction was in contact with the sample container (s. Figure 2.8a). Thermocouple wires were insulated from the Re-furnace by alumina sleeves of 0.6 mm in diameter and guided through grooves in the octahedron and through soft steel tubes in the gaskets out of the pressure chamber (Figure 2.8b). The soft steel tubes (0.6 mm in diameter and 1 cm in length) were used in order to prevent breakage of the thermocouple wires during gasket extrusion. The remaining free space in the ZrO_2-sleeve and grooves in the octahedron were filled with ceramic cement.

2.2.2.3 Pressure and temperature measurement

The actual sample pressure in the multi-anvil experiments was determined from the pressure-versus-press load calibration curve. The sample pressure as a function of the press load was calibrated for each OEL/TEL assembly using known high-pressure phase transitions (Steinberg 2005). The room temperature (RT) calibration is based on the HP phase transitions of Bi and ZnTe. At high temperatures, however, sample pressure is usually lower than at RT, therefore additional high-temperature calibration is required. The high-temperature calibration is based on the known HP-HT phase equilibria in minerals, such as $CaGeO_3$ (garnet-perovskite), SiO_2 (coesite-stishovite) and Mg_2SiO_4 (forsterite-wadsleyite). Further experimental details on the low- and high-temperature pressure calibration can be found elsewhere in the literature (e.g. Walter et al. 1995; Rubie 1999; Keppler & Frost 2005).

The actual sample temperature was obtained from the thermocouple signal. No corrections for the pressure dependence of the electromotive force of the thermocouple were made in this work. In the case of thermocouple failure (e.g. wire breakage), temperature could be alternatively estimated via monitoring of the electric power applied to the Re-furnace.

2.2.2.4 HP-HT experimental procedure

The Walker-type module with an assembled octahedron inside was compressed with the uniaxial hydraulic press (load rate 1500 kN/h) to the required sample pressure in accordance with a HT pressure-calibration curve. The sample was then heated at 50 K/min up to the intended temperature, kept at the maximum temperature for about 20 minutes and quenched

by switching off the heating electric power. The water-cooling of the Walker-type module allows holding the temperature of WC-Co cubes below 373 K (Steinberg 2005). Therefore the sample temperature falls down to about 400-430 K in a few seconds. After quenching the load has to be reduced slowly (with rate of about -180 kN/h) in order to relieve the large residual stresses in WC-Co cubes.

2.2.2.5. Sample recovery

After load reduction, the WC-Co cubes assembly was removed from the Walker module and opened. The densified MgO-octahedron was broken in order to recover the sample capsule. The capsule was then embedded in epoxy and polished with SiC-paper, until the sample surface appeared. After that, sample was cut using a diamond wire saw (Well Model 4240, Well Diamantdrahtsägen GmbH) into a few pieces for further examination using techniques described below.

2.3 Analytical methods

This chapter introduces analytical techniques used in the present work for examination of structure, composition and morphology of the synthesized high-pressure nitrides: powder X-ray diffraction, electron probe microanalysis, transmission and scanning electron microscopy, and Raman spectroscopy.

2.3.1 Powder X-ray diffraction

X-ray diffraction (XRD) is a standard non-destructive characterization method which provides detailed information about crystalline structure of investigated materials. The XRD is based on the constructive interference of X-rays elastically scattered by a regular periodic system of atoms (more precisely, electrons) in a crystalline solid. If the wavelength of the X-ray radiation is comparable with the interatomic distances, the atomic planes of crystal lattice can be considered as a three-dimensional diffraction grating for X-rays. The basic condition for the constructive interference of radiation of wavelength λ diffracted by atomic planes with spacing d is given by Bragg's law:

$$n\lambda = 2d \sin\theta,$$

where n is an integer and θ is the angle between the incident beam and the diffracting atomic planes. The angle between the incident and the diffracted beam is therefore equal to 2θ. For monochromatic X-ray radiation ($\lambda = const$) the XRD data are represented by intensity I as a

function of diffraction angle 2θ (diffraction pattern or diffractogram), where diffraction peaks (or reflections) correspond to the particular *d*-spacings of the crystal lattice. This technique is referred to as the angle dispersive X-ray diffraction (AD-XRD). For polycrystalline samples (powders) with randomly oriented grains, X-ray radiation is scattered symmetrically around the primary beam into diffraction cones. Thus AD-XRD data can be collected either in the form of concentric circles using a flat image-plate or CCD detector (s. Chapter 2.3.1.2), or in the intensity $I(2\theta)$ as a function of 2θ by a curved or linear position sensitive detector or an X-ray photon counter.

Alternatively, powder X-ray diffraction measurement can be accomplished using polychromatic X-ray radiation. In this case diffraction patterns are collected at fixed diffraction angle ($2\theta = const$) using a Si(Li) or Ge energy dispersive X-ray detector. This technique provides the diffracted intensity *I* as a function of the radiation energy $\mathbf{E} = hc/\lambda$ (where *h* is Planck's constant and *c* is the light speed in vacuum) and is referred to as energy dispersive X-ray diffraction (ED-XRD). The condition for the constructive interference of diffracted radiation at the angle 2θ is given by Bragg's law with $\lambda = hc/\mathbf{E}$.

In the present work the powder AD-XRD technique was used for phase identification, investigation of the high-temperature behaviour (Chapter 2.5) and determination of structural parameters of synthesized compounds by means of full-profile Rietveld structure refinement (s. below). The synthesized amount of high-pressure nitrides (> 1 mm^3) allowed employment of a low-intensity X-ray beam provided by standard "in-house" diffractometers at the FG Strukturforschung, FB Material- und Geowissenschaften, TU Darmstadt. Alternatively, high-brilliance monochromatic synchrotron radiation was used in order to obtain high-quality powder XRD pattern of c-Hf_3N_4 in a reasonable period of time. The ED-XRD was employed for measurement of the lattice parameters and, accordingly, specific volumes of high-pressure nitrides as a function of pressure upon compression in a diamond anvil cell (s. Chapter 2.4.1). Since the sample amount in a DAC is very small, polychromatic synchrotron radiation was used in those experiments.

2.3.1.1 In-house X-ray diffractometers

Reflection geometry. In order to preliminary examine the phase content of the synthesized products, the powder XRD patterns were measured from the polished sample surface in the reflection geometry using an automated four-circle diffractometer STOE STADI-4 (Stoe & Cie GmbH) with Co-anode (λ = 1.7890 Å). Diffraction intensity was recorded in 2θ-ω scan

mode (2θ:ω = 2:1, where 2θ is the diffraction angle and ω is the angle between the incident X-ray beam and the sample surface), so that to obtain conventional $I(2\theta)$ diffraction patterns.

Transmission geometry. The powder XRD pattern of cubic zirconium(IV) nitride was measured in the Debye-Scherrer geometry using a STOE STADI P diffractometer (Stoe & Cie GmbH) with Mo-$K_{\alpha 1}$ radiation (λ = 0.70932 Å). The diffractometer is equipped with a position sensitive detector with 6° aperture. A NIST-NBS640b Si standard was used for preliminary calibration of sample-to-detector distance. The slice of the sample was cut with a diamond wire saw and crushed into powder using a tungsten carbide tool. The powdered sample was filled in a glass capillary of 0.3 mm in diameter which was rotated in order to obtain texture-free powder XRD pattern. The sample height was about 2-2.5 mm. Intensity, $I(2\theta)$, versus diffraction angle 2θ from 10° to 61° was collected in steps of $\Delta(2\theta)$ = 0.01°.

2.3.1.2 Synchrotron radiation

Because of strong absorption of Mo-$K_{\alpha 1}$ radiation by hafnium, the above described in-house diffractometer could not provide for hafnium nitride the XRD pattern of a quality sufficient for detailed structural characterization. Use of a glass capillary of 0.1 mm in diameter also did not yield a satisfactory result, probably because of the small sample volume. Therefore a high-brilliance X-ray radiation source was necessary for the XRD study of cubic hafnium(IV) nitride. The XRD experiments were performed at the beamline ID27 of the European Synchrotron Radiation Facility (ESRF), Grenoble, France. The XRD data were collected with a MAR345 image-plate detector (MarResearch GmbH) using monochromatic synchrotron radiation (wavelength λ = 0.3738 Å). The detector distortion and sample-to-detector distance was calibrated using a NIST-NBS640c Si standard. The sample chip of about 50 μm in size was mounted on a glass capillary in the centre of a Gandolfi camera (Gandolfi 1967) and aligned in the 200×200 μm parallel synchrotron beam. A Gandolfi camera allows generation of an ideal powder X-ray diffractogram from a small single crystal by rotating the crystal around two nonparallel axes (Gandolfi 1967). Thus, texture free diffraction patterns were collected. The two-dimensional XRD patterns were integrated using Fit2D software (Hammersley et al. 1996) in order to obtain conventional diffractograms, where the diffraction intensity $I(2\theta)$ is a function of the diffraction angle 2θ.

The ED-XRD patterns of investigated material compressed in a DAC (s. Chapter 2.4.1 for details) were measured using polychromatic synchrotron radiation at the beamline F3 of the HASYLAB/DESY, Hamburg, Germany. In order to avoid diffraction from the gasket material, the X-ray beam was collimated between 50×50 and 30×30 μm. The ED-XRD

patterns were collected at the diffraction angles 2θ around 9° in the energy range from 13 to 64 keV using a Ge-detector (IGP-25, Princeton Gamma-Tech) with tungsten slits open to 200 μm. The full-width-at-half-maximum resolution of the detector was about 120 eV. The detector was calibrated using $K_{\alpha 1}$, $K_{\alpha 2}$, $K_{\beta 1}$ and $K_{\beta 2}$ X-ray fluorescent lines of Rb, Mo, Ag, Ba and Tb excited by radioactive americium-source as well as fluorescent lines of a Mo-Sn-Ba-Gd-W-doped glass excited by synchrotron radiation. The diffraction angle, 2θ, was precisely determined by means of Au powder as a standard.

2.3.1.3 Data processing

Phase identification was done with the help of the ICSD database.* The full-profile Rietveld structure refinement of powder AD-XRD data was carried out using the program Fullprof (Rodriguez-Carvajal 1990). The Rietveld method is based on the fitting of a model full powder XRD pattern to the experimentally measured one by varying a number of structural and instrumental parameters. The search of the optimal parameter combination is performed by minimisation of the difference between the calculated and the observed pattern using the least squares method (Rietveld 1969; Young 1993).

The ED-XRD patterns were processed as follows: the diffraction energies were determined by fitting four-parameter Voigt function to each diffraction peak of investigated materials. Corresponding *d*-spacings were obtained using Bragg's equation. Finally, the average lattice parameter was taken from the values calculated for each diffraction peak.

2.3.2 Electron probe microanalysis (EPMA)

Chemical composition of the synthesized products was determined by the electron probe microanalysis (EPMA). This technique is based on the analysis of the characteristic X-ray fluorescence spectra from the sample excited by a focused high-energy electron beam (≈ 1 μm in diameter). The generated X-rays are selected and counted by a wavelength dispersive X-ray (WDX) detector which includes a single-crystal monochromator and an X-ray counter. In contrast to energy dispersive Si(Li)- and Ge-detectors, it has significantly higher energy resolution and allows more accurate quantitative analysis. Chemical composition is determined by comparing the intensities of characteristic X-rays fluorescent lines from the sample material with those from standards. The incident electron beam also causes emission of secondary and back-scattered electrons which can be used for sample imaging. The EPMA

* Inorganic Crystal Structure Database by Fachinformationszentrum (FIZ) Karlsruhe

technique was chosen in the present work because it allows non-destructive quantitative analysis of light (N, O) and heavy (Zr, Hf) elements in microscopic sample volumes as well as elemental mapping of the sample surface.

Measurements were performed using an electron probe micro-analyser CAMEBAX SX-50 (CAMECA) at the FG Chemische Analytik, FB Material- und Geowissenschaften, TU Darmstadt. The analyser is equipped with four wavelength dispersive X-ray spectrometers (WDX), energy dispersive Si(Li) detector (Princeton Gamma-Tech), secondary electron (SE) and backscattered electron (BSE) detectors. The data were collected at 20 kV accelerating voltage and 20 nA beam current for all elements. In order to examine chemical homogeneity of the synthesized materials the element mappings were taken at beam operating conditions of 20 kV and 40 nA in a beam-scan mode. Chemical composition was determined using characteristic N-K_α, O-K_α, Zr-L_α and Hf-M_α fluorescent lines. Pure zirconium and hafnium metals and zirconium(IV) oxide served as standards for Zr, Hf and O, respectively. As nitrogen standard, BN and Si_3N_4 were used, because certified Zr/N and Hf/N reference materials are not commercially available. Measured spectra were corrected for matrix effects applying a standard ZAF procedure.

Prior to analysis the samples were embedded in epoxy, coarse-polished with SiC-paper down to 4000 grit and fine-polished with a diamond suspension down to 0.25 μm particle size. The polished samples were coated with a thin conductive carbon layer in order to avoid charging effects on the sample surface due to nonconducting embedding material.

2.3.3 Transmission electron microscopy (TEM)

The structure and phase content of synthesized materials were additionally examined by transmission electron microscopy. TEM exploits a high-energy fine-focused monochromatic electron beam. By passing through a thin sample, some electrons are scattered by atoms both inelastically and elastically (diffracted electrons). The rest of electrons are transmitted without any interaction occurring inside the specimen (non-scattered electrons). The latter electrons can be focused by an objective lens onto a screen in order to obtain a sample image, while the scattered electrons can be blocked by an aperture. Weakening of the beam due to the sample thickness variation, composition contrasts and/or electron scattering contributes to the *Bright field* image formation. Furthermore, elastically scattered electrons can be focused by a lens on a screen, thus providing an electron diffraction pattern formed via constructive interference of the diffracted electrons in accordance with Bragg's law (s. above). This pattern can then yield information about the crystal structure, orientation and phases present in the area being

examined. In contrast to the powder XRD, TEM allows imaging of the sample with very high spatial resolution as well as investigation of the crystal structure of its individual grains. Moreover, chemical analysis of the investigated sample volume can be performed simultaneously both via detection of the characteristic X-ray fluorescence excited by the incident electron beam (EDX) and/or by analysis of inelastically scattered electrons using electron energy-loss spectroscopy (EELS).

In the present work the TEM experiments were performed on a PHILIPS CM20 transmission electron microscope equipped with an EDX-detector (HPGe, Voyager, Noran Instruments).

2.3.4 Scanning electron microscopy (SEM)

Investigation of the morphology of the sample surface was performed using a high resolution scanning electron microscope (XL30 FEG, PHILIPS) with the acceleration voltage of 10 to 25 kV. The SEM produces images by detecting low-energy secondary electrons which are emitted from the surface of the sample due to excitation by the primary high-energy electron beam. *In situ* semi-quantitative elemental analysis was performed using energy dispersive X-ray (EDX) module (CDU, EDAX Inc.) via detection of the characteristic X-ray fluorescence excited by the incident electron beam. For SEM examination, the sample surface was polished and sputtered with carbon as described in Chapter 2.3.2.

2.3.5 Raman spectroscopy

Raman spectroscopy is used to investigate vibrational properties of molecules and crystals. In particular, a Raman spectrum of a crystal provides information about frequencies of its optical phonons (lattice vibrations). The Raman effect is based on inelastic scattering of light by optical phonons of the crystal lattice (Loudon 1964). Via interaction with crystal lattice, the incident photon can excite or destroy phonon and lose or gain energy, respectively. The light scattered with lower energy (longer wavelength) is called Stokes scattering, while that with higher energy (shorter wavelength) – anti-Stokes scattering. The change in energy of the scattered light is equal to the energy of the phonon and is referred to as Raman shift. Intensities of Raman peaks depend on the wavelength of the incident light and/or on its polarization. It should be mentioned that not all optical phonons in the crystal lattice give rise to Raman scattering: only lattice vibrations having certain symmetry are Raman active. These vibrations can be determined by factor group analysis (Loudon 1964). Moreover, for a particular lattice vibration Raman shift is independent of the wavelength of the exciting radiation. Hence, Raman spectrum is a characteristic property of a material which can be used

for identification of known phases as well as can provide information on the presence of certain structural units (e.g. SiO_4-tetrahedra) in the investigated material. For excitation of Raman spectra monochromatic light (usually laser radiation in visible, near IR or near UV range) can be used. The spectra are measured as intensity of the scattered light versus Raman shift given in wavenumbers [cm^{-1}] (relative to the laser wavelength) and converted so that the more intensive Stokes shifts are positive.

In the present work Raman spectra were excited with a continuous wave Ar-ion laser (wavelength λ = 514.5 nm, TEM00, Stabilite 2017, Spectra Physics) and measured in the reflection geometry using a micro-Raman spectrometer (Dilor XY, HORIBA Jobin Yvon) equipped with a CCD-detector cooled with liquid nitrogen. The spectra were collected from sample area down to ≈ 1 μm^2.

2.4 Elasto-mechanical properties

As discussed in Chapter 1.2.1 of the introduction, the elastic properties of polycrystalline materials are completely described by two independent elastic moduli, for example bulk and shear moduli, B and G. In the present work the bulk moduli of synthesized materials were derived from their volume-pressure dependencies, $V(P)$, also known as equation of state. For cubic zirconium(IV) nitride, the second elastic modulus (namely reduced elastic modulus, E_r) was determined employing instrumented indentation technique (Chapter 2.4.3). Moreover, hardness and fracture toughness of c-Zr_3N_4 were measured using different indentation methods which are described in Chapters 2.4.2 and 2.4.3.

2.4.1 Compressibility measurements

Compressibility of the high-pressure nitrides was studied using diamond anvil cell (DAC) technique (s. Chapter 2.2.1). This technique allows compression of microscopic samples up to several tens of gigapascals at nearly hydrostatic conditions, as well as *in situ* high-pressure investigation of the samples using X-ray diffraction or various spectroscopic methods. In the present work the specific volume-pressure dependence, $V(P)$, of investigated crystalline compounds was measured in a DAC by energy dispersive powder X-ray diffraction combined with synchrotron radiation (s. Chapter 2.3.1.2). The experimental $V(P)$ data were then fitted with the Birch-Murnaghan equation of state (s. Chapter 1.2.1.1) in order to obtain the bulk moduli of high-pressure nitrides.

For the compression measurements a DAC with bevelled anvils having culets of 350 μm in diameter was employed.* Such geometry allows routine experiments up to pressures of 50 GPa. Polycrystalline pellets of the investigated compounds (approximately 50×50×10 μm in size) and a pressure transmitting medium were loaded in a 150 μm hole in the preindented stainless steel gasket (Figure 2.9). The gasket was used in order to seal the high-pressure chamber upon compression. Argon, which solidifies above 1.2 GPa, served as a quasi-hydrostatic pressure transmitting medium (Lahr & Eversole 1962; Richet et al. 1988). The use of a nearly hydrostatic pressure medium is of prime importance for compressibility measurements, because non-hydrostatic stresses may have a strong effect on volumetric strain in the investigated material, thus leading to significant deviation of measured $V(P)$-dependence from the real equation of state (e.g. Otto et al. 1997).

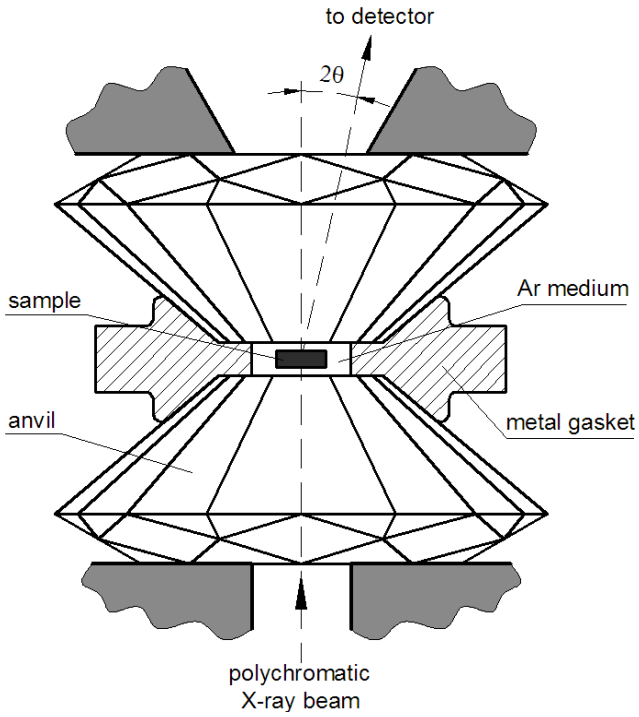

Figure 2.9. Schematic drawing of a DAC used for compressibility measurements.

The samples volumes were measured on compression up to about 45 GPa. The pressure was determined from the earlier measured equation of state of crystalline argon (Richet et al. 1988). The specific volumes of investigated material and of argon at high pressures were

* The diamond anvil cell was kindly provided by Dr. Reinhard Boehler (Hochdruckgruppe, Max-Planck-Institut für Chemie, Mainz, Germany)

derived from ED-XRD patterns, collected using polychromatic synchrotron radiation (s. Chapter 2.3.1.2).

2.4.2 Vickers indentation

The indentation hardness of hard ceramic materials is usually determined using standard sharp (pointed) indenters such as Vickers, Knoop or Berkovich (McColm 1990; Fischer-Cripps 2000). In the present work microindentation hardness of synthesized material was determined by standard Vickers test. The Vickers indenter represents a square-based diamond pyramid with a standard half-apex angle (angle between the face and the height of the pyramid) $\psi = 68°$. The Vickers hardness (H_V) is defined as the load applied to the indenter divided by the surface area of the remaining impression. Hence H_V can be expressed in terms of the applied load, L, and the average diagonal length of the impression, $\langle d_v \rangle$:

$$H_V = \frac{L}{\langle d_v \rangle^2 / (2\sin\psi)} = \frac{1.8544L}{\langle d_v \rangle^2},$$

The hardness values throughout the manuscript are given in SI units, GPa [1 GPa = 10^9 N/m^2].

2.4.2.1 Indentation size effect (ISE)

The Vickers hardness of ceramic materials usually increases with decrease of the applied load. This phenomenon is known as indentation size effect, ISE, and especially noticeable at low loads (s. Chapter 1.2.2.1). Several mechanisms and, accordingly, several analytical expressions were suggested to explain the ISE. One of the most frequently used is known as a proportional specimen resistance (PSR) model as well as its modifications. The relationship between applied load, L, and diagonal length of the remained impression, d_v, is based on an energy balance equation: $Ld_v = a_1 d_v + a_2 d_v^2 + a_3 d_v^3$, where the left part is related to the external work done by the indenter. The terms in the right part, depending on the suggested model modification, can be associated with various material related factors and processes accompanying indentation: "a_1" is related to test-specimen resistance (Hays & Kendall 1973) or residual surface stresses in the sample (Gong et al. 1999), "a_2" – to formation of new surfaces and microfracture during indentation (Bernhardt 1941; Fröhlich et al. 1977) or to elastic deformation of the indented material and to friction between indenter and material surface (Li & Bradt 1993; Li et al. 1993). The constant a_3 is concerned with permanent (plastic) volume deformation and suggested to be a measure of the load-independent "true

hardness" (Fröhlich et al. 1977; Hirao & Tomozawa 1987; Li & Bradt 1993; Quinn & Quinn 1997). Thus the true Vickers hardness can be obtained from the energy balance equation by assuming $d_v \to \infty$, so $H_V^{true} = 1.8544\, a_3$. In order to reveal the ISE in the sample material and to derive the load-independent hardness value, Vickers indentations were performed for different applied loads (s. below).

2.4.2.2 Indentation fracture toughness

Fracture toughness is a measure of resistance of a material containing a crack to crack propagation. This is an important material property characterising its ability to withstand fracture. If a specimen containing a crack is loaded perpendicularly to the crack surface (tensile mode or mode I), the magnitude of the stress field at coordinates (r, φ) near the crack tip is characterized by a scale factor K_I also known as the stress intensity factor. The stress tensor can be written as $\sigma_{ij} = K_I\, f_{ij}(\varphi)/\sqrt{2\pi r}$, where f_{ij} are nondimentional functions of angle φ and $i, j = x, y, z$. The stress intensity factor depends on the applied load, on the crack size and on the geometry of specimen, so $K_I = \sigma\sqrt{\pi c}\, Y$, where σ is the tensile stress, c is the crack length and Y is a geometric factor. The fracture toughness, K_{Ic}, is defined as the critical stress intensity factor at which crack propagation occurs (Lawn 1995; Hertzberg 1996).

The fracture toughness of cubic zirconium(IV) nitride was estimated using Vickers indentation fracture (VIF) test. This method was applied in the present work because it allows assessment of the fracture toughness for small samples, for example, from multi-anvil experiments (about $1\times1\times1$ mm^3). In contrast, the standard fracture testing techniques, such as single edge precracked beam (SEPB), surface crack in flexure (SCF) and Chevron notched beam (CNB)* require large samples (up to 50 mm in one of the dimensions) of specific shape. Basic principles of the VIF test are described below.

The indentation of hard brittle materials is usually accompanied by formation of various crack systems in the vicinity of the indenter impression. The shape and size of cracks is determined by a number of factors, such as indenter geometry, applied load, loading speed and certainly by properties of the indented material (Cook & Pharr 1990). Indentation with Vickers indenter commonly results in generation of four radial surface cracks, emanating from or close to the impression corners. With respect to under-surface geometry two types of cracks can be

* ISO 15732, ISO 18756 and ISO 24370, respectively.

distinguished: *half-penny* cracks and *Palmqvist* cracks (Figure 2.10) (Cook & Pharr 1990). According to one of the suggested mechanisms, half-penny cracks are initiated mainly under high loads at the deepest point of the plastic zone beneath the indenter and propagate to the specimen surface, thus forming the semicircular final shape with radius *c* (Figure 2.10a) (e.g. Lawn & Marshall 1979). At moderate loads the Vickers indentations of hard brittle materials generally produce *Palmqvist* cracks (Cook & Pharr 1990): directly below the surface, four radial shallow cracks of length *l* emanate from the corners of the impression (Figure 2.10b) (Palmqvist 1957). Usually crack morphology can not be unambiguously determined from the observed surface crack dimensions and/or their relation to the size of the impression and the applied load (Lankford 1981, 1982; Laugier 1985; Cook & Pharr 1990; Li et al. 1991). However, analysis of numerous experimental data have shown that moderate load Vickers indentation of the most crystalline ceramic materials is accompanied by formation of the Palmqvist cracks rather than half-penny cracks (Cook & Pharr 1990). Since the indentation loads in the present work were below 10 N, it was assumed that the observed cracks are those of Palmqvist type.

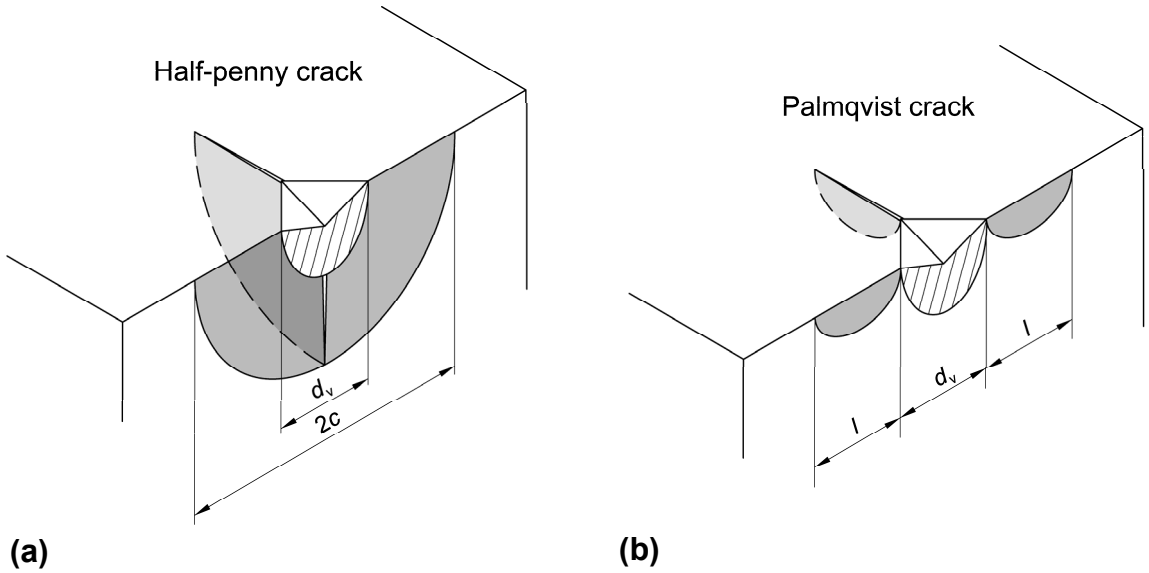

Figure 2.10. Crack systems commonly observed for Vickers indentations: (a) half-penny cracks, (b) Palmqvist cracks. The hatched area indicates the plastic zone which develops in specimen beneath the indenter during indentation.

The Vickers indentation fracture (VIF) test is based on assessment of the relation between the radius/length of cracks, generated during indentation, and the applied load. Proportionality coefficient in such relation depends on fracture toughness, hardness, Young's modulus and/or Poisson's ratio of the investigated material. Thus, if *H*, *E* and/or ν of the specimen are

known, its fracture toughness can be calculated from the length of cracks produced by Vickers indentation. The fracture toughness value obtained by the VIF test is usually referred to as the *indentation fracture toughness*, $K_{\text{Ic-if}}$, and is suggested to be comparable with the mode I critical stress intensity factor, K_{Ic}, measured on macroscopic samples using standard methods.

The VIF method was developed by Evans & Charles (1976) for half-penny crack geometry by means of the dimensional fracture mechanics analysis. Later it was modified and extended for both half-penny and Palmqvist cracks (e.g. Evans 1979; Lawn et al. 1980; Anstis et al. 1981; Niihara et al. 1982; Laugier 1985; Shetty et al. 1985). The numerous suggested analytical solutions mainly differ in the method of calculation of the elastic-plastic stress field, in the chosen crack geometry and in calibration coefficient (e.g. Ponton & Rawlings 1989b). It should be, however, mentioned that the VIF test was subjected to a strong criticism by several research groups (e.g. Morrell 2006; Quinn & Bradt 2007). The authors have questioned the ability of the indentation method to provide accurate and reliable fracture toughness values of studied material comparable with K_{Ic} from standard measurements. Since the amount of the high-pressure material synthesized in the present work is much smaller than required for standard fracture testing techniques, the reliability of the obtained $K_{\text{Ic-if}}$ values could not yet be verified. More information on comparability of the VIF test with standard fracture testing methods can be found elsewhere (Li et al. 1989; Ponton & Rawlings 1989a; Ghosh et al. 1996; Quinn & Bradt 2007).

In the present work the indentation fracture toughness of cubic zirconium(IV) nitride was estimated by means of equations suggested by Niihara et al. (1982) and Shetty et al. (1985) for Palmqvist cracks. These equations were chosen because they yield the most reliable values of fracture toughness for hard ceramic materials, such as WC-Co, Si_3N_4 and SiC (Shetty et al. 1985; Li et al. 1989; Dusza 1992; Rudnayova et al. 1993). According to Niihara et al. (1982) the indentation fracture toughness can be related to the average Palmqvist crack length l through the equation:

$$K_{\text{Ic-if}} = 0.009\, E^{0.4} H_{\text{V}}^{0.6} d_{\text{v}} / l^{0.5},$$

where E is Young's modulus and H_{V} is the Vickers hardness of the tested material, and d_{v} is the Vickers impression diagonal. In contrast to Niihara's equation, the equation of Shetty et al. (1985) does not include the Young's modulus:

$$K_{\text{Ic-if}} = \beta \sqrt{H_{\text{V}} L / 4l},$$

where β is a geometry factor, H_{V} is the Vickers hardness of tested material, L is the applied load and l is the average Palmqvist crack length. The geometry factor β is calculated from the

standard half-apex angle of the Vickers pyramid, $\psi = 68°$, and Poisson's ratio, ν, of the indented material: $\beta = 1/[3\pi^{1/2}(1-\nu^2)(2^{1/2}\pi\tan\psi)^{1/3}]$.*

Since in the indentation fracture toughness equations the hardness value is load independent, the derived Vickers true hardness value (s. Chapter 2.4.2.1) was used for calculation of $K_{Ic\text{-}if}$. Moreover, in order to minimize possible influence of ISE on the fracture toughness, only high load indentations (2.94, 4.9 and 9.8 N) were taken into consideration.

2.4.2.3 Measurement procedure

Vickers indentations were performed on a mirror polished sample surface using a LECO M-400G2 hardness tester. At least five indentations were made for each applied load from 0.49 N (50 g) to 9.8 N (1 kg). The higher loads were not applied because of comparably small sample surface (≈ 1 mm^2). The loading time was fixed at 15 seconds. The impression diagonals were measured using an optical system of the hardness tester and verified using calibrated SEM. SEM was also used for measurement of the crack length for high load impressions.

2.4.3 Instrumented nanoindentation

Hardness and elastic properties of cubic zirconium(IV) nitride were examined by means of instrumented *nanoindentation* technique. Development of this technique was stimulated by miniaturization of engineering and electronic components, as well as by an extended application of thin films and nanocomposites which required a method for probing mechanical properties of used materials on microscopic scales. During the last few decades the instrumented indentation technique has been considerably developed and, with the help of high-resolution testing equipment, extended to a nanoscale: the instrumented nanoindentation allows precise control of the applied force down to a few micronewtons with the indenter displacements in the nanometer range (Fischer-Cripps 2002). Thus, this technique can be readily employed for probing samples having surface area of about 1 mm^2. Below a brief overview of nanoindentation methods applied in the present work will be given.

The instrumented nanoindentation technique allows also collecting more information about elasto-mechanical properties of the examined material than the Vickers hardness test. In the latter only a residual impression after indentation is considered, thus only irreversible (plastic)

* In the original article the factor $1/\pi^{1/2}$ in the equation for β was missed during formula manipulation.

behaviour of material is examined. In contrast, instrumented indentation technique (EN ISO 14577) allows examination of both plastic and elastic behaviour of the tested specimen because the applied load, L, and the corresponding indenter displacement, h, are measured simultaneously upon loading and unloading. The obtained load-displacement data, $L(h)$, can be analytically processed in order to derive both hardness and reduced elastic modulus, E_r, of the indented material (s. below).

Nanoindentation measurements are usually performed using a standard Berkovich indenter which represents a three-sided diamond pyramid with a standard half-apex angle $\psi_B = 65.27°$ (angle between the face and the height of the pyramid). Berkovich indenter is designed so as to have the same cross-sectional (projected) area A_p of indenter at distance h from the indenter tip as Vickers pyramid. The $A_p(h)$-dependence is referred to as *indenter area function* and for ideal Berkovich and Vickers indenters $A_p = 24.5h^2$. Berkovich indenter, however, has an advantage over the Vickers indenter for the small scale indentations: in the three-sided pyramid it is easier to obtain a sharp single pointed vertex, while a line usually occurs at the vertex of the four-sided pyramid (e.g. Fischer-Cripps 2000).

Accordingly, in the present work nanoindentation of samples was done with Berkovich indenter. A standard Oliver-Pharr method (O&P) (Oliver & Pharr 1992) as well as continuous stiffness method (CSM) (Oliver & Pethica 1989; Li & Bhushan 2002) were used for determination of hardness and reduced elastic modulus, E_r. Alternatively, E_r was derived from the Hertzian contact analysis (Hertz 1881; Johnson 1985) of the indentation data. Basic principles of these methods are described below.

2.4.3.1 Oliver -Pharr method (O&P)

As was mentioned above, during nanoindentation both the applied force and the displacement of a diamond indenter are recorded simultaneously, thus providing a load-displacement curve, $L(h)$ (Figure 2.11a). The loading part of the load-displacement curve characterizes the resistance of the specimen to the indenter penetration, thus reflecting both elastic and plastic properties of the tested material. The unloading part is mainly determined by elastic recovery of the material. Therefore, in addition to hardness value, elastic properties of the specimen can be assessed from load-displacement data using an appropriate interpretation method.

A method for subtraction of elastic component from total load-displacement curve was suggested by Doerner & Nix (1986) and further extended by Oliver & Pharr (1992, 2004). In this method the elastic unloading curve is analysed according to a model for deformation of

an isotropic elastic half-space by an elastic indenter (Sneddon 1965). The main values which can be measured from a load-displacement curve are maximum applied load, L_{max}, maximum displacement, h_{max}, and the contact stiffness, $S_c = (dL/dh)_{h=h_{max}}$, defined as the slope of the initial portion of the unloading curve (Figure 2.11a). Using these values, the projected area of contact between indenter and specimen (A_p) under maximum load can be derived, thus providing the value for hardness (Oliver & Pharr 1992):

$$H = L_{max} / A_p \,. \tag{2.4.1}$$

Furthermore, in combination with contact stiffness, A_p can be used for determination of the reduced elastic modulus (Sneddon 1965; Doerner & Nix 1986; Oliver & Pharr 2004):

$$E_r = S_c \frac{1}{2\eta}\sqrt{\frac{\pi}{A_p}}\,, \tag{2.4.2}$$

where η is a correction constant for axially nonsymmetrical indenters, e.g. for Berkovich indenter $\eta = 1.034$ (King 1987). The reduced elastic modulus, E_r, accounts for the elastic deformation of both, the tested specimen and the indenter, during indentation and is related to the Young's modulus E and the Poisson's ratio ν of the specimen through the relationship:

$$\frac{1}{E_r} = \frac{1-\nu^2}{E} + \frac{1-\nu_i^2}{E_i}\,, \tag{2.4.3}$$

where $E_i = 1141$ GPa and $\nu_i = 0.07$ are values for diamond, the indenter material (e.g. Oliver & Pharr 1992).

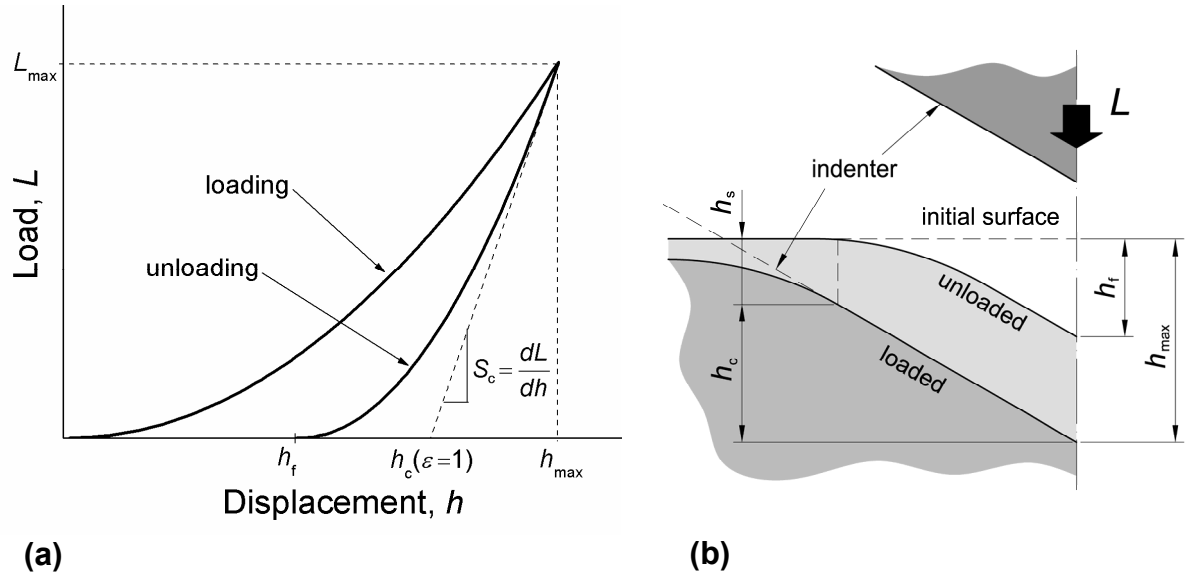

Figure 2.11. Schematic illustration of typical indentation load-displacement data $L(h)$ (a) showing parameters used for determination of hardness and reduced elastic modulus (s. text) and of indentation procedure (b) showing the displacement quantities used for analysis (Oliver & Pharr 1992).

Thus, in order to evaluate the hardness and the reduced elastic modulus of the tested material, the contact stiffness and the projected contact area at maximum load should be determined. In the present work the load-displacement data was analytically processed using the method proposed by Oliver & Pharr (1992).

Contact stiffness. In order to obtain the contact stiffness, the unloading part of the load-displacement curve is fitted by the power function: $L = \kappa(h - h_f)^q$, where κ and q are the fitting parameters and h_f is the residual impression depth (Figure 2.11). The analytical differentiation of the unloading curve fit gives the contact stiffness: $S_c = (dL/dh)_{h=h_{max}} = \kappa q(h_{max} - h_f)^{q-1}$.

Projected contact area. The projected area of contact between indenter and specimen is determined by the indenter geometry (namely its area function) and the effective contact depth h_c. The contact depth can be expressed as $h_c = h_{max} - h_s$, where h_s represents the amount of *sink in*, i.e. the elastic displacement of the surface outside the contact perimeter (Figure 2.11b) (Oliver & Pharr 1992). Under the assumption of indentation of a flat elastic half-space by a rigid indenter (Sneddon 1965), the sink in value can be determined from the load-displacement curve: $h_s = \varepsilon L_{max}/S_c$, where the constant ε depends on the indenter geometry (for Berkovich indenter $\varepsilon = 0.75$) (Oliver & Pharr 1992, 2004). The indenter area function of the ideal Berkovich pyramid is known: $A_p(h_c) = 24.5h_c^2$. However, real indenters are usually blunted and have more complicated area-depth relation. Therefore additional calibration of the indenter area function is required, using a standard material with known reduced elastic modulus (Oliver & Pharr 1992).

Finally, nanoindentation hardness and reduced elastic modulus of the tested specimen can be calculated by substituting the projected contact area and the contact stiffness into Equations 2.4.1 and 2.4.2. The above described analysis of the load-displacement data is based on the elastic contact theory, so it works well for indentation of hard ceramic material where sink in predominates (Li & Bhushan 2002; Oliver & Pharr 2004; Bull 2005).

2.4.3.2 Continuous stiffness measurement (CSM) technique

In addition to the above described method, the contact stiffness of the investigated material was measured during loading part of the indentation using a *continuous stiffness measurement* (CSM) technique (Oliver & Pethica 1989; Oliver & Pharr 1992; Li & Bhushan 2002). The CSM is accomplished by superimposing of a low amplitude harmonic force $L_{os}\exp(i\omega t)$ on a

continuous load (Figure 2.12a). The displacement response of the indenter, $h(\omega) = h_0 \exp(i\omega t + \phi)$, and the phase angle between the force and displacement signals, ϕ, are measured continuously as a function of depth. The analysis of the dynamic model of the entire indentation system (Figure 2.12b) allows calculation of the contact stiffness S_c from the measured displacement amplitude or from the phase angle using following equations:

$$\left|\frac{L_{os}}{h(\omega)}\right| = \sqrt{\left((S_c^{-1} + K_f^{-1})^{-1} + K_s - m\omega^2\right)^2 + \omega^2 D^2},$$

$$\tan\phi = \frac{\omega D}{(S_c^{-1} + K_f^{-1})^{-1} + K_s - m\omega^2},$$

where K_f and K_s are the stiffness of the load frame and the indenter support springs, respectively, D is the damping coefficient and m is the mass of the indenter, which are determined experimentally (Oliver & Pharr 1992; Li & Bhushan 2002). Further, the projected contact area can be derived using the contact stiffness value. Thus, the CSM technique allows simultaneous measurements of applied force L, indenter displacement h and contact stiffness S_c at every data point of the loading part of a single indentation, providing the hardness and the reduced elastic modulus values as functions of indentation depth.

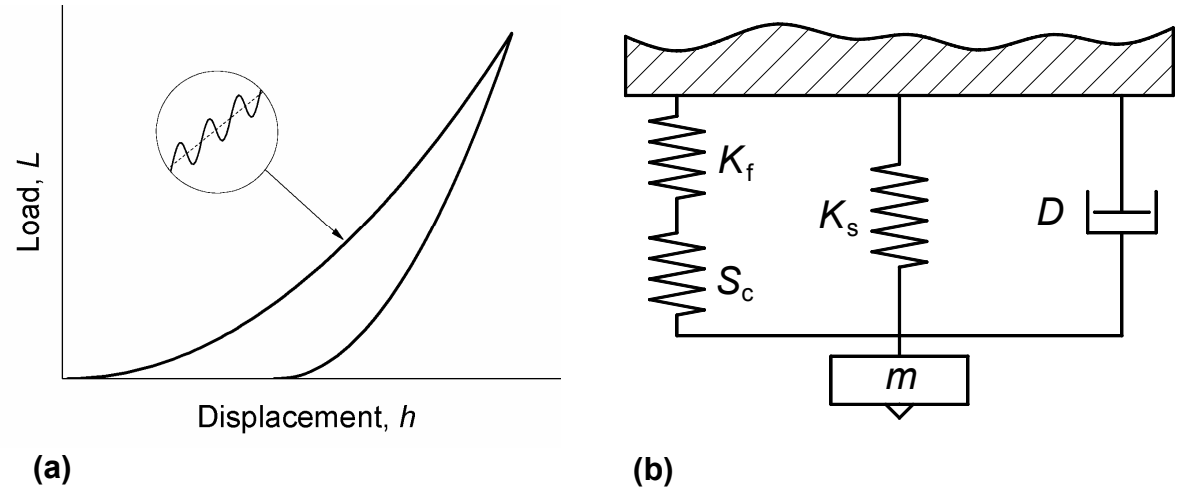

Figure 2.12. Schematic representation of CSM load-displacement curve (a) with a low amplitude oscillating force superimposed on a continuous load (inset) and of a dynamic model of the CSM module (b) (Oliver & Pethica 1989; Li & Bhushan 2002).

2.4.3.3 Hertzian contact analysis

Alternatively, the reduced elastic modulus of the synthesized material was derived using the Hertzian contact equation. In contrast to the O&P and CSM methods, for Hertzian contact

analysis only the initial loading part of the load-displacement curve is considered. Brief description of this method is given in the following.

As was mentioned above, the pointed indenters are not ideally sharp if we consider a submicron scale. For example, a standard Berkovich indenter has a radius of a tip curvature, R_i, of about 150 nm.* At low loads when displacement is much less than the tip radius ($h << R_i$) one can assume a pure elastic contact of a sphere of radius R_i with the flat surface of a specimen. The theoretical analysis of this contact model was suggested by Hertz (1881) and is commonly used today for evaluation of elastic properties of materials (Johnson 1985; Fischer-Cripps 2000).

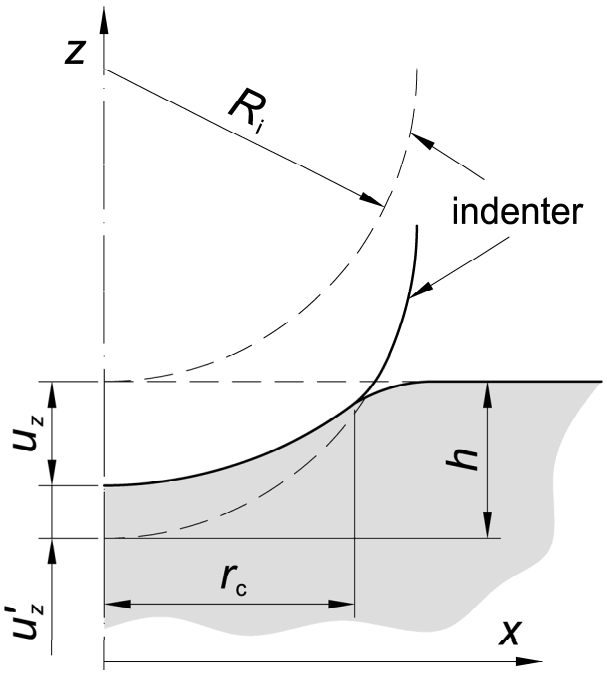

Figure 2.13. Schematic drawing of purely elastic contact between nonrigid spherical indenter of radius R_i and nonrigid flat surface.

The Hertzian elastic contact model considers the contact of a sphere of radius R_i (with Young's modulus E_i and Poisson's ratio ν_i) with the specimen surface, which radius of curvature $R \to \infty$, and Young's modulus and Poisson's ratio are E and ν, respectively. Additional assumptions of the Hertzian contact problem are: (1) each body is approximated by an isotropic elastic half-space, i.e. the dimensions of each body must be large compared to the radius of the contact area r_c; (2) the radius of the contact area is small compared to the radii of curvature of the surfaces, $r_c << R_i$; (3) the strains are small to satisfy the linear

* Hysitron, Inc. (http://www.hysitron.com), User Support, Tip Selection Guide

elasticity; (4) the contact is frictionless. Hertz showed that the pressure within the contact area is distributed as

$$P(x) = \frac{3}{2}\frac{L}{\pi r_c^2}\sqrt{1-\frac{x^2}{r_c^2}},$$

where $x \le r_c$ is the distance from the contact point and L is the applied load. This pressure distribution, in its turn, results in displacements of the specimen surface of:

$$u_z(x) = \frac{1-\nu^2}{E}\frac{3L}{8r_c^3}(2r_c^2 - x^2)$$

as well as in the similar displacements of nonrigid indenter u_z' (Figure 2.13), where Young's modulus and Poisson's ratio are those with the subscript "i". Thus, for the total indenter displacement h, deformations within the contact area can be expressed as:

$$u_z(x) + u_z'(x) = \left(\frac{1-\nu^2}{E} + \frac{1-\nu_i^2}{E_i}\right)\frac{3L}{8r_c^3}(2r_c^2 - x^2) = h - \frac{x^2}{2R_i}.$$

Substitution of $x = r_c$ and $x = 0$ in the above equation provides the relationship between the indenter displacement h, the applied load L, the indenter radius R_i and the reduced elastic modulus E_r, also known as Hertzian contact equation:

$$h^3 = \frac{9L^2}{16E_r^2 R_i}. \qquad (2.4.6)$$

The detailed derivation of the contact pressure distribution, the shape and the displacement of the contact surfaces can be found elsewhere in the literature (e.g. Landau & Lifshitz 1975; Johnson 1985).

In the present work the initial contact between indenter and the sample surface was assumed to be purely elastic. The initial loading parts of the measured load-displacement curves (up to h = 15 nm) were fitted with the Hertzian contact equation (Equation 2.4.6) taking the reduced elastic modulus as a fitting parameter. The obtained values for E_r are considered as those of an isotropic polycrystalline material.

2.4.3.4 Measurement procedure

All nanoindentation experiments were carried out at the Lehrstuhl für Allgemeine Werkstoffeigenschaften (WW1), Institut für Werkstoffwissenschaften, Friedrich-Alexander-Universität Erlangen-Nürnberg, Erlangen, Germany. Nanoindentation tests were done on a Nanoindenter XP (MTS Nano Instruments) equipped with the continuous stiffness measurement (CSM) module in the dynamic contact mode (DCM) which provided a very

high displacement resolution for low loads. For additional nanoindentation tests a nanoindenting atomic force microscope (NI-AFM; Hysitron Triboscope on a Multimode-Scanner) was employed. All indents were done with a standard Berkovich indenter. The indenter area function, $A_p(h)$, was calibrated using fused quartz ($E = 72$ GPa, $\nu = 0.170$; i.e. for diamond indenters: $E_r = 69.6$ GPa). The tip radius for Hertzian contact analysis ($R_i = 160.3$ nm) was determined on GaAs ($E_r = 99.5$ GPa (Lilleodden 1995)) and electropolished aluminium, both showing a pronounced elastic-plastic transition (pop-in).

2.4.4 Elastic moduli evaluation

The reduced elastic modulus derived from instrumented indentation is a function of the Young's moduli and Poisson's ratios of both investigated specimen and indenter material (s. Equation 2.4.3). While the values for the indenter are usually known, E and ν of the investigated specimen can not be extracted from E_r if there is no additional information on the elastic moduli. In the present work combination of experimental values for B_0 and E_r from compressibility and nanoindentation measurements, respectively, allowed experimental determination of all other elastic moduli of cubic zirconium(IV) nitride. Such combination of experimental methods to determine the isotropic elastic moduli was first introduced in the earlier work on cubic silicon nitride, γ-Si_3N_4 (Zerr et al. 2002a).

For the calculation of E_0, G_0 and ν_0 the well known relations between E, B, G and ν for an isotropic elastic material were used (Landau & Lifshitz 1975):

$$E = 9BG/(3B + G),$$

$$\nu = (3B - 2G)/(6B + 2G).$$

These expressions for E_0 and ν_0 were substituted in the equation defining E_r (Equation 2.4.3). For diamond indenter the Young's modulus and the Poisson's ratio are $E_i = 1141$ GPa and $\nu_i = 0.07$, respectively. Substituting the experimentally measured B_0 and E_r in the resulting equation, the Young's modulus, the shear modulus and the Poisson's ratio of the investigated material can be derived. The obtained elastic moduli are considered as those of isotropic polycrystalline material.

2.5 Thermal expansion and high-temperature oxidation

In addition to hardness and stiffness there are other important properties which can be useful for a certain application of hard materials. In particular, abrasive materials, coatings of cutting tools and corrosion resistant layers are usually subjected to high temperatures and chemically

aggressive environments, therefore these materials should be chemically and thermally stable and have low thermal expansion coefficient.

In the present work the investigation of thermal expansion and thermal oxidation stability of cubic zirconium(IV) nitride was conducted using *in situ* high-temperature powder X-ray diffraction. The HT-XRD patterns were collected in the Debye-Scherrer geometry using a STOE STADI P diffractometer with Mo-$K_{\alpha 1}$ radiation (λ = 0.70932 Å). The diffractometer is equipped with a curved imaging plate position sensitive detector (STOE IP-PSD, 1-90° 2θ-range with FWHM resolution of ≈ 0.1°) and a furnace (STOE HT-attachment 0.65.1). The powdered sample was filled in a quartz capillary of 0.3 mm in diameter and inserted coaxially in a quartz capillary of 1 mm in diameter so that to be rigidly fixed. The capillary was rotated inside the furnace in order to obtain texture-free XRD patterns. The HT-XRD patterns were measured in air at room temperature (RT) and starting from 373 K up to 873 K with intervals of 100 K. The sample temperature was monitored by a NiCr-Ni thermocouple. After 1 min stabilization time at a given temperature each HT-XRD pattern was recorded during 30 min. The detector distortion and the sample-to-detector distance were calibrated using a NIST-NBS640b Si standard. In order to derive the lattice parameters, the Profile Matching of diffractograms was performed using Fullprof software (Rodriguez-Carvajal 1990).

3 Results and discussion

This part of the thesis presents the first results on bulk synthesis, characterisation and investigation of properties of oxygen-bearing cubic zirconium(IV)- and hafnium(IV) nitrides having Th_3P_4-type structure, c-M_3N_4 (where M = Zr or Hf). In the original work only microscopic amounts of c-Zr_3N_4 and c-Hf_3N_4 were synthesised at high pressures and high temperatures using a laser-heated diamond anvil cell (LH-DAC) (Zerr et al. 2003). Preliminary compressibility measurements, performed in that work, have shown high bulk moduli of these materials thus suggesting their high hardness. Two years later c-Zr_3N_4 was also prepared as thin films using a filtered cathodic arc (FCA) physical vapour deposition technique (Chhowalla & Unalan 2005). The nanoindentation hardness and wear resistance of these films were found to be considerably higher than those of δ-ZrN and δ-TiN films. However, until the present work there was no information on the bulk synthesis of the new nitrides c-M_3N_4 and only limited information on their structural and functional properties was available.

The following Chapter 3.1 outlines the preparation and the chemical analysis of the nanocrystalline nitrogen-rich nitride powders used as starting materials for the high-pressure synthesis experiments performed in this work. The description of the HP-HT synthesis of macroscopic amounts of oxygen-bearing c-Zr_3N_4 and c-Hf_3N_4 using a multi-anvil apparatus is given in Chapter 3.2. Further, the examination of the composition, the crystal structure and the morphology of the synthesized new (oxy)nitrides is presented (Chapter 3.3). In the last Chapters 3.4 and 3.5 the results on the investigation of the elasto-mechanical and thermal properties of the high-pressure c-Zr_3N_4 and c-Hf_3N_4 are discussed.

3.1 Synthesis of nanocrystalline Zr_3N_{4+x} and Hf_3N_{4+x} powders

As has been mentioned in Chapter 2.1, solid zirconium and hafnium nitrides with nitrogen/metal ratio ≥ 4/3 are not commercially available. That is why the preparation of a suitable starting material for HP-HT synthesis of macroscopic amounts of c-M_3N_4 (M = Zr, Hf) in a multi-anvil apparatus had to be undertaken in the present work. As such starting nanocrystalline nitrogen-rich zirconium- and hafnium nitride powders (M_3N_{4+x}) having distorted NaCl-type structure were prepared. They were synthesised via ammonolysis of the corresponding metal-dialkylamides (Chapter 2.1) according to the method described by Li et al. (2005). The equipment available in the laboratory of the Fachgebiet Disperse Feststoffe allowed to produce in each synthesis sequence about 1-2 g of powder. The N and O contents in the obtained powders were determined using the hot-gas-extraction analysis. The results, presented in Table 3.1, are compared with the composition of products synthesised earlier (Li et al. 2005) as well as with the theoretically expected values for Zr_3N_4, ZrN, Hf_3N_4 and HfN. The nitrogen/metal ratios were measured to be 1.34-1.48 and 1.56-1.61 for zirconium and hafnium nitride, respectively, which correspond to the ammonolysis reaction of the following type:

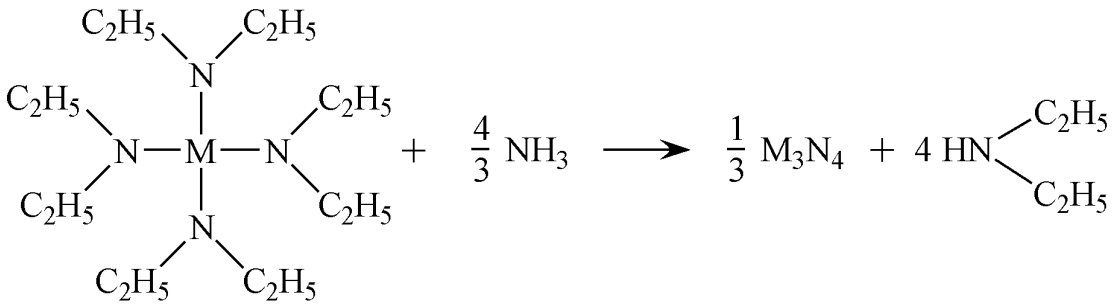

It should be noticed that preliminary high-temperature treatment of the ammonolysis glassware, as described in Chapter 2.1, improved the composition of Zr_3N_{4+x} powder so that it exhibited higher nitrogen and lower oxygen content than in the products synthesised in the earlier work. For comparison, the sample Z1 prepared without any preliminary glassware treatment was found to contain 16.72 wt.% of nitrogen and 1.73 wt.% of oxygen which is comparable with the samples Zr2 and Zr3 from previous experiments (Li et al. 2005). In contrast, the samples Z2, Z3 and Z4 were found to contain 18.28-18.44 wt.% of nitrogen and 0.53-0.67 wt.% of oxygen. A slightly higher oxygen content in the nanocrystalline Hf_3N_{4+x} obtained in this work is attributed to a minor oxidation of the starting tetrakis(diethylamido)--hafnium due to a short accidental exposure to air. Since the ammonolysis conditions (i.e.

heating schedules and NH_3 flow) were the same as described by Li et al. (2005), carbon, hydrogen and chlorine contents of the nanocrystalline powders of both Zr_3N_{4+x} and Hf_3N_{4+x} were not determined and considered to be similar to those reported earlier (Table 3.1).

Table 3.1. Elemental composition of the nanocrystalline M_3N_{4+x} (M = Zr or Hf) powders in comparison with that synthesized in the earlier work (Li et al. 2005) and with theoretical values for stoichiometric M_3N_4 and MN. The compositions are given in weight percents [wt.%]. The chlorine content in products from earlier experiments was reported to be below the detection limit of 0.1 wt.%. Zr, Hf, C, H and Cl contents were not determined in the present work. The chemical formulae were calculated assuming that the powder contained only metal, nitrogen and oxygen.

Sample	N	O	C	H	Formula	Preliminary high-temperature treatment
Z1	16.72(68)	1.73(7)	ND	ND	$ZrN_{1.34}O_{0.12}$	No treatment
Z2	18.33(36)	0.53(8)	ND	ND	$ZrN_{1.47}O_{0.04}$	Tube and boat
Z3	18.44(30)	0.54(6)	ND	ND	$ZrN_{1.48}O_{0.04}$	Tube and boat
Z4	18.28(35)	0.67(19)	ND	ND	$ZrN_{1.47}O_{0.05}$	Tube only
H1	10.88(7)	0.57(7)	ND	ND	$HfN_{1.56}O_{0.07}$	Tube and boat
H2	10.99(28)	0.56(3)	ND	ND	$HfN_{1.58}O_{0.07}$	Tube and boat
H3	11.13(30)	0.61(15)	ND	ND	$HfN_{1.61}O_{0.08}$	Tube only
Previous experiments (Li et al. 2005)						
Zr1	16.05	0.52	1.57	0.37		
Zr2	16.61	1.13	1.18	0.33		
Zr3	16.35	1.42	0.91	ND		
Hf1	11.55	0.36	<0.01	ND		
Theoretical composition						
ZrN	13.31	–	–	–	ZrN	
Zr_3N_4	16.99	–	–	–	$ZrN_{1.33}$	
HfN	7.28	–	–	–	HfN	
Hf_3N_4	9.47	–	–	–	$HfN_{1.33}$	

ND – not determined

Earlier reports on syntheses of nitrogen-rich zirconium and hafnium nitrides, with N/M ratio > 4/3, describe deposition of films using both PVD and CVD techniques (e.g. Johansson et al. 1986; Ristolainen et al. 1987; Fix et al. 1990; Fix et al. 1991; Straboni et al. 2000; Becker et al. 2004). Such methods are, however, not suitable for preparation of large powder amounts.

There are only a few reports on synthesis of powders of Zr_3N_4 (Juza et al. 1964; Yajima et al. 1983; Lerch et al. 1996) and Hf_3N_4 (Yajima et al. 1986). Since in all these works halogen-containing precursors were used, the products were contaminated with chlorine or iodine. Moreover, synthesis conditions had to be carefully controlled in order to decrease contamination of products with halogen elements and to preclude incomplete reaction or decomposition of M_3N_4 at higher temperatures.

As far as is known, the bulk synthesis of nanocrystalline Zr_3N_{4+x} and Hf_3N_{4+x} powders having distorted NaCl-type structure (Li et al. 2005) was reported for the first time. The present synthesis route has a number of advantages when compared with the above mentioned deposition and bulk synthesis methods. Firstly, relatively low temperatures of ammonolysis prevent decomposition of the products and allow to obtain the nitrides with N/M ratio exceeding 4/3. Secondly, taking a few simple precautions against oxidation/hydrolysis of dialkylamides (s. Chapter 2.1.1) one can significantly reduce the oxygen contamination of the nitride products. Furthermore, use of pure metal dialkylamide precursors (which are commercially available) excludes contamination of the resulting nitride powders with halogen elements. Next, the simplicity of the method allows an easy scale-up of the material production. Last but not least, nanocrystalline M_3N_{4+x} are more suitable for high-pressure synthesis than well crystalline compounds, because of a lower kinetic barrier for the transition to the high-pressure phase (s. Chapter 1.1.1). Use of nanocrystalline M_3N_4 powders instead of well-crystalline ones can significantly lower *P-T* conditions of their transformation to the high-pressure c-M_3N_4, however, not below the pressure of its thermodynamic stability.

3.2 High-pressure multi-anvil synthesis of c-Zr_3N_4 and c-Hf_3N_4

One of the main tasks of this work was the synthesis of macroscopic amounts of cubic zirconium(IV) and hafnium(IV) nitrides. Since in the original work the LH-DAC synthesis of c-M_3N_4 was performed at pressures above 16 GPa, an appropriate high-pressure technique able to achieve similar pressures for large sample volumes was required. The overview of available HP-techniques, given in Chapter 2.2.1, showed that only a multi-anvil apparatus fulfils these requirements. Therefore it was used in the present work for HP-HT synthesis of c-M_3N_4.

For HP-HT experiments the nanocrystalline M_3N_{4+x} powders having maximal nitrogen and minimal oxygen content, namely samples Z2, H1 and Hf1 (s. Table 3.1), were chosen as the starting materials. In HP experiments labelled as Z2-01, Z2-02 and H1-01 the nanocrystalline

powders were encapsulated with a Pt capsule. In experiments H1-02, H1-03 and H1-04 double Pt/Mo capsules were used with the aim to reduce possible contamination of the products with oxygen due to its diffusion from the surrounding oxidic pressure medium, heated to high temperatures, into the sample volume. The detailed description of sample encapsulation and HP-HT experiment can be found in Chapter 2.2.2. The samples were compressed up to the chosen pressure (P_{max}), heated to the intended temperature (T_{max}), kept at T_{max} for a time period t_{hold} and then temperature-quenched. The parameters of the HP-HT experiments including the pressure-temperature conditions of synthesis as well as the information on the obtained products are summarized in Table 3.2.

Table 3.2. Parameters of the HP-HT multi-anvil synthesis experiments along with a brief information on phase content of the products (s. below). The starting materials are denoted here in the same manner as in Table 3.1.

Exp. ID	Starting material	Capsule material	P_{max} [GPa]	T_{max} [K]	t_{hold} [min]	Products
Z2-01	Z2	Pt	12	1873	20	c-Zr_3N_4 (oxygen-bearing)
Z2-02	Z2	Pt	5	1673	20	unidentified phase(s)
H1-01	H1	Pt	12	1873	20	c-Hf_3N_4 + oxide/oxynitride
H1-02	H1	Pt/Mo	12	1773	<1	c-Hf_3N_4 + oxide/oxynitride
H1-03	Hf1	Pt/Mo	12	1873	20	c-Hf_3N_4 + oxide/oxynitride
H1-04	H1	Pt/Mo	12	1873	10	c-Hf_3N_4 + oxide/oxynitride

In the experiments Z2-01, H1-01, H1-03, H1-04 the synthesis was performed at pressures and temperatures of 12 GPa and 1873 K, respectively. The holding time at the maximal temperature was 20 minutes for the first three and 10 minutes for the latter experiment (H1-04). In the experiment H1-02 the thermocouple contacted the furnace at about 1773 K, below the intended T_{max}, and the heating electric power was switched off automatically, thus the sample was abruptly quenched from 1773 K without extended heating. Only one synthesis experiment (Z2-02) was performed at lower pressure and temperature of 5 GPa and 1673 K, respectively. It was conducted with the aim to examine a possibility of formation of c-Zr_3N_4 at *P*-*T* conditions where industrial synthesis, e.g. using belt-type high-pressure apparatuses, becomes feasible.

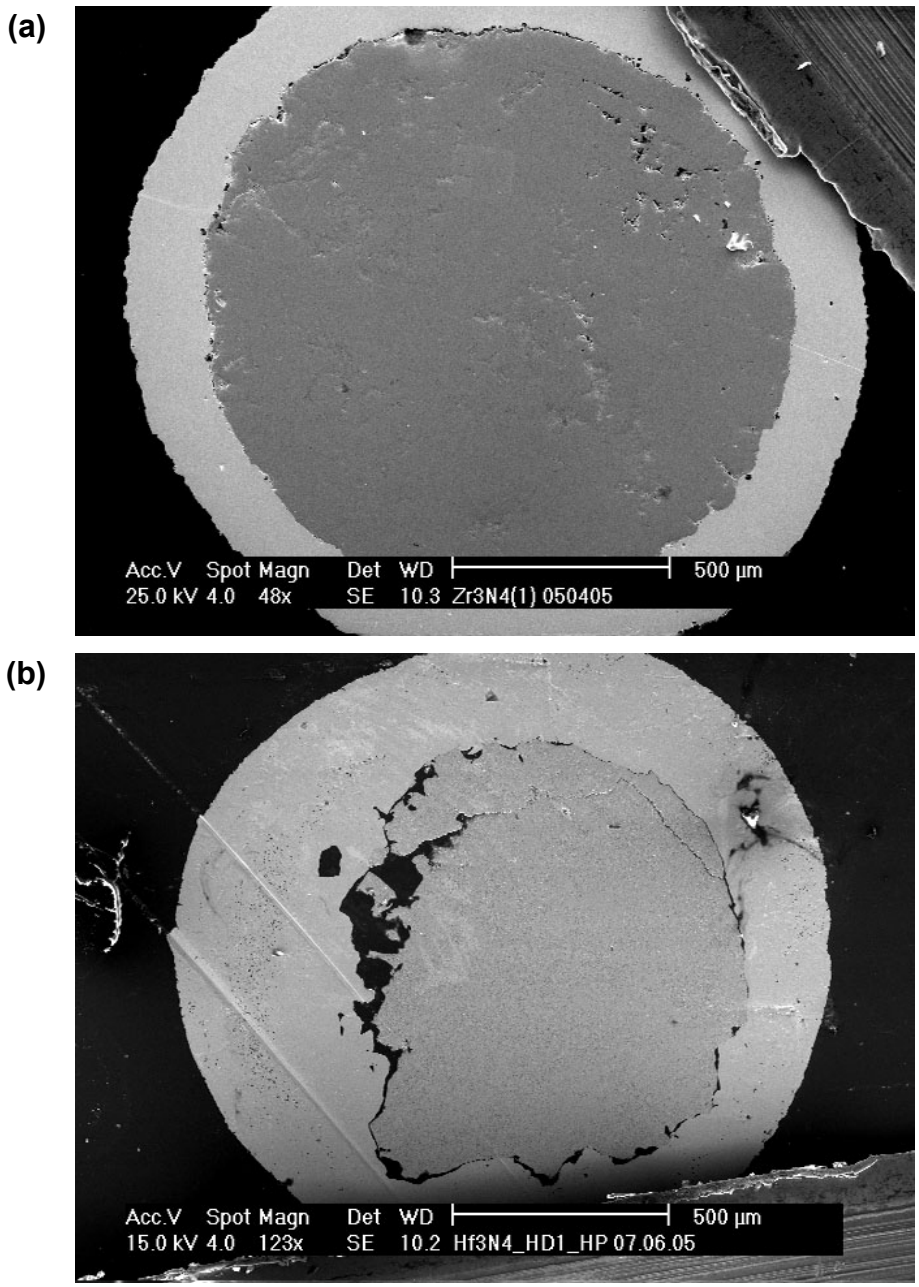

Figure 3.1. SEM pictures of preliminary polished surfaces of two high-pressure products: (a) zirconium nitride sample (Z2-01) and (b) hafnium nitride sample (H1-01). Both samples are surrounded by platinum, the capsule material.

After pressure release, undamaged sample capsules were recovered from the MgO-pressure medium, embedded in the epoxy and polished with SiC-paper, until the well compacted sample material appeared (Figure 3.1). In contrast to the starting brownish Zr_3N_{4+x} and dark-yellowish Hf_3N_{4+x} powders, the high-pressure products were opaque, dark-grey and exhibited a dull lustre after polishing with SiC-paper down to 4000 grit. It should be also mentioned that all high-pressure products could be easily recovered by unwrapping the Pt-capsule. Neither reaction of starting material with platinum nor infiltration of platinum into porous samples was observed.

In order to reveal the phase content of the synthesized products, all samples were preliminary examined by powder XRD. The diffractograms were collected from the polished samples (still surrounded by the Pt-capsules) in the reflection geometry (s. Chapter 2.3.1.1). The XRD pattern of the zirconium nitride sample Z2-01 showed, in addition to reflexes of platinum, diffraction peaks of a cubic phase which structure could be attributed to that of c-Zr_3N_4 (Figure 3.2). Therefore, this sample was further characterized using EPMA, TEM, powder XRD, SEM/EDX, and Raman spectroscopy (Chapter 3.3). As will be shown below (s. Chapter 3.3), the sample material slightly oxidised during heating at high pressures and, as a result, an oxygen-bearing zirconium(IV) nitride having Th_3P_4-type structure, c-$Zr_{2.86}(N_{0.88}O_{0.12})_4$, formed. A detailed structural characterisation of the synthesized novel zirconium oxynitride is presented in Chapter 3.3.2.1. Further, its elasto-mechanical and thermal properties such as hardness, elastic moduli, fracture toughness, thermal expansion and high-temperature oxidation stability were determined (Chapters 3.4 and 3.5).

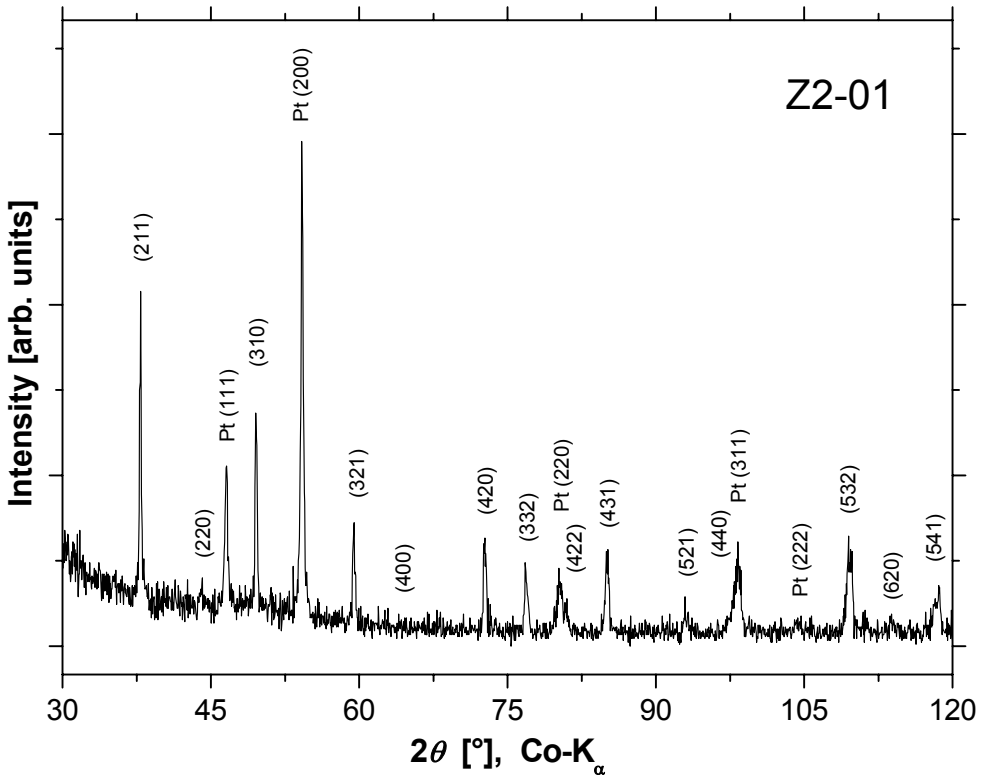

Figure 3.2. Preliminary powder XRD pattern of the zirconium nitride sample (Z2-01) synthesized in this work at 12 GPa and 1873 K using a multi-anvil apparatus. The diffractogram was collected from the polished sample surface in reflection geometry. The diffraction peaks of c-Zr_3N_4 having Th_3P_4-type structure and of platinum (Pt), the capsule material, are indicated. The intensities of the diffraction peaks of both c-Zr_3N_4 and Pt are affected by texture.

For the sample Z2-02 obtained at lower *P-T* conditions, a preliminary XRD pattern revealed reflexes which could not be attributed to any of the known zirconium nitrides, oxides or oxynitrides or their mixtures. No diffraction peaks of c-Zr_3N_4 were observed. Further investigation of this material was not performed since this was not a subject of the present work. This result, however, indicates that c-Zr_3N_4 (as well as o-Zr_3N_4) is not stable at pressures below 5 GPa and at high temperatures.

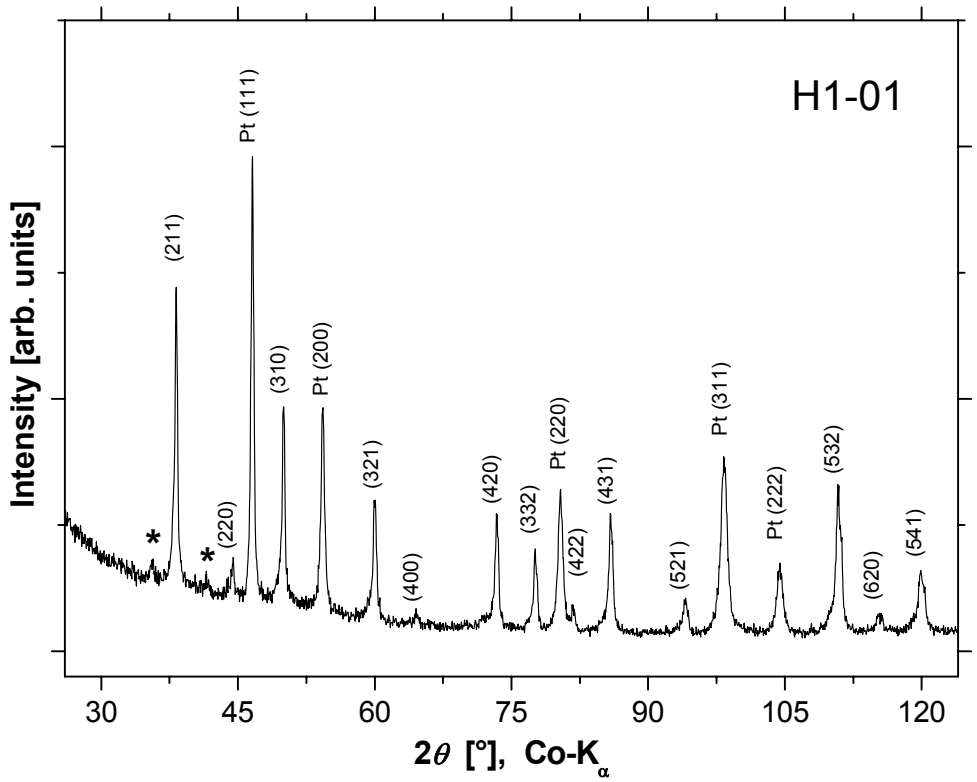

Figure 3.3. Preliminary powder XRD pattern of hafnium nitride sample (H1-01) synthesized in this work at 12 GPa and 1873 K using a multi-anvil apparatus. The diffractogram was collected from the polished sample surface in reflection geometry. The diffraction peaks of c-Hf_3N_4 having Th_3P_4-type structure and of platinum (Pt), the capsule material, are indicated. The asterisks denote the reflexes from contaminating oxidic phase (s. text). The intensities of the diffraction peaks of both c-Hf_3N_4 and Pt are affected by texture.

With respect to experiments on hafnium nitride, a cubic phase having Th_3P_4-type structure was found to be the major constituent of all high-pressure products (H1-01 - H1-04). Besides c-Hf_3N_4 and platinum, the capsule material, powder XRD revealed the presence of a minor amount of additional crystalline phase(s) (Figure 3.3). Preliminary indexing of a few weak diffraction peaks suggested that this could be one of the known ambient-pressure hafnium oxynitrides (Pialoux 1993) or high-pressure hafnium oxides (Ohtaka et al. 2001). Possible assignment of the contaminating phase is discussed below in Chapter 3.3.2.2. The

morphology and semi-quantitative composition of all hafnium nitride products was examined using SEM/EDX. Since no significant difference between the phase content and the composition of the synthesized hafnium nitride products was observed, only the sample H1-01 was further investigated. Examination of the chemical composition and crystal structure of the formed compounds is presented in Chapters 3.3.1 and 3.3.2.2. The compressibility of c-Hf_3N_4 was studied using a sample from the earlier LH-DAC experiments (Chapter 3.4.1.2). Indentation measurements have not been performed on hafnium nitride products because a sufficiently large area containing only c-Hf_3N_4 could not be found on the sample surface.

To summarize, the macroscopic amounts of oxygen-bearing zirconium(IV) nitride and hafnium(IV) nitride having Th_3P_4-type structure were synthesised for the first time at high pressures and high temperatures using a multi-anvil apparatus. These results confirm the earlier work on synthesis of c-M_3N_4 (M = Zr, Hf) using a LH-DAC, where the high-pressure nitrides were obtained via chemical reaction of pure transition metals or their mononitrides with condensed nitrogen at pressures above 16 GPa and temperatures above 2500 K. It is worth to be mentioned that the present *P-T* synthesis conditions (12 GPa and 1873 K) are considerably lower than those in the LH-DAC experiments. In the present work c-M_3N_4 were obtained from nanocrystalline M_3N_{4+x} powders with a distorted NaCl-type structure. Neither decomposition into mononitrides nor complete reaction with diffusing oxygen of the samples was observed. Thus, cubic zirconium(IV)- and hafnium(IV) nitrides having Th_3P_4-type structure appear to be thermodynamically stable phases at pressures above 12 GPa and temperatures above 1873 K. The stability regions of these compounds were not further studied in the present work. Reaction of the sample material with diffusing oxygen during heating at high pressure resulted, however, in formation of oxygen-bearing c-Zr_3N_4 (sample Z2-01) as well as in contamination of c-Hf_3N_4 with small amounts of oxidic phase(s) (samples H1-01 to H1-04). Results of a detailed characterisation of the high-pressure products using EPMA, TEM, powder XRD, Raman spectroscopy and SEM/EDX are presented in the following chapter.

3.3 Samples characterisation

The zirconium- and hafnium nitride high-pressure products (from experiments Z2-01 and H1-01, respectively) were further characterised using EPMA, SEM/EDX and powder XRD. The zirconium nitride sample was additionally investigated by TEM and Raman spectroscopy. The obtained results on chemical composition, morphology and crystal structure of the synthesised materials are described below.

3.3.1 Chemical composition of the high-pressure products

The elemental composition of the sample material from the experiment Z2-01 was determined by means of EPMA. Measurements were performed on a mirror-polished sample surface (s. Chapter 2.3.2). The results are shown in Table 3.3 along with the chemical composition of the starting material and of the ideal Zr_3N_4. The EPMA revealed the presence of 2.4 wt.% of oxygen in the high-pressure product, so that the resulted composition of the Z2-01 sample can be expressed by the formula $Zr_{2.86}(N_{0.88}O_{0.12})_4$.

Table 3.3. Elemental composition of the high-pressure zirconium nitride product (Z2-01) determined by EPMA. N- and O-content in the starting material (Z2) and the theoretical composition of the stoichiometric Zr_3N_4 are given for reference.

Sample	Composition [wt.%]			
	N	O	Zr	Hf
Z2-01	15.6(8)	2.4(3)	82.4(5)	0.12(6)
Starting material (Z2)	18.33(36)	0.53(8)	ND	ND
Theoretical (Zr_3N_4)	16.99	-	83.01	-

ND – not determined

The element mappings for zirconium, nitrogen and oxygen, collected from the sample surface, showed a homogeneous distribution for all three elements throughout the sample (Figure 3.4). The oxygen content in the high-pressure product (2.4 wt.%) is higher than that in the starting material (0.53 wt.%). This observation can be explained by diffusion, during heating, of oxygen from the surrounding oxide pressure medium, through the Pt-capsule, into the sample volume (for experimental details see Chapter 2.2.2). Further investigation of the sample material using powder XRD and TEM showed that no amorphous phase was present in the sample and, thus, oxygen is incorporated in the structure of c-Zr_3N_4. This observation

suggested that the average composition obtained from the EPMA measurements is that of the crystalline product having Th_3P_4-type structure, namely oxygen-bearing cubic zirconium(IV) nitride, c-$Zr_{2.86}(N_{0.88}O_{0.12})_4$. A detailed structure examination of this novel compound is given in the following chapter.

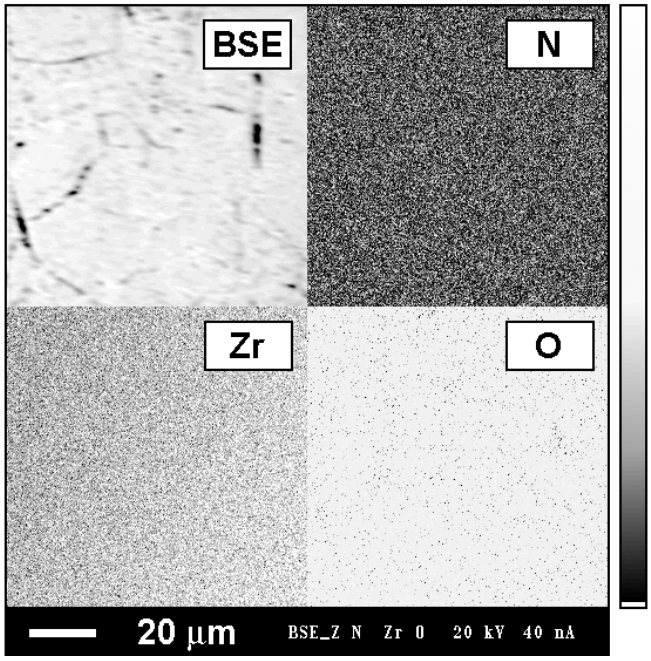

Figure 3.4. Back scattered electron (BSE) image and element mappings of a portion of the polished surface of the c-Zr_3N_4 sample (Z2-01) measured using EPMA (256×256 pixels, step size of 0.36 μm). For each element, intensity of the grey colour represents the measured content. In this sample, Zr, N and O are homogeneously distributed throughout the surface.

Similarly to the zirconium nitride sample, EPMA of the hafnium nitride product, H1-01, revealed presence of a minor amount of oxygen. The measured average nitrogen and oxygen contents in the high-pressure product were determined to be 8.4(10) and 1.9(13) wt.%, respectively. Analogous to the zirconium nitride sample, the oxygen content in H1-01 (1.9 wt.%) was found to be significantly higher than that in the starting material (0.57 wt.%). This could be explained, again, by oxygen diffusion, at HP and HT during synthesis, from the surrounding oxide pressure medium into the sample through the Pt-capsule. Element mappings of a polished surface of H1-01 revealed, however, an inhomogeneous distribution of both nitrogen and oxygen in the sample (Figure 3.5). This can be attributed to the presence of the oxidic phase(s) detected earlier by the XRD measurements (Chapter 3.2). Indeed, the oxygen- and nitrogen contents measured for each particular spot on the hafnium nitride sample varied from 0.5 to 6 wt.% and from 5 to 10 wt.%, respectively. This explains the high standard deviation values for the average O- and N-contents presented above.

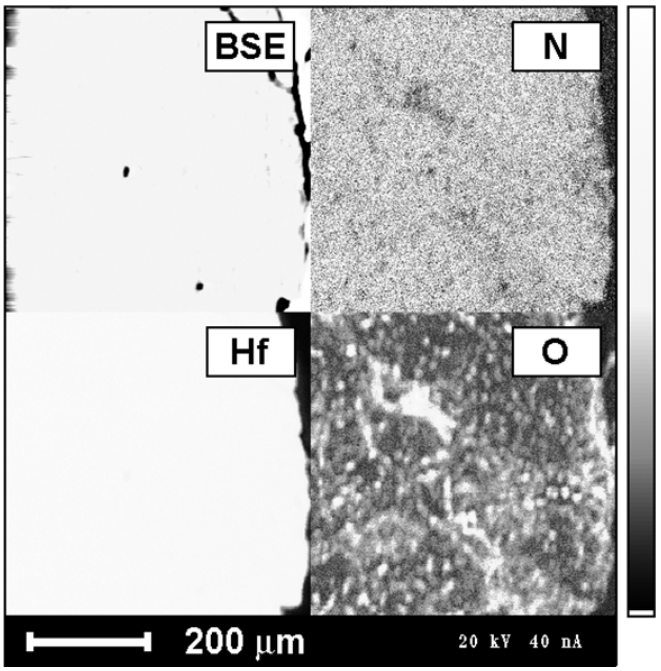

Figure 3.5. Back scattered electron (BSE) image and element mappings of the polished surface of the hafnium nitride sample (H1-01) measured using EPMA (256×256 pixels, step size of 2 µm). For each element, intensity of the grey colour represents the measured content. While hafnium is homogeneously distributed throughout the sample area, an inhomogeneous distribution of both N and O is apparent.

It was not possible to determine, in the present work, the elemental composition of each of the constituting compounds, c-Hf_3N_4 and of the oxidic phase(s), using EPMA because the spatial resolution of the electron probe micro-analyser of about 3 µm was not sufficient to examine only one of the compounds. It will be shown below that both c-Hf_3N_4 and the oxidic material were mixed on a very fine scale of less than 1 µm (Chapter 3.3.5).

Finally, it should be also mentioned that no detectable amount of platinum was found by EPMA in the high-pressure products, even in a close vicinity to the Pt-capsule. This finding indicates that platinum neither reacted with the sample material nor infiltrated into the samples at high pressures and high temperatures.

Summarizing, the presented EPMA measurements confirmed the formation of nitrogen rich compounds with average N/M ratios of 1.23 and 1.18 for zirconium- and hafnium nitride samples, respectively (M = Zr or Hf). The measured nitrogen contents in the high-pressure products were, however, slightly lower than those in the ideal M_3N_4 (N/M = 1.33). The microprobe analysis also revealed the presence of about 2 wt.% of oxygen in both zirconium and hafnium nitride samples which is considerably higher than the oxygen content in the starting powders (about 0.5 wt.%). In the hafnium nitride sample (H1-01) oxygen was found

to occur primarily in contaminating oxidic phase(s), detected by the XRD-, EPMA- and SEM/EDX-measurements. In contrast to the hafnium nitride sample, in the zirconium nitride sample (Z2-01) oxygen was found to be incorporated in the crystal structure of c-Zr_3N_4.

3.3.2 Rietveld structure refinement

3.3.2.1 Oxygen-bearing c-Zr_3N_4

One of the possible explanations of the high oxygen content of 2.4 wt.% found in the sample Z2-01 could be the presence of an oxidic phase, in addition to c-Zr_3N_4. Whould it be the case, the amount of the contaminating material would approach 9 wt.% for zirconium dioxide (ZrO_2) or even more for an oxynitride. Such amount would be easily detectable in the XRD measurements. The XRD examination of the product, however, did not reveal any other crystalline phase besides that of cubic zirconium nitride having Th_3P_4-type structure. Moreover, in a subsequent TEM study no amorphous oxidic particles or layers on the surfaces of the c-Zr_3N_4 crystallites were detected. This is in contrast to γ-Si_3N_4 synthesised in a multi-anvil apparatus where contaminating oxygen occurred as amorphous SiO_2 or SiN_xO_y layers on the crystallite surfaces (Schwarz et al. 2000). These observations allowed to conclude that oxygen was incorporated in the crystal structure of c-Zr_3N_4, thus resulting in the formation of an *oxygen-bearing* cubic zirconium(IV) nitride. In order to fulfil the electrical neutrality condition, the general composition of such oxygen-bearing nitride can be given by the formula

$$Zr_{3-u}(N_{1-u}O_u)_4, \tag{3.3.1}$$

where zirconium, nitrogen and oxygen have the oxidation states of 4+, 3- and 2-, respectively. From Formula 3.3.1 follows also that the substitution of nitrogen by oxygen at the anion sites of the Th_3P_4-type structure requires, as a consequence of the electrical neutrality condition, the formation of vacancies at the cation sites. To verify the supposition of a partial substitution of anions and formation of vacancies on the cation sites a full-profile Rietveld structure refinement of the powder XRD data was performed using the program FullProf (Rodriguez-Carvajal 1990). The X-ray powder diffractogram (Figure 3.6) was taken for the zirconium nitride sample, Z2-01, in the Debye-Scherrer transmission geometry (Chapter 2.3.1.1). The full width at half maximum (FWHM) of the diffraction peaks was found to be even smaller than that of the Si standard, used for the calibration of the sample-to-detector distance.

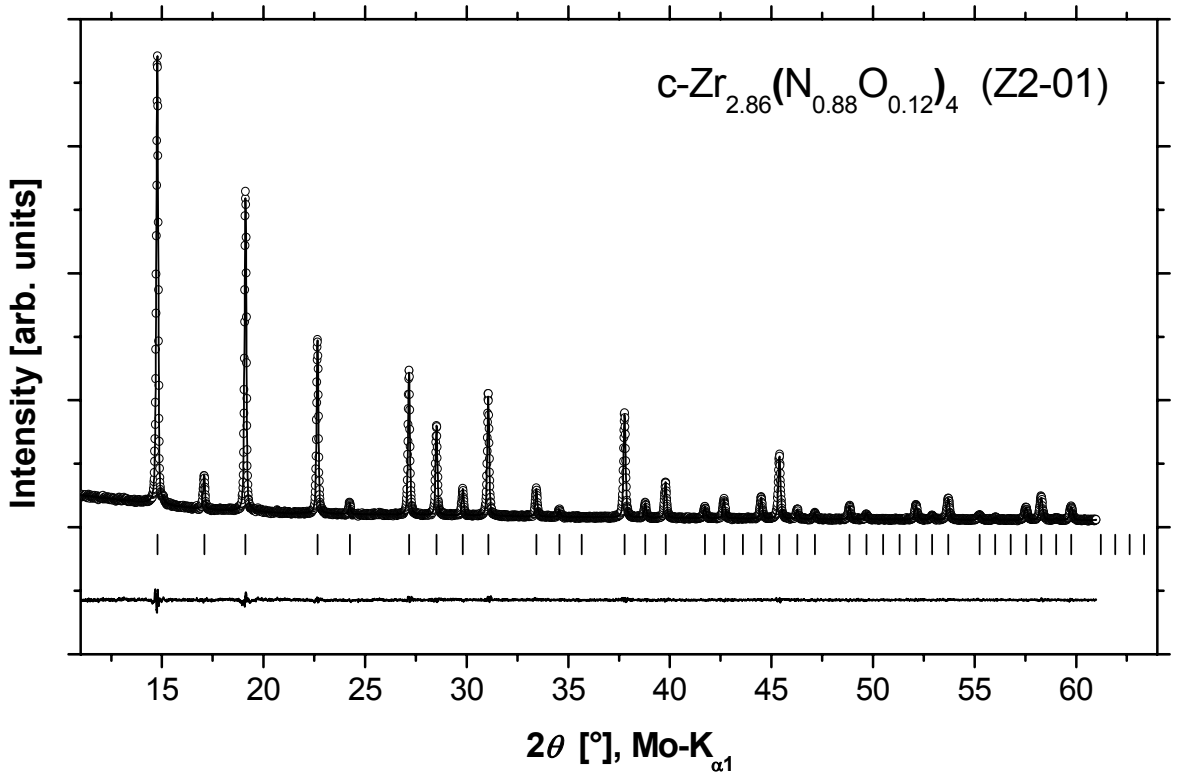

Figure 3.6. Powder XRD pattern of oxygen-bearing c-Zr_3N_4 (Z2-01) synthesized in this work using a multi-anvil apparatus: measured (circles) and calculated (solid line) intensities. The difference curve is given at the bottom of the graph. The calculated peak positions of the Th_3P_4-type structure are denoted by tick marks.

With cations and anions represented in the cubic Th_3P_4-type structure by Zr and N, respectively, and site occupation factors fixed according to the full occupancy (Zr_3N_4), the Rietveld refinement led to isotropic temperature factors B_{iso} = 0.172 Å^2 for Zr and B_{iso} = -0.344 Å^2 for N. The negative value for B_{iso} of nitrogen indicated that in our material the ratio $\xi = sf(\text{anion})/sf(\text{cation})$ of averaged atomic scattering factors, *sf*, at the anion and cation sites, respectively, was higher than for pure stoichiometric Zr_3N_4. This increase of ξ can be explained by the presence of oxygen at the anion sites (Wyckoff position 16*c*) and by a simultaneous formation of cation vacancies according to the electrical neutrality condition (Formula 3.3.1). Based on the idea that, in the first approximation, the scattering factors of Zr, O and N are related as 40:8:7 throughout the whole 2θ-range of the measured diffractogram, the dependence of ξ on u can be obtained using the Formula 3.3.1:

$$\xi(u) = (28 - 28u + 32u)/(120 - 40u) = (7 + u)/(30 - 10u). \quad (3.3.2)$$

From Equation 3.3.2 the dependence $u(\xi)$ has been derived:

$$u(\xi) = (30\xi - 7) / (10\xi + 1). \quad (3.3.3)$$

In the further Rietveld refinement the excess of the relative anion scattering power was modelled by a zirconium nitride where the site occupancy factor (SOF) of nitrogen was allowed to vary while the SOF of zirconium was fixed. The isotropic temperature factor of nitrogen was fixed at a reasonable value $B_{iso} = 0.5$ Å^2. From the Rietveld refinement the N/Zr-ratio was calculated to be 1.4538 which results in $\xi = 0.2544$. From Equation 3.3.3 followed then that $u = 0.18$ and the corresponding sample composition should be $Zr_{2.82}(N_{0.82}O_{0.18})_4$ which is reasonably close to the EPMA result. Since the elemental composition measured by EPMA corresponds, within the experimental errors, to the electrically neutral compound (Formula 3.3.1), it was used for the final step of the structure refinement. The SOFs of Zr, N and O were fixed at the values, which correspond to composition from EPMA measurement, $Zr_{2.86}(N_{0.88}O_{0.12})_4$. Following the above consideration of substitution of nitrogen by oxygen, it was presumed that oxygen is randomly distributed at the anion sites. Results of the refinement are summarized in Table 3.4 and compared with those reported for c-Zr_3N_4 synthesised in the LH-DAC experiments (Zerr et al. 2003). Low values of *R*-factors and of χ^2 obtained in these final calculations as well as a negligible difference between the measured and calculated intensities (Figure 3.6) support the conclusion that the space group of Z2-01 material is that of cubic Th_3P_4 and that oxygen is randomly distributed at the anion sites.

It appears that during heating at high pressures not only transformation of the starting material to the c-Zr_3N_4 but also substitution of nitrogen with oxygen in the Th_3P_4-type structure takes place. One can presume that the degree of substitution can vary from negligible ($u \approx 0$) to that observed in the present work ($u = 0.12$) and depends on a number of experimental parameters such as temperature, pressure, heating rate and duration, capsule material, type of the pressure media surrounding the capsule with the starting material, and so forth. Moreover, it appears that the upper limit of the *u*-value, when $Zr_{3-u}(N_{1-u}O_u)_4$ still maintain the cubic Th_3P_4-type structure, was not reached in this work since no other phases were found in the sample. Influence of all experimental parameters on the composition and structure of the high-pressure products was, however, not investigated in the present work.

The lattice parameter of the oxygen-bearing cubic zirconium(IV) nitride was found to be $a_0 = 6.7549(1)$ Å which is about 0.22 % larger than a_0 reported earlier for c-Zr_3N_4 (Table 3.4). This observation contradicts an expected decrease of a_0 due to both, substitution of N^{3-} anions by O^{2-} anions having smaller ionic radius and by formation of cation vacancies. However, recent theoretical calculations have shown that incorporation of oxygen in c-M_3N_4 (M = Zr or Hf) results in a weakening of the cation-anion bonding (Lowther 2008). This leads to reduction of elastic moduli of oxygen-bearing c-M_3N_4 and, on reaching of a critical oxygen

concentration, to expansion of the unit cell (Lowther 2008). Thus, for 12.5 % nitrogen atoms substituted by oxygen, the lattice parameter was calculated to be about 0.21 % higher than that of oxygen-free c-Zr_3N_4. Unfortunately, the influence of cation vacancies on the lattice parameter and elastic moduli of c-Zr_3N_4 was not considered in those calculations.

Table 3.4. Results of the Rietveld structure refinement for c-$Zr_{2.86}(N_{0.88}O_{0.12})_4$ (Z2-01) in comparison with structural data for c-Zr_3N_4 synthesised in a LH-DAC.

		c-$Zr_{2.86}(N_{0.88}O_{0.12})_4$ (this work)	c-Zr_3N_4 (Zerr et al. 2003)
Structure type		Th_3P_4	
Space group		$I\bar{4}3d$ (№ 220)	
Lattice parameter, a_0 [Å]		6.7549(1)	6.740(6)
Cell volume [Å^3]		308.22	306.18
Formula units per cell, Z		4	4
Molar mass [g/mol]		317.89	329.7
Calculated density, ρ_{calc} [g/cm^3]		6.850	7.159
Refined parameters (structural, profile)		4, 6	n/a
Profile function		pseudo-Voigt	n/a
R_B, R_P, R_{WP} [%]		1.71, 3.31, 4.35	6.19, n/a
χ^2		1.001	n/a
Zr:	Wyck. pos. 12*a*	3/8, 0, 1/4	3/8, 0, 1/4
	B_{iso} [Å^2]	0.165(9)	n/a
N, O:	Wyck. pos. 16*c* (x, x, x)	x = 0.0661(3)	x = 0.063(2)
	B_{iso} [Å^2]	0.457(74)	n/a
Cation-anion distances [Å]		4 × 2.217(2)	4 × 2.19(1)
		4 × 2.469(2)	4 × 2.49(2)

The increase of the cubic lattice parameter and formation of about 4.7 % of cation vacancies reduce the density of c-$Zr_{2.86}(N_{0.88}O_{0.12})_4$ to 6.85 g/cm^3 which is about 4 % lower than the density of c-Zr_3N_4 with 7.159 g/cm^3 (Zerr et al. 2003). However, the density of the oxygen-bearing cubic zirconium(IV) nitride is still about 8 % higher than that of orthorhombic Zr_3N_4 (Lerch et al. 1996). One should point out that the average cation-to-anion bond length in c-$Zr_{2.86}(N_{0.88}O_{0.12})_4$ of 2.343 Å is higher than that in o-Zr_3N_4 with about 2.24 Å (Lerch et al. 1996). Such increase of the average bond length in a high-pressure compound is, however, a common consequence and is related to the increase of the coordination number (e.g. Kleber &

Wilke 1969): in c-Zr_3N_4 the cations are eight-fold coordinated by anions while the cations in orthorhombic Zr_3N_4 are six-fold coordinated.

To summarize, the Rietveld structure refinement further supported the finding that oxygen can be incorporated in the structure of c-Zr_3N_4. Oxygen substitutes nitrogen on the anion cites, thus resulting in formation of zirconium(IV) oxynitride having Th_3P_4-type structure, c-$Zr_{3-u}(N_{1-u}O_u)_4$, where formation of cation vacancies is required by the electrical neutrality condition. It was found that this compound can accept at least 2.4 wt.% of oxygen. The oxygen incorporation in the structure of c-Zr_3N_4 resulted in minor increases of the lattice parameter (by about 0.22 %) and of the *x* value (by about 5 %) describing the position of anions in the unit cell (Table 3.4) when compared with those reported for oxygen free c-Zr_3N_4 (Zerr et al. 2003).

3.3.2.2 c-Hf_3N_4

By analogy with c-$Zr_{2.86}(N_{0.88}O_{0.12})_4$, one could expect for hafnium nitride sample (e.g. H1-01) formation of oxygen-bearing cubic hafnium(IV) nitride having general composition $Hf_{3-u}(N_{1-u}O_u)_4$. However, the presence of an oxidic phase in the obtained samples indicated that the upper limit of the *u*-value, when $Hf_{3-u}(N_{1-u}O_u)_4$ still maintain the cubic Th_3P_4-type structure, is well below $u = 0.17$ derived from the EPMA results (s. Chapter 3.3.1). Moreover, the *u*-value in c-$Hf_{3-u}(N_{1-u}O_u)_4$ can be very low and approach $u = 0$. The particular value could be estimated if the amount of the oxidic phase and its oxygen content in the sample H1-01 would be known. The spatial resolution of the EPMA technique of ≈ 3 μm was, however, not sufficient for a reliable determination of the composition of the detected compounds. For that reason, the extent of possible oxygen incorporation in the structure of c-Hf_3N_4 was not studied in the present work. The structure refinement for the synthesized cubic hafnium(IV) nitride was performed under the assumption of the oxygen free c-Hf_3N_4. This assumption was supported by the finding that the lattice parameter of the cubic hafnium(IV) nitride synthesised in this work was equal, within the experimental uncertainties, to that of c-Hf_3N_4 obtained in a LH-DAC (s. below).

In order to derive the structural parameters of the c-Hf_3N_4 synthesises in this work and to identify the contaminating oxidic phase, a high-quality X-ray powder diffractogram (Figure 3.7) was measured employing monochromatic synchrotron radiation and the Gandolfi camera technique (Chapter 2.3.1.2). A full-profile Rietveld structure refinement was performed using the program FullProf (Rodriguez-Carvajal 1990). The brilliant synchrotron radiation was required because the available in-house diffractometers could not deliver the XRD patterns of

a sufficient quality, most probably due to a high absorption of the X-ray radiation by the heavy hafnium atoms. Similar to the preliminary XRD examination (Chapter 3.2) a few weak diffraction peaks were observed in addition to the reflexes of the Th_3P_4-type structure. The three additional most intense peaks at 2θ of 7.30, 8.48 and 14.06° (Figure 3.8), which correspond to the *d*-spacings of 2.935, 2.53 and 1.527 Å, respectively, could be attributed to a few known hafnium oxides or oxynitrides. These are γ-Hf_2N_2O (Clarke et al. 1999), β-$Hf_7N_4O_8$, β′-$Hf_7N_2O_{11}$ (Pialoux 1993) with the fluorite-related structure, as well as high-pressure hafnium oxides with orthorhombic (oI-HfO_2 (Ohtaka et al. 1991)) or tetragonal (t-HfO_2 (Curtis et al. 1954; Ohtaka et al. 2001)) structures. On the other hand, presence of very weak reflexes at 2θ of 4.2, 5.2 and 5.9° (*d*-values of about 5.07, 4.13 and 3.63 Å, respectively) limited the contaminating phases to γ-Hf_2N_2O (space group $Ia\bar{3}$, No. 206), oI-HfO_2 (space group *Pbca*, No. 61) or, most probably, their mixture (Figure 3.8).

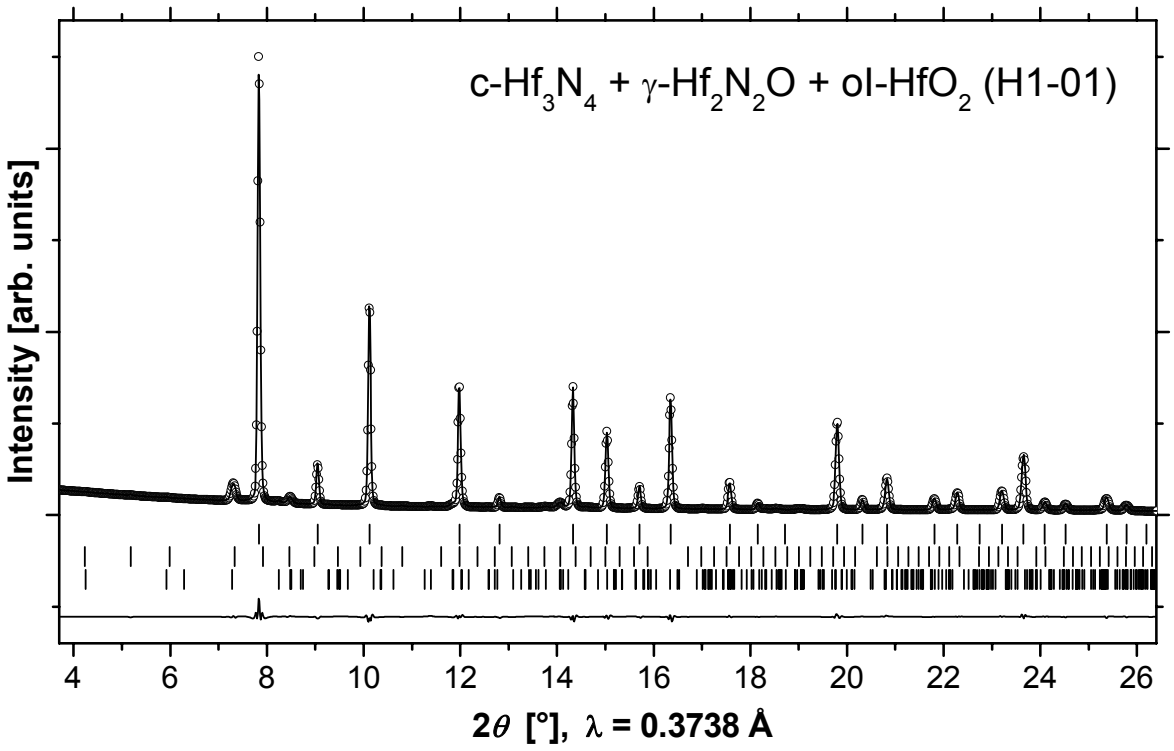

Figure 3.7. Powder XRD pattern of c-Hf_3N_4 sample (H1-01) synthesized in this work using a multi-anvil apparatus. The pattern is measured employing monochromatic synchrotron radiation and a Gandolfi camera. The sample is contaminated with γ-Hf_2N_2O and oI-HfO_2. Measured and calculated intensities are presented by circles and solid line, respectively. The difference curve is given at the bottom of the graph. The calculated peak positions of c-Hf_3N_4, γ-Hf_2N_2O and oI-HfO_2 are denoted by upper, middle and lower tick marks, respectively.

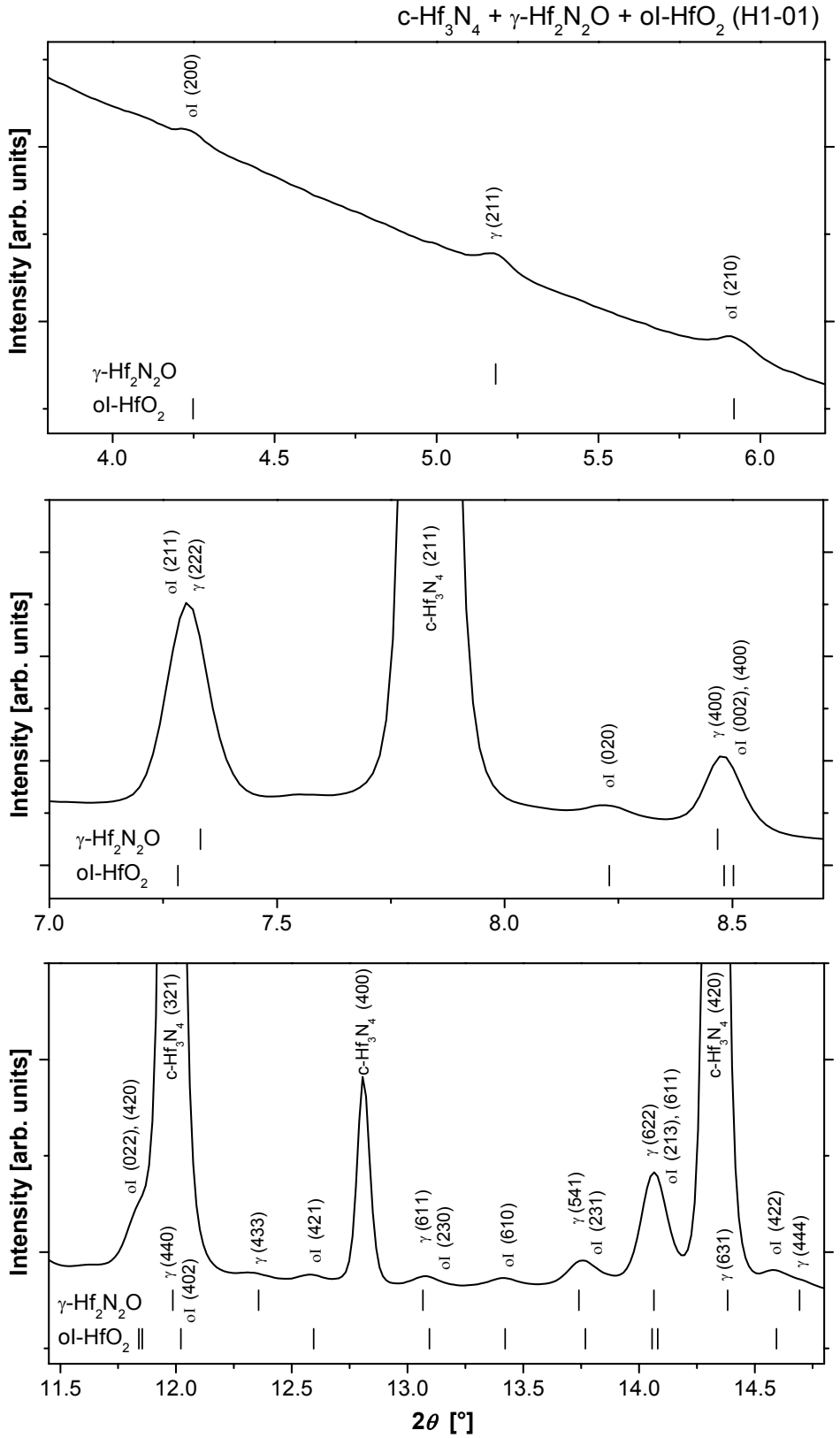

Figure 3.8. Sections of the powder XRD pattern of the hafnium nitride sample (H1-01) for different 2θ regions. The diffraction peaks of c-Hf_3N_4, γ-Hf_2N_2O (γ) and oI-HfO_2 (oI) are indicated. The calculated peak positions of γ-Hf_2N_2O and oI-HfO_2 are denoted by upper and lower tick marks, respectively. For the contaminating oxidic phases only those peaks having relative intensities above 2 % are shown.

The latter possibility is supported by the observation of T. Locherer who obtained a mixture of these two phases in experiments on the Hf-N-O system where samples were *T*-quenched after subjecting to 18 GPa and 1273 K (Locherer et al. 2008). It was also suggested that high-pressure orthorhombic-I hafnium oxide can be stabilized at ambient conditions due to the particle size and/or matrix effects.* Therefore, the structure refinement for the sample H1-01 was performed assuming a mixture of c-Hf_3N_4 with minor amounts of γ-Hf_2N_2O and oI-HfO_2.

Table 3.5. Results of the Rietveld structure refinement for c-Hf_3N_4 (sample H1-01) compared with structural data for c-Hf_3N_4 synthesised in a LH-DAC (Zerr et al. 2003). The given number of the refined parameters and *R*-values are related to the c-Hf_3N_4 phase.

		c-Hf_3N_4 (this work)	c-Hf_3N_4 (Zerr et al. 2003)
Structure type		Th_3P_4-type structure	
Space group		$I\bar{4}3d$ (№ 220)	
Lattice parameter, a_0 [Å]		6.7014(2)	6.701(6)
Cell volume [Å^3]		300.95	300.90
Formula units per cell, *Z*		4	4
Molar mass [g/mol]		591.5	591.5
Calculated density, ρ_{calc} [g/cm^3]		13.055	13.058
Refined parameters (structural, profile)		4, 6	n/a
Profile function		pseudo-Voigt	n/a
R_B, R_P, R_{WP} [%]		1.64, 1.95, 2.68	5.35, n/a
χ^2		1.13	n/a
Hf:	Wyck. pos. 12*a*	3/8, 0, 1/4	3/8, 0, 1/4
	B_{iso} [Å^2]	0.25(1)	n/a
N:	Wyck. pos. 16*c* (*x*, *x*, *x*)	*x* = 0.0616(6)	*x* = 0.063(3)
	B_{iso} [Å^2]	0.33(15)	n/a
Cation-anion distances [Å]		4 × 2.170(4)	4 × 2.17(2)
		4 × 2.486(4)	4 × 2.47(2)

The obtained structural parameters of cubic hafnium(IV) nitride are summarized in Table 3.5 and compared with those reported for c-Hf_3N_4 prepared in a LH-DAC. The lattice parameter a_0 = 6.7014(2) Å of c-Hf_3N_4 synthesized in a multi-anvil apparatus is in excellent agreement

* T. Locherer (personal communication, June, 2008)

with the value a_0 = 6.701(6) Å reported for c-Hf_3N_4 obtained via a reaction of elements in a LH-DAC (Zerr et al. 2003). Accordingly, if the lattice parameter is dependent on the amount of oxygen incorporated in c-M_3N_4 as was found for c-$Zr_{2.86}(N_{0.88}O_{0.12})_4$ (s. Chapter 3.3.2.1) and supported by calculations (Lowther 2008), cubic hafnium(IV) nitride synthesised in the present work (H1-01) appears to be oxygen-poor.

Results of the presented Rietveld structure refinement were also used to estimate the phase content of the H1-01 product: c-Hf_3N_4, γ-Hf_2N_2O and oI-HfO_2 should constitute about 83.7(4), 8.6(3) and 7.7(2) wt.% of the total material amount, respectively. According to this result, the average oxygen content in the H1-01 was estimated to be 1.5 wt.% which is in a reasonable agreement with the average composition measured by EPMA. This result also supports the above assumption on a negligible oxygen contamination of c-Hf_3N_4.

3.3.3 Raman spectroscopy of oxygen-bearing c-Zr_3N_4.

In addition to the XRD examination, the Raman spectrum of c-$Zr_{2.86}(N_{0.88}O_{0.12})_4$ was measured and compared with that of c-Zr_3N_4 synthesised from elements in a LH-DAC (Zerr et al. 2003) (Figure 3.9). In contrast to the LH-DAC material, the spectrum of c-$Zr_{2.86}(N_{0.88}O_{0.12})_4$ from the multi-anvil synthesis is not strongly dominated by only one Raman line at 323 cm^{-1}: in addition to the line at 161 cm^{-1}, five Raman lines at 136, 366, 403, 514, and 668 cm^{-1} can be clearly identified. The factor group analysis for the Th_3P_4-type structure (space group $I\bar{4}3d$ or T_d^6) yields the following symmetry species of vibrational modes: $\Gamma = A_1 + 2A_2 + 3E + 5T_1 + 5T_2$ (Karavaev & Khrapov 1975; Provenzano et al. 1977). Nine of them ($A_1 + 3E + 5T_2$) are Raman-active and five ($5T_2$) are also IR-active. Therefore all seven lines observed for the material from the multi-anvil synthesis are attributed to those of c-$Zr_{2.86}(N_{0.88}O_{0.12})_4$, including the line at 403 cm^{-1} not detected for c-Zr_3N_4. Observation of the additional line for the material from the multi-anvil synthesis could be attributed to the partial substitution of nitrogen by oxygen on the anion sites of c-Zr_3N_4 and to the presence of cation vacancies. The frequency differences (Table 3.6) could be caused by the shift of the Raman bands of the sample from the LH-DAC to lower frequencies because it could have been heated to higher temperatures by the absorbed radiation of the Ar-laser used to excite the Raman spectra. A higher temperature of the sample from the LH-DAC synthesis, compared with that from multi-anvil synthesis, could be a result of a significantly lower sample volume.

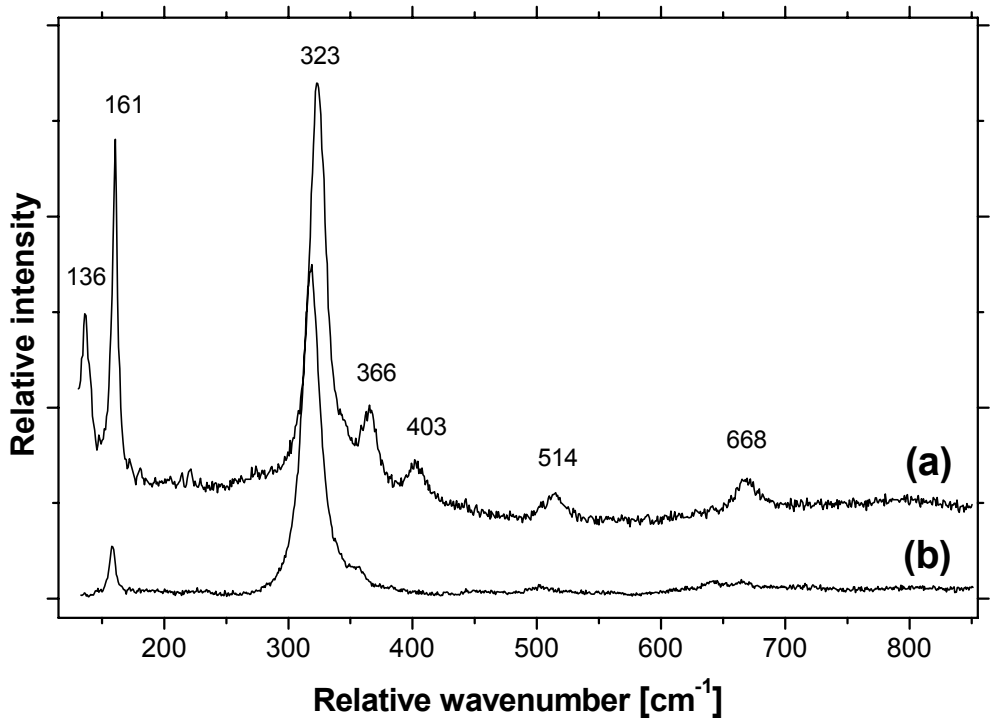

Figure 3.9. Raman spectra of c-$Zr_{2.86}(N_{0.88}O_{0.12})_4$ synthesized in this work using a multi-anvil apparatus (a) and of c-Zr_3N_4 synthesized in the earlier work (Zerr et al. 2003) using a LH-DAC (b). Both spectra were measured at ambient pressure.

The Raman shifts of c-$Zr_{2.86}(N_{0.88}O_{0.12})_4$ and c-Zr_3N_4 measured at ambient pressure are listed in Table 3.6 along with other available experimental (Zerr et al. 2003; Chhowalla & Unalan 2005) and theoretical (Kroll 2003) values for c-Zr_3N_4. The Raman shifts reported by Zerr et al. (2003) and Chhowalla & Unalan (2005) exhibit higher frequencies due to compressive stresses present in the investigated samples. After analysis of the available data for Th_3P_4-type compounds, Zerr et al. (2003) suggested that the dominant Raman band (323 and 318 cm^{-1} for c-$Zr_{2.86}(N_{0.88}O_{0.12})_4$ and c-Zr_3N_4, respectively) could be assigned to the T_2 mode. A reliable assignment of the other observed Raman bands to the symmetry species is only possible by single-crystal polarization studies. However, a single crystal of c-$Zr_{2.86}(N_{0.88}O_{0.12})_4$ with the size sufficient for such measurements was not found in the sample Z2-01. Assignment of the Raman-active lattice vibration modes of c-Zr_3N_4 and calculation of their frequencies, which are in a reasonable agreement with the present data (Table 3.6), were reported in the theoretical work of Kroll (2003).

Table 3.6. Raman shifts [cm^{-1}] of c-$Zr_{2.86}(N_{0.88}O_{0.12})_4$ (Z2-01) synthesised in the present work in a multi-anvil apparatus and of c-Zr_3N_4 synthesised earlier using a LH-DAC in comparison with other reported experimental values. Suggested assignment of the Raman-active vibrational modes of c-Zr_3N_4 and their calculated frequencies after Kroll (2003) are given for reference.

c-$Zr_{2.86}(N_{0.88}O_{0.12})_4$ [a]	c-Zr_3N_4			
1 atm	1 atm[a]	16 GPa[b]	≈ 9 GPa (film)[c]	Theoretical values[d]
136		163	165	142 (T_2)
161	158	196	195	165 (E)
				282 (T_2)
				336 (A_1)
323	318	387	387	368 (T_2)
366	356	416	415	423 (T_2)
403				
514	504	551	550	506 (T_2)
	641			609 (E)
668	665	707	710	670 (E)

[a] This work.
[b] (Zerr et al. 2003).
[c] (Chhowalla & Unalan 2005).
[d] (Kroll 2003).

3.3.4 Thermodynamics of c-$Zr_{2.86}(N_{0.88}O_{0.12})_4$

In the original experiments with a LH-DAC, c-Zr_3N_4 was obtained at high pressures (above 15.6 GPa) and high temperatures (above 2500 K) via chemical reaction of pure Zr-metal or δ-ZrN with condensed nitrogen (Zerr et al. 2003). This result unambiguously showed that c-Zr_3N_4 free of oxygen contamination exists. In contrast to these earlier experiments, results of the present work indicated that up to 12 % of nitrogen anions in c-Zr_3N_4 can be substituted by oxygen without a significant alteration of the crystal structure. Based on the existing theoretical and experimental data for the Zr-N-O system, possible influence of oxygen incorporation in the structure of c-Zr_3N_4 on the energetics of this high-pressure modification is discussed below.

As was mentioned in the introduction, two phases α and β are in equilibrium if their Gibbs free energies are equal. For a constant temperature (e.g. room temperature, RT) one can write

the Gibbs free energy as $\mathbf{G} = \mathbf{G}_0 + \int V dP$, where $\mathbf{G}_0$ is the energy at pressure $P = 0$ and $V(P)$ is the volume at the particular pressure. For a phase transition ($\alpha \rightarrow \beta$) at RT holds:

$$\Delta\mathbf{G}_{0,\alpha\beta} = -\int_0^{P_{tr}} \Delta V_{\alpha\beta} dP .$$

If the bulk moduli of the considered phases are significantly higher than the pressure of the phase transition, then ΔV is nearly independent of pressure and can be considered in the first approximation as constant. Accordingly, $\Delta\mathbf{G}_{0,\alpha\beta} = -\Delta V_{\alpha\beta} \int dP = -\Delta V_{\alpha\beta} P_{tr}$. Hence, the transition pressure can be estimated from the expression $P_{tr} = -\Delta\mathbf{G}_{0,\alpha\beta} / \Delta V_{\alpha\beta}$. From thermodynamic considerations follows that the entropy difference that contributes to $\Delta\mathbf{G}_{0,\alpha\beta}$ for solid state crystal structures is at moderate temperatures (as the case for RT) typically very small. Thus $\Delta\mathbf{G}$ in the above equation for transition pressure at RT can be replaced by the enthalpy of transformation, $\Delta\mathbf{H}$, at RT (298 K). Taking into account the above assumptions, the pressure of the $\alpha \rightarrow \beta$ phase transition can be derived as

$$P_{tr} = -\left[\, \Delta\mathbf{H}_f^{298}(\beta) - \Delta\mathbf{H}_f^{298}(\alpha) \,\right] / \left[\, V_\beta - V_\alpha \,\right],$$

where $\Delta\mathbf{H}_f^{298}$ is the standard enthalpy of formation and V is the molar volume of the corresponding phase at 298 K.

At ambient conditions the Zr-N-O system can by represented by a mixture of the thermodynamically stable orthorhombic zirconium(IV) nitride, o-Zr_3N_4, and monoclinic zirconium dioxide, m-ZrO_2, further denoted by “o” and “m”, respectively. Transformation of this mixture to the oxygen-bearing cubic zirconium(IV) nitride, c-$Zr_{3-u}(N_{1-u}O_u)_4$, can be expressed by the following equation normalized to one mol of Zr:

$$w\,\mathrm{ZrN}_{4/3}\,(\mathrm{o}) + [1-w]\,\mathrm{ZrO}_2\,(\mathrm{m}) \xrightarrow{P} \mathrm{ZrN}_{4w/3}\mathrm{O}_{2-2w}\,(\mathrm{c})$$

Since for c-$Zr_{2.86}(N_{0.88}O_{0.12})_4$ synthesized in the present work 5 GPa < P_{tr} < 12 GPa (s. Chapter 3.2), V_c = 16.2 cm^3/(mol of Zr) and V_{o+m} = 21.21 - 3.88w = 17.65 cm^3/(mol of Zr), the enthalpy of the “o + m → c” transformation is estimated to be between 7.25 and 17.4 kJ/(mol of Zr) (Figure 3.10). On the other hand the enthalpy of “o → c” transformation for pure Zr_3N_4 is calculated to be $\Delta\mathbf{H}$ = 10.84 kJ/(mol of Zr) (Kroll 2004), which is also between the above estimated limits for c-$Zr_{2.86}(N_{0.88}O_{0.12})_4$. Thus, the above estimation does not provide unambiguous information about stability of c-$Zr_{3-u}(N_{1-u}O_u)_4$ with respect to the mixture of the low-pressure modifications (Figure 3.10).

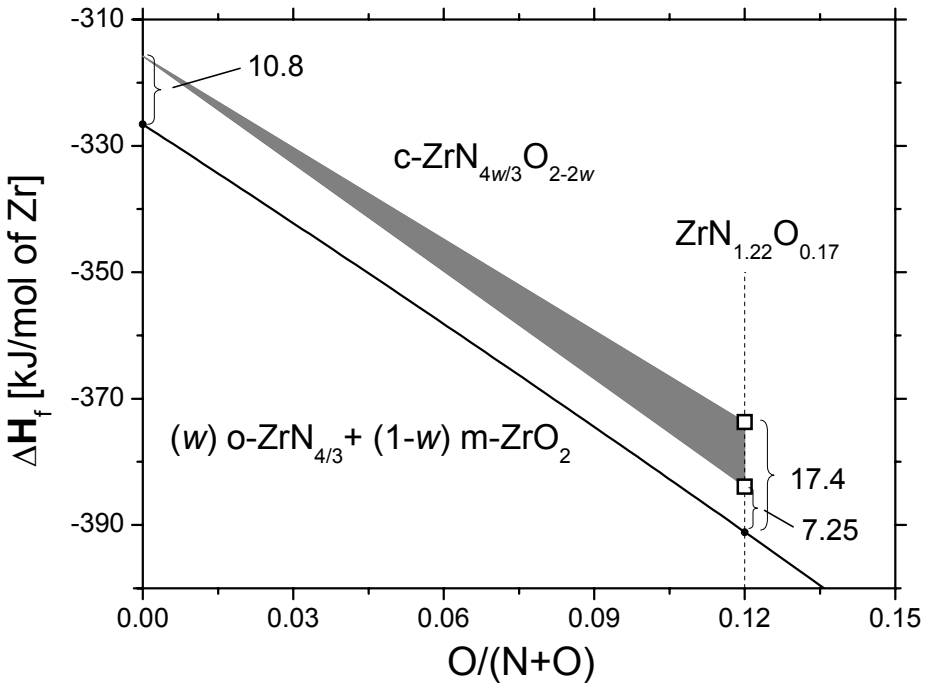

Figure 3.10. The enthalpy of formation, $\Delta\mathbf{H}_f^{298}$, of the high-pressure c-$ZrN_{3w/4}O_{2-2w}$ as a function of oxygen content, O/(O+N) = 3(1-*w*)/(3-*w*) (grey area). The estimated maximum and minimum $\Delta\mathbf{H}_f^{298}$ for c-$Zr_{2.86}(N_{0.88}O_{0.12})_4$ ($w \approx 0.92$) are denoted by squares. The enthalpy of formation of the mixture (*w*) o-$ZrN_{4/3}$ + (1-*w*) m-ZrO_2 stable at ambient pressure is given for reference (solid line). The enthalpy of the "o → c" transformation for Zr_3N_4 (Kroll 2004) and the estimated upper and lower limits for the enthalpy of the "o + m → c" transformation for $Zr_{2.86}(N_{0.88}O_{0.12})_4$ (this work) are given by numbers.

However, the obtained values can be further used for estimation of the higher and the lower limits for the standard enthalpy of formation of c-$Zr_{2.86}(N_{0.88}O_{0.12})_4$ using the known values of $\Delta\mathbf{H}_f^{298}$ for o-Zr_3N_4 and m-ZrO_2 (Table 3.7). The dependence of the "starting" mixture enthalpy on the O-content can be modelled by the equation: $\Delta\mathbf{H}_f^{298}(\text{o} + \text{m}) = -1100.6 + 774w$, which provides -391.1 kJ/(mol of Zr) for the composition of interest ($w = 0.92$). Since the enthalpy difference between the low and high pressure states is known, $\Delta\mathbf{H}_f^{298}(\text{c-}Zr_{2.86}(N_{0.88}O_{0.12})_4)$ can be found to be between -373.7 and -383.9 kJ/(mol of Zr) (Figure 3.10). It is worth mentioning that the estimated enthalpy of formation of c-$Zr_{2.86}(N_{0.88}O_{0.12})_4$ is more exothermic than that of pure c-Zr_3N_4 and even of the low-pressure o-Zr_3N_4 (Table 3.7). Accordingly, the substitution of 12 % of nitrogen by oxygen in c-Zr_3N_4 results in a stronger enthalpy change (decrease) than the enthalpy change (increase) due to the phase transition from orthorhombic to cubic phase. A detailed investigation of thermodynamic stability of c-Zr_3N_4 (as well as of c-Hf_3N_4) with respect to the oxygen incorporation could be a subject of the future experimental and theoretical work.

Table 3.7. The enthalpies of formation ($\Delta\mathbf{H}_f^{298}$), densities (ρ), molar masses (M_m), and molar volumes ($V_m = M_m / \rho$) of o-Zr_3N_4, c-Zr_3N_4, m-ZrO_2 and c-$Zr_{2.86}(N_{0.88}O_{0.12})_4$. The values are normalized to one mole of Zr.

	$\Delta\mathbf{H}_f^{298}$ [kJ/mol of Zr]	ρ [g/cm^3]	M_m [g/mol of Zr]	V_m [cm^3/mol of Zr]
o-Zr_3N_4	-326.6[a]	6.341	109.90	17.33
c-Zr_3N_4	-315.8[b]	7.159	109.90	15.35
m-ZrO_2	-1100.6[c]	5.809	123.22	21.21
c-$Zr_{2.86}(N_{0.88}O_{0.12})_4$	-383.9… -373.7[d]	6.85[e]	111.01[e]	16.2[e]

[a] (Molodetsky et al. 2000).
[b] (Kroll 2004).
[c] (Lide 2005).
[d] Estimated from 5 GPa <P_{tr} < 12 GPa.
[e] Experimental values obtained in the present work.

3.3.5 Microstructure

The microstructure of oxygen-bearing c-Zr_3N_4 (sample Z2-01) and of hafnium nitride samples (H1-01 – H1-04) was studied using SEM equipped with an EDX detector. The SEM/EDX investigation of a polished surface of Z2-01 revealed the presence of a chemically homogeneous, highly porous material with pore sizes ranging from about 0.05 to 2 μm (Figure 3.11a). The average volume fraction porosity (VFP) was estimated to be between 0.25 and 0.3. Crystallites of the c-Zr_3N_4 of about 0.8 μm in size could also be observed on pore walls (Figure 3.11b).

Similar to oxygen-bearing c-Zr_3N_4, SEM investigation of a polished surface of H1-01 revealed a highly porous material with pore sizes from 0.05 to 2 μm (Figure 3.12a). The average VFP was estimated to be about 0.27. Additionally a few areas of higher density (VFP < 0.1) were observed (Figure 3.12b). In contrast to the homogeneous Z2-01, on the majority of the H1-01 sample surface two phases could be distinguished (Figure 3.12c). The major phase is light-grey in appearance and highly porous, while the "islands" of the darker phase have a few small (< 50 nm) or no pores at all. Because of a nonuniform and texturally fine distribution of the dark phase within the sample, it was difficult to estimate its average volume fraction.

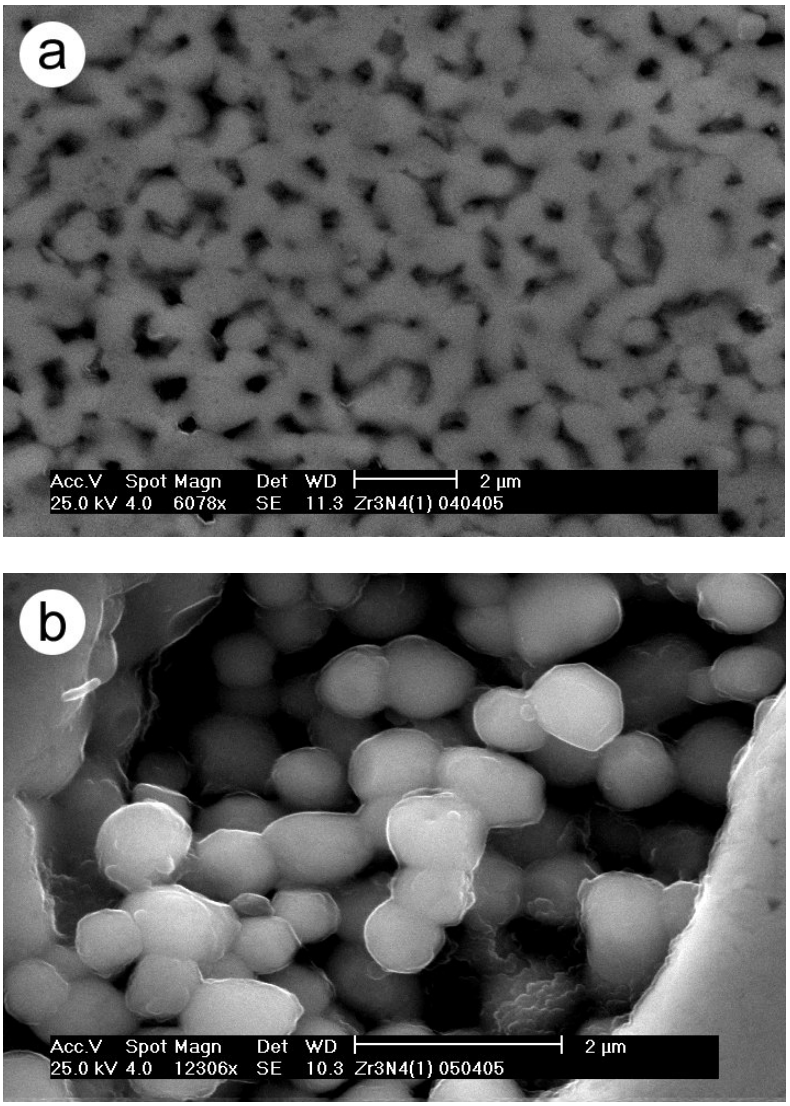

Figure 3.11. SEM pictures of c-$Zr_{2.86}(N_{0.88}O_{0.12})_4$ (sample Z2-01) synthesized in the present work in a multi-anvil high-pressure apparatus: (a) image of the polished sample surface showing highly porous material; (b) crystallites of c-$Zr_{2.86}(N_{0.88}O_{0.12})_4$ observed on pore walls.

Semi-quantitative EDX analysis of both phases revealed a significantly higher oxygen and lower nitrogen content in the dark phase when compared with those in the light phase. This was also visible from the element distributions of nitrogen and oxygen measured on the sample surface using the EDX detector (Figure 3.13). Thus, the light phase was identified as c-Hf_3N_4, while the darker phase – as the oxidic phase detected in the powder XRD experiments (s. Chapter 3.3.2.2). Additionally, crystallites up to 1 µm in size were observed on the pore walls (Figure 3.12d). The chemical composition of the crystallites was found to be similar to that of the light phase. Therefore, they were attributed to c-Hf_3N_4.

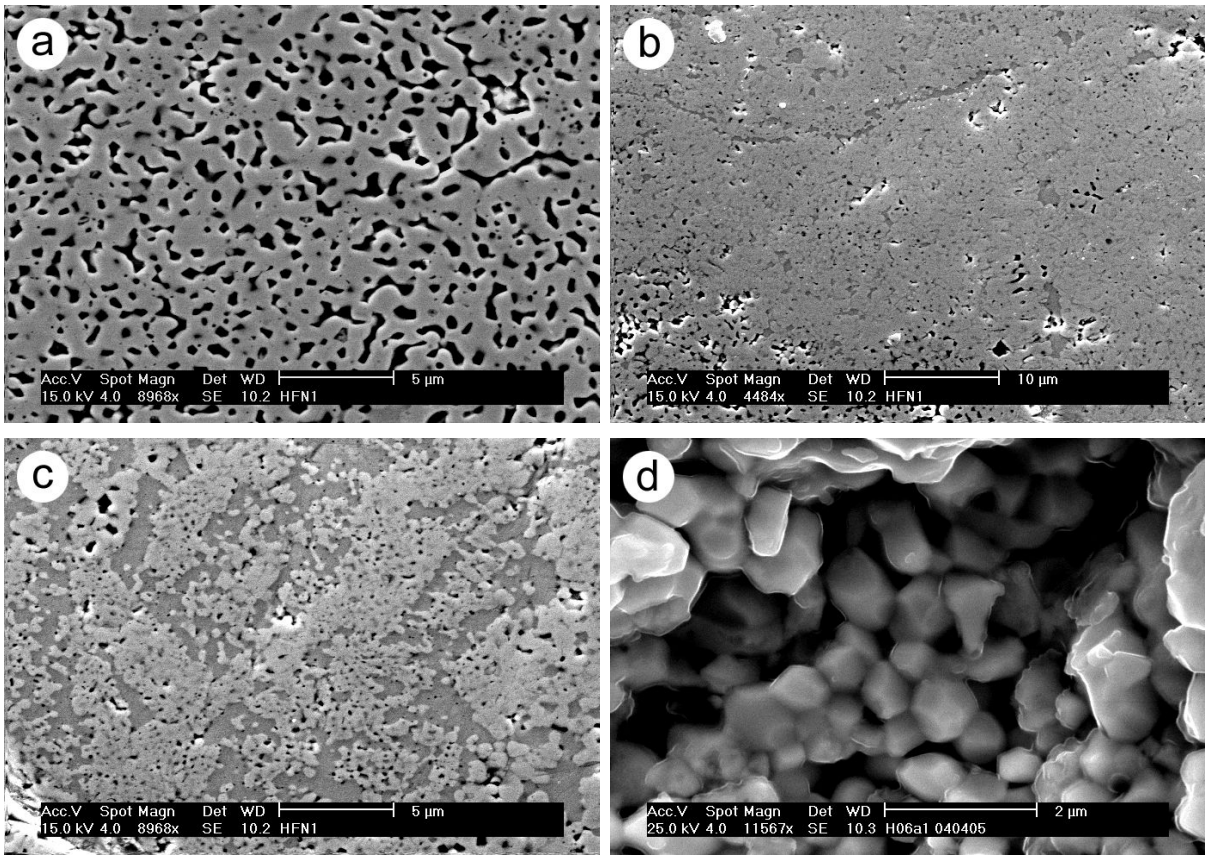

Figure 3.12. SEM pictures of hafnium nitride sample (H1-01) synthesized in the present work using a multi-anvil high-pressure apparatus: (a) porous sample surface; (b) dense sample surface; (c) light-grey c-Hf_3N_4 together with contaminating darker oxidic phase (s. text); (d) crystallites of c-Hf_3N_4 observed on pore walls.

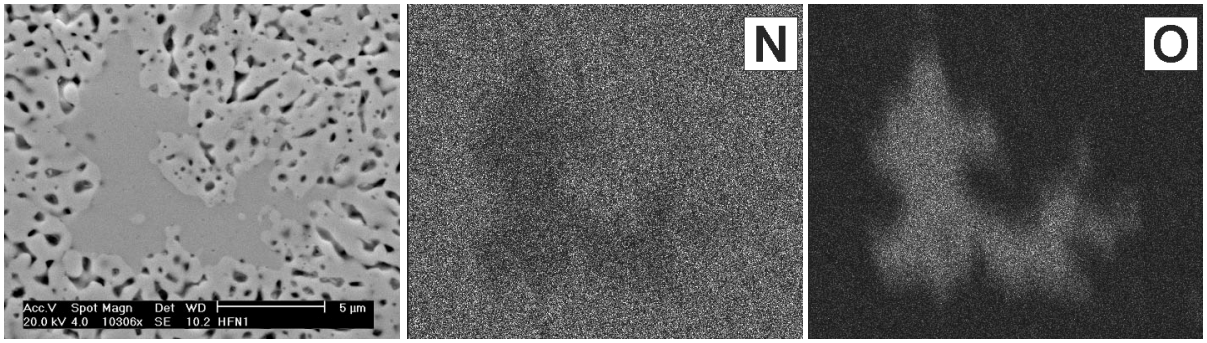

Figure 3.13. SEM picture of the surface of the hafnium nitride sample, H1-01, showing the presence of two phases of different colours (a) and corresponding element mappings of nitrogen (b) and oxygen (c) collected using the EDX detector. The intensity scale on the mappings is normalized to the maximum content of each element.

It should also be mentioned that, similar to XRD measurements, SEM/EDX examination of the other hafnium nitride samples (H1-02 – H1-04) revealed the presence of comparable amounts of the oxidic phase. Thus, application of the doubled Pt/Mo-encapsulation did not significantly reduce the oxygen diffusion from the surrounding oxide pressure medium into the sample volume during HP-HT synthesis. Most likely, the Mo/Pt-encapsulation alone doesn't work as a good oxygen-diffusion barrier, and an additional encapsulation (e.g. h-BN) is required.

An interesting feature of all investigated high pressure products is their high volume fraction porosity (VFP) up to 0.3. A possible explanation of such a high porosity is that after reduction of the specific volume due to the transition to dense and hard c-M_3N_4 phase the material did not deform plastically and thus can not be sintered even under the extreme conditions of high pressures and temperatures. Moreover, release of the nitrogen excess (about 2.7 wt.% for zirconium nitride and 2.5 wt.% for hafnium nitride) during the transformation of the starting M_3N_{4+x} powders into c-M_3N_4 at high pressures and high temperatures may have also contributed to the pore formation. In the case of hafnium nitride, the contaminating oxidic material filled pores between the c-Hf_3N_4 crystals thus forming regions with a low VFP (Figure 3.12c). This suggests a method for fabrication of dense sintered c-M_3N_4 bodies by employing appropriate oxidic sintering additives.

It is well known that porosity can significantly alter various physical properties of materials (Rice 1998). In particular, it can decrease the material hardness and effective elastic moduli. Therefore, the influence of porosity on hardness and elastic properties of oxygen-bearing c-Zr_3N_4, investigated in the present work, is taken into account in the following chapters.

3.4 Elasto-mechanical properties

In the original work on the synthesis of c-Zr_3N_4 and c-Hf_3N_4 in a LH-DAC, preliminary compressibility measurements revealed high bulk moduli of about 250 GPa which allowed to suggest high hardness for these two materials (Zerr et al. 2003). The subsequent study of the mechanical properties of deposited c-Zr_3N_4 films showed that their nanoindentation hardness (36 GPa) exceeds significantly that of δ-ZrN (27 GPa) prepared by the same deposition technique (Chhowalla & Unalan 2005). Moreover, it was found that c-Zr_3N_4 exhibits an exceptional wear resistance by milling of a low-carbon steel: it outperformed by almost one order of magnitude the wear resistance of δ-TiN. Several theoretical studies have also predicted high bulk moduli of c-Zr_3N_4 and c-Hf_3N_4 in the range of 195-283 GPa and Vickers hardness of about 20 GPa (Kroll 2003; Mattesini et al. 2003; Lowther 2005), indicating that both high-pressure nitrides can be of interest for applications as hard wear resistant materials. This is why elasto-mechanical properties of c-Zr_3N_4 and c-Hf_3N_4, important for potential industrial uses, were studied in detail in the present work.

In the following chapter compressibility measurements and determination of the bulk moduli, B_0, of oxygen-bearing c-Zr_3N_4 and of pure c-Hf_3N_4 are presented. Further, Vickers hardness and indentation fracture toughness of c-$Zr_{2.86}(N_{0.88}O_{0.12})_4$ (Z2-01) were obtained (Chapter 3.4.2). Additionally, hardness and reduced elastic modulus, E_r, of oxygen-bearing cubic zirconium(IV) nitride were measured using nanoindentation technique (Chapter 3.4.3). Finally, the shear modulus, the Young's modulus and the Poisson's ratio of c-$Zr_{2.86}(N_{0.88}O_{0.12})_4$ were estimated using experimental values for B_0 and E_r, exclusively (Chapter 3.4.4).

3.4.1 Compressibility measurement

In the present work the first accurate experimental data on the bulk moduli, B_0, and their first pressure derivatives, B_0', for both oxygen-bearing c-Zr_3N_4 and pure c-Hf_3N_4 were obtained. The values were derived from the pressure dependences of specific volumes of high-pressure nitrides, $V(P)$, measured up to about 45 GPa. Measurements were performed under quasi-hydrostatic load conditions in a diamond anvil cell (DAC) using energy dispersive powder X-ray diffraction (ED-XRD) combined with synchrotron radiation (s. Chapter 2.4.1).

3.4.1.1 Oxygen-bearing c-Zr_3N_4

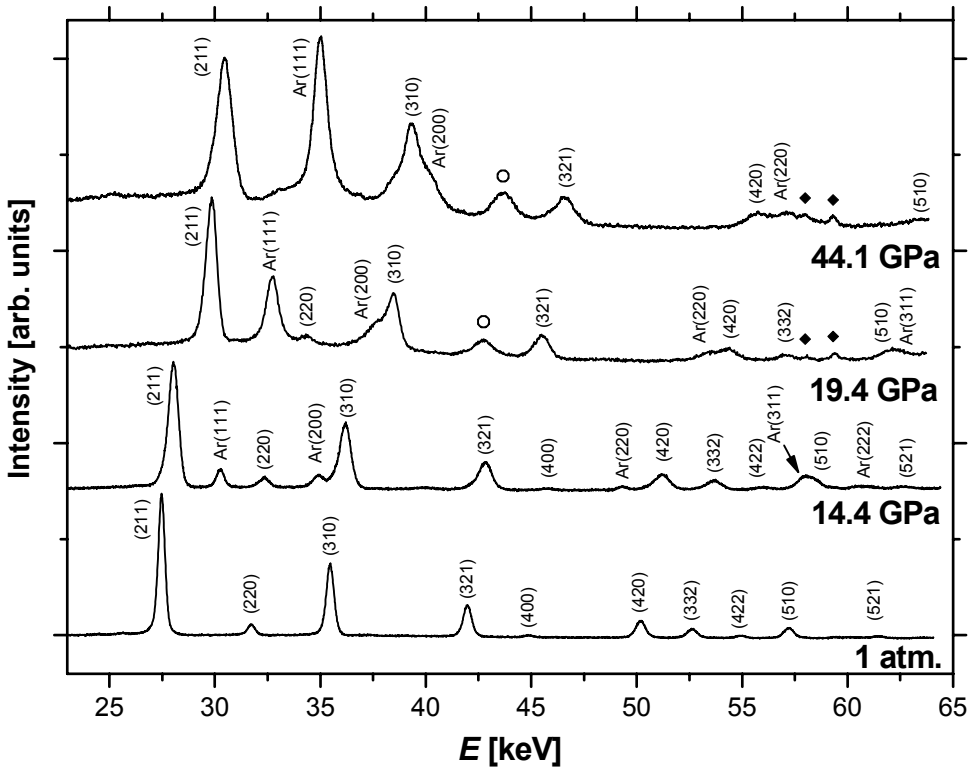

Figure 3.14. ED-XRD patterns of c-$Zr_{2.86}(N_{0.88}O_{0.12})_4$ alone at ambient pressure and embedded in the solid argon pressure medium at high pressures of 14.4, 19.4 and 44.1 GPa. The first two patterns were measured at the diffraction angle of $2\theta = 9.38°$ and the last two at $2\theta = 8.87°$. $K_{\alpha 2}$- and $K_{\alpha 1}$-fluorescence peaks of tungsten (the slits material) at 57.98 and 59.32 keV (♦) were observed at lower diffraction angles. A broad peak indicated by (○) is due to the diffraction from steel, the gasket material. The (400) diffraction peak of c-$Zr_{2.86}(N_{0.88}O_{0.12})_4$ was not observable at high pressures due to the texture.

For the compressibility measurements of c-$Zr_{2.86}(N_{0.88}O_{0.12})_4$ a thin pellet of the sample powder obtained in the experiment Z2-01 was compressed in a DAC. *In situ* high-pressure ED-XRD patterns were collected using a polychromatic synchrotron radiation (s. Chapter 2.3.1.2). At ambient and at high pressures up to ten diffraction peaks for c-$Zr_{2.86}(N_{0.88}O_{0.12})_4$, namely (211), (220), (310), (321), (400), (420), (332), (422), (510) and (521), were observed. For crystalline argon, served as a quasi-hydrostatic pressure transmitting medium, up to five peaks, (111), (200), (220), (311) and (222), were detected. On compression, the intensities of the diffraction peaks of both argon and investigated material were affected by texture. Figure 3.14 shows the ED-XRD patterns measured at ambient conditions and at 14.4 GPa at the diffraction angle $2\theta = 9.38°$ as well as patterns measured at pressures of 19.4 and 44.1 GPa at the diffraction angle $2\theta = 8.87°$. In the ED-XRD patterns measured at lower diffraction angle

the $K_{\alpha 2}$- and $K_{\alpha 1}$-fluorescence peaks of tungsten (the slits material) at 57.98 and 59.32 keV were also observed. A broad peak at about 43 keV was due to the diffraction from the gasket material.

The average specific volumes of c-$Zr_{2.86}(N_{0.88}O_{0.12})_4$ and of argon at each pressure were derived from the lattice parameters calculated for each diffraction peak. By calculation of the specific volumes, the diffraction peaks of c-$Zr_{2.86}(N_{0.88}O_{0.12})_4$ and of argon overlapping on increasing pressure with each other or with the X-ray fluorescence peaks were discarded from consideration. The lattice parameters a_0 of c-$Zr_{2.86}(N_{0.88}O_{0.12})_4$ at ambient conditions was found to be 6.759(6) Å, which is in good agreement with $a_0 = 6.7549$ Å derived by Rietveld structure refinement (Chapter 3.3.2.1). Accordingly, the former value was used for the calculations to determine the ratios V/V_0, where V and V_0 are the specific volumes of c-$Zr_{2.86}(N_{0.88}O_{0.12})_4$ at high and ambient pressure, respectively.

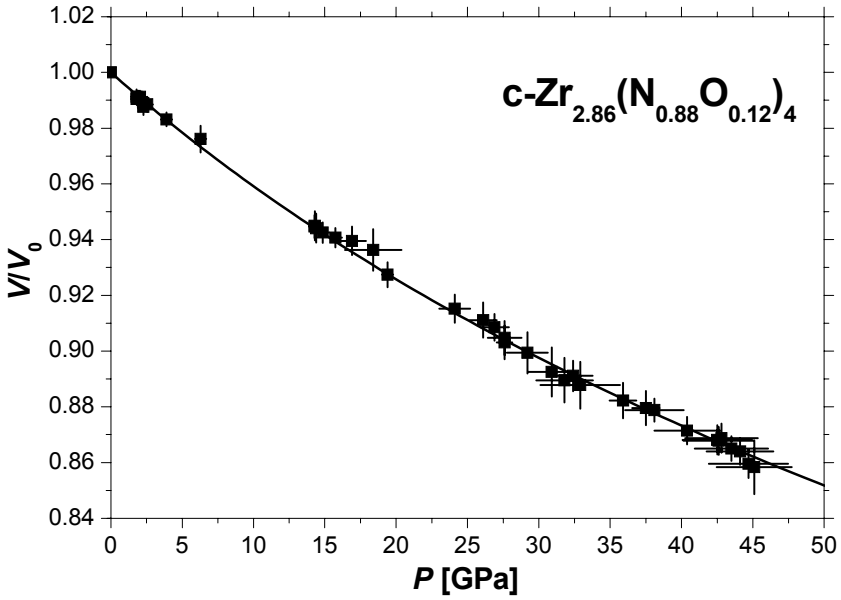

Figure 3.15. Pressure dependence of V/V_0 of c-$Zr_{2.86}(N_{0.88}O_{0.12})_4$ measured on compression at room temperature to 45 GPa. The experimental data are shown by solid squares. The solid line represents the least-squares fit of the third-order BM-EOS to the experimental data. The fit yielded $B_0 = 219(13)$ GPa and $B_0' = 4.4(1.0)$.

The results of the compression measurements for c-$Zr_{2.86}(N_{0.88}O_{0.12})_4$ are shown in Figure 3.15. As the uncertainty in the V/V_0-ratios, the maximum difference among all observed diffraction peaks was chosen. Similarly, the pressure uncertainties correspond to the maximum difference in the pressure values calculated for each diffraction peak of argon. This was necessary because argon exhibits a significant elastic anisotropy on compression (Zerr et

al. 1993). A small change of the specific volume by about 14 % at the maximum pressure of 45 GPa indicated a high bulk modulus of c-$Zr_{2.86}(N_{0.88}O_{0.12})_4$. From the least-squares fit of the third-order Birch-Murnaghan equation of state (s. Chapter 1.2.1.1) to the experimental data we obtained the bulk modulus $B_0 = 219(13)$ GPa and its first pressure derivative $B_0' = 4.4(1.0)$ for c-$Zr_{2.86}(N_{0.88}O_{0.12})_4$. In Figure 3.15 the result of the fit is represented by a solid line. For the second-order Birch-Murnaghan EOS, with B_0' fixed at 4, $B_0 = 224(5)$ GPa was obtained. This experimental value is about 10 % lower than the previously reported $B_0 \approx 250$ GPa ($B_0' = 4$ fixed) for pure c-Zr_3N_4 (Zerr et al. 2003). Such decrease of B_0 for the oxygen-bearing zirconium(IV) nitride could have been caused by the substitution of nitrogen with oxygen leading to a weakening of the cation-anion bonding (Lowther 2008). The theoretical predictions for B_0 of c-Zr_3N_4 (195-265 GPa) (Kroll 2003; Mattesini et al. 2003; Lowther 2005) scatter around the present value (Table 3.8).

In Figure 3.16 the experimental data and both fit results are shown on the $F(f)$-plot, where F is the normalized pressure and f is the Eulerian strain (s. Chapter 1.2.1.1). The third- and second-order Birch-Murnaghan EOSs are presented here by straight solid and dashed lines, respectively. The intercept of the line with the F-axis yields B_0 and the slope corresponds to B_0'. This form of representation is, in contrast to the $V(P)$ plot in Figure 3.15, very sensitive to the experimental uncertainties. It can be clearly recognised in Figure 3.16 that all experimental data points agree, within the experimental uncertainties, with both fit results.

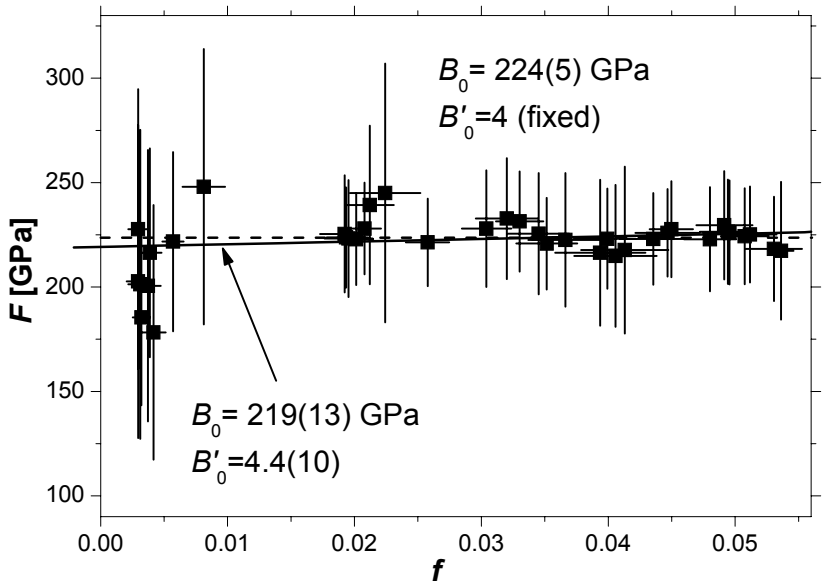

Figure 3.16. Compression data of c-$Zr_{2.86}(N_{0.88}O_{0.12})_4$ in terms of normalized pressure, F, and Eulerian strain, f. This form of representation is very sensitive to experimental uncertainties. Fits to the third- and second-order BM-EOS are represented by solid and dashed lines, respectively.

Table 3.8. Experimental and theoretical values of bulk modulus and its first pressure derivative for c-$Zr_{2.86}(N_{0.88}O_{0.12})_4$, c-$Zr_3(N,O)_4$, c-$Zr_3N_4$, δ-ZrN, c-$Hf_3N_4$, δ-HfN. Typical experimental bulk moduli of c-Si_3N_4, c-BN and diamond are given for comparison.

Phase	B_0 [GPa]	B_0'	Ref.
c-$Zr_{2.86}(N_{0.88}O_{0.12})_4$	219(13)	4.4(1.0)	This work
	224(5)	4-fixed	This work
c-$Zr_3N_{3.75}O_{0.25}$	241[a]	6.56	(Lowther 2008)
c-$Zr_3(N_{0.875}O_{0.125})_4$	227[a]	7.05	(Lowther 2008)
c-Zr_3N_4	≈ 250	4-fixed	(Zerr et al. 2003)
	265[a], 195[b]		(Kroll 2003)
	262[a], 218[b]		(Mattesini et al. 2003)
	251[a]	6.75	(Lowther 2005)
δ-ZrN	248	4-fixed	(Chen et al. 2005)
	285[a]		(Chen et al. 2005)
c-Hf_3N_4	227(7)	5.3(6)	This work
	241(2)	4-fixed	This work
	≈ 260	4-fixed	(Zerr et al. 2003)
	283[a], 215[b]		(Kroll 2003)
	276[a], 228[b]		(Mattesini et al. 2003)
	268[a]	6.56	(Lowther 2005)
δ-HfN	260	4-fixed	(Chen et al. 2005)
	306[a]		(Chen et al. 2005)
	313[a], 270[b]		(Kroll 2003)
c-Si_3N_4	290	4.9	(Zerr et al. 2002a)
	302	4-fixed	(Zerr et al. 2002a)
c-BN	369-382		(Brazhkin et al. 2002)
C_d (diamond)	433-442		(Brazhkin et al. 2002)

[a] Theoretical bulk modulus calculated employing the local density approximation (LDA).
[b] Theoretical bulk modulus calculated employing the generalized gradient approximation (GGA).

3.4.1.2 c-Hf_3N_4

For the compressibility studies of c-Hf_3N_4, the sample material was synthesised in a LH-DAC via a chemical reaction of hafnium mononitride with molecular nitrogen at high pressures and temperatures* in accordance with the earlier work (Zerr et al. 2003). Synthesis was performed using the equipment of the Hochdruckgruppe (leader - Dr. R. Boehler), Max-Planck-Institut für Chemie, Mainz. A platelet of the compacted mononitride powder (δ-HfN, 99 %, Chempur), isolated from the lower diamond anvil by a thin layer of NaCl, was embedded in the nitrogen pressure medium, squeezed to about 19 GPa and heated up to 2850 K with the radiation of a Nd:YLF laser. After synthesis the polycrystalline sample of c-Hf_3N_4 was recovered from the DAC, washed by dissolving NaCl in bi-distilled water, and loaded again in a DAC for compression measurements.

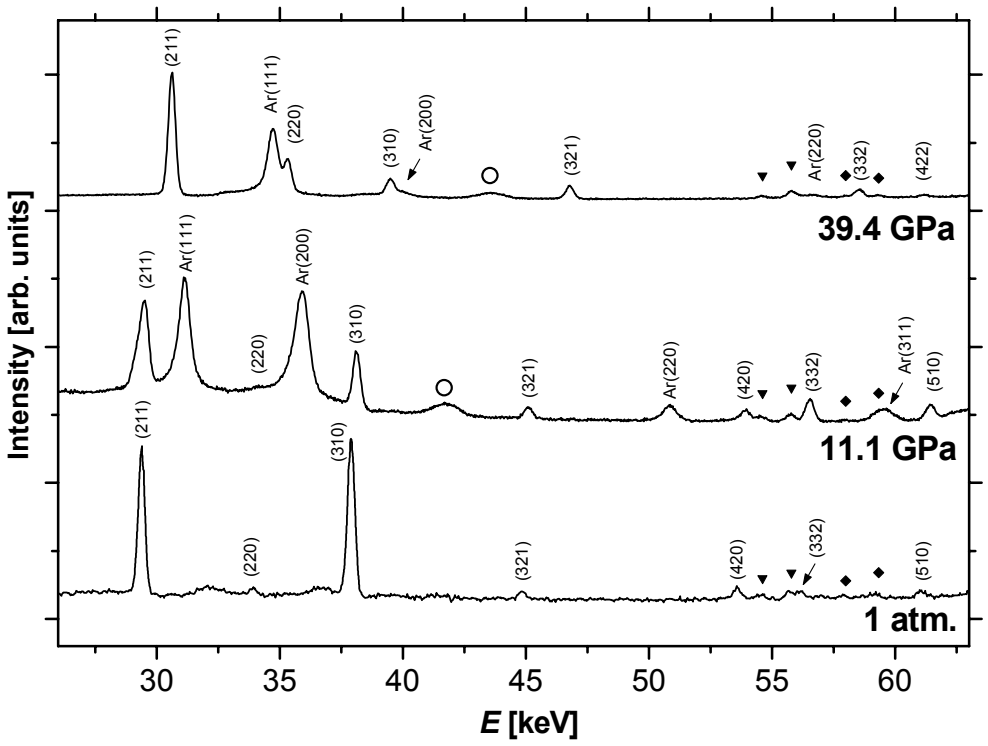

Figure 3.17. ED-XRD-patterns of c-Hf_3N_4 and of the solid argon pressure medium measured at 11.1 GPa (at the diffraction angle of 8.92°), at 39.4 GPa ($2\theta = 8.85°$). The lower pattern was obtained only for the sample material at ambient conditions ($2\theta = 8.85°$). $K_{\alpha 2}$ - and $K_{\alpha 1}$-fluorescence peaks of hafnium at 54.61 and 55.79 keV (▼) and of tungsten (the detector slits material) at 57.98 and 59.32 keV (♦) were observed in all patterns. A broad peak (○) is due to the diffraction from steel, the gasket material. The (400) diffraction peak of c-Hf_3N_4 was not observable due to the texture.

* The material was kindly provided by Dr. Andreas Zerr

The c-Hf_3N_4 compressibility studies were carried out in a similar way as those for c-$Zr_{2.86}(N_{0.88}O_{0.12})_4$ (s. above Chapter 3.4.1.1): sample was compressed in a DAC and the specific volumes of sample and the solid argon pressure medium were measured using ED-XRD. Up to ten diffraction peaks of c-Hf_3N_4, namely (211), (220), (310), (321), (420), (332), (422) and (510), were observed. For the crystalline argon up to four peaks, (111), (200), (220) and (311), were detected. Typical ED-XRD patterns measured at ambient and high pressures are presented in Figure 3.17. By comparison of the patterns one should bear in mind that they were measured at diffraction angles of 8.92° (11.1 GPa) and 8.85° (39.4 GPa and ambient pressure). In the ED-XRD patterns the $K_{\alpha 2}$- and $K_{\alpha 1}$-fluorescence peaks of hafnium at 54.61 and 55.79 keV and of tungsten (the slits material) at 57.98 and 59.32 keV were also observed. A broad peak around 43 keV was due to the diffraction from the gasket material. Similar to the compressibility measurement of oxygen-bearing c-Zr_3N_4, the peaks of argon and of c-Hf_3N_4 overlapping with each other and/or with the X-ray fluorescence peaks were not considered by the calculation of the specific volumes. The lattice parameter of c-Hf_3N_4 at ambient conditions was determined to be 6.707(9) Å, which is in good agreement with that reported earlier (a_0 = 6.701(6) Å (Zerr et al. 2003)) as well as with that of c-Hf_3N_4 synthesised in the present work using multi-anvil apparatus (a_0 = 6.7014(2) Å, s. Chapter 3.3.2.2) In these measurements the former value was used for calculation of the specific volume ratios V/V_0 of c-Hf_3N_4 on compression.

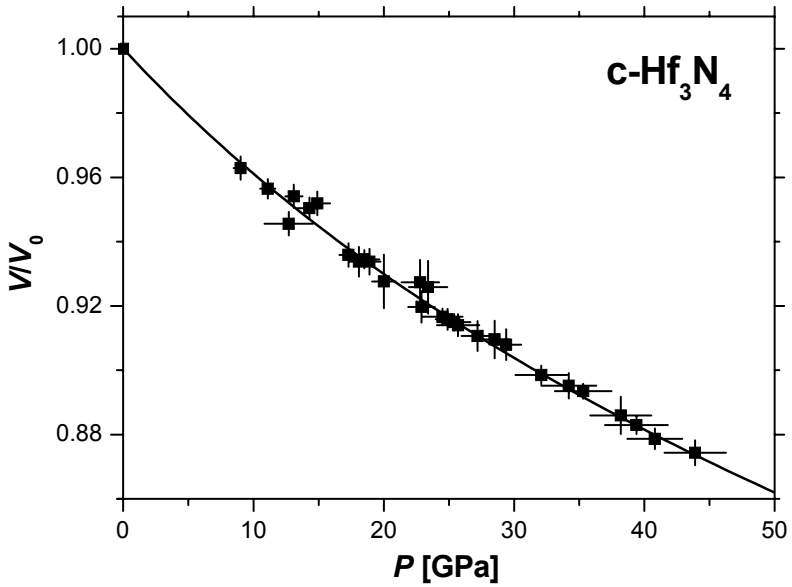

Figure 3.18. Relative volume V/V_0 of c-Hf_3N_4 at high pressures to 44 GPa and room temperature. The experimental data are shown by solid squares. The solid line represents the least-squares fit of the third-order BM-EOS to the experimental data. The fit yielded B_0 = 227(7) GPa and B_0' = 5.3(6).

The results of the compression measurements are presented in Figure 3.18. Similar to c-$Zr_{2.86}(N_{0.88}O_{0.12})_4$, the uncertainties in the V/V_0-ratios and in the pressure values correspond to the maximum difference in their values calculated from the observed diffraction peaks of c-Hf_3N_4 and argon, respectively. The specific volume change for c-Hf_3N_4 at the maximum pressure of 44 GPa was found to be about 12 %, thus again indicating a high bulk modulus of the investigated material. From the least-squares fit of the third-order Birch-Murnaghan EOS to the experimental data, the bulk modulus $B_0 = 227(7)$ GPa and its first pressure derivative $B_0' = 5.3(6)$ were derived for c-Hf_3N_4. With fixed $B_0' = 4$ the bulk modulus was found to be $B_0 = 241(2)$ GPa, which is similar to the earlier reported preliminary result of 260 GPa (Zerr et al. 2003).

In Figure 3.19 the experimental data for c-Hf_3N_4 and both fit results are presented in terms of normalized pressure F and Eulerian strain f (s. Chapter 1.2.1.1). Very sensitive to the experimental uncertainties, the $F(f)$-plot shows that all experimental data points agree, within the error bars, with both fit results. The obtained bulk modulus $B_0 = 227(7)$ GPa ($B_0' = 5.3$) or $B_0 = 241(2)$ GPa (with B_0' fixed at 4) for c-Hf_3N_4 is only 13 % and 7 %, respectively, below the preliminary estimated value of ≈ 260 GPa (Zerr et al. 2003). Results of the first-principles calculations on B_0 of c-Hf_3N_4 (Kroll 2003; Mattesini et al. 2003; Lowther 2005) scatter around the present experimental value (Table 3.8).

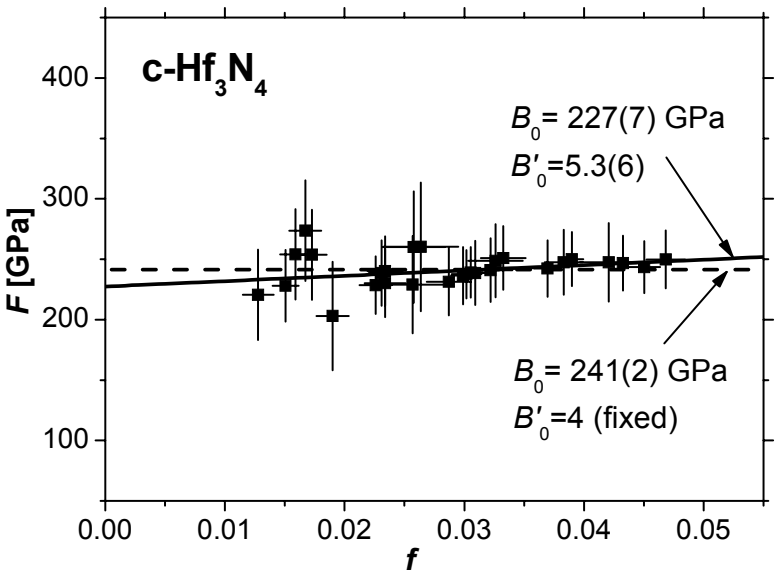

Figure 3.19. Compression data of c-Hf_3N_4 in terms of normalized pressure, F, and Eulerian strain, f. Fits to the third- and second-order BM-EOS are represented by solid and dashed lines, respectively.

In Table 3.8 (page 103) the present experimental data on B_0 and B_0' of c-$Zr_{2.86}(N_{0.88}O_{0.12})_4$ and c-Hf_3N_4 are compared with the results of earlier measurements and of first-principles calculations for c-Zr_3N_4, c-$Zr_3(N,O)_4$ and c-Hf_3N_4. The experimental values for bulk moduli of δ-ZrN, δ-HfN, c-Si_3N_4, c-BN and diamond are also given for reference. Similar to theoretical calculations and preliminary estimation, the bulk modulus for c-Hf_3N_4 is about 4 % higher than that measured for c-$Zr_{2.86}(N_{0.88}O_{0.12})_4$. Since the bulk moduli of oxygen-bearing c-Zr_3N_4 and c-Hf_3N_4 are significantly lower than those of superhard materials, the hardness of c-M_3N_4 is unlikely to surpass the "superhard limit" of 40 GPa. However, it could be comparable with or exceed the hardness of the corresponding mononitrides, δ-MN. This suggestion is only of a qualitative character since the correlation between bulk modulus and hardness is not straightforward and should be applied with care (s. Chapter 1.2.2.2). Obviously, direct measurements of the hardness of c-Hf_3N_4 and c-Zr_3N_4 would clarify the issue.

3.4.2 Vickers indentation of c-$Zr_{2.86}(N_{0.88}O_{0.12})_4$

3.4.2.1 Vickers microhardness

Despite the apparent porosity of the c-$Zr_{2.86}(N_{0.88}O_{0.12})_4$ sample (Chapter 3.3.5), reliable Vickers microhardness (H_V) measurements could be performed. Indentations with Vickers pyramid were carried out on a polished sample surface with loads from 0.49 N to 9.8 N according to the procedure described in Chapter 2.4.2.3. The SEM pictures of typical Vickers impressions made at loads of 0.98, 2.94 and 9.8 N are shown in Figure 3.20. The observed dependence of H_V in these microhardness measurements on the applied load is presented in Figure 3.21 and compared with earlier published data for a single crystal of δ-ZrN (Chen et al. 2005) and for polycrystalline δ-ZrN samples having various volume fraction porosities (VFP) (Adachi et al. 2006). The Vickers microhardness of the porous c-$Zr_{2.86}(N_{0.88}O_{0.12})_4$ (having VFP between 0.25 and 0.3) at the load of 9.8 N was found to be 12.0(6) GPa which is only slightly below that for the single crystal δ-ZrN (12.2 GPa) and almost 2.5 times higher than that of a polycrystalline δ-ZrN sample (4.9 GPa) having a lower VFP of about 0.18 (Figure 3.21).

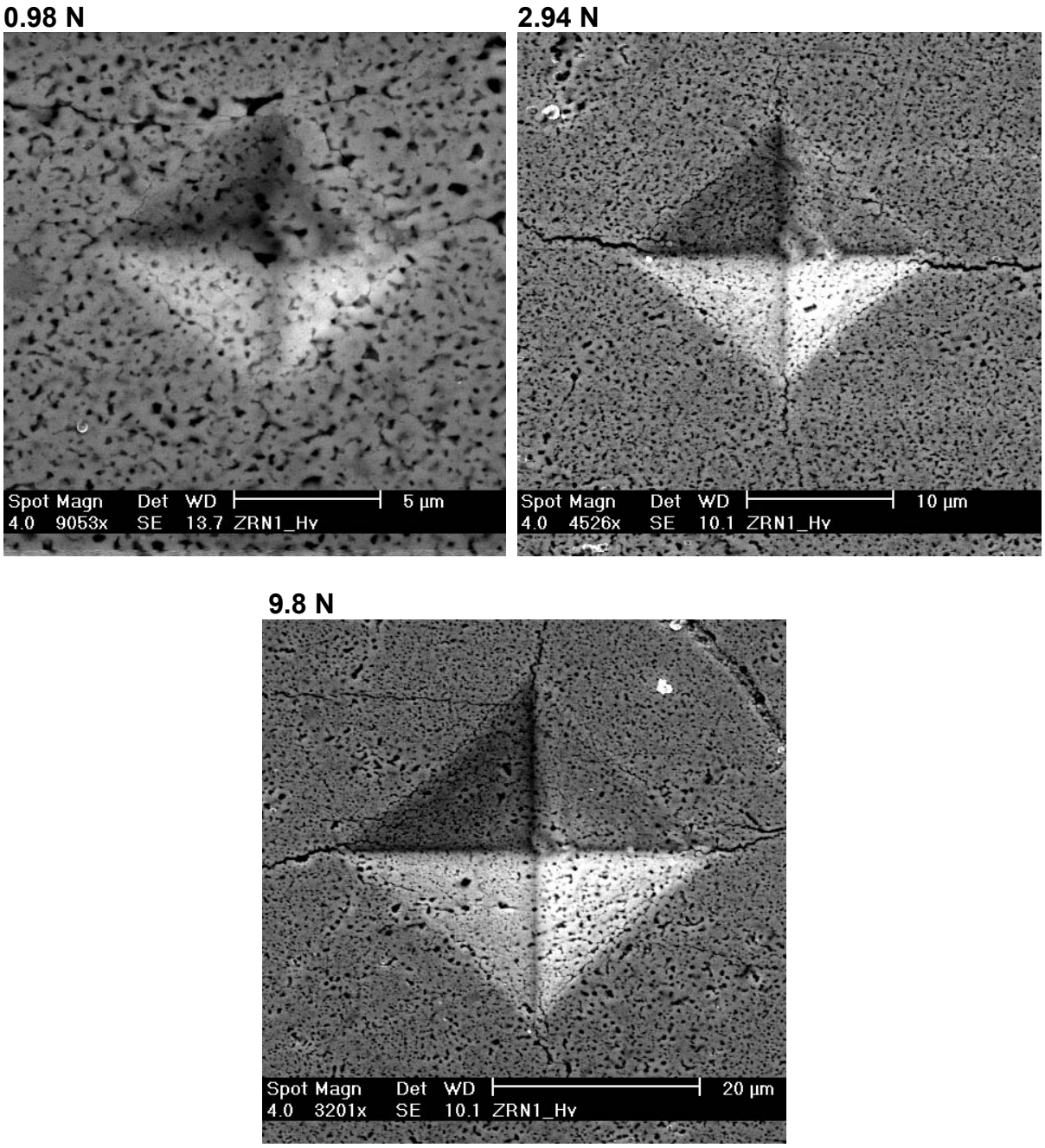

Figure 3.20. SEM pictures of typical Vickers indentations made in c-$Zr_{2.86}(N_{0.88}O_{0.12})_4$ (sample Z2-01) with the applied loads of 0.98, 2.94 and 9.8 N. The loading time was fixed at 15 seconds. The Vickers hardness values were determined to be 14.2, 12.1 and 12.0 GPa for these indentations, respectively.

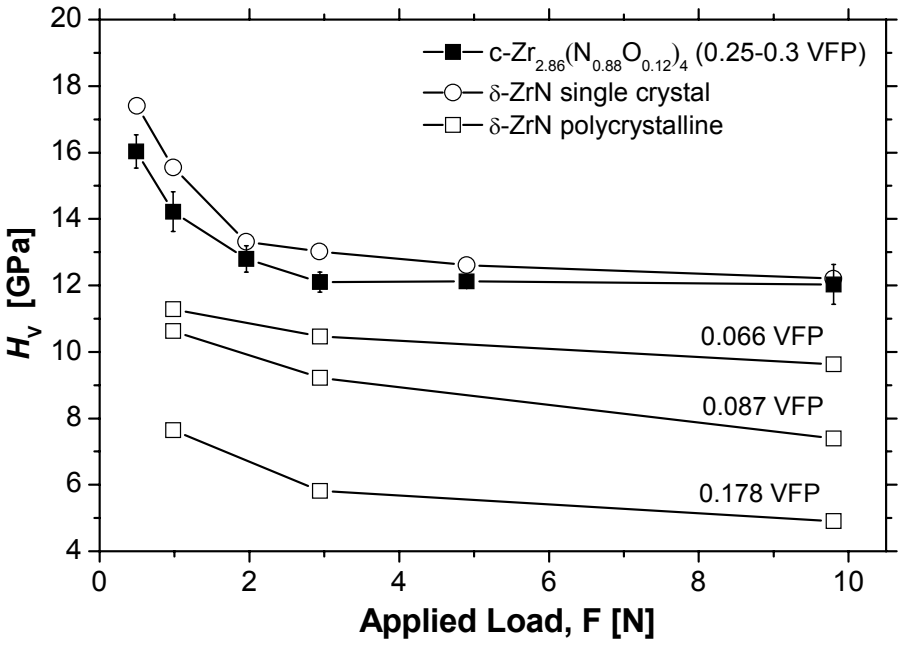

Figure 3.21. Vickers microhardness of the porous (VFP of 0.25-0.3) oxygen-bearing cubic Zr_3N_4, c-$Zr_{2.86}(N_{0.88}O_{0.12})_4$, synthesised in the present work as a function of the applied load (■), compared with hardness of the δ-ZrN single crystal (○) (Chen et al. 2005) and with those of polycrystalline δ-ZrN having various VFP (□) (Adachi et al. 2006).

It should be noticed that micro-Raman examination of the indented sample surfaces did not show any changes in the spectra of c-$Zr_{2.86}(N_{0.88}O_{0.12})_4$. The latter finding indicated that no phase transition to another Raman-active phase or even amorphisation of the synthesized material occurred due to plastic deformation during indentation.

It follows from the results presented in Figure 3.21 that indentation size effect (ISE) takes place for the investigated sample: the hardness value of c-$Zr_{2.86}(N_{0.88}O_{0.12})_4$ was found to be $H_V(0.05)$ = 16.0(5) GPa at the load of 0.49 N and to gradually decrease with the load increase. At the loads of 2.94 N and higher the hardness appears to preserve nearly a constant value of about 12 GPa. In order to derive the load independent hardness value, the modified proportional specimen resistance (M-PSR) equation, describing the indentation size effect (s. Chapter 2.4.2.1), was fitted to the experimental data $L(d)$, where L is the applied load and d is the mean diagonal of the Vickers impression (Figure 3.22). The results of the least-squares fit are given in Figure 3.22. The true hardness value was calculated from the fit parameter a_3 (s. Chapter 2.4.2.1) to be $H_V^{true} = 1.8544\ a_3 = 11.5(9)$ GPa. This value agrees within the errors with those measured at high indentation loads ($\geq$ 2.94 N). The load independent hardness value was used in the present work for estimation of the indentation fracture toughness of c-$Zr_{2.86}(N_{0.88}O_{0.12})_4$ (s. below), as was suggested by Gong et al. (1999, 2002).

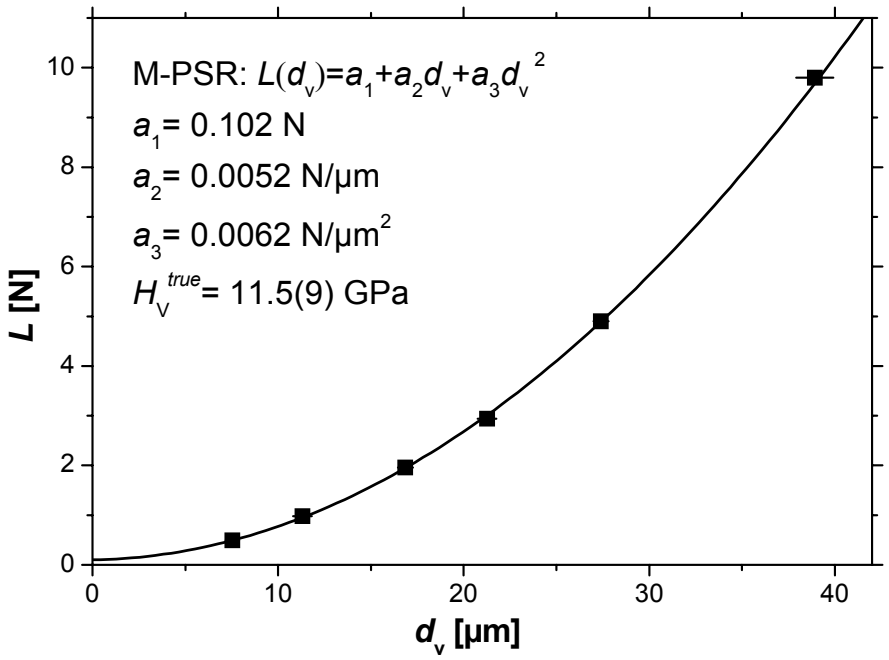

Figure 3.22. The applied load, L, as a function of the corresponding mean diagonal of the resulting Vickers impression d_v (solid squares) for c-$Zr_{2.86}(N_{0.88}O_{0.12})_4$ (sample Z2-01). The solid line represents the least-square fit of M-PSR equation, describing the indentation size effect (ISE), to the experimental data. In the plot the final fitting parameters of the M-PSR equation and the calculated load-independent hardness value are given.

As discussed in Chapter 1.2.2.1, the hardness of most materials decreases with an increase of their volume fraction porosity. It was suggested to describe the hardness-to-porosity relation by an exponential law, $H = H_0 \exp(-bp)$, where b is a constant, p is the volume fraction porosity (VFP), H and H_0 are the hardness values of porous and dense specimen, respectively. Analysis of a wide range of hardness data for hard ceramic materials (such as Si_3N_4, SiC, TiC, B_4C, Al_2O_3, ZrO_2, etc.) has shown that typical values of b are between 3 and 7 (Rice 1998; Cho et al. 1999; Luo & Stevens 1999; Milman et al. 1999). Moreover, recent studies of the porosity influence on hardness of polycrystalline zirconium mononitride have shown that $H_V(1)$ of δ-ZrN drops by almost 70 % for VFP of 0.2 (i.e. $b = 5.9$) as compared with fully dense material (Adachi et al. 2006). Assuming $b = 3$ (minimum) and $b = 7$ (maximum), the lower and the upper limit values for $H_V(1)$ of fully dense c-Zr_3N_4 were estimated to be 25 GPa and 69 GPa, respectively. Thus the Vickers microhardness expected for dense c-Zr_3N_4 (> 25 GPa) significantly exceeds that of dense δ-ZrN (12-15 GPa) (Samsonov 1969; Lengauer 2000; Chen et al. 2005) as well as that of 19 GPa, estimated for c-Zr_3N_4 by Mattesini et al. (2003) who employed theoretical shear modulus and empirical correlation between H_V and G_0 for hard ceramic materials (Chapter 1.2.2.2).

3.4.2.2 Indentation fracture toughness

The SEM investigation of the indented sample surface revealed for high loads (≥ 2.94 N) the presence of radial cracks having their origin directly at or close to corners of the Vickers impressions (Figure 3.23). Usually unsymmetrical cracking patterns were observed which are, most probably, due to microstructural inhomogeneity and/or porosity of the investigated material. The average crack length, l, was measured to be 6.7, 10.5 and 21.0 μm for the indentation loads of 2.94, 4.9 and 9.8 N, respectively. The average crack length for each impression was then used for estimation of the indentation fracture toughness, $K_{Ic\text{-}if}$, of c-$Zr_{2.86}(N_{0.88}O_{0.12})_4$ using equations of Niihara et al. (1982) and Shetty et al. (1985) described in Chapter 2.4.2.2.

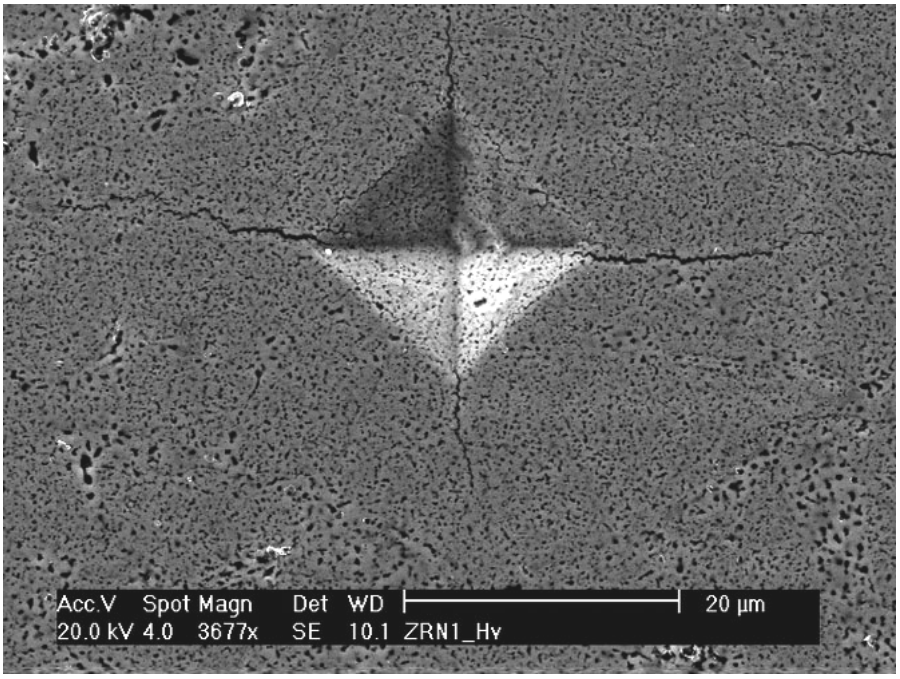

Figure 3.23. The SEM picture of the Vickers impression made on the polished surface of porous c-$Zr_{2.86}(N_{0.88}O_{0.12})_4$ (sample Z2-01) with the load of 2.94 N. Four radial cracks having their origin directly at or close to corners of the impression can be clearly recognised.

The Niihara's equation was derived for crack lengths, l, satisfying the condition $0.25 < 2l/d_v < 2.5$, where d_v is the impression diagonal (Niihara et al. 1982). Thus, this equation can be used in the present work, since for the observed cracks $0.6 < 2l/d_v < 1.2$ holds for all loads. In both equations the knowledge of hardness value is required, so the derived load-independent hardness of c-$Zr_{2.86}(N_{0.88}O_{0.12})_4$ of 11.5 GPa (Chapter 3.4.2.1) was used. For Niihara's equation the Young's modulus of the indented specimen is also needed. It can be

obtained by combination of experimentally determined bulk and reduced elastic moduli of material as described above in Chapter 2.4.4. In the present work the Young's modulus of c-$Zr_{2.86}(N_{0.88}O_{0.12})_4$ was determined to be 252 GPa (s. below Chapter 3.4.4). This value was substituted in Niihara's equation for the determination of $K_{Ic\text{-}if}$. In contrast to Niihara's equation, Shetty's equation does not include Young's modulus. However, the geometry factor β in this equation depends (in addition to standard half-apex angle of the Vickers pyramid $\psi = 68°$) on the Poisson's ratio ν of the indented material. For c-$Zr_{2.86}(N_{0.88}O_{0.12})_4$ this value was measured to be $\nu = 0.31$ (s. Chapter 3.4.4). Accordingly, the geometry factor in Shetty's equation was calculated to be $\beta = 0.093$. It should be also mentioned that the β value calculated for diamond (for $\nu = 0.07$) differs by less than 10 % from that obtained for the investigated material. Thus, the Poisson's ratio does not significantly influence the geometry factor in the Shetty's equation and, accordingly, the indentation fracture toughness value.

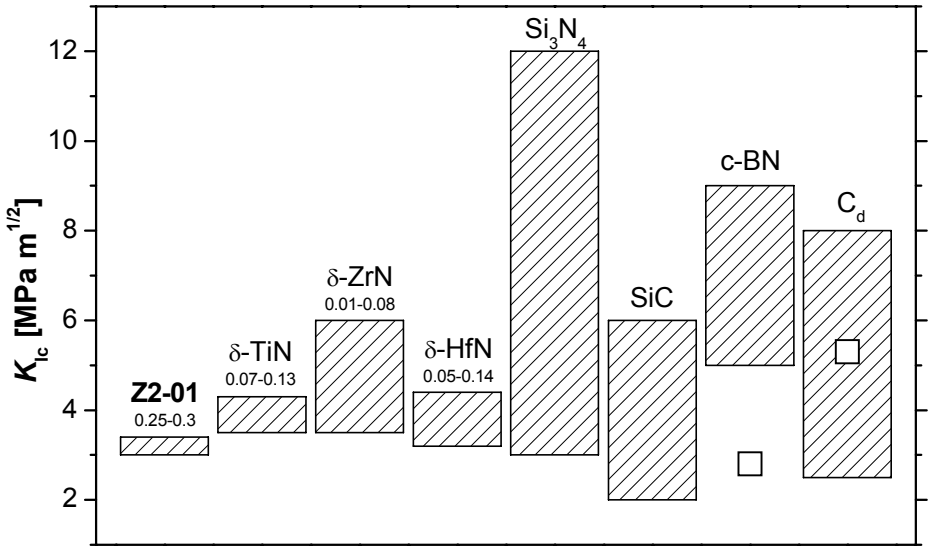

Figure 3.24. Indentation fracture toughness of porous c-$Zr_{2.86}(N_{0.88}O_{0.12})_4$ (Z2-01) in comparison with the K_{Ic} values reported for porous hot-isostatically-pressed δ-MN (M = Ti, Zr, Hf). The ranges of VFP of these materials are specified by numbers. Typical K_{Ic} values for sintered SiC and Si_3N_4 ceramics and polycrystalline c-BN and diamond are shown for reference. K_{Ic} of single crystal c-BN and diamond are given by open squares.

The indentation fracture toughness for porous c-$Zr_{2.86}(N_{0.88}O_{0.12})_4$ was calculated to be 3.0(2) and 3.4(2) MPa m$^{1/2}$ from Niihara's and Shetty's equation, respectively, and was found to be almost independent on the applied indentation load. The obtained $K_{Ic\text{-}if}$ values are plotted in Figure 3.24 along with fracture toughness values for hot-isostatically-pressed δ-MN (M = Ti, Zr, Hf) having various porosities (Alexandre et al. 1993; Moriyama et al. 1993; Desmaison-

Brut et al. 1994; Kuwahara et al. 2001). Additionally, ranges of fracture toughness values reported for sintered SiC (Ghosh et al. 1989; Kim et al. 1995; Liu et al. 1995) and Si_3N_4 ceramics (e.g. Sajgalik et al. 1995; Petzow & Herrmann 2002; Yang et al. 2002) as well as for superhard polycrystalline and single crystal c-BN (Brookes 1986; Rai 1991; Utsumi et al. 1991; Taniguchi et al. 1996) and diamond (Sussmann et al. 1994; Drory et al. 1995; Miess & Rai 1996; Novikov & Dub 1996; Jiang et al. 2000b) are given in Figure 3.24 for reference.

Similar to other mechanical properties (e.g. hardness, elastic moduli), fracture toughness of a material usually decreases with increase of the material porosity (e.g. Wagh et al. 1993; Rice 1998). Such behaviour was observed for a number of hard ceramic materials with various porosities (e.g. Alexandre et al. 1993; Desmaison-Brut et al. 1994; Liu et al. 1995; Tancret et al. 1997; Milman et al. 1999; Yang et al. 2002). Therefore, the present indentation fracture toughness of 3.2(3) MPa $m^{1/2}$ for porous c-$Zr_{2.86}(N_{0.88}O_{0.12})_4$ (VFP of 0.25-0.3) can be considered as the lower limit for dense c-Zr_3N_4. The fracture toughness of dense c-Zr_3N_4 is expected to be comparable or even to exceed that of δ-MN and SiC ceramics.

3.4.3 Nanoindentation measurements on c-$Zr_{2.86}(N_{0.88}O_{0.12})_4$

In order to determine nanoindentation hardness, *H*, and reduced elastic modulus of c-$Zr_{2.86}(N_{0.88}O_{0.12})_4$, nanoindentation measurements were carried out by E. Schweitzer at the Lehrstuhl für Allgemeine Werkstoffeigenschaften (WW1), Friedrich-Alexander-Universität Erlangen-Nürnberg, Erlangen. The tests were performed on a mechanically polished surface of the Z2-01 sample since electropolishing of the sample surface resulted in increase of the surface roughness, most probably due to submicron porosity.[*] The size of the observed pores varied between 100 nm and 2 μm while in some areas the pores of about 50 nm or less could be recognised. The size of the uniform and well sintered sample areas was < 1 μm in one of the lateral directions.

The nanoindentation measurements were performed for two maximum loads of about 23 and 14 mN which correspond to the indentation depths of about 260 and 210 nm, respectively. Additionally, the sample was indented stepwise: ten load-unload cycles with successively increasing maximum loads from 0.027 to 13.8 mN were performed. Typical load-displacement curves obtained by nanoindentation testing for stepwise loading and continuous stiffness measurement (CSM) are shown in Figure 3.25.

[*] E. Schweitzer (personal communication, April, 2005)

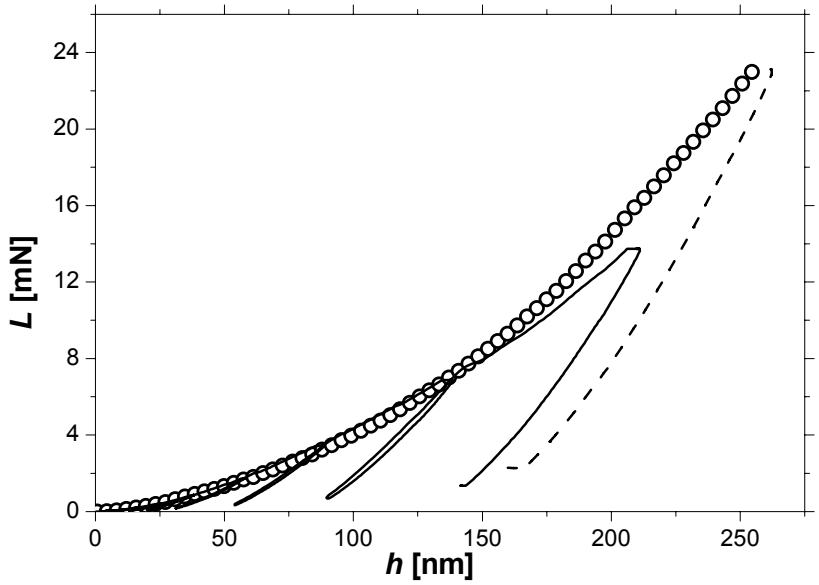

Figure 3.25. Typical load-displacement curves for c-$Zr_{2.86}(N_{0.88}O_{0.12})_4$ (Z2-01) measured by nanoindentation techniques: stepwise mode (solid line) and CSM (circles and dashed line) where E_r and H were determined on loading portion of the indentation curve (circles).

The unloading parts of the obtained load-displacement curves were evaluated using the Oliver-Pharr method (O&P) (Oliver & Pharr 1992) (s. Chapter 2.4.3.1) in order to derive nanoindentation hardness, H, and reduced elastic modulus, E_r, of c-$Zr_{2.86}(N_{0.88}O_{0.12})_4$ (Table 3.9). For the stepwise loadings, the results scattered significantly at low loads. Owing to this, only the unloading part of the last cycle of every load-displacement curve was evaluated.

Alternatively, H and E_r were measured on the loading portion of the load-displacement curves as a function of the contact depth h applying CSM technique (Li & Bhushan 2002) (s. Chapter 2.4.3.2). Figure 3.26 presents results of two CSM measurements for hardness and reduced elastic modulus of c-$Zr_{2.86}(N_{0.88}O_{0.12})_4$. Apparent variations in the dependences of H and E_r on depth at $h < 100$ nm (Figure 3.26) are most probably due to surface imperfections and presence of the pores beneath the indented area. Since E_r and H values did not change significantly for $h > 150$ nm, they were averaged for higher depths over all CSM measurements (Table 3.9).

In addition to the O&P and CSM methods the reduced elastic modulus E_r was estimated from the initial part of the load-displacement curves applying Hertzian contact theory (Johnson 1985) (Chapter 2.4.3.3). The very beginning loading part (up to $h = 15$ nm) of 16 load-displacement curves were fitted with Hertzian contact equation assuming a purely elastic initial contact. This method led to E_r = 203(38) GPa, slightly below the values obtained using

Oliver-Pharr and CSM methods (Table 3.9). Since no pop-in event indicating a transition from pure elastic to plastic deformation (Göken & Kempf 2001) was observed during indentations, the lower E_r value from Hertzian fit could be explained by partial plastic deformation of the indented material, even during initial contact. This finding was confirmed by atomic force microscopy (AFM) investigation which revealed plastic impressions for all applied loads. It appeared that the multiple microstructural defects in the sample could have promoted plasticity even for very low loads.

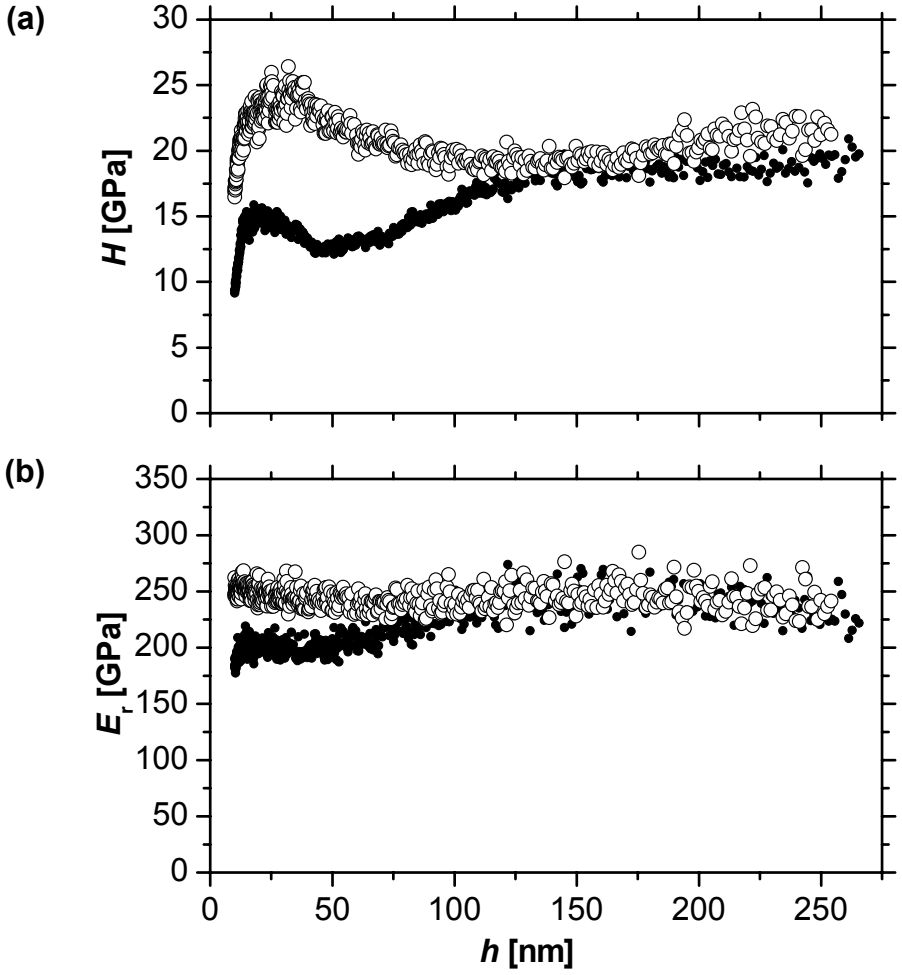

Figure 3.26. Two examples of measurements of (a) nanoindentation hardness, H, and (b) reduced elastic modulus, E_r, as functions of indentation depth using CSM technique. Variations in H and E_r with indentation depth are attributed to material imperfections, e.g. presence of pores beneath the indented area. At $h > 150$ nm hardness and corresponding elastic modulus are only weakly dependent on indentation depth.

Table 3.9. Elastic moduli and nanoindentation hardness of c-$Zr_{2.86}(N_{0.88}O_{0.12})_4$ as measured in the present work and compared with earlier experimental and theoretical results for c-Zr_3N_4 and c-$Zr_3(N,O)_4$. For hardness data, the indentation load values are given in curly braces.

Phase	B_0 [GPa] / B_0'	E_r [GPa]	H [GPa]	G_0 [GPa]	E_0 [GPa]	ν_0
c-$Zr_{2.86}(N_{0.88}O_{0.12})_4$ (this work)	219(13) / 4.4(10) 224(5) / 4 fixed	224(16) O&P 238(15) CSM 203(38) Hertzian	16.9(2.4) O&P {13.8 and 23 mN} 18.6(1.8) CSM {8-23 mN}	96(13) (lower limit)	252(31) (lower limit)	0.31(2) (upper limit)
c-Zr_3N_4	250 / 4 fixed [a] 195-265 [b,c] 218-262 [b,d] 251 / 6.75 [b,e]	n/a	36 {5 mN} [g] 17.5-19.7 [b,d]	129-145 [b,d] 158 [b,f]	324-368 [b,d] 396 [b,f]	0.25-0.27 [b,d] 0.26 [b,f]
c-$Zr_3N_{3.75}O_{0.25}$	241 / 6.56 [b,f]	n/a	n/a	142 [b,f]	365 [b,f]	0.28 [b,f]
c-$Zr_3(N_{0.875}O_{0.125})_4$	227 / 7.05 [b,f]	n/a	n/a	67 [b,f]	182 [b,f]	0.36 [b,f]

[a] (Zerr et al. 2003).
[b] Theoretical values.
[c] (Kroll 2003).
[d] (Mattesini et al. 2003).
[e] (Lowther 2005).
[f] (Lowther 2008).
[g] (Chhowalla & Unalan 2005).

3.4.4 Elastic moduli of c-$Zr_{2.86}(N_{0.88}O_{0.12})_4$

In the above described experiments two independent elastic moduli, bulk and reduced elastic modulus, were measured for oxygen-bearing c-Zr_3N_4. Their combination was used in the present work for determination of all other elastic moduli of c-$Zr_{2.86}(N_{0.88}O_{0.12})_4$ using known relations between E, B, G and ν for an isotropic elastic material (s. Chapter 2.4.4). Using the experimental values of $B_0 = 219(13)$ GPa and $E_r = 224(16)$ GPa, the shear modulus $G_0 = 96(13)$ GPa and, subsequently, the Young's modulus E_0 and the Poisson's ratio ν_0 of c-$Zr_{2.86}(N_{0.88}O_{0.12})_4$ were derived (s. Table 3.9, page 116). The obtained elastic moduli are considered as those of isotropic polycrystalline c-Zr_3N_4 material.

It is well known that elastic moduli of a hard ceramic material strongly depend on the material porosity (e.g. Coble & Kingery 1956; Spriggs 1961; Wang 1984; Rice 1998). For example, Young's modulus, E, decreases with increasing porosity, p, and can be expressed by an equation $E = E_0 \exp(-bp)$, where E_0 is the elastic modulus of the dense specimen and b is a constant (Spriggs 1961; Andersson 1996; Rice 1996, 1998). Similarly, gradual decrease of reduced elastic modulus with increase of porosity was observed for various hard ceramic materials (e.g. Duan & Steinbrech 1998; Velez et al. 2001; Jang & Matsubara 2005). Therefore, the derived values for G_0 and E_0 of c-$Zr_{2.86}(N_{0.88}O_{0.12})_4$ should be considered as the lower limits, since the results of the nanoindentation measurements could have been altered by the presence of submicron defects and pores in the sample. Nevertheless, the differences between the present experimental values of G_0 and E_0 for c-$Zr_{2.86}(N_{0.88}O_{0.12})_4$ and the predicted ones for c-Zr_3N_4 and c-$Zr_3(N,O)_4$ (Table 3.9) appear to be substantial and demand further theoretical and experimental verification.

Similarly, microstructural defects could explain an even larger difference between the nanoindentation hardness values obtained for the present material (16.9 GPa) and that for dense c-Zr_3N_4 films (36 GPa) (Chhowalla & Unalan 2005). This explanation is supported by the fact that indentation measurement on thin films showed pronounced pop-in behaviour indicating pure elastic to plastic transition.*

* M. Chhowalla (personal communication, January, 2007)

3.5 Thermal properties of c-$Zr_{2.86}(N_{0.88}O_{0.12})_4$

3.5.1 Thermal expansion coefficient

In order to obtain the thermal expansion coefficient of c-$Zr_{2.86}(N_{0.88}O_{0.12})_4$, its powder XRD patterns were collected on heating in air from room temperature (RT) to 873 K (Figure 3.27). The lattice parameter as a function of temperature (Figure 3.28) and its standard deviation were determined by Le Bail fit (Le Bail et al. 1988) of powder XRD data using the profile matching mode of the Fullprof software (Rodriguez-Carvajal 1990). A high standard deviation of the lattice parameter obtained at T = 873 K is due to a gradual oxidation of the sample material which started already at 773 K (Figure 3.27).

The observed non-linear temperature dependence of the lattice parameter of c-$Zr_{2.86}(N_{0.88}O_{0.12})_4$ was fitted with a third order polynomial function (Figure 3.28):

$$a(T) = 6.746 + 8.422\times10^{-8}T^2 - 2.205\times10^{-11}T^3 \text{ [Å]}.$$

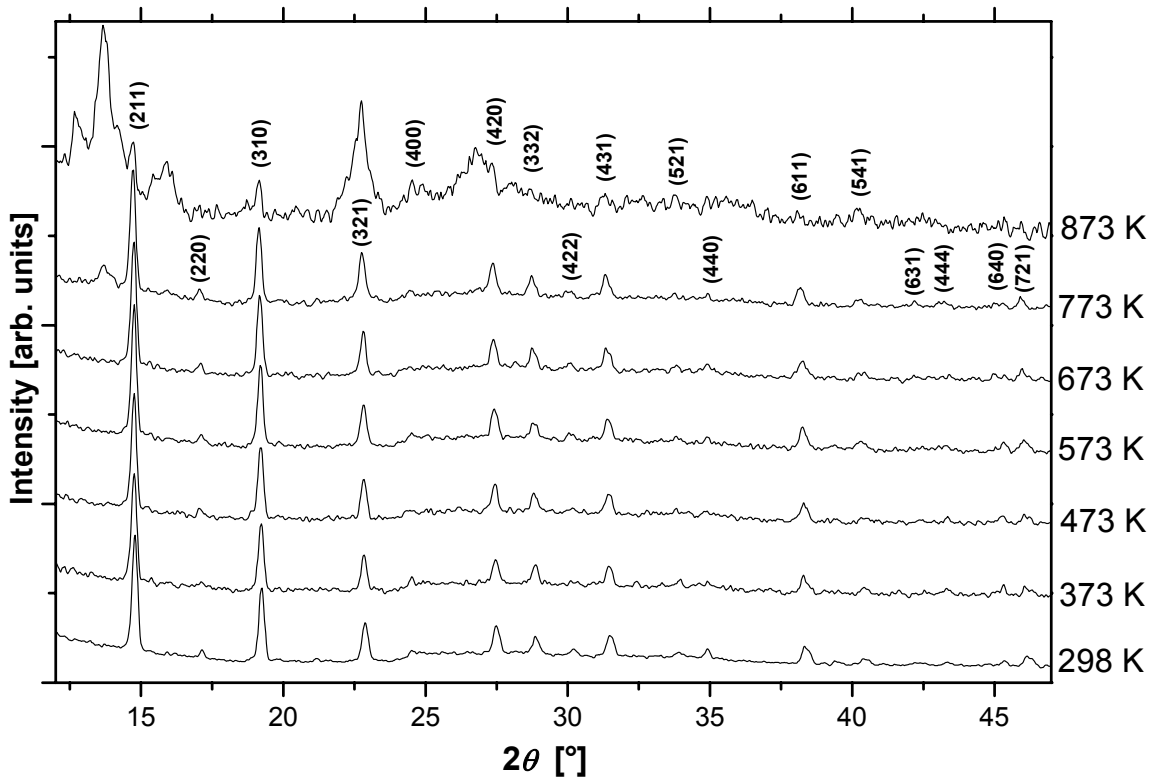

Figure 3.27. *In situ* high-temperature X-ray powder diffractograms of c-$Zr_{2.86}(N_{0.88}O_{0.12})_4$ (sample Z2-01) measured in steps from 298 K to 873 K. The diffraction peaks of the Th_3P_4-type structure are indicated.

In this equation the first order T-term is omitted in order to fulfil the boundary condition for the thermal expansion coefficient ($\lim \alpha(T) = 0$ for $T \to 0$) and to model the tendency of $\alpha(T)$ to a constant value at high temperatures (Ashcroft & Mermin 1976; Kittel 1986; Elliott 1998). Similar $a(T)$ dependence was used by Hintzen et al. (2003) in their work on thermal expansion of γ-Si_3N_4. Applying the above mentioned $a(T)$ relationship for c-$Zr_{2.86}(N_{0.88}O_{0.12})_4$ the linear thermal expansion coefficient $\alpha(T)$, defined as

$$\alpha(T) = \frac{1}{a(T)} \frac{\partial a(T)}{\partial T},$$

was derived. The obtained $\alpha(T)$ is plotted in Figure 3.29 along with the earlier experimental data for δ-ZrN (Baker 1958; Houska 1964; Aigner et al. 1994; Adachi et al. 2007; Takano et al. 2007) and o-Zr_3N_4 (Lerch et al. 1996). It can be seen from the Figure that $\alpha(T)$ of c-$Zr_{2.86}(N_{0.88}O_{0.12})_4$ increases from 6.6×10^{-6} K^{-1} to 14.2×10^{-6} K^{-1} in the investigated temperature region and is about two times higher that those of δ-ZrN and o-Zr_3N_4 at 900 K. Such a high $\alpha(T)$ value of c-$Zr_{2.86}(N_{0.88}O_{0.12})_4$ can be explained by a less symmetric interatomic potential (i.e. higher anharmonicity) in c-Zr_3N_4 due to higher atomic coordinations (e.g. Rochegude 1998; Schwarz 2005) and, accordingly, more delocalized electron density along the atomic bonding when compared with δ-ZrN and o-Zr_3N_4.

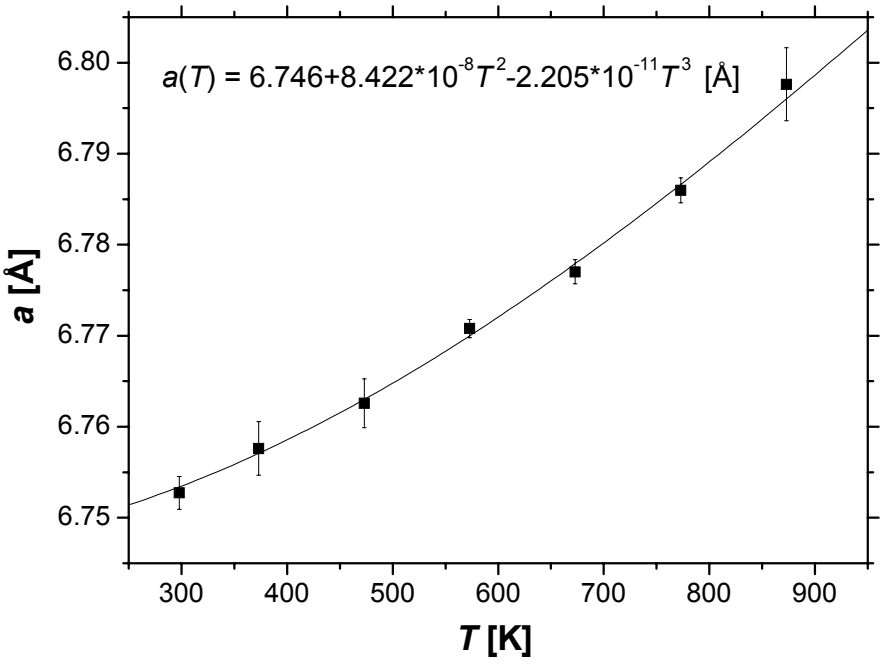

Figure 3.28. Lattice parameter of c-$Zr_{2.86}(N_{0.88}O_{0.12})_4$ (sample Z2-01) as a function of temperature. The experimental data points are given by solid squares. Solid line represents the least-square fit of the third order polynomial function (s. inset) to the experimental data.

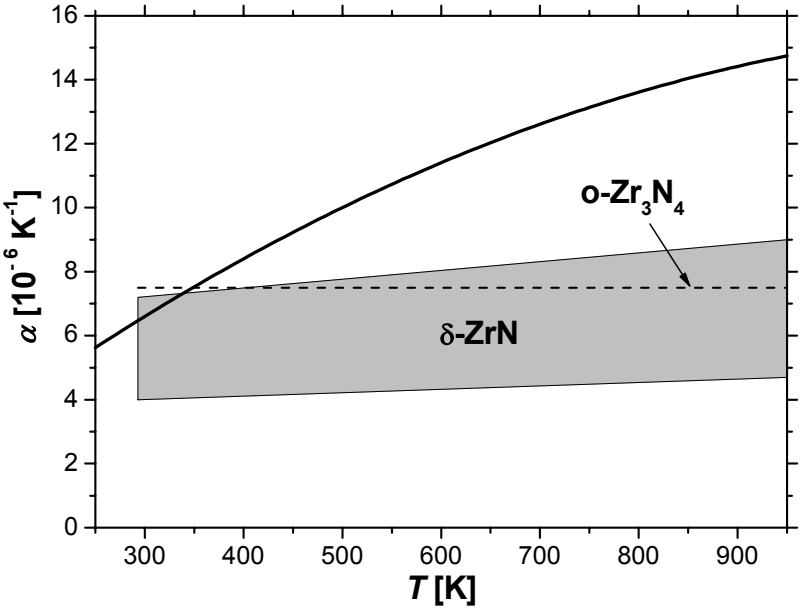

Figure 3.29. Linear thermal expansion coefficient α of c-$Zr_{2.86}(N_{0.88}O_{0.12})_4$ (sample Z2-01) as a function of temperature (solid line) in comparison with values reported for δ-ZrN (grey area) and o-Zr_3N_4 (dashed line).

3.5.2 High-temperature oxidation stability

During heating of c-$Zr_{2.86}(N_{0.88}O_{0.12})_4$ up to 673 K in air no phase transition, decomposition or oxidation of the sample material was detected by *in situ* XRD measurements. As already mentioned in the previous chapter, after heating of the sample at 773 K for about 30 min, new weak diffraction peaks appeared at $2\theta = 13.6°$ and 15.7° (Figure 3.30). The new reflexes can be attributed to one of the known zirconium oxynitride phases, namely γ (Zr_2N_2O), β ($Zr_7N_4O_8$) or β′ ($Zr_7N_2O_{11}$) (Lerch 1997), in particular to the (222) and (400) reflexes of γ-phase, (211) and (122) of β-phase and/or (122) and (214) of β′-phase. This observation indicates the onset of material oxidation. Heating to 873 K led to further accelerated oxidation of c-$Zr_{2.86}(N_{0.88}O_{0.12})_4$ resulting in formation of oxynitride and monoclinic zirconium dioxide, m-ZrO_2 (Figure 3.30). After holding for one hour at 873 K all diffraction peaks of c-$Zr_{2.86}(N_{0.88}O_{0.12})_4$ disappeared. The final oxidation product was cooled down to RT and its powder XRD was measured again. This allowed to confirm the main oxidation products to be cubic γ-Zr_2N_2O (Clarke et al. 1999) and m-ZrO_2 (Figure 3.30).

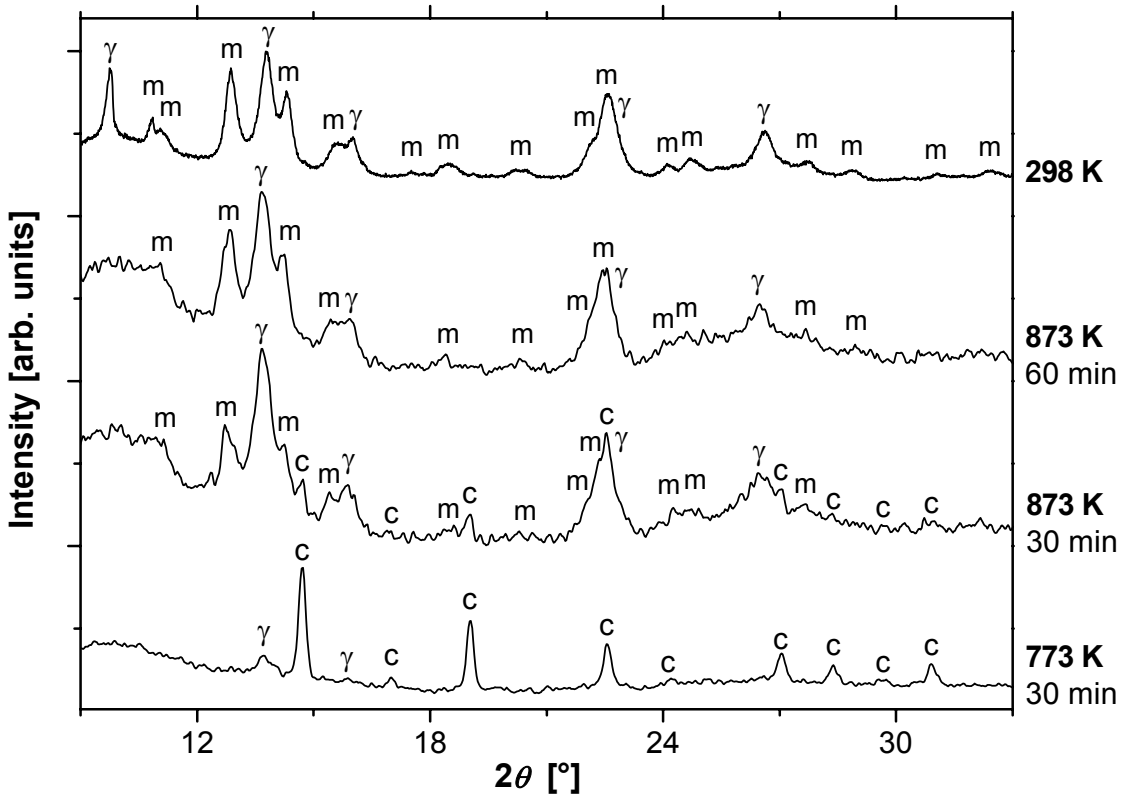

Figure 3.30. X-ray powder diffractograms of c-$Zr_{2.86}(N_{0.88}O_{0.12})_4$ (sample Z2-01) heated in air to 773 K and 873 K, and of the final oxidation product measured at room temperature. The holding time at the indicated temperature is given below the *T*-value. The letters "c", "γ" and "m" denote the diffraction peaks of c-$Zr_{2.86}(N_{0.88}O_{0.12})_4$, γ-$Zr_2N_2O$ and m-ZrO_2, respectively.

Similar to orthorhombic Zr_3N_4, γ- and all β-oxynitrides (Lerch 1997), c-$Zr_{2.86}(N_{0.88}O_{0.12})_4$ starts to slowly oxidise in air above 773 K. However, in contrast to other zirconium (oxy)nitrides which oxidise directly to m-ZrO_2 (Lerch 1997), cubic zirconium(IV) nitride transforms to γ-Zr_2N_2O first, which further oxidises to give zirconium dioxide. Accordingly, the high-temperature oxidation reaction of c-Zr_3N_4 can be described as the following sequence:

$$4\,\text{c-}Zr_3N_4 \xrightarrow{+3O_2-2N_2} 6\,\gamma\text{-}Zr_2N_2O \xrightarrow{+9O_2-6N_2} 12\,\text{m-}ZrO_2$$

It is worth to be mentioned that the determined oxidation temperature for c-$Zr_{2.86}(N_{0.88}O_{0.12})_4$ is also comparable with the values reported for δ-ZrN powders (760-850 K) and thin films (723-773 K) (Lyutaya et al. 1970; Luridiana & Miotello 1996; Wiame et al. 1998; Reddy et al. 2007). In some textbooks the oxidation temperature of δ-ZrN in air is reported to be 1073-1173 K (Samsonov 1969; Pierson 1996) which is significantly higher than that of powders and thin films. In these literature sources, however, neither nature of the investigated samples nor measurement technique is given. The only possible explanation of such a high difference

is that high oxidation temperatures are obtained for dense compacted samples, where formation of an oxidic passivating layer on the sample surface hindered a rapid oxidation of the sample at temperatures between about 750 K and 1073 K. Since in the present work measurements were performed on powdered micro-porous sample, the comparison of the obtained result with oxidation temperature of δ-ZrN powders and thin films surface appears to be more relevant.

The present result indicates also that c-$Zr_{2.86}(N_{0.88}O_{0.12})_4$ is metastable at least to about 700 K, since no phase transition and/or decomposition of sample material was observed below this temperature. The investigation of thermal (meta)stability of cubic zirconium(IV) nitride under inert atmospheres (N_2, Ar) could be a subject of future experiments.

4 Summary

The present work deals with recently discovered high-pressure nitrides of zirconium and hafnium having Th_3P_4-type structure, c-M_3N_4 (M = Zr or Hf), which were originally synthesized in microscopic amounts from elements in a laser-heated diamond anvil cell at pressures above 16 GPa and temperatures above 2500 K (Zerr et al. 2003). Existent experimental and theoretical data suggested for this new family of high-pressure nitrides to be potential hard wear-resistant materials with interesting optoelectronic and superconducting properties (Kroll 2003; Mattesini et al. 2003; Zerr et al. 2003; Chhowalla & Unalan 2005; Xu et al. 2006). They were also expected to surpass in mechanical and thermal properties the corresponding mononitrides, δ-TiN, δ-ZrN and δ-HfN, the well known technological materials widely used for various wear, chemical and thermal protective applications. In the present work the main goals of the research were: (i) synthesis of macroscopic amounts (milligram quantities) of c-Zr_3N_4 and c-Hf_3N_4, (ii) experimental investigation of their structure, composition and morphology and (iii) measurement of the properties related to potential industrial applications of these compounds as hard wear-resistant materials.

As a starting material for high-pressure high-temperature synthesis of macroscopic samples nanocrystalline powders of M_3N_{4+x} with distorted NaCl-type structure were used. Such materials had to be prepared in this work due to the following two reasons: firstly, the high-pressure multi-anvil technique chosen for high-pressure synthesis of macroscopic amounts of c-M_3N_4 does not allow utilization of condensed nitrogen or ammonia as a reactant. Secondly, nitrogen-rich zirconium and hafnium nitrides with $N/M \geq 4/3$ are not commercially available. In the present work nanocrystalline M_3N_{4+x} powders were obtained via high-temperature ammonolysis of corresponding metal dialkylamides (Li et al. 2005). This method allows to obtain nitrogen-rich compounds ($N/M > 4/3$) insignificantly contaminated with other elements. Careful handling of the metal dialkylamides and preliminary high-temperature treatment of quartz glassware allowed to obtain nanocrystalline Zr_3N_{4+x} of better quality in this work, i.e. with higher nitrogen and lower oxygen content, when compared with earlier results (Li et al. 2005).

Macroscopic amounts (≈ 2-3 mm^3) of both c-Zr_3N_4 and c-Hf_3N_4 were synthesized at 12 GPa and 1873 K in a multi-anvil high-pressure apparatus. These pressure-temperature conditions are significantly lower than those in the original LH-DAC experiments (Zerr et al. 2003). The obtained sample amounts allowed detailed characterisation of the products using various standard methods and techniques. Powder XRD proved the formation of c-M_3N_4 for both zirconium- and hafnium nitride samples. In the case of zirconium nitride, formation of a single phase crystalline material was verified by both XRD and TEM. In addition to zirconium and nitrogen, EPMA revealed the presence of a small amount of oxygen homogeneously distributed in the sample. Since no amorphous phase was detected, the composition of the obtained crystalline material was derived to be $Zr_{2.86}(N_{0.88}O_{0.12})_4$. Thus, oxygen-bearing zirconium(IV) nitride having Th_3P_4-type structure with composition described by the general formula $Zr_{3-u}(N_{1-u}O_u)_4$ was synthesised. This formula accounts for the formation of cation vacancies when nitrogen is substituted by oxygen, as required by the electrical neutrality condition. Assignment of the structure of the obtained zirconium oxynitride to the Th_3P_4-type was further confirmed by Raman spectroscopic measurements. In the case of hafnium nitride, in contrast, a minor oxidation of the sample led to formation of a mixture of oxygen-poor c-Hf_3N_4 and oxidic material. The latter was detected by XRD-, EPMA-, SEM- and EDX measurements. A detailed analysis of the powder XRD patterns and Rietveld structure refinement suggested for the oxidic material to be a mixture of the known γ-Hf_2N_2O and oI-HfO_2 polymorphs.

The lattice parameters (a_0), anion coordinates and isotropic temperature (Debye-Waller) factors for both c-$Zr_{2.86}(N_{0.88}O_{0.12})_4$ and c-Hf_3N_4 were derived from the Rietveld structure refinement of the measured powder XRD patterns. The patterns of zirconium- and hafnium nitride samples were collected using a standard X-ray diffractometer and a set-up utilizing synchrotron radiation, respectively. A high-brilliance X-ray synchrotron radiation was necessary for the XRD study of hafnium nitride, because of a strong absorption of X-rays by hafnium. In contrast to in-house diffractometer, synchrotron radiation allowed to collect for the hafnium nitride sample XRD patterns of a high quality allowing a detailed structural characterization. The lattice parameter of c-$Zr_{2.86}(N_{0.88}O_{0.12})_4$ was found to be 0.22 % higher than that of pure c-Zr_3N_4 obtained in a LH-DAC (Zerr et al. 2003). This deviation is attributed to the presence of oxygen in the crystal structure, which is in agreement with results of recent theoretical studies where substitution of nitrogen by oxygen in c-M_3N_4 results in expansion of the crystal lattice due to a weakening of the anion-cation bonding (Lowther 2008). In the hafnium nitride sample, c-Hf_3N_4 was found to coexist with a crystalline oxidic material. The

lattice parameter of this c-Hf_3N_4 synthesized in a multi-anvil apparatus was found to be in excellent agreement with that reported for oxygen-free material obtained in a LH-DAC (Zerr et al. 2003). These observations imply that, in contrast to c-Zr_3N_4, a significantly lower degree of nitrogen substitution by oxygen is accepted in the hafnium nitride having Th_3P_4-type structure.

The next part of this work concerned an experimental examination of properties of the synthesized nitrides. The compressibility of the oxygen-bearing cubic zirconium(IV) nitride, c-$Zr_{2.86}(N_{0.88}O_{0.12})_4$, synthesized in a multi-anvil apparatus and of cubic hafnium(IV) nitride, c-Hf_3N_4, synthesized in a LH-DAC was measured. Further, elastic shear and Young's moduli, nanoindentation- and Vickers hardness, and indentation fracture toughness of c-$Zr_{2.86}(N_{0.88}O_{0.12})_4$ were determined. Finally, the thermal expansion and high-temperature oxidation of c-$Zr_{2.86}(N_{0.88}O_{0.12})_4$ in air were investigated.

The specific volume change on compression was measured up to 45 GPa under quasi-hydrostatic load conditions in a diamond anvil cell. From these data the bulk moduli of c-$Zr_{2.86}(N_{0.88}O_{0.12})_4$ and of c-Hf_3N_4 were determined to be $B_0 = 219$ GPa ($B_0' = 4.4$) and $B_0 = 227$ GPa ($B_0' = 5.3$), respectively. The obtained values are slightly lower than those from preliminary compression measurements (≈ 250 GPa) (Zerr et al. 2003) and within the limits of the theoretically predicted ones (Kroll 2003; Mattesini et al. 2003; Lowther 2005). It should be mentioned that a decrease of B_0 for the oxygen-bearing zirconium(IV) nitride could be caused by a substitution of nitrogen with oxygen leading to a weakening of the cation-anion bonding (Lowther 2008). The influence of oxygen impurities on structural parameters and properties of the c-M_3N_4 materials could be a subject of future experimental and theoretical work.

The second elastic modulus of c-$Zr_{2.86}(N_{0.88}O_{0.12})_4$, namely the reduced elastic modulus E_r, was measured using nanoindentation technique. The obtained $E_r = 224$ GPa, in combination with the bulk modulus from compression measurements, was then used for determination of the shear modulus (G_0) and the Young's modulus (E_0) of c-$Zr_{2.86}(N_{0.88}O_{0.12})_4$. The derived $G_0 = 96$ GPa and $E_0 = 252$ GPa are considered as the lower limits since the nanoindentation data could have been altered by defects and pores in the investigated sample. Microstructural defects could also explain a large difference between the nanoindentation hardness value obtained for c-$Zr_{2.86}(N_{0.88}O_{0.12})_4$ (≈ 18 GPa) and that reported for dense c-Zr_3N_4 films (36 GPa) (Chhowalla & Unalan 2005). Even so, the differences between the present

experimental values of G_0 and E_0 for c-$Zr_{2.86}(N_{0.88}O_{0.12})_4$ and the predicted ones for c-Zr_3N_4 (G_0 = 129-145 GPa, E_0 = 324-368 GPa) (Mattesini et al. 2003) and for c-$Zr_3N_{3.5}O_{0.5}$ (G_0 = 67 GPa, E_0 = 182 GPa) (Lowther 2008) are substantial and demand further theoretical and experimental verifications.

Vickers indentation measurements were performed on a polished surface of the synthesized c-$Zr_{2.86}(N_{0.88}O_{0.12})_4$. Despite a high volume fraction of porosity (about 0.3) present in the material, its Vickers hardness was found to be $H_V(1)$ = 12 GPa. The $H_V(1)$ of fully dense c-Zr_3N_4 is expected to exceed 25 GPa which is significantly higher than that of the corresponding mononitride, δ-ZrN (12-15 GPa) (Ettmayer & Lengauer 1991; Chen et al. 2005). An even higher hardness can be expected for c-Hf_3N_4, since its experimental bulk modulus is about 4 % higher than that of c-$Zr_{2.86}(N_{0.88}O_{0.12})_4$. This supposition is of a qualitative character since the correlation between bulk modulus and hardness is not straightforward (Teter 1998; Zerr & Riedel 2000). However, a higher hardness of c-Hf_3N_4 with respect to c-Zr_3N_4 was also estimated from their theoretical shear moduli (Mattesini et al. 2003), which are considered to be "a significantly better qualitative predictor of hardness" than the bulk moduli (Teter 1998). Obviously, direct measurements of the hardness of pure and dense c-Hf_3N_4 (as well as of c-Zr_3N_4) will clarify the issue. The indentation fracture toughness (3.2 MPa $m^{1/2}$) of porous c-$Zr_{2.86}(N_{0.88}O_{0.12})_4$, estimated from the Vickers indentation cracks, was found to be comparable with that reported for δ-ZrN. Similarly to the hardness, the fracture toughness of dense c-Zr_3N_4 is expected to be significantly higher and to surpass those of δ-MN (M = Ti, Zr or Hf) and SiC ceramics.

Finally, the high-temperature behaviour of c-$Zr_{2.86}(N_{0.88}O_{0.12})_4$ was studied in air. Thermal expansion of the oxygen-bearing c-Zr_3N_4 was found to be comparable with that of δ-ZrN and o-Zr_3N_4 at room temperature, but significantly higher at elevated temperatures. This observation can be explained by a higher anharmonicity of the interatomic potential in the Th_3P_4-type structure due to high (eight-fold) cation coordination. The oxynitride c-$Zr_{2.86}(N_{0.88}O_{0.12})_4$ was found to be metastable up to at least 700 K. The maximum temperature of its metastability was not determined because at 773 K the material started to slowly oxidise in air, similar to o-Zr_3N_4 (Lerch 1997) and δ-ZrN powders and thin films (Lyutaya et al. 1970; Luridiana & Miotello 1996; Wiame et al. 1998; Reddy et al. 2007).

Thus, oxygen-bearing c-Zr_3N_4 synthesized and characterized in the present work represents a new class of high-pressure compounds with hardness and wear resistance superior to those of group 4 transition metal mononitrides. Even more advanced elasto-mechanical properties are

expected for c-Hf_3N_4 which can also be obtained at high pressures and temperatures in macroscopic amounts. Report on deposition of c-Zr_3N_4 as thin films exhibiting extraordinary wear resistance upon machining of low-carbon steels opens a wide area for application of these nitrides as hard protective coatings. Another potential industrial application of c-Zr_3N_4 and c-Hf_3N_4 may be based on their predicted semiconducting and superconducting properties or on large static dielectric constants (Kroll 2003; Mattesini et al. 2003; Xu et al. 2006; Lowther 2008). Therefore, the experimental investigation and evaluation of these functional properties of cubic zirconium(IV)- and hafnium(IV) nitrides could be a subject of future research.

References

Adachi, J., K. Kurosaki, M. Uno & S. Yamanaka, "Porosity influence on the mechanical properties of polycrystalline zirconium nitride ceramics", *J. Nucl. Mater. 358*, 106 (2006).

Adachi, J., K. Kurosaki, M. Uno & S. Yamanaka, "Effect of porosity on thermal and electrical properties of polycrystalline bulk ZrN prepared by spark plasma sintering", *J. Alloys Compd. 432*, 7 (2007).

Aigner, K., W. Lengauer, D. Rafaja & P. Ettmayer, "Lattice-Parameters and Thermal-Expansion of $Ti(C_xN_{1-x})$, $Zr(C_xN_{1-x})$, $Hf(C_xN_{1-x})$ and TiN_{1-x} from 298 K to 1473 K as Investigated by High-Temperature X-Ray-Diffraction", *J. Alloys Compd. 215*, 121 (1994).

Alexandre, N., M. Desmaisonbrut, F. Valin & M. Boncoeur, "Mechanical-Properties of Hot Isostatically Pressed Zirconium Nitride Materials", *J. Mater. Sci. 28*, 2385 (1993).

Andersson, C. A., "Derivation of the exponential relation for the effect of ellipsoidal porosity on elastic modulus", *J. Am. Ceram. Soc. 79*, 2181 (1996).

Andrievski, R. A., "Films of interstitial phases: synthesis and properties", *J. Mater. Sci. 32*, 4463 (1997).

Anstis, G. R., P. Chantikul, B. R. Lawn & D. B. Marshall, "A Critical-Evaluation of Indentation Techniques for Measuring Fracture-Toughness. 1. Direct Crack Measurements", *J. Am. Ceram. Soc. 64*, 533 (1981).

Ashcroft, N. W. & N. D. Mermin, *Solid State Physics* (Saunders College, Fort Worth, 1976).

Atkins, P. W., *Physical Chemistry* (Oxford University Press, Oxford, 1998).

Auckland, G. J., "High-pressure phases of group IV and III-V semiconductors", *Rep. Prog. Phys. 64*, 483 (2001).

Badding, J. V., L. J. Parker & D. C. Nesting, "High-Pressure Synthesis of Metastable Materials", *J. Solid State Chem. 117*, 229 (1995).

Badding, J. V., "Solid-state carbon nitrides", *Adv. Mater. 9*, 877 (1997).

Badding, J. V., "High-pressure synthesis, characterization, and tuning of solid state materials", *Annu. Rev. Mater. Sci. 28*, 631 (1998).

Badding, J. V., J. F. Meng & D. A. Polvani, "Pressure tuning in the search for new and improved solid state materials", *Chem. Mater. 10*, 2889 (1998).

Bagayoko, D. & G. L. Zhao, "Predicted electronic properties of cubic Si_3N_4", *Physica C 364*, 261 (2001).

Baker, T. W., "The Coefficient of Thermal Expansion of Zirconium Nitride", *Acta Cryst. 11*, 300 (1958).

Becker, J. S., E. Kim & R. G. Gordon, "Atomic layer deposition of insulating hafnium and zirconium nitrides", *Chem. Mater. 16*, 3497 (2004).

Bernhardt, E. O., "Über die Mikrohärte der Feststoffe im Grenzbereich des Kick'schen Ähnlichkeitssatzes", *Z. Metallkde 33*, 135 (1941).

Birch, F., "Finite Elastic Strain of Cubic Crystals", *Phys. Rev. 71*, 809 (1947).

Birch, F., "Finite Strain Isotherm and Velocities for Single-Crystal and Polycrystalline NaCl at High-Pressures and 300 K", *J. Geophys. Res. 83*, 1257 (1978).

Boehler, R. & A. Chopelas, "A new approach to laser-heating in high-pressure mineral physics", *Geophys. Res. Lett. 18*, 1147 (1991).

Boehler, R., "High-pressure experiments and the phase diagram of lower mantle and core materials", *Rev. Geophys. 38*, 221 (2000).

Boyd, F. R. & J. L. England, "Apparatus for phase-equilibrium measurements at pressures up to 50 kilobars and temperatures up to 1750 °C", *J. Geophys. Res. 65*, 741 (1960).

Bradley, R. S., "The Energetics and Statistical Mechanics of the Kinetics of Solid-Solid Reactions", *J. Phys. Chem. 60*, 1347 (1956).

Bradley, R. S., "Ch. 5.iii: First and Second Order Phase Changes in One Component System" in *High Pressure Physics and Chemistry* (ed. Bradley, R. S.), pp. 265-297 (Academic Press, London, 1963a).

Bradley, R. S. (ed.) *High Pressure Physics and Chemistry* (Academic Press, London, 1963b).

Bradley, R. S., D. C. Munro & Whitfiel.M, "Reactivity and Polymorphism of Selected Nitrides at High Temperatures and High Pressures", *J. Inorg. Nucl. Chem. 28*, 1803 (1966).

Brazhkin, V., N. Dubrovinskaia, A. Nicol, N. Novikov, R. Riedel, R. Solozhenko & Y. Zhao, "What-does 'harder than diamond' mean?" *Nat. Mater. 3*, 576 (2004).

Brazhkin, V. V., A. G. Lyapin, S. V. Popova, Y. A. Klyuev & A. M. Naletov, "Mechanical properties of the 3D polymerized, sp^2-sp^3 amorphous, and diamond-plus-graphite nanocomposite carbon phases prepared from C_{60} under high pressure", *J. Appl. Phys. 84*, 219 (1998).

Brazhkin, V. V., A. G. Lyapin & R. J. Hemley, "Harder than diamond: dreams and reality", *Phil. Mag. A 82*, 231 (2002).

Brazhkin, V. V., "High-pressure synthesized materials: treasures and hints", *High Pressure Res. 27*, 333 (2007).

Bridgman, P. W., "The Resistance of 72 Elements, Alloys and Compounds to 100 000 kg/cm^2", *Proc. Am. Acad. Arts Sci. 81*, 165 (1952).

Brookes, C. A., "The mechanical properties of cubic boron nitride - A perspective view", *Inst. Phys. Conf. Ser. 75*, 207 (1986).

Bull, S. J., T. F. Page & E. H. Yoffe, "An Explanation of the Indentation Size Effect in Ceramics", *Phil. Mag. Lett. 59*, 281 (1989).

Bull, S. J., "On the origins and mechanisms of the indentation size effect", *Z. Metallkde 94*, 787 (2003).

Bull, S. J., "Nano-indentation of coatings", *J. Phys. D 38*, R393 (2005).

Chandran, L., H. R. Krishna-murthy & T. V. Ramakrishnan, "Pressure-induced valence changes in mixed-valent systems", *J. Phys.: Condens. Matter 4*, 7067 (1992).

Chen, X. J., V. V. Struzhkin, Z. G. Wu, M. Somayazulu, J. Qian, S. Kung, A. N. Christensen, Y. S. Zhao, R. E. Cohen, H. K. Mao & R. J. Hemley, "Hard superconducting nitrides", *Proc. Natl. Acad. Sci. U.S.A. 102*, 3198 (2005).

Chhowalla, M. & H. E. Unalan, "Thin films of hard cubic Zr_3N_4 stabilized by stress", *Nat. Mater. 4*, 317 (2005).

Ching, W. Y., S. D. Mo, L. Ouyang, I. Tanaka & M. Yoshiya, "Prediction of the new spinel phase of Ti_3N_4, and $SiTi_2N_4$ and the metal-insulator transition", *Phys. Rev. B 61*, 10609 (2000).

Ching, W. Y., S. D. Mo, I. Tanaka & M. Yoshiya, "Prediction of spinel structure and properties of single and double nitrides", *Phys. Rev. B 63*, 064102 (2001).

Ching, W. Y., S. D. Mo, L. Z. Ouyang, P. Rulis, I. Tanaka & M. Yoshiya, "Theoretical prediction of the structure and properties of cubic spinel nitrides", *J. Am. Ceram. Soc. 85*, 75 (2002a).

Ching, W. Y., Y. N. Xu & L. Ouyang, "Electronic and dielectric properties of insulating Zr_3N_4", *Phys. Rev. B 66*, 235106 (2002b).

Ching, W. Y. & P. Rulis, "Ab initio calculation of the electronic structure and spectroscopic properties of spinel gamma-Sn_3N_4", *Phys. Rev. B 73*, 045202 (2006).

Cho, S. A., I. B. de Arenas, F. J. Arenas, J. Ochoa & J. L. Ochoa, "Porosity; microhardness correlation of sintered $(Al_{1-y}Cr_y)_2O_3$ solid solutions", *J. Alloys Compd. 288*, 211 (1999).

Christian, J. W., *The theory of transformations in metals and alloys I: Equilibrium and general kinetic theory* (Pergamon Press, Oxford, 1975).

Clarke, S. J., C. W. Michie & M. J. Rosseinsky, "Structure of Zr_2ON_2 by neutron powder diffraction: The absence of nitride-oxide ordering", *J. Solid State Chem. 146*, 399 (1999).

Coble, R. L. & W. D. Kingery, "Effect of Porosity on Physical Properties of Sintered Alumina", *J. Am. Ceram. Soc. 39*, 377 (1956).

Cohen, M. L., "Calculation of Bulk Moduli of Diamond and Zincblende Solids", *Phys. Rev. B 32*, 7988 (1985).

Cook, R. F. & G. M. Pharr, "Direct Observation and Analysis of Indentation Cracking in Glasses and Ceramics", *J. Am. Ceram. Soc. 73*, 787 (1990).

Crowhurst, J. C., A. F. Goncharov, B. Sadigh, C. L. Evans, P. G. Morrall, J. L. Ferreira & A. J. Nelson, "Synthesis and characterization of the nitrides of platinum and iridium", *Science 311*, 1275 (2006).

Curtis, C. E., L. M. Doney & J. R. Johnson, "Some Properties of Hafnium Oxide, Hafnium Silicate, Calcium Hafnate, and Hafnium Carbide", *J. Am. Ceram. Soc. 37*, 458 (1954).

Cynn, H., J. E. Klepeis, C. S. Yoo & D. A. Young, "Osmium has the lowest experimentally determined compressibility", *Phys. Rev. Lett. 88*, 135701 (2002).

Davis, R. F., "III-V nitrides for electronic and optoelectronic applications", *Proc. IEEE 79*, 702 (1991).

Davison, L., Y. Hori & T. Sekine, *Shock Compression of Solids* (Springer-Verlag, New York, 2002).

Demazeau, G., "High pressure in solid-state chemistry", *J. Phys.: Condens. Matter 14*, 11031 (2002).

Desmaison-Brut, M., J. Montintin, F. Valin & M. Boncoeur, "Mechanical properties and oxidation behaviour of HIPed hafnium nitride ceramics", *J. Eur. Ceram. Soc. 13*, 379 (1994).

DiSalvo, F. J., "Solid-State Chemistry - a Rediscovered Chemical Frontier", *Science 247*, 649 (1990).

DiSalvo, F. J. & S. J. Clarke, "Ternary nitrides: A rapidly growing class of new materials", *Curr. Opin. Solid State Mater. Sci. 1*, 241 (1996).

Doerner, M. F. & W. D. Nix, "A method for interpreting the data from depth-sensing indentation instruments", *J. Mater. Res. 1*, 601 (1986).

Dong, J. J., O. F. Sankey, S. K. Deb, G. Wolf & P. F. McMillan, "Theoretical study of beta-Ge_3N_4 and its high-pressure spinel gamma phase", *Phys. Rev. B 61*, 11979 (2000).

Dong, J. J., J. Deslippe, O. F. Sankey, E. Soignard & P. F. McMillan, "Theoretical study of the ternary spinel nitride system Si_3N_4-Ge_3N_4", *Phys. Rev. B 67*, 094104 (2003).

Drory, M. D., R. H. Dauskardt, A. Kant & R. O. Ritchie, "Fracture of synthetic diamond", *J. Appl. Phys. 78*, 3083 (1995).

Duan, K. & R. W. Steinbrech, "Influence of sample deformation and porosity on mechanical properties by instrumented microindentation technique", *J. Eur. Ceram. Soc. 18*, 87 (1998).

Dubrovinsky, L. S., N. A. Dubrovinskaia, V. Swamy, J. Muscat, N. M. Harrison, R. Ahuja, B. Holm & B. Johansson, "Materials science - The hardest known oxide", *Nature 410*, 653 (2001).

Duckworth, W. H., "Discussion of Ryshkewitch Paper by Winston Duckworth", *J. Am. Ceram. Soc. 36*, 68 (1953).

Dusza, J., "Comparison of Fracture-Toughness Testing Methods Applied to Si_3N_4 + Si_3N_4-Whisker System", *Scripta Metall. Mater. 26*, 337 (1992).

Elliott, S. R., *The physics and chemistry of solids* (J. Wiley & Sons, Chichester, 1998).

Eremets, M. I., *High Pressure Experimental Methods* (Oxford University Press, Oxford, 1996).

Eremets, M. I., A. G. Gavriliuk, I. A. Trojan, D. A. Dzivenko & R. Boehler, "Single-bonded cubic form of nitrogen", *Nat. Mater. 3*, 558 (2004).

Eremets, M. I., I. A. Trojan, P. Gwaze, J. Huth, R. Boehler & V. D. Blank, "The strength of diamond", *Appl. Phys. Lett. 87*, 141902 (2005).

Ettmayer, P. & W. Lengauer, "Nitrides" in *Ullmann's Encyclopedia of Industrial Chemistry*, p. 341 (Wiley-VCH, Weinheim, 1991).

Evans, A. G. & E. A. Charles, "Fracture Toughness Determinations by Indentation", *J. Am. Ceram. Soc. 59*, 371 (1976).

Evans, A. G., "Fracture Toughness: The Role of Indentation Techniques" in *Fracture Mechanics Applied to Brittle Materials, ASTM STP 678* (ed. Freiman, S. W.), pp. 112-135 (ASTM, Philadelphia, PA, 1979).

Fang, C. M., G. A. de Wijs, H. T. Hintzen & G. de With, "Phonon spectrum and thermal properties of cubic Si_3N_4 from first-principles calculations", *J. Appl. Phys. 93*, 5175 (2003).

Fang, P. H., "On the beta-C_3N_4 search", *J. Mater. Sci. Lett. 14*, 536 (1995).

Fischer-Cripps, A. C., *Introduction to Contact Mechanics* (Springer-Verlag, New York, 2000).

Fischer-Cripps, A. C., *Nanoindentation* (Springer-Verlag, New York, 2002).

Fix, R., R. G. Gordon & D. M. Hoffman, "Chemical Vapor-Deposition of Titanium, Zirconium, and Hafnium Nitride Thin-Films", *Chem. Mater. 3*, 1138 (1991).

Fix, R. M., R. G. Gordon & D. M. Hoffman, "Solution-Phase Reactivity as a Guide to the Low-Temperature Chemical Vapor-Deposition of Early-Transition-Metal Nitride Thin-Films", *J. Am. Chem. Soc. 112*, 7833 (1990).

Fortov, V. E., L. V. Al'tshuler, R. F. Trunin & A. I. Funtikov, *Shock Waves and Extreme States of Matter* (Springer-Verlag, New York, 2004).

Fröhlich, F., P. Grau & W. Grellmann, "Performance and Analysis of Recording Microhardness Tests", *Phys. Status Solidi A 42*, 79 (1977).

Gandolfi, G., "Discussion upon methods to obtain X-ray "powder patterns" from a single crystal", *Miner. Petrogr. Acta 13*, 67 (1967).
Gerk, A. P., "Effect of Work-Hardening Upon Hardness of Solids - Minimum Hardness", *J. Mater. Sci. 12*, 735 (1977).
Ghosh, A., M. G. Jenkins, K. W. White, A. S. Kobayashi & R. C. Bradt, "Elevated-Temperature Fracture-Resistance of a Sintered Alpha-Silicon Carbide", *J. Am. Ceram. Soc. 72*, 242 (1989).
Ghosh, A., Z. Li, C. H. Henager, A. S. Kobayashi & R. C. Bradt, "Vickers microindentation toughness of a sintered SiC in the median crack regime" in *Fracture Mechanics of Ceramics, Vol. 11* (ed. Bradt, R. C.), (Plenum Press, New York, 1996).
Gilman, J. J., "Escape of Dislocations from Bound States by Tunneling", *J. Appl. Phys. 39*, 6086 (1968).
Goglio, G., D. Foy & G. Demazeau, "State of Art and recent trends in bulk carbon nitrides synthesis", *Mater. Sci. Eng. R 58*, 195 (2008).
Göken, M. & M. Kempf, "Pop-ins in nanoindentations - the initial yield point", *Z. Metallkd. 92*, 1061 (2001).
Gong, J. H., "Determining indentation toughness by incorporating true hardness into fracture mechanics equations", *J. Eur. Ceram. Soc. 19*, 1585 (1999).
Gong, J. H., J. J. Wu & Z. D. Guan, "Examination of the indentation size effect in low-load Vickers hardness testing of ceramics", *J. Eur. Ceram. Soc. 19*, 2625 (1999).
Gong, J. H., J. Q. Wang & Z. D. Guan, "Indentation toughness of ceramics: A modified approach", *J. Mater. Sci. 37*, 865 (2002).
Gregory, D. H., "Structural families in nitride chemistry", *J. Chem. Soc. Dalton Trans.*, 259 (1999).
Gregoryanz, E., C. Sanloup, M. Somayazulu, J. Badro, G. Fiquet, H. K. Mao & R. J. Hemley, "Synthesis and characterization of a binary noble metal nitride", *Nat. Mater. 3*, 294 (2004).
Griffen, D. T., *Silicate Crystal Chemistry* (Oxford University Press, New York, 1992).
Haines, J., J. M. Leger & G. Bocquillon, "Synthesis and design of superhard materials", *Annu. Rev. Mater. Res. 31*, 1 (2001).
Hall, E. O., "The Deformation and Ageing of Mild Steel .3. Discussion of Results", *Proc. Phys. Soc. Lond. B 64*, 747 (1951).
Hall, H. T., "Some high-pressure, high-temperature apparatus design considerations: Equipment for use at 100 000 atmospheres and 3000 °C", *Rev. Sci. Instrum. 29*, 267 (1958).
Hall, H. T., "Ultra-High-Pressure, High-Temperature Apparatus - the Belt", *Rev. Sci. Instrum. 31*, 125 (1960).
Hama, J. & K. Suito, "The search for a universal equation of state correct up to very high pressures", *J. Phys.: Condens. Matter 8*, 67 (1996).
Hamann, S. D., "Ch. 7.ii: Chemical Equilibria in Condensed Systems; Ch. 8: Chemical Kinetics" in *High Pressure Physics and Chemistry* (ed. Bradley, R. S.), pp. 131-207 (Academic Press, London, 1963).
Hammersley, A. P., S. O. Svensson, M. Hanfland, A. N. Fitch & D. Hausermann, "Two-dimensional detector software: From real detector to idealised image or two-theta scan", *High Pressure Res. 14*, 235 (1996).
Hasegawa, M. & T. Yagi, "Synthesis of Co_2N by a simple direct nitriding reaction between nitrogen and cobalt under 10 GPa and 1800 K using diamond anvil cell and YAG laser heating", *Solid State Commun. 135*, 294 (2005).
Hays, C. & E. G. Kendall, "An analysis of Knoop microhardness", *Metallography 6*, 275 (1973).
Hazen, R. M., *The Diamond Makers* (Cambridge University Press, Cambridge, 1999).
He, H. L., T. Sekine, T. Kobayashi, H. Hirosaki & I. Suzuki, "Shock-induced phase transition of beta-Si_3N_4 to c-Si_3N_4", *Phys. Rev. B 62*, 11412 (2000).
He, H. L., T. Sekine, T. Kobayashi & K. Kimoto, "Phase transformation of germanium nitride (Ge_3N_4) under shock wave compression", *J. Appl. Phys. 90*, 4403 (2001).
Hemley, R. J., "Effects of high pressure on molecules", *Annu. Rev. Phys. Chem. 51*, 763 (2000).
Hertz, H., "Über die Berührung fester elastischer Körper", *J. Reine Angew. Math. 92*, 156 (1881).
Hertzberg, R. W., *Deformation and Fracture Mechanics of Engineering Materials* (J. Wiley & Sons, New York, 1996).
Hintzen, H. T., M. Hendrix, H. Wondergem, C. M. Fang, T. Sekine & G. de With, "Thermal expansion of cubic Si_3N_4 with the spinel structure", *J. Alloys Compd. 351*, 40 (2003).

Hirao, K. & M. Tomozawa, "Microhardness of SiO_2 Glass in Various Environments", *J. Am. Ceram. Soc. 70*, 497 (1987).

Hofmeister, A. M., "Interatomic Potentials Calculated from Equations of State: Limitation of Finite Strain to Moderate K′ ", *Geophys. Res. Lett. 20*, 635 (1993).

Holleck, H., *Binäre und ternäre Carbid- und Nitridsysteme der Übergangsmetalle* (Gebrüder Borntraeger, Berlin, 1984).

Holloway, J. R. & B. J. Wood, *Simulating the Earth* (Harper Collins Academic, London, 1988).

Holzapfel, W. B., "Physics of solids under strong compression", *Rep. Prog. Phys. 59*, 29 (1996).

Holzapfel, W. B. & N. S. Isaacs (eds.) *High-pressure Techniques in Chemistry and Physics* (Oxford University Press, Oxford, 1997).

Holzapfel, W. B., "Equations of state for solids under strong compression", *High Pressure Res. 16*, 81 (1998).

Horvath-Bordon, E., R. Riedel, A. Zerr, P. F. McMillan, G. Auffermann, Y. Prots, W. Bronger, R. Kniep & P. Kroll, "High-pressure chemistry of nitride-based materials", *Chem. Soc. Rev. 35*, 987 (2006).

Houska, C. R., "Thermal Expansion + Atomic Vibration Amplitudes for TiC TiN ZrC ZrN + Pure Tungsten", *J. Phys. Chem. Solids 25*, 359 (1964).

Huppertz, H., "Multianvil high-pressure high-temperature synthesis in solid state chemistry", *Z. Kristallogr. 219*, 330 (2004).

Jang, B. K. & H. Matsubara, "Influence of porosity on hardness and Young's modulus of nanoporous EB-PVD TBCs by nanoindentation", *Mater. Lett. 59*, 3462 (2005).

Jayaraman, A., W. Lowe, L. D. Longinotti & E. Bucher, "Pressure-Induced Valence Change in Cerium Phosphide", *Phys. Rev. Lett. 36*, 366 (1976).

Jeanloz, R., "Universal equation of state", *Phys. Rev. B 38*, 805 (1988).

Jiang, J. Z., K. Stahl, R. W. Berg, D. J. Frost, T. J. Zhou & P. X. Shi, "Structural characterization of cubic silicon nitride", *Europhys. Lett. 51*, 62 (2000a).

Jiang, J. Z., F. Kragh, D. J. Frost, K. Stahl & H. Lindelov, "Hardness and thermal stability of cubic silicon nitride", *J. Phys.: Condens. Matter 13*, L515 (2001).

Jiang, J. Z., H. Lindelov, L. Gerward, K. Stahl, J. M. Recio, P. Mori-Sanchez, S. Carlson, M. Mezouar, E. Dooryhee, A. Fitch & D. J. Frost, "Compressibility and thermal expansion of cubic silicon nitride", *Phys. Rev. B 65*, 161202 (2002).

Jiang, Z., F. X. Lu, W. Z. Tang, S. G. Wang, Y. M. Tong, T. B. Huang & J. M. Liu, "Accurate measurement of fracture toughness of free standing diamond films by three-point bending tests with sharp pre-cracked specimens", *Diamond Relat. Mater. 9*, 1734 (2000b).

Johansson, B. O., H. T. G. Hentzell, J. M. E. Harper & J. J. Cuomo, "Higher nitrides of hafnium, zirconium, and titanium synthesized by dual ion beam deposition", *J. Mater. Res. 1*, 442 (1986).

Johnson, K. L., *Contact mechanics* (Cambridge University Press, Cambridge, 1985).

Juza, R., A. Rabenau & I. Nitschke, "Über ein braunes Zirkonnitrid Zr_3N_4", *Z. Anorg. Allg. Chem. 332*, 1 (1964).

Kaner, R. B., J. J. Gilman & S. H. Tolbert, "Materials science - Designing superhard materials", *Science 308*, 1268 (2005).

Kanke, Y., M. Akaishi, S. Yamaoka & T. Taniguchi, "Heater cell for materials synthesis and crystal growth in the large volume high pressure apparatus at 10 GPa", *Rev. Sci. Instrum. 73*, 3268 (2002).

Karavaev, G. F. & A. V. Khrapov, "Group-Theoretical Study of Phonon Spectrum in Th_3P_4-Type Crystals", *Izv. Vyssh. Uchebn. Zaved., Fiz.*, 62 (1975).

Kawai, N., "Apparatus with Tapering Multi-Pistons Forming a Sphere", *Proc. Jpn. Acad. 42*, 385 (1966).

Kawai, N. & S. Endo, "Generation of Ultrahigh Hydrostatic Pressures by a Split Sphere Apparatus", *Rev. Sci. Instrum. 41*, 1178 (1970).

Kelly, A. & N. H. Macmillan, *Strong Solids* (Clarendon Press, Oxford, 1986).

Keppler, H. & D. J. Frost, "Introduction to minerals under extreme conditions" in *EMU Notes in Mineralogy, Vol. 7: Mineral Behaviour at Extreme Conditions* (ed. Miletich, R.), pp. 1-30 (Eötvös University Press, Budapest, 2005).

Khvostantsev, L. G., L. F. Vereshchagin & A. P. Novikov, "Device of toroid type for high pressure generation", *High Temp. - High Pressures 9*, 637 (1977).

Khvostantsev, L. G., V. N. Slesarev & V. V. Brazhkin, "Toroid type high-pressure device: History and prospects", *High Pressure Res. 24*, 371 (2004).

Kim, Y. W., M. Mitomo & H. Hirotsuru, "Grain-growth and fracture toughness of fine-grained silicon-carbide ceramics", *J. Am. Ceram. Soc. 78*, 3145 (1995).

King, R. B., "Elastic analysis of some punch problems for a layered medium", *Int. J. Solids Struct. 23*, 1657 (1987).

Kittel, C., *Introduction to solid state physics, 6th ed.* (J. Wiley & Sons, New York, 1986).

Kleber, W. & K. T. Wilke, "Synthese und Kristallchemie anorganischer Stoffe bei hohen Drücken und Temperaturen", *Krist. Techn. 4*, 165 (1969).

Kniep, R., "Ternary and quaternary metal nitrides: A new challenge for solid state chemistry", *Pure Appl. Chem. 69*, 185 (1997).

Kondo, T., H. Sawamoto, A. Yoneda, M. Kato, A. Matsumuro & T. Yagi, "Ultrahigh-pressure and high-temperature generation by use of the MA8 system with sintered-diamond anvils", *High Temp. - High Pressures 25*, 105 (1993).

Kral, C., W. Lengauer, D. Rafaja & P. Ettmayer, "Critical review on the elastic properties of transition metal carbides, nitrides and carbonitrides", *J. Alloys Compd. 265*, 215 (1998).

Kroke, E., "High-pressure syntheses of novel binary nitrogen compounds of main group elements", *Angew. Chem. Int. Edit. 41*, 77 (2002).

Kroke, E. & M. Schwarz, "Novel group 14 nitrides", *Coord. Chem. Rev. 248*, 493 (2004).

Kroll, P., "Hafnium nitride with thorium phosphide structure: Physical properties and an assessment of the Hf-N, Zr-N, and Ti-N phase diagrams at high pressures and temperatures", *Phys. Rev. Lett. 90*, 125501 (2003).

Kroll, P., "Assessment of the Hf-N, Zr-N and Ti-N phase diagrams at high pressures and temperatures: balancing between MN and M_3N_4 (M = Hf, Zr, Ti)", *J. Phys.: Condens. Matter 16*, S1235 (2004).

Kubo, R., *Thermodynamics: an advanced course with problems and solutions* (North-Holland, Amsterdam, 1968).

Kuwahara, H., N. Mazaki, M. Takahashi, T. Watanabe, X. Yang & T. Aizawa, "Mechanical properties of bulk sintered titanium nitride ceramics", *Mater. Sci. Eng. A 319*, 687 (2001).

Lahr, P. H. & W. G. Eversole, "Compression isotherms of argon, krypton, and xenon through the freezing zone", *J. Chem. Eng. Data 7*, 42 (1962).

Landau, L. D. & E. M. Lifshitz, *Course of Theoretical Physics, vol. 7: Theory of Elasticity* (Pergamon Press, London, 1975).

Landskron, K., H. Huppertz, J. Senker & W. Schnick, "High-pressure synthesis of gamma-P_3N_5 at 11 GPa and 1500 °C in a multianvil assembly: A binary phosphorus(v) nitride with a three-dimensional network structure from PN_4 tetrahedra and tetragonal PN_5 pyramids", *Angew. Chem. Int. Edit. 40*, 2643 (2001).

Landskron, K., H. Huppertz, A. Senker & W. Schnick, "Multianvil synthesis, X-ray powder diffraction analysis, P-31-MAS-NMR, and FTIR spektroscopy as well as material properties of gamma-P_3N_5, a high-pressure polymorph of binary phosphorus(V) nitride, built up from distorted PN_5 square pyramids and PN_4 tetrahedra", *Z. Anorg. Allg. Chem. 628*, 1465 (2002).

Lankford, J., "Threshold Microfracture during Elastic-Plastic Indentation of Ceramics", *J. Mater. Sci. 16*, 1177 (1981).

Lankford, J., "Indentation Microfracture in the Palmqvist Crack Regime - Implications for Fracture-Toughness Evaluation by the Indentation Method", *J. Mater. Sci. Lett. 1*, 493 (1982).

Laugier, M. T., "Palmqvist Crack Extension and the Center-Loaded Penny Crack Analogy", *J. Am. Ceram. Soc. 68*, C51 (1985).

Lawn, B. R. & D. B. Marshall, "Hardness, Toughness, and Brittleness - Indentation Analysis", *J. Am. Ceram. Soc. 62*, 347 (1979).

Lawn, B. R., A. G. Evans & D. B. Marshall, "Elastic-Plastic Indentation Damage in Ceramics - the Median-Radial Crack System", *J. Am. Ceram. Soc. 63*, 574 (1980).

Lawn, B. R., *Fracture of Brittle Solids* (Cambridge University Press, Cambridge, 1995).

Le Bail, A., H. Duroy & J. L. Fourquet, "Ab-initio structure determination of $LiSbWO_6$ by X-ray powder diffraction", *Mater. Res. Bull. 23*, 447 (1988).

Le Chatelier, H., "Sur un énoncé général des lois des équilibres chimiques", *C. R. Acad. Sci. Paris 99*, 786 (1884).

Leger, J. M., J. Haines & B. Blanzat, "Materials Potentially Harder Than Diamond - Quenchable High-Pressure Phases of Transition-Metal Dioxides", *J. Mater. Sci. Lett. 13*, 1688 (1994).

Leger, J. M., J. Haines, M. Schmidt, J. P. Petitet, A. S. Pereira & J. A. H. daJornada, "Discovery of hardest known oxide", *Nature 383*, 401 (1996).

Leger, J. M. & J. Haines, "The search for superhard materials", *Endeavour 21*, 121 (1997).

Leger, J. M., P. Djemia, F. Ganot, J. Haines, A. S. Pereira & J. A. H. daJornada, "Hardness and elasticity in cubic ruthenium dioxide", *Appl. Phys. Lett. 79*, 2169 (2001).

Leinenweber, K., M. O'Keeffe, M. Somayazulu, H. Hubert, P. F. McMillan & G. H. Wolf, "Synthesis and structure refinement of the spinel, gamma-Ge_3N_4", *Chem. Eur. J. 5*, 3076 (1999).

Leitch, S., A. Moewes, L. Ouyang, W. Y. Ching & T. Sekine, "Properties of non-equivalent sites and bandgap of spinel-phase silicon nitride", *J. Phys.: Condens. Matter 16*, 6469 (2004).

Lengauer, W., "Transition Metal Carbides, Nitrides, and Carbonitrides" in *Handbook of Ceramic Hard Materials* (ed. Riedel, R.), pp. 202-252 (WILEY-VCH, Weinheim, 2000).

Lerch, M., E. Füglein & J. Wrba, "Synthesis, crystal structure, and high temperature behavior of Zr_3N_4", *Z. Anorg. Allg. Chem. 622*, 367 (1996).

Lerch, M., "Neue Anionendefizit-Materialen auf der Basis von ZrO_2: Synthese, Charakterisierung und Eigenschaften von ternären und quaternären Nitridoxiden des Zirconiums", *Postdoctoral thesis* (Fakultät für Chemie und Pharmazie, Bayerische Julius-Maximilians-Universität, Würzburg, 1997).

Li, H. & R. C. Bradt, "The Microhardness Indentation Load Size Effect in Rutile and Cassiterite Single-Crystals", *J. Mater. Sci. 28*, 917 (1993).

Li, H., A. Ghosh, Y. H. Han & R. C. Bradt, "The Frictional Component of the Indentation Size Effect in Low Load Microhardness Testing", *J. Mater. Res. 8*, 1028 (1993).

Li, J., C. Hadidiacos, H. K. Mao, Y. W. Fei & R. J. Hemley, "Behavior of thermocouples under high pressure in a multi-anvil apparatus", *High Pressure Res. 23*, 389 (2003).

Li, J. W., D. A. Dzivenko, A. Zerr, C. Fasel, Y. P. Zhou & R. Riedel, "Synthesis of nanocrystalline Zr_3N_4 and Hf_3N_4 powders from metal dialkylamides", *Z. Anorg. Allg. Chem. 631*, 1449 (2005).

Li, X. D. & B. Bhushan, "A review of nanoindentation continuous stiffness measurement technique and its applications", *Mater. Charact. 48*, 11 (2002).

Li, Z., A. Ghosh, A. S. Kobayashi & R. C. Bradt, "Indentation Fracture-Toughness of Sintered Silicon-Carbide in the Palmqvist Crack Regime", *J. Am. Ceram. Soc. 72*, 904 (1989).

Li, Z., A. Ghosh, A. S. Kobayashi & R. C. Bradt, "Indentation Fracture-Toughness of Sintered Silicon-Carbide in the Palmqvist Crack Regime - Reply", *J. Am. Ceram. Soc. 74*, 889 (1991).

Lide, D. R. (ed.) *CRC Handbook of Chemistry and Physics* (CRC Press, Boca Raton, FL, 2005).

Liu, A. Y. & R. M. Wentzcovitch, "Stability of carbon nitride solids", *Phys. Rev. B 50*, 10362 (1994).

Liu, D. M., B. W. Lin & C. T. Fu, "Porosity Dependence of Mechanical Strength and Fracture-Toughness in SiC-Al_2O_3-Y_2O_3 Ceramics", *J. Ceram. Soc. Jpn. 103*, 878 (1995).

Locherer, T., D. J. Frost & H. Fuess, "High-pressure high-temperature behavior of nitrogen-doped zirconia", *J. Solid State Chem.*, doi:10.1016/j.jssc.2008.07.033 (2008).

Loudon, R., "Raman Effect in Crystals", *Adv. Phys. 13*, 423 (1964).

Lowther, J. E., "Influence of nitrogen stoichiometry on properties of low-compressibility advanced nitrides", *Physica B 358*, 72 (2005).

Lowther, J. E., "Elastic and electronic properties of oxygen and carbon incorporated into Zr_3N_4 and Hf_3N_4", *Solid State Commun.*, doi:10.1016/j.ssc.2008.09.046 (2008).

Luo, J. & R. Stevens, "Porosity-dependence of elastic moduli and hardness of 3Y-TZP ceramics", *Ceram. Int. 25*, 281 (1999).

Luo, S. N., O. Tschauner, P. D. Asimow & T. J. Ahrens, "A new dense silica polymorph: A possible link between tetrahedrally and octahedrally coordinated silica", *Amer. Mineral. 89*, 455 (2004).

Luridiana, S. & A. Miotello, "Spectrophotometric study of oxide growth on arc evaporated TiN and ZrN coatings during hot air oxidation tests", *Thin Solid Films 291*, 289 (1996).

Lyutaya, M. D., O. P. Kulik & E. T. Kachkovskaya, "Thermal decomposition of the nitrides of some transition metals in air", *Powder Metall. Met. Ceram. 9*, 233 (1970).

Malkow, T., "Critical observations in the research of carbon nitride", *Mater. Sci. Eng. A 292*, 112 (2000).

Marchand, R., F. Tessier & F. J. DiSalvo, "New routes to transition metal nitrides: preparation and characterization of new phases", *J. Mater. Chem. 9*, 297 (1999).

Markel, E. J. & M. E. Leaphart, "Nitrides" in *Kirk-Othmer Encyclopedia of Chemical Technology, Vol. 17*, p. 57 (J. Wiley & Sons, New York, 1998).
Maruska, H. P. & J. J. Tietjen, "Preparation and Properties of Vapor-Deposited Single-Crystalline GaN", *Appl. Phys. Lett. 15*, 327 (1969).
Matsumoto, S., E. Q. Xie & F. Izumi, "On the validity of the formation of crystalline carbon nitrides, C_3N_4", *Diamond Relat. Mater. 8*, 1175 (1999).
Mattesini, M., R. Ahuja & B. Johansson, "Cubic Hf_3N_4 and Zr_3N_4: A class of hard materials", *Phys. Rev. B 68*, 184108 (2003).
McColm, I. J., *Ceramic Hardness* (Plenum Press, New York, 1990).
McMillan, P. F., "High pressure synthesis of solids", *Curr. Opin. Solid State Mater. Sci. 4*, 171 (1999).
McMillan, P. F., "New materials from high-pressure experiments", *Nat. Mater. 1*, 19 (2002).
McMillan, P. F., "New materials from high pressure experiments: Challenges and opportunities", *High Pressure Res. 23*, 7 (2003).
Miess, D. & G. Rai, "Fracture toughness and thermal resistance of polycrystalline diamond compacts", *Mater. Sci. Eng. A 209*, 270 (1996).
Milman, Y. V., S. I. Chugunova, I. V. Goncharova, T. Chudoba, W. Lojkowski & W. Gooch, "Temperature dependence of hardness in silicon-carbide ceramics with different porosity", *Int. J. Refract. Met. Hard Mater. 17*, 361 (1999).
Ming, L. & W. A. Bassett, "Laser-Heating in Diamond Anvil Press up to 2000 °C Sustained and 3000 °C Pulsed at Pressures up to 260 Kilobars", *Rev. Sci. Instrum. 45*, 1115 (1974).
Mo, S. D., L. Z. Ouyang, W. Y. Ching, I. Tanaka, Y. Koyama & R. Riedel, "Interesting physical properties of the new spinel phase of Si_3N_4 and C_3N_4", *Phys. Rev. Lett. 83*, 5046 (1999).
Molodetsky, I., A. Navrotsky, F. J. DiSalvo & M. Lerch, "Energetics of oxidation of oxynitrides: Zr–N–O, Y–Zr–N–O, Ca–Zr–N–O, and Mg–Zr–N–O", *J. Mater. Res. 15*, 2558 (2000).
Monemar, B., "Fundamental Energy-Gap of GaN from Photoluminescence Excitation-Spectra", *Phys. Rev. B 10*, 676 (1974).
Moriyama, M., H. Aoki, Y. Kobayashi & K. Kamata, "The Mechanical-Properties of Hot-Pressed TiN Ceramics with Various Additives", *J. Ceram. Soc. Jpn. 101*, 279 (1993).
Morrell, R., "Fracture toughness testing for advanced technical ceramics: internationally agreed good practice", *Adv. Appl. Ceram. 105*, 88 (2006).
Muhl, S. & J. M. Mendez, "A review of the preparation of carbon nitride films", *Diamond Relat. Mater. 8*, 1809 (1999).
Mujica, A., A. Rubio, A. Munoz & R. J. Needs, "High-pressure phases of group-IV, III-V, and II-VI compounds", *Rev. Mod. Phys. 75*, 863 (2003).
Murakami, M., K. Hirose, S. Ono & Y. Ohishi, "Stability of $CaCl_2$-type and alpha-PbO_2-type SiO_2 at high pressure and temperature determined by in-situ X-ray measurements", *Geophys. Res. Lett. 30*, 1207 (2003).
Murnaghan, F. D., "The Compressibility of Media under Extreme Pressures", *Proc. Natl. Acad. Sci. U.S.A. 30*, 244 (1944).
Neuhaus, A., "Synthese Strukturverhalten + Valenzzustande Der Anorganischen Materie Im Bereich Hoher + Hoechster Drucke", *Chimia 18*, 93 (1964).
Niewa, R. & F. J. DiSalvo, "Recent developments in nitride chemistry", *Chem. Mater. 10*, 2733 (1998).
Niihara, K., R. Morena & D. P. H. Hasselman, "Evaluation of K_{Ic} of Brittle Solids by the Indentation Method with Low Crack-to-Indent Ratios", *J. Mater. Sci. Lett. 1*, 13 (1982).
Novikov, N. V. & S. N. Dub, "Hardness and fracture roughness of CVD diamond film", *Diamond Relat. Mater. 5*, 1026 (1996).
Ohtaka, O., T. Yamanaka & S. Kume, "Synthesis and X-Ray Structural-Analysis by the Rietveld Method of Orthorhombic Hafnia", *J. Ceram. Soc. Jpn. 99*, 826 (1991).
Ohtaka, O., H. Fukui, T. Kunisada, T. Fujisawa, K. Funakoshi, W. Utsumi, T. Irifune, K. Kuroda & T. Kikegawa, "Phase relations and volume changes of hafnia under high pressure and high temperature", *J. Am. Ceram. Soc. 84*, 1369 (2001).
Ohtani, E., O. Shimomura, M. Togaya, K. Suito, A. Onodera, H. Sawamoto, A. Yoneda, S. Tanaka, W. Utsumi, E. Ito, A. Matsumuro & T. Kikegawa, "High pressure generation by a multiple anvil system with sintered diamond anvils", *Rev. Sci. Instrum. 60*, 922 (1989).

Olijnyk, H., "High pressure x-ray diffraction studies on solid N_2 up to 43.9 GPa", *J. Chem. Phys. 93*, 8968 (1990).

Oliver, W. C. & J. B. Pethica, "Method for continuous determination of the elastic stiffness of contact between two bodies". *U.S. Patent No. 4848141* (July 1989).

Oliver, W. C. & G. M. Pharr, "An Improved Technique for Determining Hardness and Elastic-Modulus Using Load and Displacement Sensing Indentation Experiments", *J. Mater. Res. 7*, 1564 (1992).

Oliver, W. C. & G. M. Pharr, "Measurement of hardness and elastic modulus by instrumented indentation: Advances in understanding and refinements to methodology", *J. Mater. Res. 19*, 3 (2004).

Onodera, A., "Octahedral-anvil high-pressure devices", *High Temp. - High Pressures 19*, 579 (1987).

Osugi, J., K. Shimizu, K. Inoue & K. Yasunami, "A compact cubic anvil high pressure apparatus", *Rev. Phys. Chem. Jpn. 34*, 1 (1964).

Otto, J. W., J. K. Vassiliou & G. Frommeyer, "Compression behaviour of elastically anisotropic polycrystals using energy-dispersive X-ray diffraction", *J. Synchrotron Rad. 4*, 155 (1997).

Oyama, S. T. (ed.) *The Chemistry of Transition Metal Carbides and Nitrides* (Blackie Academic & Professional, London, 1996).

Palmqvist, S., "A method to determine the toughness of brittle materials, especially hard metals (in Swed.)", *Jernkontorets Ann. 141*, 303 (1957).

Petch, N. J., "The Cleavage Strength of Polycrystals", *J. Iron Steel Institute 174*, 25 (1953).

Petzow, G. & M. Herrmann, "Silicon Nitride Ceramics" in *High Performance Non-Oxide Ceramics II* (ed. Jansen, M.), pp. 47-167 (2002).

Pialoux, A., "Carbothermal Nitridation of Hafnium Dioxide Using High-Temperature X-Ray-Diffraction", *J. Nucl. Mater. 200*, 1 (1993).

Pierson, H. O., *Handbook of Refractory Carbides and Nitrides* (William Andrew Publishing, Noyes, 1996).

Poirier, J. P. & A. Tarantola, "A logarithmic equation of state", *Phys. Earth Planet. Inter. 109*, 1 (1998).

Ponton, C. B. & R. D. Rawlings, "Vickers indentation fracture toughness test Part 2: Application and critical evaluation of standardised indentation toughness equations", *Mater. Sci. Technol. 5*, 961 (1989a).

Ponton, C. B. & R. D. Rawlings, "Vickers indentation fracture toughness test Part 1: Review of literature and formulation of standardised indentation toughness equations", *Mater. Sci. Technol. 5*, 865 (1989b).

Provenzano, P. L., S. I. Boldish & W. B. White, "Vibrational-Spectra of Ternary Sulfides with Th_3P_4 Structure", *Mater. Res. Bull. 12*, 939 (1977).

Quinn, G. D. & R. C. Bradt, "On the Vickers indentation fracture toughness test", *J. Am. Ceram. Soc. 90*, 673 (2007).

Quinn, J. B. & G. D. Quinn, "Indentation brittleness of ceramics: A fresh approach", *J. Mater. Sci. 32*, 4331 (1997).

Rai, G., "Microstructure and mechanical properties of cubic boron nitride twinsert" in *New Diamond Science and Technology. MRS Int. Conf. Proc.*, pp. 1069-1079 (MRS, Pittsburgh, PA, 1991).

Reddy, G. L. N., J. V. Ramana, S. Kumar, S. V. Kumar & V. S. Raju, "Investigations on the oxidation of zirconium nitride films in air by nuclear reaction analysis and backscattering spectrometry", *Appl. Surf. Sci. 253*, 7230 (2007).

Reuss, A., "Berechnung der Fliesgrenzen von Mischkristallen", *Z. Angew. Math. Mech. 9*, 49 (1929).

Reynaud, C. & F. Thevenot, "Porosity dependence of mechanical properties of porous sintered SiC. Verification of the minimum solid area model", *J. Mater. Sci. Lett. 19*, 871 (2000).

Rice, R. W., "Evaluation and extension of physical property-porosity models based on minimum solid area", *J. Mater. Sci. 31*, 102 (1996).

Rice, R. W., *Porosity of ceramics* (Marcel Dekker, New York, 1998).

Richet, P., J. A. Xu & H. K. Mao, "Quasi-Hydrostatic Compression of Ruby to 500 Kbar", *Phys. Chem. Miner. 16*, 207 (1988).

Riedel, R., "Novel Ultrahard Materials", *Adv. Mater. 6*, 549 (1994).

Riedel, R. (ed.) *Handbook of Ceramic Hard Materials* (WILEY-VCH, Weinheim, 2000).

Rietveld, H. M., "A Profile Refinement Method for Nuclear and Magnetic Structures", *J. Appl. Cryst. 2*, 65 (1969).

Ristolainen, E. O., J. M. Molarius, A. S. Korhonen & V. K. Lindroos, "A Study of Nitrogen-Rich Titanium and Zirconium Nitride Films", *J. Vac. Sci. Technol. A 5*, 2184 (1987).

Rochegude, P., "Thermal Expansion from Universal Potential and Atomic Coordination", *Phys. Status Solidi B 208*, 379 (1998).

Rodriguez-Carvajal, J., "FULLPROF: A Program for Rietveld Refinement and Pattern Matching Analysis" in *The Satellite Meeting on Powder Diffraction of the XV Congress of the IUCr*, (Toulouse, France, July 16-18, 1990).

Rubie, D. C., "Characterising the sample environment in multianvil high-pressure experiments", *Phase Transitions 68*, 431 (1999).

Rudnayova, E., J. Dusza & M. Kupkova, "Comparison of Fracture-Toughness Measuring Methods Applied on Silicon-Nitride Ceramics", *J. Phys. IV 3*, 1273 (1993).

Ruoff, A. L., H. Xia & Q. Xia, "The effect of a traped aperture on x-ray diffraction from sample with a pressure gradient: Studies on three samples with a maximum pressure of 560 GPa", *Rev. Sci. Instrum. 63*, 4342 (1992).

Ruoff, A. L. & T. Li, "Phase-Transitions in III-V Compounds to Megabar Pressures", *Annu. Rev. Mater. Sci. 25*, 249 (1995).

Ryshkewitch, E., "Compression Strength of Porous Sintered Alumina and Zirconia. 9th Communication to Ceramography", *J. Am. Ceram. Soc. 36*, 65 (1953).

Sajgalik, P., J. Dusza & M. J. Hoffmann, "Relationship between microstructure, toughening mechanisms, and fracture toughness of reinforced silicon-nitride ceramics", *J. Am. Ceram. Soc. 78*, 2619 (1995).

Samsonov, G. V., *Nitrides (in russian)* (Naukova Dumka, Kiev, 1969).

Schettino, V. & R. Bini, "Molecules under extreme conditions: Chemical reactions at high pressure", *Phys. Chem. Chem. Phys. 5*, 1951 (2003).

Schnick, W., "Solid-State Chemistry with Nonmetal Nitrides", *Angew. Chem. Int. Edit. 32*, 806 (1993).

Schwarz, M., G. Miehe, A. Zerr, E. Kroke, B. T. Poe, H. Fuess & R. Riedel, "Spinel-Si_3N_4: Multi-anvil press synthesis and structural refinement", *Adv. Mater. 12*, 883 (2000).

Schwarz, M., "High Pressure Synthesis of Novel Hard Materials: Spinel-Si_3N_4 and Derivatives", *PhD thesis* (FB Material- und Geowissenschaften, TU Darmstadt, Darmstadt, 2005).

Scotti, N., W. Kockelmann, J. Senker, S. Trassel & H. Jacobs, "Sn_3N_4, a tin(IV) nitride - Syntheses and the first crystal structure determination of a binary tin-nitrogen compound", *Z. Anorg. Allg. Chem. 625*, 1435 (1999).

Sekine, T., H. L. He, T. Kobayashi, M. Zhang & F. F. Xu, "Shock-induced transformation of beta-Si_3N_4 to a high-pressure cubic-spinel phase", *Appl. Phys. Lett. 76*, 3706 (2000).

Sekine, T. & T. Mitsuhashi, "High-temperature metastability of cubic spinel Si_3N_4", *Appl. Phys. Lett. 79*, 2719 (2001).

Serghiou, G., G. Miehe, O. Tschauner, A. Zerr & R. Boehler, "Synthesis of a cubic Ge_3N_4 phase at high pressures and temperatures", *J. Chem. Phys. 111*, 4659 (1999).

Shemkunas, M. P., G. H. Wolf, K. Leinenweber & W. T. Petuskey, "Rapid synthesis of crystalline spinel tin nitride by a solid-state metathesis reaction", *J. Am. Ceram. Soc. 85*, 101 (2002).

Shemkunas, M. P., W. T. Petuskey, A. V. G. Chizmeshya, K. Leinenweber & G. H. Wolf, "Hardness, elasticity, and fracture toughness of polycrystalline spinel germanium nitride and tin nitride", *J. Mater. Res. 19*, 1392 (2004).

Sherman, D. & D. Brandon, "Mechanical Properties and their Relation to Microstructure" in *Handbook of Ceramic Hard Materials* (ed. Riedel, R.), pp. 66-103 (WILEY-VCH, Weinheim, 2000).

Shetty, D. K., I. G. Wright, P. N. Mincer & A. H. Clauer, "Indentation Fracture of Wc-Co Cermets", *J. Mater. Sci. 20*, 1873 (1985).

Sigalas, I. & R. J. Caveney, "Diamond Materials and their Applications" in *Handbook of Ceramic Hard Materials* (ed. Riedel, R.), pp. 479-572 (WILEY-VCH, Weinheim, 2000).

Singh, B. P., "A comparison of equations of state including the generalized Rydberg EOS", *Physica B 369*, 111 (2005).

Sneddon, I. N., "The relation between load and penetration in the axisymmetric boussinesq problem for a punch of arbitrary profile", *Int. J. Eng. Sci. 3*, 47 (1965).

Soignard, E., M. Somayazulu, J. J. Dong, O. F. Sankey & P. F. McMillan, "High pressure-high temperature synthesis and elasticity of the cubic nitride spinel gamma-Si_3N_4", *J. Phys.: Condens. Matter 13*, 557 (2001a).

Soignard, E., M. Somayazulu, H. K. Mao, J. J. Dong, O. F. Sankey & P. F. McMillan, "High pressure-high temperature investigation of the stability of nitride spinels in the systems Si_3N_4-Ge_3N_4", *Solid State Commun. 120*, 237 (2001b).

Soignard, E., P. F. McMillan, T. D. Chaplin, S. M. Farag, C. L. Bull, M. S. Somayazulu & K. Leinenweber, "High-pressure synthesis and study of low-compressibility molybdenum nitride (MoN and MoN_{1-x}) phases", *Phys. Rev. B 68*, 132101 (2003).

Soignard, E., P. F. McMillan, C. Hejny & K. Leinenweber, "Pressure-induced transformations in alpha- and beta-Ge_3N_4: in situ studies by synchrotron X-ray diffraction", *J. Solid State Chem. 177*, 299 (2004a).

Soignard, E., P. F. McMillan & K. Leinenweber, "Solid solutions and ternary compound formation among Ge_3N_4-Si_3N_4 nitride spinels synthesized at high pressure and high temperature", *Chem. Mater. 16*, 5344 (2004b).

Solozhenko, V. L., D. Andrault, G. Fiquet, M. Mezouar & D. C. Rubie, "Synthesis of superhard cubic BC_2N", *Appl. Phys. Lett. 78*, 1385 (2001).

Somayazulu, M. S., K. Leinenweber, H. Hubert, P. F. McMillan & G. Wolf, "High pressure-high temperature synthesis of spinel Ge_3N_4" in *Science and Technology of High Pressure, Proceedings of AIRAPT-17* (eds. Manghnani, M. H., W. J. Nellis & M. F. Nicol), p. 663 (Universities Press, Hyderbad, India, 2000).

Spain, I. L. & P. Bolsaitis, "Phase Transformations at High Pressures" in *High Pressure Technology, Vol. 2* (eds. Spain, I. L. & J. Paauwe), pp. 109-160 (Marcel Dekker, New York, 1977).

Spain, I. L. & J. Paauwe (eds.) *High Pressure Technology* (Marcel Dekker, New York, 1977).

Spriggs, R. M., "Expression for effect of porosity on elastic modulus of polycrystalline refractory materials, particularly aluminum oxide", *J. Am. Ceram. Soc. 44*, 628 (1961).

Stacey, F. D., "The K-primed approach to high-pressure equations of state", *Geophys. J. Int. 143*, 621 (2000).

Stacey, F. D. & P. M. Davis, "High pressure equations of state with applications to the lower mantle and core", *Phys. Earth Planet. Inter. 142*, 137 (2004).

Steinberg, H., "Hochdruckexperimente an Calciumsilikatphasen zur Rekonstruktion der Aufstiegsgeschichte von Diamanten", *PhD thesis* (Institut für Geowissenschaften, J. W. Goethe-Universität, Frankfurt / Main, 2005).

Stishov, S. M. & S. V. Popova, "New dense polymorphic modification of silica", *Geokhimiya 10*, 923 (1961).

Stolen, S. & T. Grande, *Chemical Thermodynamics of Materials* (J. Wiley & Sons, Chichester, 2004).

Straboni, A., L. Pichon & T. Girardeau, "Production of stable and metastable phases of zirconium nitrides by NH_3 plasma nitridation and by double ion beam sputtering of zirconium films", *Surf. Coat. Technol. 125*, 100 (2000).

Su, Y. L. & W. H. Kao, "Optimum multilayer TiN-TiCN coatings for wear resistance and actual application", *Wear 223*, 119 (1998).

Sung, C. M. & M. Sung, "Carbon nitride and other speculative superhard materials", *Mater. Chem. Phys. 43*, 1 (1996).

Sussmann, R. S., J. R. Brandon, G. A. Scarsbrook, C. G. Sweeney, T. J. Valentine, A. J. Whitehead & C. J. H. Wort, "Properties of bulk polycrystalline CVD diamond", *Diamond Relat. Mater. 3*, 303 (1994).

Szymanski, A. & J. M. Szymanski, *Hardness Estimation of Minerals, Rocks and Ceramic Materials* (Elsevier, Amsterdam, 1989).

Tabor, D., *The hardness of metals* (Clarendon Press, Oxford, 1951).

Takano, M. & A. Onodera, "High pressure synthesis in inorganic systems", *Curr. Opin. Solid State Mater. Sci. 2*, 166 (1997).

Takano, M., S. Tagami, K. Minato, T. Kozaki & S. Sato, "Lattice thermal expansions of (Dy, Zr)N solid solutions", *J. Alloys Compd. 439*, 215 (2007).

Tanaka, I., F. Oba, T. Sekine, E. Ito, A. Kubo, K. Tatsumi, H. Adachi & T. Yamamoto, "Hardness of cubic silicon nitride", *J. Mater. Res. 17*, 731 (2002).

Tancret, F., G. Desgardin & F. Osterstock, "Influence of porosity on the mechanical properties of cold isostatically pressed and sintered $YBa_2Cu_3O_{7-x}$ superconductors", *Philos. Mag. A 75*, 505 (1997).

Taniguchi, T., M. Akaishi & S. Yamaoka, "Mechanical properties of polycrystalline translucent cubic boron nitride as characterized by the vickers indentation method", *J. Am. Ceram. Soc. 79*, 547 (1996).

Teter, D. M. & R. J. Hemley, "Low-Compressibility Carbon Nitrides", *Science 271*, 53 (1996).

Teter, D. M., "Computational alchemy: The search for new superhard materials", *MRS Bull. 23*, 22 (1998).

Toth, L. E., *Transition metal carbides and nitrides* (Academic Press, New York, 1971).

Tsuchida, Y. & T. Yagi, "A new, post-stishovite highpressure polymorph of silica", *Nature 340*, 217 (1989).

Utsumi, Y., S. Yamata, H. Hara, N. Kaneki & K. Shimada, "Cutting performance of sintered cubic boron nitride with Al_2O_3-TiC binder" in *New Diamond Science and Technology. MRS Int. Conf. Proc.*, pp. 1081-1086 (MRS, Pittsburgh, PA, 1991).

van Eldik, R. & C. D. Hubbard, *Chemistry under extreme or non-classical conditions* (J. Wiley & Sons, New York, 1997).

Vel, L., G. Demazeau & J. Etourneau, "Cubic boron nitride - Synthesis, physicochemical properties and applications", *Mater. Sci. Eng. B 10*, 149 (1991).

Velez, K., S. Maximilien, D. Damidot, G. Fantozzi & F. Sorrentino, "Determination by nanoindentation of elastic modulus and hardness of pure constituents of Portland cement clinker", *Cement Concrete Res. 31*, 555 (2001).

Veprek, S., "The search for novel, superhard materials", *J. Vac. Sci. Technol. A 17*, 2401 (1999).

Vinet, P., J. H. Rose, J. Ferrante & J. R. Smith, "Universal Features of the Equation of State of Solids", *J. Phys.: Condens. Matter 1*, 1941 (1989).

Voigt, W., *Lehrbuch der Kristallphysik* (Teubner, Leipzig, 1928).

Von Platen, B., "A multiple piston, high-pressure, high-temperature apparatus" in *Modem very high pressure technics* (ed. Wentorf, R. H.), pp. 118-136 (Butterworths, London, 1962).

Wagh, A. S., J. P. Singh & R. B. Poeppel, "Dependence of Ceramic Fracture Properties on Porosity", *J. Mater. Sci. 28*, 3589 (1993).

Walker, D., M. A. Crpenter & C. Hitch, "Some simplifications to multianvil devices for high pressure experiments", *Amer. Mineral. 75*, 1020 (1990).

Walter, M. J., Y. Thibault, K. Wei & R. W. Luth, "Characterizing experimental pressure and temperature conditions in multi-anvil apparatus", *Can. J. Phys. 73*, 273 (1995).

Wang, J. C., "Young modulus of porous materials. 1. Theoretical derivation of modulus porosity correlation", *J. Mater. Sci. 19*, 801 (1984).

West, A. R., "Phase Transitions" in *Solid State Chemistry and its Applications*, pp. 417-451 (J. Wiley & Sons, Chichester, 1989).

Wiame, H., M. A. Centeno, S. Picard, P. Bastians & P. Grange, "Thermal oxidation under oxygen of zirconium nitride studied by XPS, DRIFTS, TG-MS", *J. Eur. Ceram. Soc. 18*, 1293 (1998).

Xu, M., S. Y. Wang, G. Yin, J. Li, Y. X. Zheng, L. Y. Chen & Y. Jia, "Optical properties of cubic Ti_3N_4, Zr_3N_4, and Hf_3N_4", *Appl. Phys. Lett. 89*, 151908 (2006).

Yajima, A., Y. Segawa, R. Matsuzaki & Y. Saeki, "Reaction process of zirconium tetrachloride with ammonia in the vapor phase and properties of the zirconium nitride formed", *Bull. Chem. Soc. Jpn. 56*, 2638 (1983).

Yajima, A., M. Akiyama & Y. Saeki, "Formation Process of Hafnium Nitride by the Reaction of Hafnium Tetrachloride with Ammonia in the Vapor-Phase and Properties of the Hafnium Nitride Formed", *J. Chem. Soc. Jpn.*, 1175 (1986).

Yang, J. F., T. Ohji, S. Kanzaki, A. Diaz & S. Hampshire, "Microstructure and mechanical properties of silicon nitride ceramics with controlled porosity", *J. Am. Ceram. Soc. 85*, 1512 (2002).

Young, A. F., C. Sanloup, E. Gregoryanz, S. Scandolo, R. J. Hemley & H. K. Mao, "Synthesis of novel transition metal nitrides IrN_2 and OsN_2", *Phys. Rev. Lett. 96*, 155501 (2006).

Young, R. A., *The Rietveld Method* (Universities Press, Oxford, 1993).

Zerr, A., L. Chudinovskikh, L. Zhang, H.-J. Reichmann & R. Boehler, "Pressure Induced Anisotropy of Argon, Pressure Scale and Equation of State" in *HASYLAB Annual Report*, p. 650 (HASYLAB at DESY, Hamburg, 1993).

Zerr, A., G. Miehe, G. Serghiou, M. Schwarz, E. Kroke, R. Riedel, H. Fuess, P. Kroll & R. Boehler, "Synthesis of cubic silicone nitride", *Nature 400*, 340 (1999).

Zerr, A. & R. Riedel, "Introduction: Novel Ultrahard Materials" in *Handbook of Ceramic Hard Materials* (ed. Riedel, R.), pp. XLV-LXXVII (WILEY-VCH, Weinheim, 2000).

Zerr, A., G. Serghiou & R. Boehler, "Phase Transitions and Material Synthesis using the CO_2-Laser Heating Technique in a Diamond Cell" in *Handbook of Ceramic Hard Materials* (ed. Riedel, R.), pp. 41-65 (WILEY-VCH, Weinheim, 2000).

Zerr, A., M. Kempf, M. Schwarz, E. Kroke, M. Goken & R. Riedel, "Elastic moduli and hardness of cubic silicon nitride", *J. Am. Ceram. Soc. 85*, 86 (2002a).

Zerr, A., M. Schwarz, R. Schmechel, R. Kolb, H. von Seggern & R. Riedel, "New high-pressure nitrides", *Acta Cryst. A 58*, C47 (2002b).

Zerr, A., G. Miehe & R. Riedel, "Synthesis of cubic zirconium and hafnium nitride having Th_3P_4 structure", *Nat. Mater. 2*, 185 (2003).

Zerr, A., R. Riedel, T. Sekine, J. E. Lowther, W. Y. Ching & I. Tanaka, "Recent advances in new hard high-pressure nitrides", *Adv. Mater. 18*, 2933 (2006a).

Zerr, A., G. Serghiou, R. Boehler & M. Ross, "Decomposition of alkanes at high pressures and temperatures", *High Pressure Res. 26*, 23 (2006b).

Acknowledgements

First I would like to thank Prof. Dr. Dr. h. c. Ralf Riedel, my doctoral advisor, for giving me the opportunity to perform this research in his group, for his great interest in high-pressure science, for supervision and ongoing encouragement throughout my work. I also thank him for a certain freedom given me in this research.

Likewise, I express my heartfelt gratitude to Dr. Andreas Zerr, my doctoral co-advisor, for continuous support, guidance and strong motivation, fruitful discussions and constructive criticism. I deeply appreciate his valuable advices and help in different life situations. I also thank him for reading the drafts and for useful comments. His suggestions significantly improved the thesis.

My special thanks go to Prof. Dr. Dr. h. c. Hartmut Fueß for introducing me into the "Methods of Materials Science", for his kind acceptance to act as co-referee of my thesis as well as for his carefull reading of the manuscript and valuable remarks and corrections.

I would like to acknowledge Prof. Dr. Gerhard Brey for the allowance to perform high-pressure experiments in his group of Petrology and Geochemistry (Institut für Geowissenschaften, J.W. Goethe Universität, Frankfurt/Main). I am very grateful to Dr. Vadim Bulatov for teaching me the multi-anvil technique, for advices and help in high-pressure experiments. I also thank Thomas Kautz, Dr. Holger Steinberg and Margaret Hanrahan for assistance and technical support during my work in the Petrology and Geochemistry Group.

I am very thankful to Dr. Gerhard Miehe for TEM measurements and for fruitful discussions and fresh ideas regarding XRD data and structure refinement.

I am indebted to Brunhilde Thybusch for her interest and patience with problematical EPMA measurements.

I am very grateful to Elmar Schweitzer and Prof. Dr. Mathias Göken for nanoindentation measurements, fruitful discussions and their experimental initiative.

I am also thankful to Dr. Reinhard Boehler, Dr. Mikhail Eremets and all former colleagues from the High Pressure Group of the Max-Planck-Institut für Chemie in Mainz, where I performed my undergraduate studies. I had a very nice time there and gained invaluable experience in laser-heated diamond anvil cells-, powder XRD- and Raman techniques. I also thank Dr. Reinhard Boehler for the open access to the facilities in his group, e.g. diamond anvil cells and gas-loader.

My further thanks go to:

Dr. Mohamed Mezouar (beam-line ID27, ESRF, Grenoble) for his great assistance during synchrotron experiments with a Gandolfi-camera

Dr. Thomas Wroblewski (HASYLAB/DESY, Hamburg) for technical support in experiments at the beam-line F3.

Dr. Joachim Brötz and Aleksandra Gruzdeva for preliminary XRD measurements

Jean-Christophe Jaud for assistance in high-temperature XRD measurements

Claudia Fasel for introduction to the hot-gas-extraction elemental analysis

Dr. Dmytro Trots for discussions and advices regarding “pitfalls” of the Fullprof software

Dr. Thomas Locherer for discussions and sharing his unpublished (at that time) data

Dr. Isabel Kinski for introduction to the Schlenck-glassware and pyrolysis technique

Dr. Björn Schwarz for attempts to perform SQUID measurements on my “too small” samples

I am also very thankful to all my colleagues at the FG Disperse Feststoffe, FB Material- und Geowissenschaften, TU Darmstadt, for the great and friendly working atmosphere, their cheerful mood, useful advices and good humor.

Last but not least, I express my hearty thanks to my parents Valentina and Anatoliy, my sister Iulia, my wife Galyna as well as to my friends, Dmitry Goryntsev, Igor and Elena Abakumov for their love, understanding and support during my stay in Germany and for their belief in me which inspired me in my endeavors.

This work was financially supported by the Deutsche Forschungsgemeinschaft (Bonn, Germany), the Fonds der Chemischen Industrie (Frankfurt, Germany), DESY (Hamburg, Germany) and ESRF (Grenoble, France).

Eidesstattliche Erklärung

Hiermit erkläre ich an Eides Statt, dass ich meine Dissertation selbständig und nur mit den angegebenen Hilfsmitteln angefertigt habe und noch keinen Promotionsversuch unternommen habe.

Darmstadt, den

Curriculum Vitae

Personal Data

Name:	Dmytro A. Dzivenko
Date and Place of Birth:	5 August 1981, Kramatorsk (Ukraine)
Marital Status:	Married
Nationality:	Ukrainian

Education

2004 - 2008	Doctoral studies, FG Disperse Feststoffe, FB Material- und Geowissenschaften, TU Darmstadt, Darmstadt, Germany
2002 - 2004	MSc, Moscow Institute of Physics and Technology – State University, Moscow, Russian Federation
1998 - 2002	BSc, Moscow Institute of Physics and Technology – State University, Moscow, Russian Federation
1988 - 1998	Secondary School, Kramatorsk, Ukraine

Professional Experience

2009 -	Research scientist, FG Disperse Feststoffe, FB Material- und Geowissenschaften, TU Darmstadt, Darmstadt, Germany
2004 - 2008	Research associate, FG Disperse Feststoffe, FB Material- und Geowissenschaften, TU Darmstadt, Darmstadt, Germany
2002 - 2004	Research assistant, Hochdruckgruppe, Max-Planck-Institut für Chemie, Mainz, Germany
2001 - 2002	Research assistant, Analytic Department, Institute for High Pressure Physics, Troitsk, Russian Federation

Related publications

- J. Li, D. A. Dzivenko, A. Zerr, C. Fasel, Y. P. Zhou, R. Riedel, Synthesis of nanocrystalline Zr_3N_4 and Hf_3N_4 powders from metal dialkylamides, *Z. Anorg. Allg. Chem. 631*, 1449 (2005).

- D. A. Dzivenko, A. Zerr, R. Boehler, R. Riedel, Equation of state of cubic hafnium(IV) nitride having Th_3P_4-type structure, *Solid State Commun. 139*, 255 (2006).

- D. A. Dzivenko, A. Zerr, V. K. Bulatov, G. Miehe, J. Li, B. Thybusch, J. Brötz, H. Fuess, G. Brey, R. Riedel, High-pressure multi-anvil synthesis and structure refinement of oxygen-bearing cubic zirconium(IV) nitride, *Adv. Mater. 19*, 1869 (2007).

- D. A. Dzivenko, A. Zerr, E. Schweitzer, M. Göken, R. Boehler, R. Riedel, Elastic moduli and hardness of c-$Zr_{2.86}(N_{0.88}O_{0.12})_4$ having Th_3P_4-type structure, *Appl. Phys. Lett. 90*, 191910 (2007).

- D. A. Dzivenko, E. Horvath-Bordon, A. Zerr, G. Miehe, P. Kroll, R. Boehler, P. F. McMillan, R. Riedel, High-pressure high-temperature synthesis of novel binary and ternary nitride phases of group 4 and 14 elements, *J. Phys.: Conf. Ser. 121*, 062003 (2008).

- D. A. Dzivenko, A. Zerr, G. Miehe, R. Riedel, Synthesis and properties of oxygen-bearing c-Zr_3N_4 and c-Hf_3N_4, *J. Alloys Compd. 420* (2009) 46.

Other publications

- M. I. Eremets, A. G. Gavriliuk, I. A. Trojan, D. A. Dzivenko, R. Boehler, Single-bonded cubic form of nitrogen, *Nat. Mater. 3*, 558 (2004).
- M. I. Eremets, A. G. Gavriliuk, N. R. Serebryanaya, I. A. Trojan, D. A. Dzivenko, R. Boehler, H. K. Mao, R. J. Hemley, Structural transformation of molecular nitrogen to a single-bonded atomic state at high pressures, *J. Chem. Phys. 121*, 11296 (2004).
- R. Riedel, E. Horvath-Bordon, P. Kroll, G. Miehe, D. A. Dzivenko, H.-J. Kleebe, P. A. van Aken, S. Lauterbach, Novel binary and ternary phases in the Si-C-N System, *J. Ceram. Soc. Jpn. 116*, 674 (2008).
- A. Gurlo, D. A. Dzivenko, P. Kroll, R. Riedel, High-pressure high-temperature synthesis of Rh_2O_3-II-type In_2O_3 polymorph, *Phys. Stat. Sol. (RRL) 2* (2008) 269.
- R. Niewa, D. Rau, A. Wosylus, K. Meier, M. Hanfland, M. Wessel, R. Dronskowski, D. A. Dzivenko, R. Riedel, U. Schwarz, High-pressure high-temperature single-crystal growth, ab initio electronic structure calculations and equation of state of ε-Fe_3N_{1+x}, *Chem. Mater. 21* (2009) 392.
- A. Zerr, G. Miehe, J.-W. Li, D. A. Dzivenko, V. K. Bulatov, H. Höfer, N. Bolfan-Casanova, M. Fialin, G. Brey, T. Watanabe, M. Yoshimura, High-pressure synthesis of tantalum nitride having orthorhombic U_2S_3 structure, *Adv. Funct. Mater. 19* (2009) 2282.